

SENSORS AND ACTUATORS FOR 2D AND 3D CELL CULTURE MODELS BASED ON OXYGEN SENSITIVE CULTURE SUBSTRATES

DISSERTATION

zur Erlangung des

DOKTORGRADES DER NATURWISSENSCHAFTEN (Dr. rer. nat.)

der Fakultät für Chemie und Pharmazie

der Universität Regensburg



vorgelegt von

Carina Schmittlein aus Ingolstadt

im November 2017

SENSORS AND ACTUATORS FOR 2D AND 3D CELL CULTURE MODELS BASED ON OXYGEN SENSITIVE CULTURE SUBSTRATES

DISSERTATION

zur Erlangung des

DOKTORGRADES DER NATURWISSENSCHAFTEN (Dr. rer. nat.)

der Fakultät für Chemie und Pharmazie

der Universität Regensburg



vorgelegt von

Carina Schmittlein aus Ingolstadt

im November 2017

Diese Arbeit entstand in der Zeit von Juni 2013 bis November 2017 am Institut für Analytische Chemie, Chemo- und Biosensorik der Fakultät Chemie und Pharmazie der Universität Regensburg.

Die Arbeit wurde unter der Leitung von Prof. Dr. Joachim Wegener angefertigt.

Promotionsgesuch eingereicht am: _____

Kolloquiumstermin: _____

Prüfungsausschuss:

Vorsitzender: Apl. Prof. Dr. Rainer Müller

Erstgutachter: Prof. Dr. Joachim Wegener

Zweitgutachter: Prof. Dr. Jörg Heilmann

Drittprüferin: PD Dr. Miriam Breunig

Für meine Familie

井の中の蛙大を知らず。

“a frog in the well doesn't know the sea.”

CONTENTS

1	INTRODUCTION	1
1.1	Oxygen in Biological Systems	1
1.2	State-of-the-Art of Oxygen Sensing	5
2	OBJECTIVES	21
3	MATERIALS AND METHODS	23
3.1	Cell Culture Techniques	23
3.1.1	Cultivation of Adherent Cell Lines	23
3.1.2	Subcultivation	25
3.1.3	Cultivation of Spheroids	26
3.1.4	Composition of Buffers and Solutions	27
3.1.5	Cyropreservation	28
3.2	Ratiometric Optical Oxygen Sensing	29
3.2.1	Principles of Ratiometric Optical Oxygen Sensing	29
3.2.2	Commercial Sensor Systems	31
3.2.2.1	VisiSens A1	32
3.2.2.2	VisiSens TD mic	33
3.2.3	Preparation of Oxygen Sensor Foils for Cell Experiments	35
3.2.4	Coating of Oxygen Sensor Foils with Adhesion Promoting Reagents	37
3.2.5	Calibration	38
3.2.6	Determination of the (Apparent) Oxygen Consumption Rates	39
3.3	Microscopic Techniques	41
3.3.1	Phase Contrast Microscopy	41
3.3.2	Stereomicroscopy	41
3.3.3	Confocal Laser Scanning Microscopy (CLSM)	42
3.3.4	Cytochemical Staining	43

3.4	Impedance Spectroscopy	46
3.4.1	Principles of Impedance Spectroscopy	46
3.4.2	Electric Cell-Substrate Impedance Sensing (ECIS)	48
3.4.3	Set-Up for Oxygen Sensing and Impedance Measurements: ECIS-O ₂	49
3.4.3.1	Electrode Layout and Chip Fabrication	49
3.4.3.2	Measurement Set-Up	51
3.4.3.3	Experimental Procedure	52
3.4.3.4	Correction of Spectra	53
3.5	Wound Healing Assays	54
3.5.1	Optical Assay	54
3.5.2	Scratch Assay	56
3.5.3	Barrier Assay	57
3.5.4	Electrical ECIS [®] Assay	58
3.5.5	Determination of Wound Healing Rate	59
4	IMAGING THE OXYGEN CONSUMPTION OF ADHERENT CELLS IN MONOLAYERS	61
4.1	Biocompatibility and Photostability of Oxygen Sensitive Culture Substrates	62
4.1.1	Photostability	62
4.1.2	Cytocompatibility	63
4.2	Oxygen Consumption in Open and Closed Systems	67
4.3	Dependency of Oxygen Consumption Rates on Medium Composition	69
4.4	Oxygen Consumption in Dependency on Seeding Density	71
4.4.1	MDCK II Cells	71
4.4.2	NRK Cells	73
4.5	Oxygen Consumption of BAEC & U-373 MG Cells	74
4.6	Influence of pH on Oxygen Consumption	76
4.7	Influence of Drugs on Oxygen Consumption	78
4.8	Influence of Toxins on Oxygen Consumption	80

4.8.1	Treatment of NRK Cells with Carbon Dots	80
4.8.2	Treatment of NRK Cells with CdCl ₂	82
4.9	Imaging Oxygen Gradients within an Isolated Cell Patch	85
4.10	Discussion	87
4.10.1	Oxygen Consumption in Open and Closed Systems	87
4.10.2	Influence of Medium Composition	88
4.10.3	Influence of Cell Seeding Density on Oxygen Consumption	89
4.10.4	Influence of pH on Oxygen Consumption	92
4.10.5	Influence of Drugs and Toxins on Oxygen Consumption	93
4.11	Outlook	96
5	ECIS-O ₂ – A DUAL TRANSDUCER FOR ELECTRICAL AND LUMINESCENT READOUT	99
5.1	Characterization of the Dual Sensor Set-Up	100
5.1.1	1 st Generation Sensor Layout	100
5.1.2	2 nd Generation Sensor Layout	102
5.1.3	Electrode Characterization and Baseline Measurements	103
5.2	Monitoring of Cell Adhesion	106
5.3	Monitoring of Drug Exposure	108
5.3.1	Influence of Uncouplers of Oxidative Phosphorylation	108
5.3.2	Influence of Blockers of Oxidative Phosphorylation	110
5.4	Discussion	112
5.5	Outlook	114
6	IMAGING OXYGEN GRADIENTS IN MCF-7 SPHEROIDS	115
6.1	Cytocompatibility of Sensor Foils and Spheroid Adhesion	116
6.2	Imaging Oxygen Gradients in MCF-7 Spheroids	118
6.2.1	Gradient Formation	118

6.2.2	Oxygen Gradients in MCF-7 Spheroids of different age	120
6.2.3	Comparison of VisiSens TD mic Performance with VisiSens A1	123
6.3	Exposure to Drugs influencing Oxidative Phosphorylation	125
6.4	Discussion	131
6.4.1	Imaging Oxygen Gradients in MCF-7 Spheroids	131
6.4.2	Exposure to Drugs influencing Oxidative Phosphorylation	133
6.5	Outlook	135
7	DEVELOPMENT OF AN OPTICAL WOUND HEALING ASSAY	137
7.1	Characterization of Substrates for Oxygen-based Wound Healing Assays	138
7.1.1	Biocompatibility and Wound Geometry	138
7.1.2	Dependency on Excitation Wavelength	141
7.1.3	Dependency on Culture Medium	142
7.1.4	Dependency on Filters	143
7.1.5	Scavenging the Cytotoxic Influence of Singlet Oxygen by Vitamin E	145
7.2	Comparison of Different Wound Healing Assays	147
7.2.1	Oxygen-based Optical Wound Healing Assay	147
7.2.2	Scratch Assay	150
7.2.3	Barrier Assay	152
7.2.4	Electrical ECIS® Assay	155
7.3	Proof-of-Concept Studies	157
7.3.1	Influence of Serum Starvation on the Wound Healing Rate	157
7.3.2	Influence of Cytochalasin D on the Wound Healing Rate	159
7.3.3	Influence of Extracellular pH on the Wound Healing Rate	161
7.4	Discussion	163
7.4.1	Characterization of Substrates for Oxygen-based Wound Healing Assays	163
7.4.2	Comparison of Different Wound Healing Assays	165
7.4.3	Proof-of-Concept Studies	168

7.5	Outlook	170
8	SUMMARY	171
9	ZUSAMMENFASSUNG	175
10	REFERENCES	179
11	APPENDIX	204
11.1	Supplementary Information	204
11.2	List of Abbreviations	225
11.3	Materials and Instrumentations	227
11.4	Curriculum Vitae	230
11.5	Danksagung	233
11.6	Eidesstattliche Erklärung	235

1 INTRODUCTION

1.1 OXYGEN IN BIOLOGICAL SYSTEMS

In the early 17th century scientists found out that a compound in air was necessary for life. This finding was based on experiments performed by John Mayow who realized that when a mouse and a burning candle were put together in an enclosed chamber, the candle efficiently depleted the compound in the air which was necessary for the mouse to stay alive (Mayow et al. 1907). One century later work on Mayow's theory of the "nitro aerial spirit" that was necessary for living was continued in experiments conducted by Lavoisier, Scheele and Priestley. The results led to the recognition of a component named "eminently breathable air" that was later known as oxygen (Severinghaus 2002).

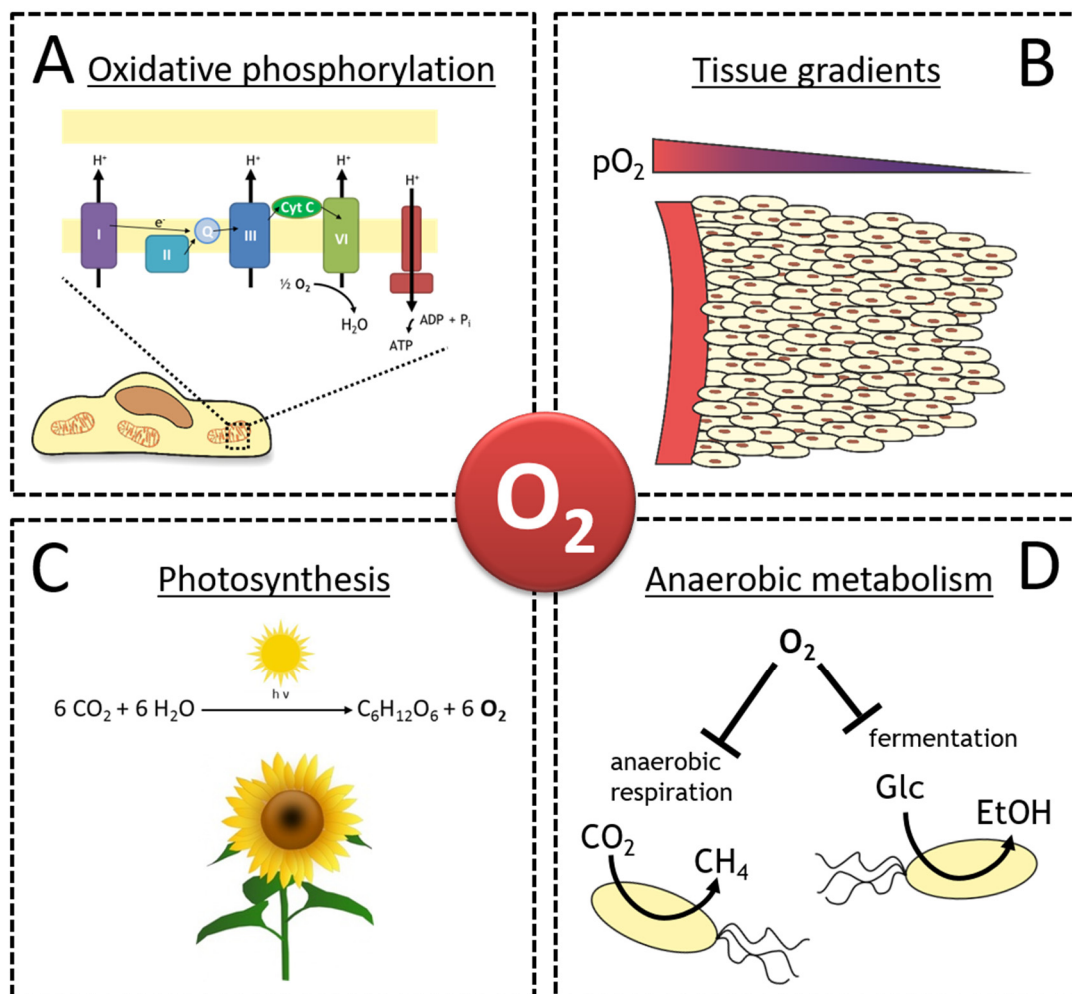


Fig. 1.1 Overview of the biological relevance of oxygen. (A) Oxygen is the fuel for cellular oxidative phosphorylation – a highly efficient mechanism to generate ATP. (B) Oxygen gradients regulate cellular behavior in multicellular organisms. (C) Oxygen is produced as a by-product of photosynthesis. (D) Anaerobic metabolism which relies on energy generation by fermentation or anaerobic respiration is heavily impaired by the presence of oxygen.

Oxygen is a molecule of utmost importance for biological systems because its presence or absence is either necessary to sustain life or to induce detrimental damage in living organisms as depicted in **Fig. 1.1**. Thus, oxygen concentration is an important analytical parameter to describe the conditions and metabolic activity of biological systems. Molecular oxygen enables organisms to extract energy more efficiently by aerobic metabolism. With oxygen as oxidant, energy efficacy of aerobic metabolism is increased compared to anaerobic metabolism or sole glycolysis as aerobes can produce 16 – 18 times more adenosine triphosphate (ATP) per hexose (Catling et al. 2005). This process of cellular energy generation is called oxidative phosphorylation (**Fig. 1.1, A**). In eukaryotes, such as mammalian cells, the machinery driving oxidative phosphorylation is located in the inner membrane of the mitochondria – small organelles inside the cell. This machinery consists of multiple proteins named complex I – IV that transfer electrons along the inner membrane via the electron transport chain. Products generated in the citric acid cycle, such as NADH and succinate are fed as e^- and H^+ donors to the electron transport chain. Oxygen is used as terminal acceptor molecule for the transferred electrons at complex VI and is reduced to water. At the same time, enzymes of the electron transport chain pump protons from the mitochondrial matrix to the intermembrane space. This leads to the creation of an electrical potential and a proton gradient across the mitochondrial membrane. This proton motive force is needed to drive ATP synthesis by the ATP-synthase (Berg et al. 2012). Consequently, changes of mitochondrial respiration rates and oxygen consumption caused by mitochondrial dysfunction have a deep impact on cellular energy metabolism. Measuring oxygen consumption rates of cells allows not only to study cellular bioenergetics but also to get a deeper insight into the impact of genetic defects or toxic compounds on mitochondrial oxidative phosphorylation (Brand and Nicholls 2011).

Changes in oxygen level are a factor that not only drastically influences cellular bioenergetics but also behavior and viability. Especially in multicellular organisms and tissues oxygen transport is limited which leads to the formation of oxygen gradients (**Fig. 1.1, B**). In humans, oxygen is transported to the tissue via hemoglobin in the blood circulation system. Due to cellular respiration and differences in oxygen supply, oxygen partial pressure (pO_2) ranges from 5 – 75 torr in human organs while the atmospheric pO_2 value is about 160 torr. Oxygen levels vary depending on the organism and organ and need to be tightly controlled to maintain homeostasis (Carreau et al. 2011). Homeostasis of oxygen levels is not only needed to maintain normal physiology. Adaption to low pO_2 is a necessary condition for cell differentiation and development that is regulated by HIF (hypoxia-inducible factor) mediated gene expression. During embryonic development, low oxygen

levels induce cell aggregation and differentiation of stem cells. Oxygen is also a key factor in angiogenesis, adipogenesis, bone morphogenesis and hematopoiesis (Simon and Keith 2008). Also in adults, low oxygen levels are required in the microenvironment of the stem cell niches to maintain their undifferentiated status (Jez et al. 2015). Disruption of oxygen homeostasis due to elevated or decreased oxygen levels is often linked to erroneous HIF signaling and may cause disease. High pO_2 can lead to increased formation of reactive oxygen species that cannot be scavenged by cellular antioxidants. This oxidative stress evokes damage due to oxidation of lipids, amino acids or nucleic acids which are connected to phenomena such as apoptosis, ageing and cancer (Maltepe and Saugstad 2009). On the other hand, oxygen deficiency can result in pathological hypoxia which is an important factor in pathobiological diseases, such as stroke or heart disease. Oxygen delivery to certain brain areas of patients suffering from stroke is inhibited due to occlusions or lesions of the blood vessels. This induces the formation of highly hypoxic brain areas. Low pO_2 rapidly induces neurological damage resulting in severe cognitive and neuromuscular impairment (Ferdinand and Roffe 2016). Hypoxia is also closely linked to kidney disease. Studies have shown, that prolonged low oxygen levels induce inflammation of the glomeruli and chronic kidney disease, leading to a breakdown of renal filtration which can ultimately result in kidney failure (Nangaku and Eckardt 2007). Oxygen levels in tumorous tissue are often lower compared to healthy tissue. Hypoxic cancer tissue possesses a higher resistance to drug and radiation treatment, resulting in higher death rates of patients. Low pO_2 leads to increased transcription of HIF in cancer cells, which may activate the expression of genes which induce neovascularization, immune evasion, metabolic re-programming, tumor invasion and metastasis (Semenza 2011). Thus, monitoring oxygen content in cell or tissue cultures, animal models and patients is of utmost importance to study the impact of pO_2 on drug efficacy or disease progression. Furthermore, oxygenation in cell culture and tissue culture is an important parameter for differentiation and wound closure which is particularly interesting for regenerative medicine and bioengineering (Orlando et al. 2013).

Plants, algae and cyanobacteria release oxygen as a by-product of photosynthetic activity (**Fig. 1.1, C**). The photosynthetically driven production of oxygen and simultaneous fixation of carbon dioxide into carbohydrates provides not only a habitable atmosphere, but it is also required for most aerobic organisms as fuel for energy extraction. Photosynthesis is defined as the light driven generation of chemical energy in the form of carbohydrates. In higher plants, the enzymatic machinery engaged in photosynthesis is located inside small organelles – the chloroplasts. These organelles contain a third inner so-called thylakoid membrane which contains protein complexes that are necessary for

the light dependent generation of ATP and NADPH. Upon irradiation, electrons are translocated from a chlorophyll molecule inside the photosystem II complex. The electrons are transported across the thylakoid membrane by cofactors and protein complexes to generate NADPH. During this process, protons are pumped to the thylakoid lumen and both, a chemiosmotic and an electrical gradient are established that drive photophosphorylation of ATP by the F-ATPase. NADPH and ATP, which are generated during the light dependent reaction, are introduced in the light-independent Calvin cycle to drive carbohydrate synthesis by CO₂ fixation. To replace electrons translocated from photosystem II, two molecules of water are oxidized to molecular oxygen which is then released as waste product (Nelson and Ben-Shem 2004). However, photosynthetically active organisms also consume oxygen by respiration. Oxygen consumption can easily exceed photosynthetic oxygen production in photosynthetic inactive root or seed tissue and during night. As plants do not have an active distribution system for oxygen, occurrence of oxygen gradients and hypoxia is quite common and needs tight regulation including metabolic and morphologic changes to adapt to variations of oxygen levels (Ast et al. 2012). Therefore, monitoring oxygenation is an essential tool in basic and agricultural research to gain insight into photosynthetic activity and to understand oxygen dependent adaptations.

The presence or absence of oxygen is also an important factor for the survival of organisms with anaerobic metabolism. Under anoxic conditions which predominate in environments such as sediments, intestinal tracts of animals or the deep subsurface of the earth, energy is transformed by other processes that are inhibited in the presence of oxygen, as shown in **Fig. 1.1, D**. These include for example fermentation of hexoses to ethanol or lactic acid or anaerobic respiration which uses molecules such as CO₂, NO₃⁻ or SO₃²⁻ instead of O₂ as terminal electron acceptors. Facultative anaerobes can adapt their metabolism depending on oxygen availability. Some prominent examples, such as yeast or strains of *Lactobacillus*, are also extensively used in food and beverage production. Under anoxic conditions, they use fermentation as energy supply but can switch to aerobic respiration when oxygen is present. However, for obligate anaerobes, such as numerous bacteria and archaea, some fungi and protozoans, oxygen is a potent toxin. As anaerobes possess only low amounts of detoxifying enzymes, such as catalase or superoxide dismutase, oxygen and reactive oxygen species, such as O₂⁻ and H₂O₂ induce DNA damage and enzyme inhibition. This oxidative damage causes an irreversible breakdown of central metabolism, quickly leading to cell death (Madigan 2015). Consequently, monitoring and controlling oxygen levels is not only interesting for basic research in the field of microorganisms but also for industrial applications, such

as quality and safety control in biogas plants and production of food or pharmaceuticals, which rely on anaerobic fermentation and respiration.

Its deep impact on biological systems makes oxygen a very informative analytical parameter for the analysis of biological activity. Hence, a broad spectrum of methods has been developed that enable determination of oxygen levels in biological samples. A short overview of currently used analytical methods for oxygen sensing will be presented in the following section.

1.2 STATE-OF-THE-ART OF OXYGEN SENSING

Traditional methods for the quantification of dissolved oxygen content usually rely on physical (manometry) or chemical (titration) measurement methods. Introduced first by Winkler in 1888, dissolved oxygen can be determined chemically by iodometric titration (Winkler 1888). The titration is based on oxygen in the sample that first reacts with a manganese(II) salt, forming a precipitate which then leads to the oxidation of iodide to iodine. The amount of oxygen in the sample can be determined by a final reduction of iodine. Today, this method is mainly applied for the analysis of water samples (Tai et al. 2012). The principle of manometry was developed in the early 20th century as a physical means to quantify blood oxygenation (Barcroft and Haldane 1902). The sample is monitored at a constant temperature and pressure in a sealed vessel and volume changes due to production or consumption of oxygen are recorded. Many important findings were based on manometric measurements, such as the investigation of cell respiration by Krebs (Krebs 1951) or the formulation of the Warburg hypothesis postulating that cancer cells undergo a metabolic shift from oxidative phosphorylation to glycolysis (Warburg 1924; Koppenol et al. 2011). However, both methods are no longer used to study biological samples, as they are time-consuming, prone to errors and hard to apply for studies of complex tissues or sensitive cells (Renger and Hanssum 2009). To overcome these drawbacks, methods have been developed, that allow a continuous and minimal or even non-invasive monitoring of biological samples. These include electrochemical sensors of the Clark-type electrode, sophisticated methods based on positron emission tomography (PET), magnetic resonance imaging (MRI) or electron paramagnetic resonance (EPR). Additionally, optical sensors based on luminescence or photoacoustics are widely used to quantify O₂ levels. Current methods for the determination of oxygen *in vivo* and *in vitro* are summarized in **Tab. 1.1** with a special focus on advantages and limitations of the respective detection method. These commonly used techniques will be described in more detail in the following section.

Tab. 1.1 List of methods commonly used for oxygen detection in biological samples adapted from (Amao 2003; Amesz and Hoff 2006; Vikram et al. 2007; Dierckx et al. 2014; Wolfbeis 2015).

Method	Advantages	Limitations
Clark-electrode	Mechanically robust; easy sterilizable; well established	Consumption of O ₂ ; prone to drift; poor performance at low pO ₂ ; low spatial resolution; invasive
PET	3D oxygen mapping of large-areas; visualization of hypoxic tumor regions; non-invasive; high penetration depth	Low resolution (~ 5 mm); exposure to radiation; expensive; sophisticated equipment required (PET scanner, cyclotron); slow data acquisition; difficult to apply for routine/long term measurements; difficult calibration
MRI	Non-radioactive; non-invasive; high penetration depth; 3D oxygen mapping (resolution ranging from submillimeter to few mm); BOLD-MRI: fast data acquisition	Expensive; difficult to apply for routine/long term measurements; slow data acquisition; BOLD-MRI: no quantitative information on pO ₂
EPR	Non-radioactive; 3D oxygen mapping max. resolution of 0.5 mm; non-invasive, high sensitivity and penetration depth	Slow data acquisition (min to h); expensive; some EPR probes with toxic effects; repeated measurements possible, but limited by retention of the probe
Optical	Non-radioactive; inexpensive; (minimally) invasive; easy to miniaturize; no electrical interference; multiparametric measurements; high versatility	Photobleaching; generation of ¹ O ₂ ; limited penetration depth; interference by probe autofluorescence

Electrochemical sensors mainly based on amperometric detection were first described by Clark to measure *in vivo* oxygenation of blood in dogs (Clark et al. 1953). The structure and working principle of the polarographic electrode are depicted in **Fig. 1.2, A**. The electrode consists of a sensing Pt-wire electrode and a reference Ag/AgCl electrode. The electrode compartment is enclosed by an oxygen permeable polymer, mainly Teflon. Upon application of a polarizing voltage of 0.7 – 0.8 V, oxygen at the electrode surface gets reduced to hydroxide ions. This results in the occurrence of a current flow, which is directly proportional to the oxygen concentration (Ramamoorthy et al. 2003). Generally, electrode tip sizes ranging from hundreds of μm to a few μm are commercially available depending on the application (<http://www.unisense.com/O2/>). Clark-type electrodes have been applied in many scientific studies, ranging from measuring oxygenation in whole organisms to the determination of oxygen consumption of monolayer cells. For example, von Heimburg et al.

monitored the differentiation process of preadipocytes to adipocytes. They found that oxygen consumption of differentiated adipocytes was significantly higher compared to non-differentiated cells (von Heimburg et al. 2005). Furthermore, microelectrodes were applied to monitor the viability and, thus, the quality of engineered myoblast tissue during the cultivation process (Kagawa et al. 2016). Amperometric electrodes are not only extensively used to measure the oxygen content of cell samples and tissues but also often applied in whole organisms or biofilms (Braun et al. 2001; Kinh et al. 2017). Although Clark-type oxygen sensors are well established and highly robust, they possess some major drawbacks, especially for measurements in tissue or adherent cell cultures (see **Tab. 1.1**). First, they consume small amounts of oxygen during the measurement, which can lead to false results when dealing with minor changes of oxygen levels caused by small samples like cells. Second, the electrodes are mainly applied for bulk-phase measurements. Insertion into tissue, tissue models or cell multilayers is invasive and can cause damage (Wolfbeis 2015). However, efforts are undertaken to develop planar Clark-type oxygen chips that allow cell growth directly on the permeable electrode membrane for a direct measurement beneath the cell layer (Wu et al. 2010). Additionally, electrochemical sensing systems based on the principle of the cytosensor microphysiometer are an emerging tool for the metabolic analysis of cells (McConnell et al. 1992). The microphysiometer is often used for the electrochemical detection of multiple analytes, such as pO_2 , pH (extracellular acidification rate), lactate and glucose. Multianalyte microphysiometry utilizes for example a light-addressable potentiometric sensor (LAPS) in combination with platinum electrodes for the potentiometric and amperometric detection of the respective analytes (Eklund et al. 2004; Shinawi et al. 2013). Another approach comprises sensing elements, such as ISFETs (ion sensitive field effect transistors), noble metal electrodes and interdigitated electrode structures to simultaneously monitor extracellular acidification and oxygen consumption of metabolically active cells, as well as changes in cell adhesion and cell density (Wiest et al. 2005).

Radioisotope techniques, such as PET, rely on the radioactive decay of substances like ^{18}F , ^{15}O , ^{13}N and ^{11}C . These compounds emit positrons that quickly recombine with electrons resulting in two γ -quants which can be detected at an angle of 180° (**Fig. 1.2, B**). By measuring different γ intensities, 2D and 3D quantitative images are constructed showing the distribution of the positron emitter in the sample. Usually, ^{15}O is used as radiotracer for *in vivo* PET measurements of perfusion rates, oxygen metabolic rates in organs/tissue and imaging of hypoxic tumor environments (Valk et al. 2006). Therefore, gaseous ^{15}O or liquid $H_2^{15}O$ is introduced into the tissue under study by inhalation or injection (Temma et al. 2014). The non-invasive monitoring of multiple parameters allowed PET

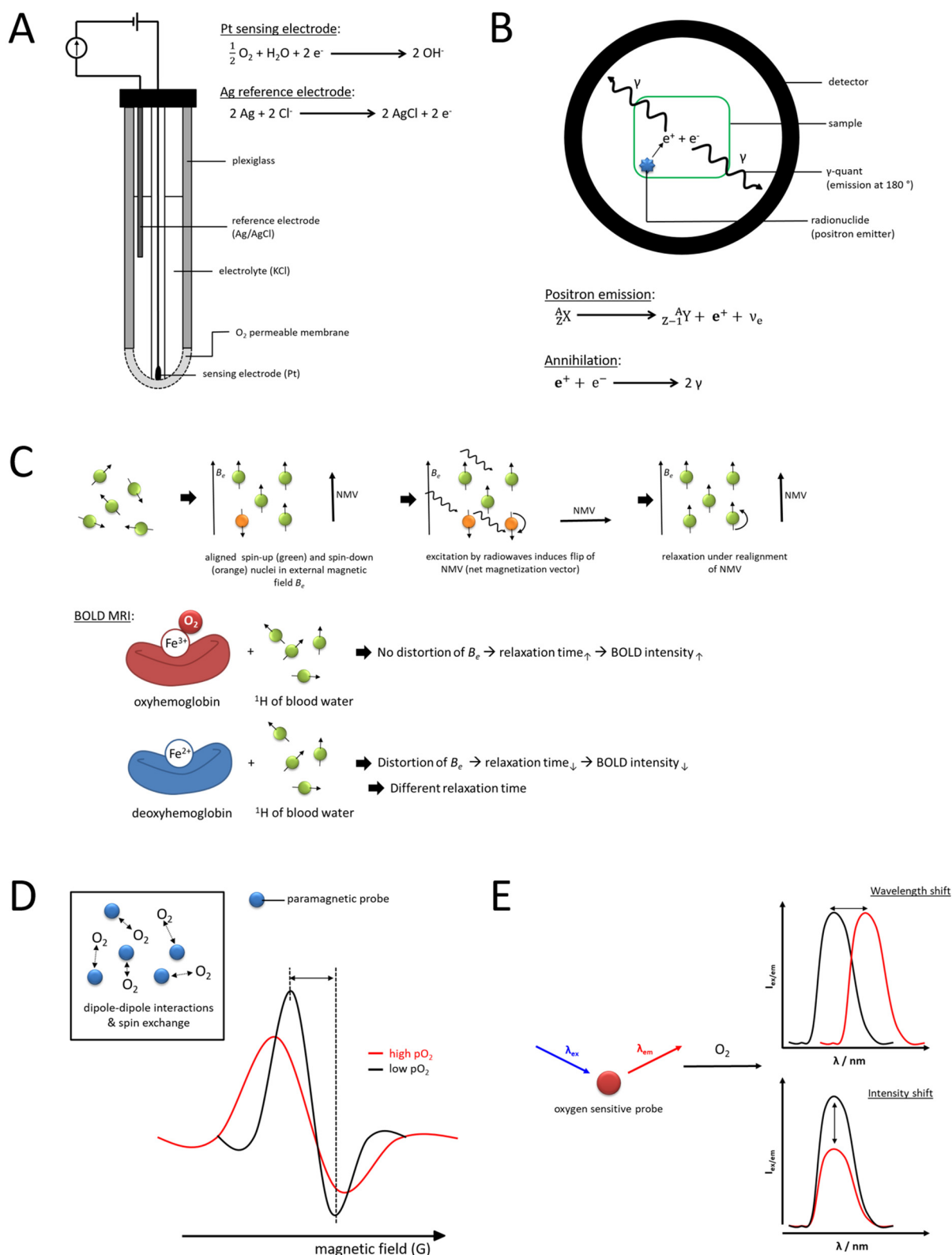


Fig. 1.2 Overview of techniques commonly used to determine oxygen levels in biological samples. (A) Electrochemical oxygen detection by Clark-type electrodes based on amperometric measurements adapted from (Hajek et al. 2016). (B) PET imaging based on positron emission of radioactive tracer substances. (C) MRI based on magnetic resonance of ¹H nuclei from blood water upon irradiation with radio waves. BOLD MRI uses endogenous hemoglobin as contrast agent to measure blood oxygenation adapted from (Westbrook et al. 2011). (D) Oxygen measurements by EPR use molecular interactions between oxygen and a paramagnetic probe in a magnetic field adapted from (Ahmad and Kuppasamy 2010). (E) Optical detection of oxygen relies on sensor probes that change their spectral characteristics with oxygen concentration.

to become a standard technique for imaging (patho-)physiological procedures in human patients, especially for monitoring the brain (Hoeffner 2005). However, PET imaging has a relatively low spatial resolution of about a few mm when compared to other oxygen sensing techniques and image acquisition is rather slow which limits its applicability when monitoring cell monolayers or small tissue samples (Kudomi et al. 2013; Lopci et al. 2014). Furthermore, most radioisotopes have a short half-life, e.g. ^{15}O about 2.03 min, so radio tracers need to be produced immediately before application in a medical cyclotron (Schlyer 2004).

Additionally, methods based on magnetic resonance, such as magnetic resonance imaging or electron paramagnetic resonance imaging, are known whose field of application is similar to PET. MRI of pO_2 is mainly done by using probes containing ^{19}F or ^1H . In ^{19}F magnetic resonance imaging, the nuclear magnetic resonance spin-lattice relaxation rate of perfluorinated carbon compounds is read out to quantify oxygen levels, while the variation of relaxation time of ^1H in blood water is used to measure oxygenation in BOLD (blood oxygen level-dependent) MRI (Vikram et al. 2007). BOLD MRI uses the paramagnetic characteristics of deoxygenated hemoglobin as endogenous contrast agent which causes changes in the local magnetic field. The paramagnetic deoxyhemoglobin affects the relaxation rates of surrounding water protons in the blood vessels. The intermolecular dipole-dipole relaxation causes a change in MRI signal intensity depending on the concentration of deoxygenated hemoglobin as shown in **Fig. 1.2, C** (Zhao et al. 2009). BOLD MRI has a relatively good spatial resolution, ranging from hundreds of μm to a few mm depending on the sample (Goense et al. 2016). The technique was for example used to study the influence of oxygenation levels in the human kidney on water diuretic function (Tumkur et al. 2006). In contrast to MRI, electron paramagnetic resonance oximetry uses injectable probes containing unpaired electrons, like nitroxides or lithium phthalocyanine. Oxygen partial pressure is determined by the change of EPR linewidth caused by the interaction of the paramagnetic probe and paramagnetic molecular oxygen. As illustrated in **Fig. 1.2, D**, elevated pO_2 leads to an proportional increase of spin-spin relaxation rates of the probe, thus resulting in a decrease of relaxation time that causes broadening of the EPR lines (Swartz et al. 2014). EPR spectroscopy was used to continuously measure oxygenation of live spheroids (Langan et al. 2016). With suitable instrumentation, EPR can be easily adapted for imaging thus enabling two and three-dimensional mapping of pO_2 . EPR imaging has been used for the successful determination and comparison of normal oxygenation and stroke induced hypoxia in rabbit brains (Khan et al. 2015) or for monitoring oxygenation during wound healing processes in model mice (Desmet et al. 2015). Both, MRI and EPR, are mainly used for mapping oxygen

distribution in large parts of the body as they are non-invasive. However, these methods are hardly applied for smaller biological samples, as they are expensive and possess limited spatial resolution. The respective limitations and advantages are listed in **Tab. 1.1**.

By now, a huge bandwidth of techniques based on optical detection of oxygen has been developed. As oxygen itself cannot be detected by optical means, these techniques rely on suitable sensor probes. The presence or absence of oxygen alters the spectral properties of the applied probe, resulting in changes of absorption/emission wavelength and/or intensity as shown in **Fig. 1.2, E**. Probes can have endogenous origin, which means they are expressed by cultivated cells and tissues. One example is the luciferase reporter system. This method uses the oxygen dependent induction of luciferase expression in transfected cells. However, the luciferase assay does not provide quantitative measurements of pO_2 and is strongly dependent on the successful transfection of cells (Wu and Yotnda 2011). Furthermore, genetically encoded fluorescent proteins, like GFP or UnaG, can be used for non-quantitative measurements of intracellular oxygenation. Suitable modifications of the gene sequence enable a cell compartment specific accumulation and location of the probes. The fluorescent emission of the proteins is either modified by an oxygen dependent red shift of the signal or the expression of transcription factors (Takahashi et al. 2005; Erapanedi et al. 2016). Another approach is to use endogenous molecules, such as the mitochondrial protoporphyrin IX. Mitochondrial pO_2 can be determined by the delayed fluorescence of the protein that is caused by the presence of oxygen. This method allows the quantitative determination of oxygen levels in the mitochondria of live cells (Mik et al. 2006). On the other hand, many external synthetic probes have been developed for measurements of pO_2 in cells and tissue. Marker molecules, such as misonidazole and pimonidazole, are widely used to distinguish between hypoxic and normoxic tissues and cells. Low pO_2 leads to a reductive activation of the compounds, which then bind specifically to thiol containing proteins in hypoxic cells. The marker molecule-protein adducts can then be detected for example by immunostaining (Raleigh et al. 1985; Varia et al. 1998). Hypoxia staining is often used to label hypoxic cores for the characterization of tissue models such as spheroids (Laurent et al. 2013; Mikhail et al. 2013). Photoacoustic spectroscopy is an emerging technique that combines optical absorption of either endogenous (e.g. hemoglobin) or exogenous probes (e.g. metalloporphyrins) with ultrasound and its interference by the presence of oxygen. Upon excitation of the probe, optical energy is absorbed and converted into heat. The rise of temperature leads to a thermoelastic expansion, which causes the release of acoustic waves (Xia et al. 2014). This hybrid approach combines high penetration depths of a few centimeters with good

spatial resolution that allows a quantitative readout of pO_2 *in vivo* (Ray et al. 2012). The main field of application of photoacoustic spectroscopy is monitoring of vascular oxygenation and tissue oxygenation (Cui and Yang 2010; Tsytsarev et al. 2011). Molecular oxygen can also be measured by colorimetric probes. Here, the optical probe reacts (in most cases irreversibly) with oxygen. The reaction causes a chromogenic shift that can be either read out by reflectometry or by eye (Wang and Wolfbeis 2014). For example, absorption based sensors use the endogenous protein myoglobin. When oxygen is bound to myoglobin, there is a strong shift in its absorption spectrum that correlates linearly to the dissolved oxygen concentration (Chung et al. 1995). A synthetic cobalt complex was also used as oxygen sensor. In the presence of oxygen, absorbance of the complex is enhanced. The fiber-based sensor allows quantitative measurements of low oxygen concentrations which is convenient for monitoring an anaerobic environment (Baldini et al. 1992).

Most optical approaches used for the detection of oxygen have certain limitations. The number of endogenous probes as described above is small and the systems often rely on genetic modification of cultivated cells. In many cases, pO_2 is only assessed semi-quantitatively and the amount of expression of the sensor molecules strongly depends on cell culture conditions. Synthetic hypoxia markers, such as pimonidazole, require relatively thick tissue samples prepared by cryosectioning and are tailored for end-point measurements. Furthermore, hypoxia markers can only be used to distinguish between normoxic and hypoxic areas with $pO_2 < 10$ torr. Probing samples with photoacoustic spectroscopy allows deep tissue penetration and 3D mapping. However, a sophisticated, expensive set-up comprising two NIR lasers is needed (Papkovsky and Dmitriev 2013). Absorption based systems with biological application are scarce as their response time and resolution is slow, most reactions are not reversible and they are prone to error due to interference with factors such as pH or ionic strength. These types of sensors are mainly used for the detection of oxygen in the gas phase e.g. in food packaging (Mills 2005). Oxygen sensing based on luminescence quenching of a sensor dye provides a good alternative when measuring oxygen levels in live cells and tissue. Quenching of fluorescence and phosphorescence by oxygen was first described in 1935 (Kautsky and Hirsch 1935). It is based on the photochemical process of collisional quenching of the oxygen sensor dye in its excited state by molecular oxygen that leads to a decrease of luminescence intensity and lifetime that is proportional to the oxygen content (Lakowicz 2006). A more detailed explanation of luminescence quenching is described in **chapter 3.2.1**. Multiple measurement modalities are possible to determine oxygen levels that work either by determining luminescence intensity or lifetime.

i) Intensity based measurements rely on monitoring intensity changes of the oxygen sensor dye at a single wavelength. However, this type of detection method is prone to errors due to optical interferences and light scattering. These effects are particularly pronounced in biological samples, as they possess a high autofluorescence. This can negatively affect calibration and lead to incorrect determination of oxygen values. Additionally, intensity changes of a single dye are also heavily influenced by parameters such as dye concentration, photobleaching and illumination uniformity. Inhomogeneity of the biological sample and geometry of the measurement set-up are further factors that can lead to erroneous results (Quaranta et al. 2012). To achieve a better accuracy of intensity based sensing, auxiliary techniques such as pixel-by-pixel calibration or implementation of calibration functions can be adopted that include corrections for photobleaching and dye-leaching (Itoh et al. 1994).

ii) Ratiometric sensing is another approach which overcomes at least some of the drawbacks of intensity based oxygen sensing. Here, the sensor contains both, oxygen sensor dye and an oxygen insensitive reference dye, that are in most cases incorporated in the same matrix. The reference dye should neither be quenched nor degrade in the presence of oxygen. The two dyes are at the best excited with the same illumination source and have different emission spectra. On the one hand, this allows spectral separation of the sensor and the reference signal, on the other hand energy transfer between the two dyes is prevented. Oxygen levels are determined by the ratio of the intensities of the reference dye and the indicator dye. Ratiometric sensing circumvents optical interference coming from the excitation source and the set-up as long as they affect both emissions to the same degree. Inaccuracies of the readout caused by photobleaching, sample inhomogeneity or detector fluctuations are reduced (Grist et al. 2010).

iii) A third option to determine oxygen levels is the luminescence lifetime determination of the sensor dye. The lifetime is defined as the time after excitation during which the indicator remains in the excited state. Lifetime can be measured in two modalities – either in time-domain or in frequency-domain mode. In time-domain mode, the time-dependent intensity decay after dye excitation is measured and the decay time is calculated. Background fluorescence caused by biological samples is completely eliminated by a short delay between excitation and recording of the usually longer-lived phosphorescence signal of the indicator dye (Lakowicz 2006). The most common time-domain detection method is a pulse-and-gate technique often referred to as rapid lifetime determination (RLD). For this method, the sensor dye is first excited by a suitable illumination source like an LED. Afterwards, illumination is switched off and the luminescence

intensity decay is collected in two different time gates with the same integration time (Holst et al. 1998). In contrast, lifetime with frequency-domain detection is determined by exciting the sample with intensity-modulated light. The luminescence emission is delayed in time relative to the excitation. This phase shift can be used to calculate the lifetime. Because the decay time is an intrinsic parameter of the respective luminophore, it is not affected by dye concentration, photobleaching, fluctuations of the illumination source, detector sensitivity and optical geometry of the measurement set-up (Wang and Wolfbeis 2014).

Tab. 1.2 Overview of commercialized optical oxygen sensor types and their field of application. OCR: oxygen consumption rate.

Sensor type	Application	Commercialized product
<u>Soluble</u>		
Molecular dye	Measurement of dissolved oxygen (DO) in bulk phase; intra- and extracellular measurement of pO ₂	Porphyrin Systems GbR (metal-ligand complexes)
Dendrimers	Measurement/imaging of intracellular pO ₂	Oxygen Enterprises Ltd. (Oxyphor™ probes)
Micro-/Nanoparticles	Measurement of dissolved oxygen (DO) in bulk phase; intra- and extracellular measurement/imaging of pO ₂ ;	Ibidi OPAL O ₂ (extra-/intracellular oxygen monitoring with CPOx, NanO ₂); Luxcel Biosciences (MitoXpress® probes); Abcam (extra-/intracellular oxygen concentration assay)
<u>Solid</u>		
Fiber-optics	measurement of gaseous and dissolved O ₂ in bioreactors, sediments, soil, tissue and cell culture	PreSens GmbH (PM-PSt7 microsensors); Oxford Optronix (OxyLite™ for medical monitoring); Terumo Inc. (CDI Blood Parameter Monitoring System); Agilent Technologies (Seahorse XF for analysis of OCR)
Planar sensor foils	Spatial and temporal mapping/imaging of oxygen gradients in cells/ tissue, sediments, soil, bioreactors	PreSens GmbH (SF-RPSu4 ratiometric foil); Finesse (TruFluor™); Aandera (AADI oxygen optode for marine applications)
3D scaffolds	3D mapping of oxygen levels for tissue engineering	Not yet commercialized

For all measurement modalities, a large number of oxygen sensitive indicator dyes is known. These can be classified into organic compounds, such as hydrocarbons and fullerenes, nanomaterials (e.g. quantum dots) and metal-ligand complexes (e.g. metalloporphyrins or transition metal-ligand complexes). The latter include three of the most widely used indicator dyes, namely PtTFPP (tetrakis(fluorophenyl)-porphyrin-platinum), PdTFPP (tetrakis(fluorophenyl)-porphyrin-palladium) and Ru(dpp)₃ (tris(diphenylphenanthroline)-ruthenium). Metal-ligand complexes are particularly interesting because of their attractive features, such as long luminescence lifetimes, high photostability, high quantum yields, absorption in the visible range and large Stokes shifts (Feng et al. 2012). Oxygen sensitive dyes can be used in different sensor designs that are commercialized by many companies for the application within biological samples. An overview of commercialized optical oxygen sensors based on luminescence quenching and their applications is provided by **Tab. 1.2**.

The simplest approach for oxygen sensing in living cells introduces dye molecules into the samples (**Fig. 1.3, A**). Depending on its cell-permeability the sensor dye can be either applied for extracellular or intracellular pO₂ measurements. For example, a Japanese group introduced a platinum porphyrin to murine pancreatic cells to image intracellular oxygenation of single cells and oxygenation changes upon glucose stimulation. Oxygen levels were determined via lifetime measurements with a confocal laser scanning system that also enabled standard microscopy of the cells (Kurokawa et al. 2015). A similar system was used to monitor oxygen partial pressure *in vitro* and *in vivo*. Therefore, cultivated kidney cells were incubated with a cationic iridium complex. Intracellular oxygen content was imaged with a fluorescence microscope via phosphorescence decay. For *in vivo* studies, the indicator was injected intravenously into mice. Oxygenation of healthy and damaged kidneys was compared by point-measurements of phosphorescence lifetime using a fiber-optic based sensor (Hirakawa et al. 2015). Although the use of free dyes is a straightforward approach which does not require sophisticated synthesis or fabrication steps, it has certain disadvantages. Because the dye molecules are not separated from the environment by encapsulation, they tend to interact with the surrounding biological environment. This results in changes of luminescence by interfering molecules or binding of the dye to biomolecules. Dyes are also prone to degradation when taken up by cells (O'Donovan et al. 2005). The free dye is often highly phototoxic due to production of singlet oxygen, especially when it is directly taken up by cells, a characteristic that is made use of in photodynamic therapy (Chandra et al. 2000). Alternatively, probe encapsulation in a suitable matrix is used to form dendritic, macromolecular or particle-based probes and planar sensor spots.

Fig. 1.3, B shows a dendritic probe which consists of a central luminophore that is surrounded by repeatedly branched structures (dendrimers) forming a protective barrier between dye and environment (Lebedev et al. 2009). This shielding results in a lower phototoxicity compared to the molecular dye as the interaction with the cellular environment is lower and singlet oxygen needs first to diffuse out of the dendrimers to induce cell damage, yielding highly dispersive macromolecules. Furthermore, these dyes are readily taken up into cells and are highly compatible with microscopy and lifetime imaging applications (Ceroni et al. 2011). This type of sensor has been developed to study oxygenation of spheroids with near-infrared confocal microscopy (Nichols et al. 2014). Another study used a two-photon excitable dendritic probe with antennae chromophores containing a Pt porphyrin in the core. Intramolecular FRET between antenna and sensor dye leads to an enhancement of the two-photon induced luminescence. This sensor was applied for high resolution 3D imaging of capillary oxygenation in the mouse brain yielding a tissue penetration depth of 240 nm (Sakadzic et al. 2010). Additionally, dendritic Oxyphor™ probes were used to image vascular and interstitial oxygenation of tumors in mice (Esipova et al. 2011). A macromolecular, near infrared emitting Ir-probe was tested for ratiometric *in vivo* whole body imaging of tumor hypoxia in mice. The probe was injected subcutaneously, showed a high biocompatibility, a specific accumulation in tumor tissue and allowed localization of tumor tissue up to 120 h after probe injection (Zheng et al. 2015).

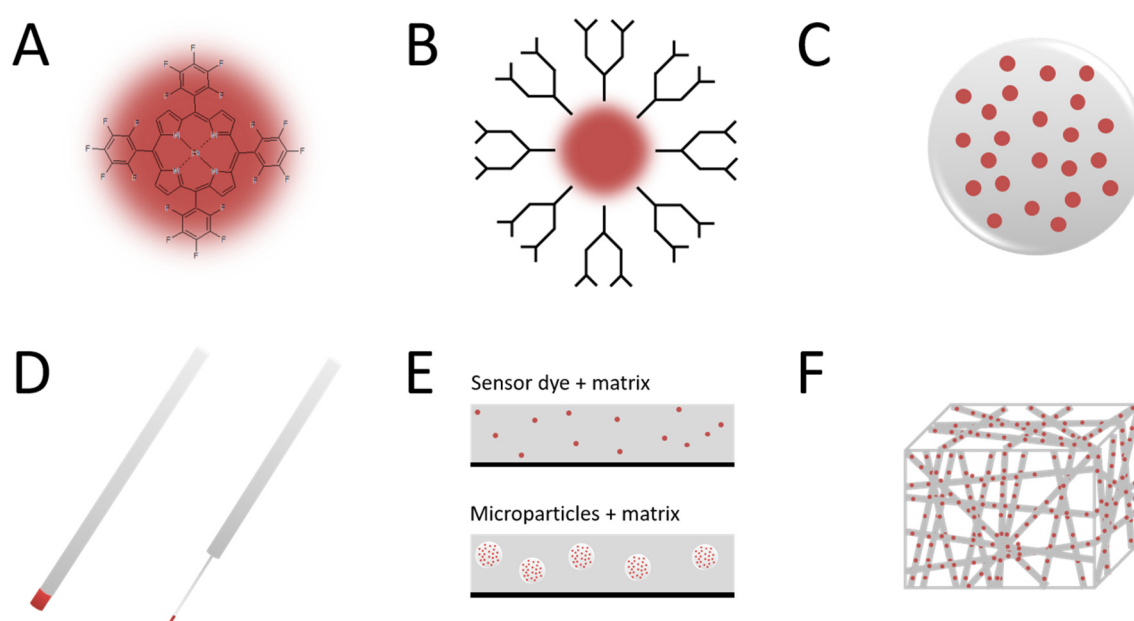


Fig. 1.3 Different sensor formats for optical oxygen sensors based on luminescence quenching. (A) Molecular dyes such as metal-ligand complexes or organic compounds, (B) dendrimers, (C) micro- and nanoparticles, (D) fiber optics with flat tip or needle tip, (E) planar thin film sensors consisting of an oxygen permeable polymer matrix with incorporated sensor dye or microparticles and an oxygen impermeable support (black), and (F) 3D oxygen sensitive scaffolds.

Other soluble probes based on nano- and microparticles are considered as useful tools to study intracellular and tissue oxygenation because of their excellent compatibility with microscopic techniques (**Fig. 1.3, C**). To ensure biocompatibility, materials such as organically modified silica (ormosil), sol-gel or polymers such as polystyrene, polyacrylonitrile or cellulose acetate are used in particle synthesis. Depending on material and method of synthesis particles can be functionalized on the surface to inhibit or improve endocytosis. Special modifications allow the easy manipulation of the particles as it is the case for magnetic beads (Papkovsky and Dmitriev 2013). Since the dye is usually entrapped inside the particle, the used materials need a sufficient oxygen permeability (Wang and Wolfbeis 2014). Particle based sensors are easy to produce by standardized methods, such as Stöber synthesis (Xu et al. 2001), swelling-stain technique (Wang et al. 2011), monomer polymerization (Wang et al. 2011) or precipitation (Kurner et al. 2001). Their size can be tailored ranging from a few nanometers to the micrometer range and they usually possess a higher brightness than the sole molecular dye (O'Donovan et al. 2005; Cywinski et al. 2009). One type of nanoparticle based sensor known as PEBBLE (photonic explorer for biomedical use with biologically localized embedding) exhibits excellent biocompatibility and the particle shell protects the probes from potential interfering cytosolic molecules (Lee et al. 2009). Ormosil based PEBBLEs were introduced into rat C6 glioma cells for a ratiometric readout of pO_2 (Koo et al. 2004). Monodisperse, dye doped organically modified silica nanoparticles were also developed for the analysis of intracellular oxygen levels in human osteosarcoma epithelial cells. The particles are readily taken up by the cells via lysosomal trafficking and long term exposure to cells is not cytotoxic (Korzeniowska et al. 2015). Dmitriev et al. produced phosphorescent nanoparticles that are highly cell permeable. The sensors are highly specific for neuronal cells and were successfully applied to image oxygen levels in 2D cultures and 3D neurosphere aggregates with phosphorescence lifetime imaging microscopy (PLIM). Besides, they possess good stability and low cytotoxicity. However, like mentioned above, the particles are not located in the cytosol but accumulate in lysosomes (Dmitriev et al. 2015). Sensor particles in the micrometer range are mostly applied for extracellular, bulk phase measurements or as doping material for sensor foils because their size is rather unsuitable for intracellular sensing (Wang and Wolfbeis 2014). Microparticles have been integrated in the extracellular matrix of ATDC5 spheroids to determine oxygenation and hypoxic regions in these cell aggregates (Lambrechts et al. 2013). However, it is still questionable if incorporation of huge particle does not affect the 3D structure of spheroids and tissues. Most particle based oxygen sensors are invasive, as they are readily taken up inside cells and accumulate in certain organelles such as

lysosomes. In many cases particle stability, aggregation and reproducibility of the synthesis as well as a potential photo-/cytotoxicity is also an issue (Papkovsky and Dmitriev 2013). Another sensor format that is frequently used are optical fiber sensors as depicted in **Fig. 1.3, D**. Oxygen sensitive (micro-)optodes can be fabricated by attaching a suitable matrix containing the oxygen sensitive dye at the tip of an optical fiber. An additional protective layer can be optionally applied to enhance the sensor stability. Fiber optic sensors possess high signal stability, fast response time and enable remote determination of oxygen as well as the determination of pO_2 in the z-axis. This makes them an attractive tool for geobiological applications. Fiber optics are for example extensively used for monitoring aquatic systems, biofilms and sediments (Klimant et al. 1995; Chipman et al. 2012; Rickelt et al. 2013). Furthermore, small needle-type sensors are often applied to measure pO_2 in blood vessels, as presented in a study of a Chinese group. They developed a portable, miniaturized oxygen fiber sensor for rapid frequency-domain based detection of oxygenation in blood and tissue (Fang et al. 2013). Commercially available, needle-type optodes were used for online monitoring of the oxygenation of a porcine muscle tissue model inside a bioreactor to improve transplantation conditions in future plastic surgery (Dragu et al. 2012). Fiber optics were employed for point measurements of oxygen tension in 3D collagen scaffolds that were used as culture substrates for human fibroblasts and stromal cells. A drop of oxygen partial pressure depending on the cell density inside the scaffolds was observed (Streeter and Cheema 2011). However, to reach the samples, fiber optic based sensors need to penetrate the biological material, which can lead to measurement artifacts and altered pO_2 due to oxygen diffusion. Without a micromanipulator, the spatial resolution of this sensor technique is low and it only allows point-measurements. Fabrication of small needle-type fibers is tedious and most probes are still unsuitable for small samples, as they are highly fragile and the diameter ($d > 40 \mu\text{m}$) is still bigger than some samples (Wilson 2008). Planar thin-film oxygen sensors overcome the limitations of low spatial resolution and invasiveness of fiber optodes. Planar oxygen sensor films typically consist of an optically transparent, oxygen impermeable support layer and an oxygen permeable sensor layer which is usually a polymer matrix with embedded dyes or microparticles (**Fig. 1.3, E**). Additionally, some sensor foils contain an optical isolation layer to prevent sample luminescence interfere with the sensor response. Films with variable thickness are easily produced by knife coating, spin coating or spray coating (Wolfbeis 2008; Thomas et al. 2009; Fischer and Wenzhofer 2010). Their dynamic working range, robustness and sensitivity can be adjusted by choosing a suitable polymer with appropriate permeability (Koren et al. 2013). Planar sensor foils allow non-invasive measurements, as they are not taken up by

biological samples, like nanoparticles or free dye molecules, and possess a good biocompatibility depending on the chosen matrix. Because the dyes are entrapped in a matrix which is at least a few μm in thickness, sensor foils show a low phototoxicity because the lifetime of the generated singlet oxygen is too short that the molecule can diffuse out of the sensing layer. Damage to the biological sample is avoided (Quaranta et al. 2012; Papkovsky and Dmitriev 2013). Furthermore, the films have a fast response time and high photostability especially when dyes such as metalloporphyrins are used. The geometry of the sensor foils can be tailored to a suitable size. Small spots can be for example punched out of the sensor foil or be produced by soft lithography and plasma etching and can be easily incorporated in cell culture substrates and microfluidics (Nock et al. 2008). The planar layout allows 2D mapping of oxygen levels and visualization of oxygen gradients within heterogeneous samples on both, macroscopic and microscopic scale without being invasive, as samples can be placed (or in case of cells or tissue grown) on top of the sensing layer. Imaging with oxygen sensor foils can be easily expanded towards multiparametric imaging by embedding additional sensor dyes e.g. to sense pH, CO_2 or temperature (Stich et al. 2010). Ungerböck et al. implemented a ratiometric thin film sensor into a microfluidic device to measure oxygen consumption of HeLa cells and fibroblasts. An additional PDMS layer was deposited on the sensor film to provide a cultivation surface and to prevent diffusion of singlet oxygen towards the cells. Because of the low thickness of the sensor layer, the set-up was accessible to both, oxygen imaging and microscopy (Ungerböck et al. 2013). Thin film sensors can also be used to monitor oxygen levels in tissue slices *in vitro* (Kellner et al. 2002). Recent studies also report on dual planar sensors that monitor the spatial distribution of pH and pO_2 in chronic wounds of patients (Schreml et al. 2014). Because of their good biocompatibility, planar sensors can be transplanted into living organisms. For example, transplantable sensors have been used for online *in vivo* monitoring of changes in tissue oxygenation in the mouse brain (Tsytarev et al. 2017). However, their planar geometry makes sensor foils inept for intracellular applications and depending on the sample, providing a suitable interface between sample and sensor may be difficult to realize. Furthermore, planar oxygen sensitive substrates can be combined with scaffolds used for 3D cell culture. This approach was used in a set-up for intensity based measurement of pO_2 inside a homemade perfusion chamber. The culture chamber contained the planar film with a Matrigel scaffold containing adenocarcinoma cells on top (Boyce et al. 2016). However, this method is limited because pO_2 is only detected in the lower part of the 3D scaffold facing the thin film oxygen sensor, yielding a low resolution in the z-axis. To overcome this disadvantage, a system combining both, planar foils and a

fiber optic sensor, has been developed for mapping oxygen levels of human mesenchymal cells cultivated inside demineralized bone matrix scaffolds (Westphal et al. 2017). A more elegant method is the direct incorporation of the sensor dye inside the scaffold to create 3D oxygen sensitive culture scaffolds, as shown in **Fig. 1.3, F**. The advantage of this 3D layout is that the scaffold architecture mimics the physiological tissue/cell environment more closely than planar culture substrates. 3D oxygen scaffolds were for example produced by soaking a porous scaffold with polymer/dye solution. This method has been used to implement a Pt porphyrin inside a 3D scaffold for measuring the oxygenation of cancer cells and aggregates with confocal phosphorescence lifetime imaging microscopy (Jenkins et al. 2015). Oxygen sensitive scaffolds that enable non-invasive, high resolution 3D mapping of pO_2 can also be fabricated by electrospinning. These sensor scaffolds were cultivated with human colon cancer cells and tested for lifetime based, localized oxygen monitoring. However, similar to planar sensor foils, 3D scaffolds only allow monitoring of extracellular oxygenation and specialized microscopic equipment is needed (Yazgan et al. 2017). Oxygen sensing methods such as EPR, MRI and PET are mainly used for clinical applications and electrochemical sensors are limited, especially for measuring cells and tissue due to internal oxygen consumption and invasiveness. Therefore, optical oxygen sensors based on luminescence quenching are an established but still emerging tool to monitor oxygen levels and consumption in living organisms because their design can be tailored for the designated application, they do not consume oxygen, and allow online monitoring with minimal invasiveness.

2 OBJECTIVES

Oxygen consumption is an important analytical indicator for metabolic activity of cells and tissue. Cellular energy metabolism is altered in diseases, such as mitochondrial disease and cancer or upon applications of toxins or drugs (Giang et al. 2013; Andreux et al. 2014). This makes oxygen an informative marker for biomedicine, drug screening or cytotoxicity measurements. So far, determination of oxygen levels is either sophisticated and expensive, or invasive, or does have low spatial resolution (Wolfbeis 2015). Oxygen sensing based on luminescent quenching of oxygen sensitive dyes overcomes most of these drawbacks. However, so far cellular oxygen consumption is mainly assessed either by online monitoring of an integrated signal with low or no spatial resolution (Neal et al. 2015) or by discontinuous, high resolution imaging using sensor particles located inside cells and tissues (Dmitriev and Papkovsky 2012).

One aim of this thesis was the development and application of 2D oxygen sensor foils which should be used as growth substrates for monolayer cells and 3D tissue models and should enable online and non-invasive measurement of pO_2 beneath cells and tissue models.

The first project was focused on the development and application of an imaging system which enables a quantitative 2D mapping of oxygen concentration by using planar, ratiometric oxygen sensor foils as cultivation substrates for adherent cells. Because cells and sensor layer are in close proximity and the cell membrane is highly permeable for oxygen, the novel set-up should allow the determination of cellular oxygen content. The new microscopy based imaging system should enable imaging of pO_2 with high spatial and temporal resolution, it should fit inside a standard cell culture incubator and the used sensor foils should exhibit biocompatibility and photostability. The functionality of the oxygen sensor system should be evaluated in proof-of-concept studies in which cellular oxygen consumption was monitored under various experimental conditions and oxygen gradients caused by respiring cell spots were imaged.

Simultaneous recording of two or more cellular parameters is a useful approach that allows obtaining multiple information about the metabolic and physiological status of cells in one measurement. Therefore, the planar oxygen sensor substrates were modified in the second project so that they would enable a combined impedimetric and luminescent readout. The dual ECIS- O_2 chip should allow non-invasive, online monitoring of pO_2 and impedance measurements of monolayer cells cultivated on the sensor surfaces to assess information about cell metabolism and cell morphology changes at the same time.

Monolayer cells are known to be a non-ideal model to mimic physiological conditions found in 3D tissue. Therefore, 3D tissue models, such as multicellular spheroids, have been developed whose physiology and structure resemble tissue but their cultivation is easier compared to 3D tissue culture. Especially multicellular tumor spheroids have come into the focus of research as they offer an attractive alternative to study (chemotherapeutic) drug efficacy and delivery, cell responses to radiotherapy, angiogenesis, tumor growth and proliferation, as well as invasion and migration processes (Weiswald et al. 2015). Thus, the third project addressed the application of 2D oxygen sensor foils to tumor spheroids. Half-spherical MCF-7 tumor spheroids should be cultivated on oxygen sensitive foils without influencing their cell viability. Oxygenation levels should be monitored with high spatio-temporal resolution under standard growth conditions using the imaging system introduced in the first project. Additionally, the influence of drugs on oxygen gradients and on oxygen consumption of metabolically active spheroids should be studied.

Although oxygen monitoring based on luminescence quenching possesses many benefits compared to other detection methods, collisional quenching of sensor dyes by triplet oxygen leads to the production of singlet oxygen. Without shielding by additional protecting layers, highly cytotoxic singlet oxygen is produced close to the cells which quickly leads to cell death (Klotz et al. 2003). This undesirable side-effect was used in the fourth project to convert oxygen sensitive substrates into substrates for an optical wound healing assay. Monolayer cells should be cultivated on planar thin film substrates with incorporated oxygen sensor dyes. Wounds should be introduced to the cell layer by an optical wounding procedure using a suitable light source, such as a confocal laser of desired wavelength that excites the oxygen sensitive molecule and produces singlet oxygen. Wounds with defined geometry should be generated by illumination and wound healing behavior of the undamaged adherent cells adjacent to the wound should be studied using the novel wound healing substrates.

3 MATERIALS AND METHODS

3.1 CELL CULTURE TECHNIQUES

To avoid contamination of the mammalian cell lines used in this work, all cell culture work was done under a laminar air flow work bench (Thermo Fisher Scientific Inc.). Consumables were autoclaved before usage and cells were exposed to sterile media and reagents only. All buffers, media and reagents were warmed in a water bath at 37 °C before they were applied to the cells. Cells were usually grown on the bottom of culture flasks with a growth area of 25 cm², containing 4 ml of culture medium. All cells were cultivated in an incubator (Thermo Fisher Scientific Inc.) at 37 °C in a humidified atmosphere containing 5% CO₂. They were fed with fresh culture medium every third day and one day before every cell experiment.

3.1.1 CULTIVATION OF ADHERENT CELL LINES

In this work five different adherent mammalian cell lines were used, which are described in more detail below.

The Madin-Darby canine kidney II (MDCK II) cell line is an adherent mammalian cell line derived from the distal tubule of the nephron of an adult female cocker spaniel in 1958. MDCK II cells exhibit a low epithelial resistance of about 50 – 70 Ω cm² of a leaky epithelium found in the distal tubule and show a cuboidal cobblestone-like morphology (Richardson et al. 1981). Cultivated cells grow to stable monolayers with domes or so called blisters due to transport of salt and water from the apical to the basolateral side (Lang and Paulmichl 1995). The MDCK II cell line was purchased from the *German Collection of Microorganisms and Cell Cultures (Leibniz Institute DSMZ)*.

Normal rat kidney (NRK-52E) cells are kidney epithelial-like cells first described in 1978 (Delarco and Todaro 1978) derived from the species *rattus norvegicus*. Morphologically, NRK-52E cells are similar to MDCK II cells. However, they do not exhibit domes during cultivation. NRK-52E cells were purchased from the *DSMZ*. MCF-7 (Michigan Cancer Foundation) cells are human breast adenocarcinoma cells which were isolated from a 69-year-old Caucasian woman with a metastatic mammary carcinoma. The cell line was derived directly from the pleural effusion of the patient in 1970. MCF-7 cells form adherent, epithelial-like monolayers with a tendency to form domes and display a morphological structure close to the mammary epithelium, including the expression of

estrogenic receptors (Soule et al. 1973). U-373 MG (Uppsala) cells are human glioblastoma astrocytoma cells which originate from malignant brain tumor tissue. They exhibit an astrocyte phenotype and grow in adherent monolayers (Ponten and Macintyre 1968). The U-373 MG cell line was kindly provided by Prof. Buschauer (Institute of Pharmacy, University of Regensburg, Germany). BAEC (bovine aortic endothelial cells) are derived from bovine aorta. They exhibit a typical cobblestone-like morphology, are known for their active synthesis of prostaglandins, and are often used to study the effect of β -adrenoceptor agonists on endothelial permeability (Zink et al. 1993). BAEC cells were provided by Dr. Zink and Prof. Rösen from the *DDZ (Deutsches Diabetes Zentrum, Düsseldorf, Germany)*.

All cell lines were cultured in suitable medium. The composition of the medium of the respective adherent cell lines is listed in **Tab. 3.1**.

Tab. 3.1 Medium composition for the five different cell lines used in this work. FCS: fetal calf serum.

Cell line	Culture medium	FCS	L- Glutamine	Pyruvate	Penicillin/ streptomycin
BAEC	Dulbecco's Modified Eagle's Medium (DMEM) 3.7 g/l NaHCO ₃ 1.0 g/l D-Glucose	10 % (v/v)	4 mM	-	100 µg/ml
MCF-7	Minimum Essential Medium Eagle (MEM-Eagle) 2.2 g/l NaHCO ₃ 1 g/l D-Glucose	10 % (v/v)	2 mM	1 mM	100 µg/ml
MDCK II	Minimum Essential Medium Eagle (MEM-Eagle) 2.2 g/l NaHCO ₃ 1 g/l D-Glucose	5 % (v/v)	4 mM	-	100 µg/ml
NRK-52E	Dulbecco's Modified Eagle's Medium (DMEM) 3.7 g/l NaHCO ₃ 4.5 g/l D-Glucose	5 % (v/v)	2 mM	-	100 µg/ml
U-373 MG	Minimum Essential Medium Eagle (MEM-Eagle) 2.2 g/l NaHCO ₃ 1 g/l D-Glucose	5 % (v/v)	2 mM	-	100 µg/ml

3.1.2 SUBCULTIVATION

MDCK II, NRK and U-373 MG cells were usually subcultured once a week while BAEC and MCF-7 cells were subcultured twice a week using the protocol shown in **Tab. 3.2**. Buffer compositions for subcultivation are summarized in **Tab. 3.3**.

For the subcultivation of MDCK II and NRK cells, the cell culture medium was removed first and cells were washed twice with 4 ml PBS⁻ to remove dead cells and medium residues. After washing, the cells were incubated for 10 min at 37 °C with 4 ml 1 mM EDTA in PBS⁻ to sequester bivalent cations such as Ca²⁺ and Mg²⁺ which are necessary to form and maintain cell-cell-contacts as well as cell-matrix-contacts. Cells detached from the culture substrates by addition of 1 ml 0.05% (w/v) trypsin in PBS⁻ after an incubation period of 10 min at 37 °C. MCF-7, BAEC and U-373 MG cells were washed with 4 ml PBS⁻ buffer solution and incubated with trypsin as described in **Tab. 3.2**. To inactivate the digesting activity of the enzyme, 10 ml medium was added to all cell suspensions before centrifugation at room temperature (RT) for 5 – 10 min. After centrifugation, the cell pellet was resuspended in 4 ml culture medium and seeded in cell culture flasks or on other substrates suitable for cell culture. Usually, cells were diluted 1:20 referenced to the growth area of the flask.

Tab. 3.2 Subcultivation protocol for the different cell lines. PBS: phosphate buffered saline, EDTA: ethylenediaminetetraacetic acid.

Cell line	Washing with PBS ⁻	Washing with PBS ⁻ /EDTA	Incubation time with PBS ⁻ /EDTA	Incubation time with trypsin	Centrifugation time
BAEC	2x	-	-	3 min, 0.05 % (w/v)	10 min, 110 x g
MCF-7	2x	1x	-	3 min, 0.25 % (w/v)	5 min, 110 x g
MDCK II	2x	-	10 min	10 min, 0.05 % (w/v)	10 min, 110 x g
NRK-52E	2x	-	10 min	10 min, 0.05 % (w/v)	10 min, 110 x g
U-373 MG	1x	1x	-	3 min, 0.05 % (w/v)	10 min, 110 x g

Tab. 3.3 Composition of subcultivation buffers.

Name	Composition
PBS⁻	140 mM NaCl 2.7 mM KCl 8.1 mM Na ₂ HPO ₄ 1.5 mM KH ₂ PO ₄
PBS⁻/EDTA	PBS ⁻ with 1 mM EDTA
Trypsin_{0.25}/EDTA	PBS ⁻ with 0.25% trypsin (w/v) 1 mM EDTA
Trypsin_{0.05}/EDTA	PBS ⁻ with 0.05 % trypsin (w/v) 1 mM EDTA

3.1.3 CULTIVATION OF SPHEROIDS

For spheroid formation, the liquid overlay technique was used. After having reached about 90 % confluency, MCF-7 breast cancer cells were trypsinized from the bottom of the culture flask and centrifuged as described in **Tab. 3.2**. The cell pellet was resuspended in culture medium supplemented with 20 mM HEPES (4-(2-hydroxyethyl)-1-piperazineethane-sulfonic acid), as spheroid formation over the first hours was initialized in an incubator without CO₂. Then, 200 µl of the cell suspension with a seeding density of 15000 c/ml were added to each well of a 96-well plate containing a 1.5 % (w/v) agarose gel prepared in serum free MCF-7 culture medium (50 µl per well). To support spheroid formation, the 96-well plate was covered with Parafilm[®] and put on an orbital shaker inside an incubator (0 % CO₂, 37 °C). Spheroid formation was induced by shaking the plate at 120 rpm for 4 h directly after seeding and then reducing the rotation speed to 50 rpm overnight. Subsequently, the 96-well plate was transferred from the orbital shaker to an incubator at 5 % CO₂ and 37 °C for static cultivation. In this work, 7 – 11 day old spheroids were used for experimental work.

3.1.4 COMPOSITION OF BUFFERS AND SOLUTIONS

All basic buffers used for experiments are listed in **Tab. 3.4**. Buffers were stored at 4 °C until usage and filtered sterile if necessary.

Malonoben (stock solution 10 mM in DMSO) was stored at – 18 °C and diluted to 100 nM in L-15 medium for uncoupling experiments. A 5 mM antimycin A stock solution was prepared by dissolving the compound in DMSO and stored in aliquots at – 18 °C. For cell applications, the stock solution was diluted to 2 µM in L-15. All dilutions were prepared freshly before use.

A 3 % (w/v) saponin solution was prepared in L-15 medium for cell membrane permeabilization and stored at 4 °C before diluting it to a final working concentration of 0.3 % directly before use.

Carbon Dots (C-dots) were synthesized by Michael Lemberger (Institute of Analytical Chemistry, Chemo- and Biosensors, University of Regensburg, Germany) and stored as a sterile stock solution (85 mg/ml in culture medium) at – 18 °C. The working solution was diluted with culture medium to final concentrations of 1.0 mg/ml and 2.5 mg/ml. Diluted solutions were stored at 4 °C.

Cadmium chloride dihydrate ($\text{CdCl}_2 \cdot 2 \text{H}_2\text{O}$) was dissolved in $\text{H}_2\text{O}_{\text{millipore}}$. The stock solution (20 mM) was stored at 4 °C and diluted with culture medium to final working concentrations of 100 µM and 300 µM. The diluted solutions were stored at 4 °C until usage.

A 5 mg ml⁻¹ Cytochalasin D (Cyt D) stock solution (9.85 mM in DMSO) was stored at – 18 °C and further diluted to a final working concentration of 0.1 µM in L-15 medium directly before usage.

Tab. 3.4 Overview of basic buffers used in experiments.

Name	Composition
Leibovitz medium (L-15)	w/o phenol red supplemented with 5 % (v/v) FCS, 1 % (v/v) P/S
L-15, pH 6.4	L-15, pH adjusted with 1 M/0.1 M NaH_2PO_4
L-15, pH 7.2	L-15, pH adjusted with 0.1 M NaH_2PO_4
L-15, pH 7.8	L-15, pH adjusted with 1 M/0.1 M K_3PO_4
PBS⁺⁺	PBS ⁻ with 0.9 mM Ca^{2+} , 0.5 mM Mg^{2+}
PBS⁺⁺/Gal	PBS ⁺⁺ with 1 g/l D-galactose
PBS⁺⁺/Glc	PBS ⁺⁺ with 1 g/l D-glucose

3.1.5 CYROPRESERVATION

For cryopreservation, adherent mammalian cells were detached from the standard cultivation flask according to the subcultivation protocol (see **chapter 3.1.2**). After centrifugation, the cell pellet was resuspended in 1.5 – 1.8 ml cryopreservation medium composed of 10 % (v/v) dimethyl sulfoxide (DMSO) in FCS before it was transferred to 2 ml cryovials. Cryovials were cooled down to – 80 °C using an isopropanol bath (Nalgene® CryoBox™) providing a constant cooling rate of 1 °C/min for the cell suspension. After this slow down cooling step, the cryovials were transferred to a liquid nitrogen tank for long term storage.

For recultivation, cryovials were carefully removed from the liquid nitrogen storage and stored at – 20 °C for 1 – 2 h. Then, the frozen cell suspension was quickly thawed in a water bath at 37 °C and transferred to a 50 ml centrifugation tube. 10 ml of pre-warmed culture medium were added dropwise to the suspension and the sample was centrifuged according to the parameters of the respective cell type (see **chapter 3.1.2**). Afterwards the cell pellet was resuspended in culture medium and the cell suspension was seeded to standard culture flasks at different ratios with respect to the original cell density per cm². 24 h after recultivation, the cell culture medium was exchanged and cells were cultivated under standard conditions.

3.2 RATIOMETRIC OPTICAL OXYGEN SENSING

3.2.1 PRINCIPLES OF RATIOMETRIC OPTICAL OXYGEN SENSING

Principles of Luminescence Quenching

Luminescence is the emission of light from a molecule or substance which occurs usually at a longer wavelength than that of the excitation light (Stokes shift). Luminescent emission can be divided into fluorescence and phosphorescence. **Fig. 3.1** shows the Jablonski diagram which depicts the processes that occur between absorption and emission of light. When a fluorophore absorbs light, it is excited to a higher electronic state S_1 or S_2 , which is usually followed by a fast relaxation to the lowest vibrational level of S_1 . This process is called *internal conversion*. Because the electron in the excited singlet orbital is paired by opposite spin to the non-excited electron in the ground state, the return to the ground state is spin allowed and usually occurs within a nanosecond range. Thus, fluorescence is a short-lived phenomenon and rapid emission of a photon can be observed. Moreover, fluorescence emission intensity can also be decreased by quenching processes.

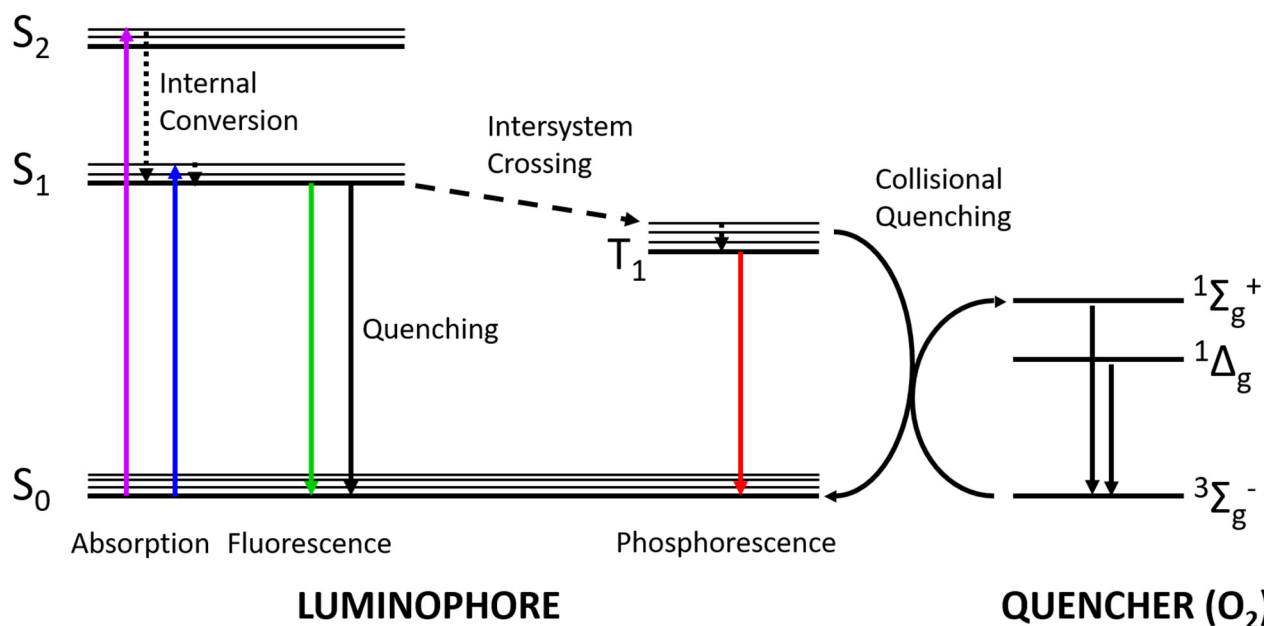


Fig. 3.1 Jablonski diagram showing the processes between absorption and emission of light by a luminophore. The diagram was adapted from (Lakowicz 2006).

However, oxygen sensing as performed in this work relies on phosphorescent emission of dyes and the quenching characteristics of bimolecular oxygen. Upon excitation with a suitable source such as a laser or LED, the phosphorescent molecule absorbs photons and is raised to higher vibrational levels of the electronically excited state (S_1) followed by a fast, *internal conversion* to the lowest

vibrational level of the excited state S_1 . By reversing the spin of the electron, molecules can undergo a transition from S_1 to the first triplet state T_1 , a process which is called *intersystem crossing*. Because return from T_1 state to the ground state by phosphorescent emission is spin forbidden, emission from this state is usually slow. In contrast to fluorophores, phosphorescent dyes show a bigger Stokes shift and long phosphorescence lifetimes ranging from hundreds of μs to a few seconds (Lott and Hurtubise 1974; Lakowicz 2006). Since the lifetime of phosphorescent molecules is quite long, the probability of energy transfer by collision with other molecules in solution is high. The principle of reduction of phosphorescent emission and lifetime of a sensor dye by quenching is exploited in phosphorescent oxygen sensing since its discovery in 1935 (Kautsky and Hirsch 1935). Bimolecular, paramagnetic oxygen in its triplet ground state ($^3\Sigma_g^-$) is a very efficient collisional quencher, that accepts energy from the excited triplet state of the luminophore, which leads first to the conversion to singlet oxygen in its first ($^1\Delta_g$) or second ($^1\Sigma_g^+$) excited state, and second to the radiationless return of the luminophore to the ground state (Quaranta et al. 2012). Return of oxygen from the singlet to the triplet ground state is fast due to interaction with solvent molecules or oxidation reactions with neighboring molecules yielding a lifetime in H_2O of about 3 μs (Egorov et al. 1989; Mitra and Foster 2000). Collisional quenching by molecular oxygen is a photophysical process that leads to a decrease of phosphorescence intensity and lifetime in a concentration dependent manner. This enables direct, non-chemical and reversible oxygen sensing (Papkovsky and Dmitriev 2013).

Ratiometric Optical Oxygen Sensing

Different from sensing oxygen levels by measuring changes in luminescence intensity, which is heavily influenced by photobleaching, fluctuations of light source intensity or changes of dye concentration, ratiometric optical oxygen sensing provides less error-prone measurements. Usually both, an oxygen sensitive dye and a reference dye are incorporated in the same matrix environment (**Fig. 3.2, A**). However, using a single ratiometric dye which shows both, oxygen sensitive phosphorescence and oxygen insensitive fluorescence is also possible (Zhang et al. 2009; Yoshihara et al. 2012). The reference dye requires being unquenchable by oxygen while showing low susceptibility to photobleaching comparable to the sensor dye. Further, there should be no overlapping of the emission spectra of reference and sensor dye or any other energy transfer (Quaranta et al. 2012). At best, reference and sensor dye can be excited with the same wavelength

and their individual emission signals are measured by using different bandpass filters or different RGB color channels (Wang et al. 2010). **Fig. 3.2, B** shows the spectral separation of the emission of reference and oxygen sensitive dye. While the emission intensity of the sensor dye is decreased by collisional quenching with oxygen, the emission intensity of the reference dye is not influenced. By division of the measured intensity of the reference dye by the intensity of the sensor dye in dependency of the present oxygen concentration or partial pressure, a calibration curve can be generated (**Fig. 3.2, C**).

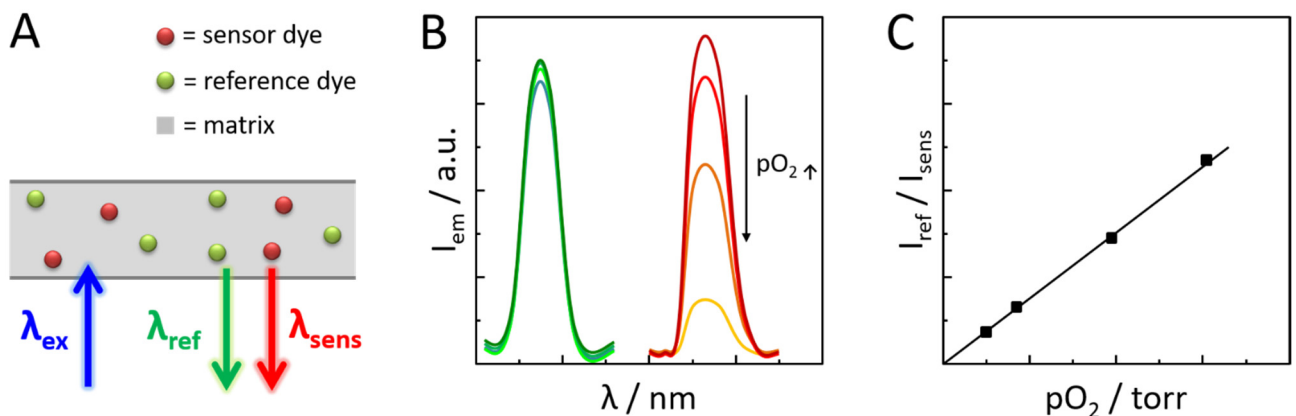


Fig. 3.2 Overview of ratiometric oxygen sensing. (A) Embedding of sensor and reference dye in one oxygen permeable matrix. The dyes can be excited at the same wavelength but emit at different wavelengths. (B) Emission intensity of the sensor dye (red) is quenched in the presence of oxygen while intensity of the reference dye (green) is unchanged. (C) Example of a linear calibration curve in ratiometric intensity mode.

3.2.2 COMMERCIAL SENSOR SYSTEMS

For ratiometric oxygen measurements of adherent cells two different systems were used. The VisiSens A1 series is an already commercially available imaging system to laterally map the oxygen distribution. It is developed and distributed by PreSens GmbH (Regensburg, Germany). The second system, VisiSens TD mic was developed in the course of this work and is also an experimental set-up to image the lateral oxygen concentration. Both systems use the ratiometric method to measure oxygen levels. Commercially available, planar oxygen sensitive foils (SF-RPSu4, PreSens GmbH, Regensburg, Germany) were used as culture substrates for adherent cells in all experiments. The oxygen sensor foils have a thickness of 150 – 190 μm and consist of three layers. The support layer is made up of polyester which is transparent and impermeable to oxygen. A second, 6 – 8 μm thick oxygen sensitive layer which contains an oxygen sensitive dye and a reference dye is directly deposited upon the support layer. The third layer is a silicone-based, oxygen permeable optical

isolation layer (20 – 50 μm) that blocks ambient light and does not respond to changes in oxygen concentration. Due to patent-protection, no further descriptions regarding the composition of the foils will be made. As trans-illumination was used in most experiments conducted in this work, the optical isolation layer of SF-RPSu4 sensor foils was removed to allow excitation light from the side of the protection layer to reach the foils. Sensor foils were stored in the dark till usage. Usually, the oxygen sensitive foils were glued to the bottom of either a cell culture petri dish or a microscope slide, dried and stored in the dark until usage as described in **chapter 3.2.3**.

3.2.2.1 VISISENS A1

The VisiSens A1 is a commercially available system which can be directly incorporated in a standard cell culture incubator (volume 48 l) due to its small size (length = 10 cm, diameter = 3.8 cm). It consists of a USB connectable detector unit with an integrated CMOS chip for readout of the sensor response. Eight blue LEDs are incorporated into the detector unit and are used for epi-illumination of the oxygen sensitive probes as well as the reference dye. **Fig. 3.3, A** shows the measurement set-up with the sample directly positioned on top of the detector unit. Different sets of available adapter tubes allow the magnification to be varied from 10x up to 220x via manual focusing (**Fig. 3.3, B**). **Tab. 3.5** shows technical data of the two tubes which were used in this work. VisiSens A1 uses epi-illumination for the excitation of the probes in the sensor foil (**Fig. 3.3, C**). VisiSens A1 was used as comparison and reference to the novel imaging system. Because the camera system is watertight, it was also used for studies conducted with the ECIS- O_2 chip, which required a humidified incubation system.

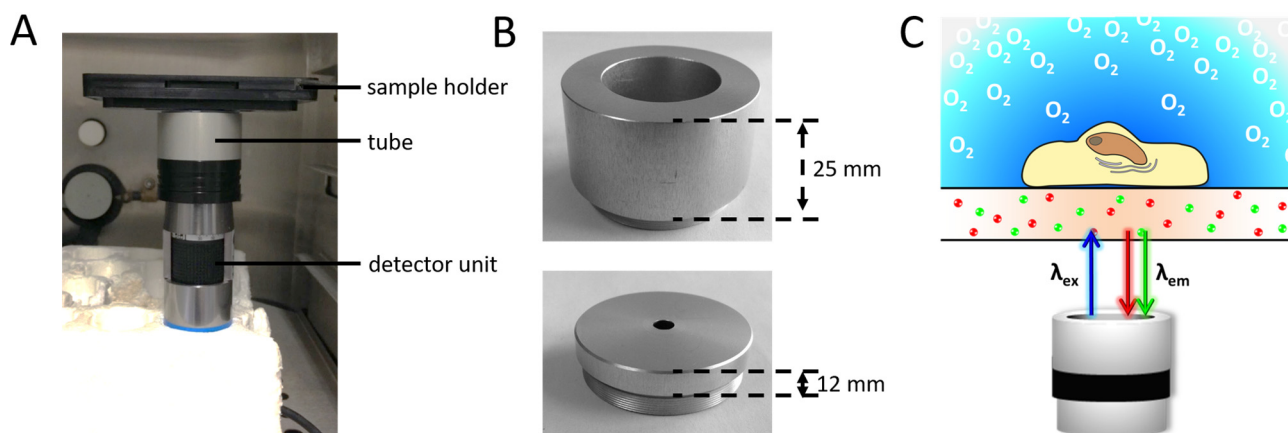


Fig. 3.3 (A) Measurement set-up for oxygen imaging experiments measured with VisiSens A1. (B) Two different tubes were used for different magnifications. (C) Schematic of ratiometric readout of the biocompatible oxygen sensitive foils based on epi-illumination of the biological samples.

Before each measurement, the camera parameters brightness and exposure time were adjusted and were kept constant for both, measurement and calibration. Usually, the whole measurement set-up was kept inside a humidified standard cell culture incubator at 37 °C, 0 % CO₂ and images of the sample that was placed directly on the tube were recorded every 15 minutes. VisiSens A1 is controlled by VisiSens AnalytiCal 1® software, which allows automated time resolved measurements as well as conversion of raw data images in false color images of oxygen partial pressure after proper calibration.

Tab. 3.5 Technical data of the tubes used for measurements with VisiSens A1.

	Tube 1	Tube 2
Tube length	25 mm	12 mm
Field of view	1280 x 1024 Px (11728 x 9383 μm)	1280 x 1024 Px (7131 x 5705 μm)
Pixel resolution	~ 9 μm	~ 6 μm

3.2.2.2 VISISENS TD MIC

VisiSens TD mic is based on the commercial VisiSens TD imaging system manufactured by PreSens GmbH. In contrast to VisiSens TD, which is applied for a measurement field in the range of tens of cm, the newly developed system can be used to image structures in the μm range.

Fig. 3.4, A shows a schematic of the measurement set-up. With a total height of 28 cm VisiSens TD mic can be easily incorporated into a standard cell culture incubator (48 l volume) so that measurements with biological samples in L-15 medium or PBS can be conducted at 37 °C, 0 % CO₂. The system is connected by a software interface to a PC. **Fig. 3.4, B** shows the structure of the detector unit in detail. The imaging detector is connected to a 0.32x extension TV-tube (Opto, Graefelfing, Germany) via a C-mount lens adapter. Emission filters between tube and detector unit cut off any interfering light from the excitation source. A 5x microscope objective (EC Epiplan-Neofluar 5x/0.13 HD, Zeiss, Jena, Germany) is mounted on the TV-tube for microscopic image magnification. The working distance between microscope objective and the small petri dish containing the oxygen sensitive foil and cell samples is about 1.2 cm. A trans-illumination light source holder that matches the top cover of the small petri dish was printed using a 3D plotter. This holder is equipped with a 3 mm blue LED to excite the luminescent dyes in the sensor foil. To

guarantee a homogeneous distribution of the excitation light the surface of the LED was roughened. The newly developed system has a field of view of 1292 x 946 Px (2064 x 1540 μm) yielding a pixel resolution of 1.6 μm .

VisiSens TD mic uses fluorescence ratiometric imaging via trans-illumination to determine oxygen levels (**Fig. 3.4, C**). The oxygen sensor foil that serves as growth substrate for the cells is excited by the blue LED. Red emission of the sensor dye and green emission of the reference dye passes through the microscope objective and are collected by the detection unit. Image acquisition is fully automated and controlled by a customized version of the AnalytiCal[®] software. Usually, experiments were conducted with an LED voltage set to 10 mV and an exposure time of 250 – 350 ms. Parameters were kept constant for the measurement and subsequent calibration. Images were taken every 10 – 15 min. Typically, oxygen measurements were conducted using the newly developed system VisiSens TD mic unless mentioned otherwise.

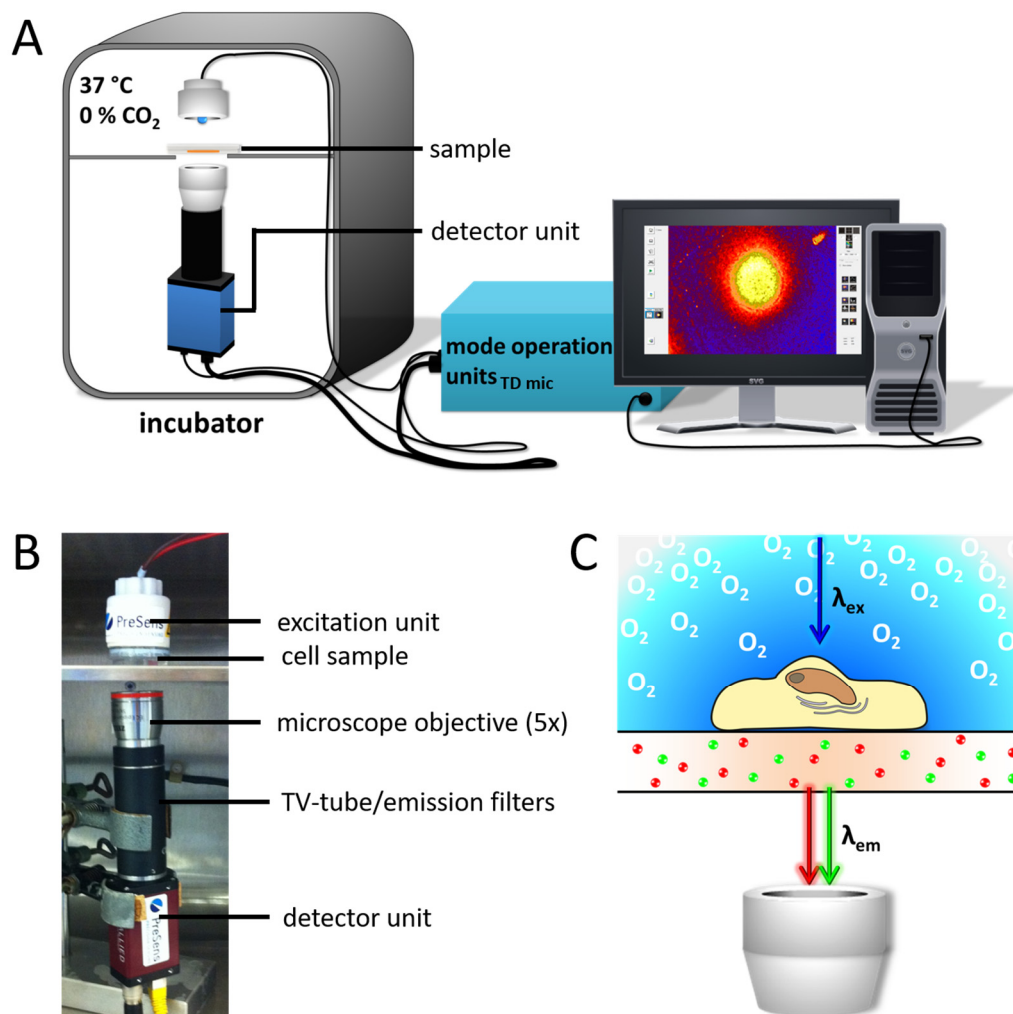


Fig. 3.4 (A) Schematic of the newly developed oxygen imaging set-up. Miniaturization allows the detector and the excitation unit to be incorporated in a standard 48 l cell culture incubator. (B) Detailed image of the detection unit based on microscopy optics. (C) Schematic of ratiometric readout of the biocompatible oxygen sensitive foils based on trans-illumination of the biological samples.

3.2.3 PREPARATION OF OXYGEN SENSOR FOILS FOR CELL EXPERIMENTS

Incorporation of Oxygen Sensor Foils into Petri Dishes

The detailed procedure for preparation of the oxygen sensor foils for cell experiments can be seen in **Fig. 3.5**. First, the optical isolation layer was removed to enable usage of the foils in trans-illumination mode. The layer was carefully detached using tweezers to avoid scratching the surface of the oxygen sensor foils (SF-RPSu4). Round spots of 0.7 cm diameter were stamped out of the oxygen sensitive foils with a punching tool. These sensor spots were glued with silicone glue (type SG-1) to the bottom of a standard petri dish with a diameter of 3.5 cm. The silicone glue was dried for at least 24 h before experiments were conducted and the immobilized spots were stored at RT protected from light. Before cells were seeded, the petri dishes containing the sensor spots were exposed to an argon plasma for 1 min to hydrophilize and sterilize the surface.

When MCF-7 spheroids were analyzed, a PDMS (Polydimethylsiloxane) ring with a diameter of 1 cm and a height of 3 mm was used as cell culture chamber. The PDMS ring was exposed for 1 min to an argon plasma and was attached only by adhesive force around the sensor spot to facilitate spheroid seeding. 200 μ l of MCF-7 cell culture medium containing at least one spheroid were added to the inner compartment of the PDMS ring. To prevent the sample from falling dry, 1.5 ml of medium were added to the outer compartment of the PDMS ring. Spheroids were allowed to attach for 24 h at 5 % CO₂, 37 °C. Before the experiment was started, the PDMS ring was carefully removed and spheroids were washed two times with 1 ml L-15 medium to remove remaining phenol red from the culture medium. Then, the petri dish was covered with a custom-built, air-tight cover lid. Therefore, a small opening for medium addition was introduced in the lid of a standard petri dish and the rim was covered with Blu-Tack® for air-tight sealing of the sample. The sample was completely filled with 9.6 ml of the respective buffer (see **Tab. 3.4**) through the opening in the lid using a 10 ml syringe. The inlet was sealed, the petri dish was put inside the incubator containing the imaging system and imaging was started immediately after adjusting the camera focus to the oxygen sensor foil.

When monolayer cells were measured, 2 ml cell suspension of the desired density were seeded in the petri dish. 24 h after seeding cells were washed twice with 1 ml of the respective buffer. Then the sample was sealed airtight with the custom-built lid and filled with 9.6 ml buffer.

Because imaging of confluent monolayers resulted in homogeneous spatial distribution of pO_2 , both, changes in spatial and temporal distribution of pO_2 were imaged using a small spot of monolayer cells cultivated on the oxygen sensor film.

Due to the weak adhesion of PDMS to the sensor foils, another approach was chosen to provide a cultivation chamber. Thus, the petri dish was covered with a lid containing a small inlet for cell seeding which served as a barrier. The rim of the lid was covered with Blu-Tack® and pressed firmly on the bottom of the petri dish that no medium could leak out between sensor foil and inlet. Then 100 μ l of cell suspension (2.0×10^5 cells cm^{-2} , growth area = 3.2 mm^2) were added to the inlet. The inlet was covered with a small lid to prevent the sample from falling dry. Cells were incubated for 24 h at 37 °C, 5 % CO_2 . Then, the lid was removed, the sample was washed twice with 1 ml L-15 medium, sealed air-tight with the custom-built lid and the Petri dish filled up with 9.6 ml L-15 medium.

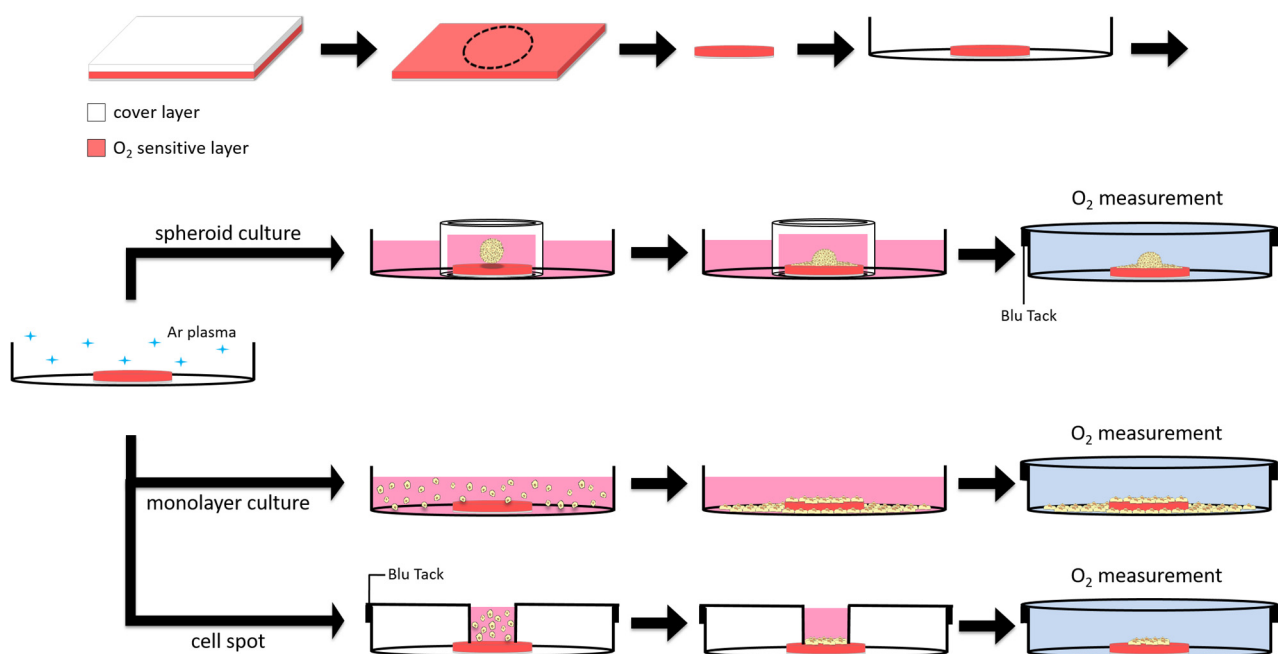


Fig. 3.5 Preparation procedure of oxygen sensitive culture substrates. After removal of the light impermeable cover layer, a round oxygen sensor spot was punched out, glued to the bottom of a small petri dish and allowed to dry. Treatment with argon plasma was used to sterilize petri dishes and sensor spots for use in cell culture. When spheroids were seeded to the oxygen sensor foil a PDMS ring was used as cell culture chamber. The spheroids were allowed to adhere to the sensor surface for 24 h and oxygen was measured after medium exchange from culture medium to L-15 medium. Monolayer cells were seeded in the petri dish and allowed to adhere over a period of 24 h before oxygen measurements were carried out. A monolayer cell spot was created by seeding the cells in a pre-defined compartment.

Fabrication of Cultivation Chambers with Different Volumes of Medium

Round spots of SF-RPSu4 oxygen sensor foils ($d = 0.7$ cm) were glued centrally on the bottom of a cell culture petri dish ($d = 9$ cm) using silicone glue. A glass ring was glued to the petri dish to create a cell cultivation chamber. Three different chambers with a volume of 4.8 ml, 9.6 ml and 19.2 ml were fabricated using three different glass rings with a respective height of 0.5 cm, 1 cm and 2 cm and a diameter of 3.5 cm. The silicone glue was allowed to dry for at least 24 h before usage. Before cell seeding the chambers were sterilized by argon plasma exposure for 1 min.

3.2.4 COATING OF OXYGEN SENSOR FOILS WITH ADHESION PROMOTING REAGENTS

To investigate the biocompatibility of the oxygen sensitive foils, small rectangular pieces of foil (~ 0.5 cm x 0.5 cm) were cut out and glued to the bottom of a cell culture petri dish ($d = 9.2$ cm) with silicone glue. An 8-well Lab-Tek[®] chamber was glued on top of an arrangement of foil pieces, so that the bottom of six wells consisted of oxygen sensor foil while two wells had the surface of a normal cell culture petri dish as bottom. Afterwards, the arrays were dried for at least 24 h and stored in the dark until usage. Before cell inoculation the array was exposed to an argon plasma for 1 minute. Wells containing sensor foil were coated with 100 μ l of different adhesion promoting agents listed in **Tab. 3.6**. Afterwards, the coating solution was aspirated and cells were seeded with a density ranging from 2.0×10^4 – 4.5×10^5 c cm^{-2} . 24 h after seeding cells were stained with a mixture of Calcein Acetoxymethylester and Ethidium homodimer-1 or Alexa Fluor[®] 488 phalloidin according to the protocol described in **chapter 3.3.4** to analyze cell adhesion and viability on the oxygen sensor foils.

Tab. 3.6 Applied substances, concentration and incubation parameters for the coating of oxygen sensitive foils.

Substance	Concentration	Incubation parameters
Culture medium	-	1 h, 37 °C, 5 % CO ₂
FCS	-	1 h, 37 °C, 5 % CO ₂
Fibronectin (from human plasma)	25 μ g/ml	1 h, RT
Gelatin	0.5 % (w/v)	1 h, 37 °C, 5 % CO ₂
Poly-L-lysine	100 μ g/ml	1 h, RT

3.2.5 CALIBRATION

Calibration of the oxygen sensor foils was usually done after the imaging experiment was finished, as cells inoculated on a pre-calibrated sensor spot were more often affected by contamination. To remove the cells from the sensor surface, cells were washed twice with PBS⁻ and incubated for 10 min with PBS⁻/EDTA. Then, cells were incubated for 20 minutes with trypsin. Afterwards the surfaces were washed three times with deionized water. The clean sensors were either put back inside the incubator for the immediate calibration, or were dried and stored in the dark until calibration was performed.

The oxygen sensor foils were calibrated via a two-point calibration at 37 °C, 0 % CO₂. Therefore, two solutions were prepared from L-15 medium. A normoxic solution (pO₂ = 149.3 torr or 20.9 % oxygen saturation) was prepared by bubbling compressed air through L-15 medium for 15 min. A second, deoxygenized solution (pO₂ = 0 torr or 0 % oxygen saturation) was prepared by addition of 10 g/l Na₂SO₃ to the medium. All calibration solutions were pre-warmed to 37 °C during preparation. During the calibration process, a droplet of oxygenated calibration solution was added to the oxygen sensitive foil and the signal was recorded by using the snapshot mode of the VisiSens software. Then, the solution was aspirated, a droplet of deoxygenated medium was added and the signal was recorded. Camera and LED settings during calibration were kept identical to the parameters of the respective experiment. Images of the respective oxygen-free and normoxic conditions were uploaded into the VisiSens AnalytiCal[®] software and a linear calibration function was generated by choosing an appropriate ROI (region of interest) as shown in **Fig. 3.6**.

The calibration function was used to convert the r/g ratio of the images taken in one time-series into a false color image which shows the spatial 2D distribution of the oxygen partial pressure. The calibration data was used to convert the respective individual raw data images into false color oxygen images as a function of time. Changes in oxygen partial pressure as a function of time were determined with the z-profile function. Therefore, an appropriate ROI was chosen and the averaged pO₂ and the standard error were determined. Usually, pO₂ was averaged over the whole image section except when smaller structures (e.g. MCF-7 spheroids, microchannels or cell spots) were analyzed. Calibrated false color oxygen images were exported as jpeg and converted into avi. files using the software NIH ImageJ.

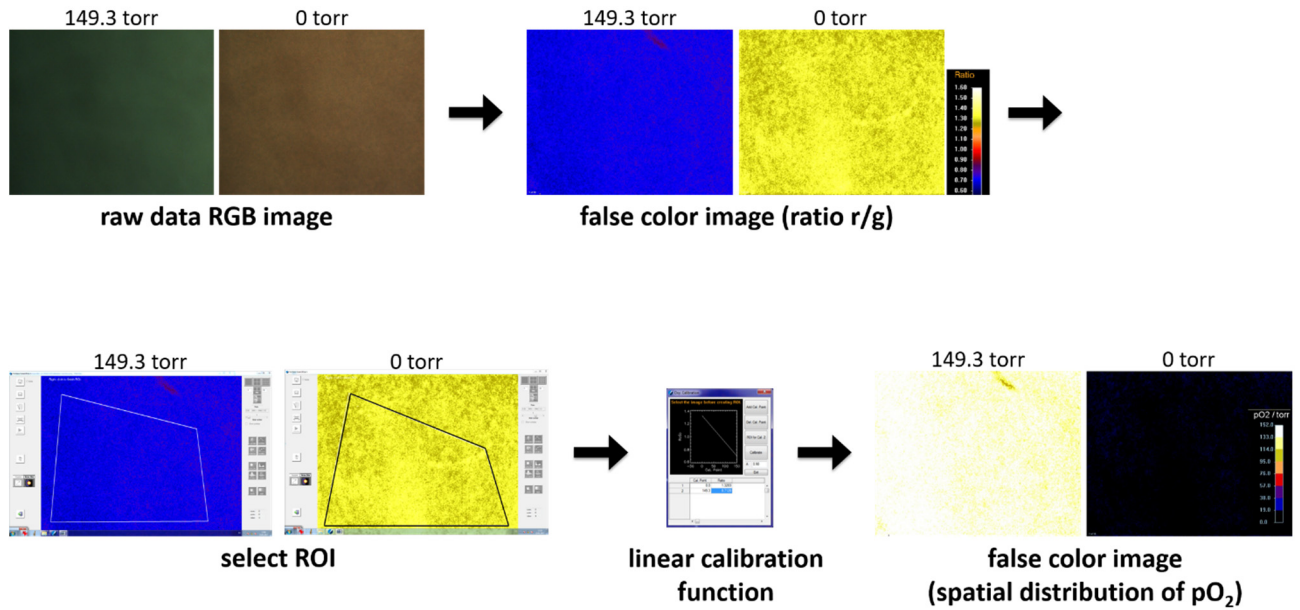


Fig. 3.6 Two-point calibration of the oxygen sensor foils using the AnalytiCal® software. The intensity of the oxygen sensor dye is recorded in the red channel (r), while the signal output of the reference dye is recorded in the green channel (g) of an RGB raw data image. The raw data RGB images are converted into false color images containing the ratio r/g . A linear calibration function is created by the selection of a suitable ROI for normoxic (149.3 torr) and anoxic (0 torr) conditions. The calibration function is used to convert raw data images into false color images which show the 2D distribution of oxygen partial pressure.

3.2.6 DETERMINATION OF THE (APPARENT) OXYGEN CONSUMPTION RATES

The apparent oxygen consumption rate (AOCR) for closed systems was determined by linear fitting of the decrease of oxygen partial pressure as a function of time.

$$y = A + Bx \quad (3.1)$$

Where $-B$ yields the AOCR.

As different cell lines show differences in their basal oxygen profiles and the time resolution was quite low ($\Delta t = 10 - 15$ min) different data ranges were used for analysis. Data fitting was done using Origin Pro 8 software.

The oxygen consumption rate (OCR) for open systems was calculated with the following equation (Mamchaoui and Saumon 2000):

$$OCR = \frac{-D S \alpha [pO_2(h) - pO_2(0)]}{h} \quad (3.2)$$

Where D is the diffusion coefficient of O_2 in water ($3.3 \cdot 10^{-5} \text{ cm}^2 \text{ s}^{-1}$), S is the cell-covered area of the petri dish (9.6 cm^2), α is the solubility coefficient at 37°C ($0.94 \text{ } \mu\text{mol cm}^{-3} \text{ atm}^{-1}$), h is the height of

the medium column (0.5 cm), the $pO_2(h)$ is the oxygen partial pressure at the height of the cell layer and $pO_2(0)$ is the oxygen partial pressure at the medium surface determined at $t = 5$ h.

3.3 MICROSCOPIC TECHNIQUES

3.3.1 PHASE CONTRAST MICROSCOPY

When thin, unstained specimens such as live cells are examined in brightfield illumination with a standard light microscope, they possess poor contrast due to poor light absorption. Phase contrast microscopy is a technique to enhance contrast of unstained biological samples and was first described by Frits Zernike in the 1930s (Zernike 1935). The principle of phase contrast microscopy is based on the phase shift of light which is caused by the specimen, also called the phase object. The resulting phase shift is translated into a corresponding change in amplitude (difference in intensity) which can be discerned by the human eye as difference in image contrast. A standard brightfield microscope can easily be converted into a phase contrast microscope by introduction of a condenser annulus and a matching phase plate which enhances phase differences and reduces the amplitude of surrounding light passing through the specimen, thus further enhancing contrast (www.microscopyu.com).

In this study, phase contrast images of adherent cells were taken with a Nikon Diaphot microscope with the 4x (PLAN, 4x / 0.13) or 10x (E 10x / 0.25) magnification objective. Images were recorded with a digital camera attached to the microscope.

3.3.2 STEREO MICROSCOPY

Stereomicroscopy is a technique which is frequently used in material research, biotechnology and biomedical research. It allows a detailed investigation of sample surfaces and their three dimensional properties (www.leica-microsystems.com/science-lab/). The design of a stereomicroscope uses two different optical paths that include separate intermediate lenses, objective and eyepiece. Thus, when looking on an object, the viewer sees the sample from two slightly different angles. The projection of two different images to the retina of the right and left eye will be fused together to form one 3D image. Usually, stereomicroscopes can be divided into two types. The Greenough type consists of two separate optical trains with separate objectives incorporated into twin body tubes that produce the stereo effect. The common main objective (CMO) type uses a single large objective that is shared between both eyepieces and lens systems. By choosing the

appropriate illumination mode such as incident light illumination, transmitted light illumination or darkfield illumination, the structures of an object can be visualized (www.microscopyu.com).

Stereomicroscopic images of the surface of oxygen sensor foils were taken with a Nikon SMZ 1500 C-DSD230 CMO stereomicroscope equipped with a digital camera. Objects can be analyzed with magnifications varying from 3.75x to 540x with a zoom range from 0.75x to 11.25x depending on the combination of zoom lenses, objective lenses and eyepiece.

3.3.3 CONFOCAL LASER SCANNING MICROSCOPY (CLSM)

The principle of confocal laser scanning microscopy (CLSM) was first described by Marvin Minsky in 1955 and is currently used to visualize fluorescently labeled living or fixed biological samples in 3D. CLSM uses a focused beam of a monochromatic laser to scan samples through a pinhole. Out-of-focus light is eliminated by combining point-by-point illumination with suitable pinhole apertures. When the laser beam is focused to the optical plane using an objective, it excites only fluorophores in the light path, allowing optical sectioning of the samples. By scanning the sample laterally scattered light is excluded. Light emitted by the fluorophores is guided through a dichroic mirror eliminating undesired wavelengths. The axial resolution of the images can be varied by using detection pinholes of different sizes. After passing a confocal detection pinhole which excludes any axially scattered light, the emitted fluorescence is collected by a photomultiplier tube or a CCD (charge coupled device) camera. In contrast to conventional wide-field microscopy, CLSM enables visualizing biological structures in more detail due to its higher lateral and axial resolution. Next to single recordings of optical xy-sections, samples can be imaged in 3D using a series of optical sections collected at different z-planes of the sample. xy-sections and z-series can be collected as 4D data sets using time-lapse mode. This four-dimensional imaging gives a better insight into cellular processes and dynamic changes of cell morphology (Minsky 1988; Paddock 2000; Stephens and Allan 2003).

In this work a Nikon Eclipse 90i microscope with a C1 scanning unit was used to record fluorescence micrographs. The microscope is equipped with three different lasers (Melles Griot, Rochester, USA) for excitation of the fluorescent probes and three different detectors to record the signals emitted by the fluorophores. Three different objectives were used to record fluorescence micrographs and phase contrast images. An overview of lasers, detectors and objectives with their individual magnification and numerical aperture (NA) is listed in **Tab. 3.7**. Usually, the PLAN / 10x magnification

objective was used for acquisition of overview images of cell covered oxygen sensor foils presented in **chapter 4.1** and **5.1**, and excitation of oxygen sensitive dyes in the optical wound healing assay (see **chapter 7**). For high-resolution micrographs, such as z-stacks of MCF-7 spheroids, the 60x magnification water immersion objective was used. Typically, images were recorded with a resolution of 1024 x 1024 pixels with the pinhole set to a diameter of 30 μm (pinhole 5). Images were acquired with the Nikon EZ-C1 software and further processed with the NIH ImageJ software.

Tab. 3.7 List of different lasers, detectors and objectives of the Nikon Eclipse 90i confocal laser scanning microscope used in this work. BP: band pass filter, LP: long pass filter.

Lasers	Detector	Objectives / Magnification / NA
408 nm / < 500 mW	450/35 nm BP (blue)	PLAN / 10x / 0.25
488 nm / < 50 mW	515/30 nm BP (green)	PLAN / 20x / 0.40
543 nm / < 5 mW	650 nm LP (red)	NIR Apo / 60x / 1.0 / water

3.3.4 CYTOCHEMICAL STAINING

Unspecific Cell Staining using Carbofuchsin

Carbofuchsin solution (according to Ziehl-Neelsen) was used for unspecific staining of a patch of MDCK II monolayer cells grown on oxygen sensor foils. A cell spot was cultivated in a petri dish containing an oxygen sensor spot as described in **chapter 3.2.3**. Cells were either stained immediately after barrier removal or after 40 h of oxygen imaging. First, the medium was aspirated and cells were washed twice with 1 ml PBS⁺⁺. Then, cells were fixed with 1 ml 4 % (w/v) paraformaldehyde (PFA) in PBS⁺⁺ buffer for 10 min at room temperature. After two washing steps with 1 ml PBS⁺⁺, cells were incubated with 500 μl carbofuchsin solution (5 min, RT). Excess dye solution was removed by washing the cell layer at least five times with 1 ml PBS⁺⁺ buffer until the supernatant washing buffer solution remained clear and colorless. The stained cell patch was dried under nitrogen flow and microscopic images were taken with a Nikon SMZ 1500 C-DSD230 CMO stereomicroscope equipped with an attached digital camera.

Live-Dead Staining with Calcein Acetoxymethylester and Ethidium-Homodimer

A common staining technique to distinguish between living and dead cells is to use a mixture of two dyes for cell labelling (see **Fig. 3.7**). Calcein Acetoxymethylester (AM) is used to label living cells. The esterified molecule is non-fluorescent and highly membrane permeable. After entering a healthy cell, the acetoxymethylester groups are cleaved off by intracellular esterases. The free dye has a high affinity for binding Ca^{2+} ions, upon which it becomes highly fluorescent. This bright, green fluorescence of Calcein specifically marks live cells. To label dead cells the membrane impermeable, weakly fluorescent dye Ethidium homodimer-1 (EthD-1) is used. When cells are heavily damaged or dead, their membrane integrity is lost and the dye can enter the cells freely. EthD-1 labels mainly the cell nucleus because of its strong tendency to intercalate into DNA. Upon DNA intercalation, the dye shows bright red fluorescence when excited with 543 nm light.

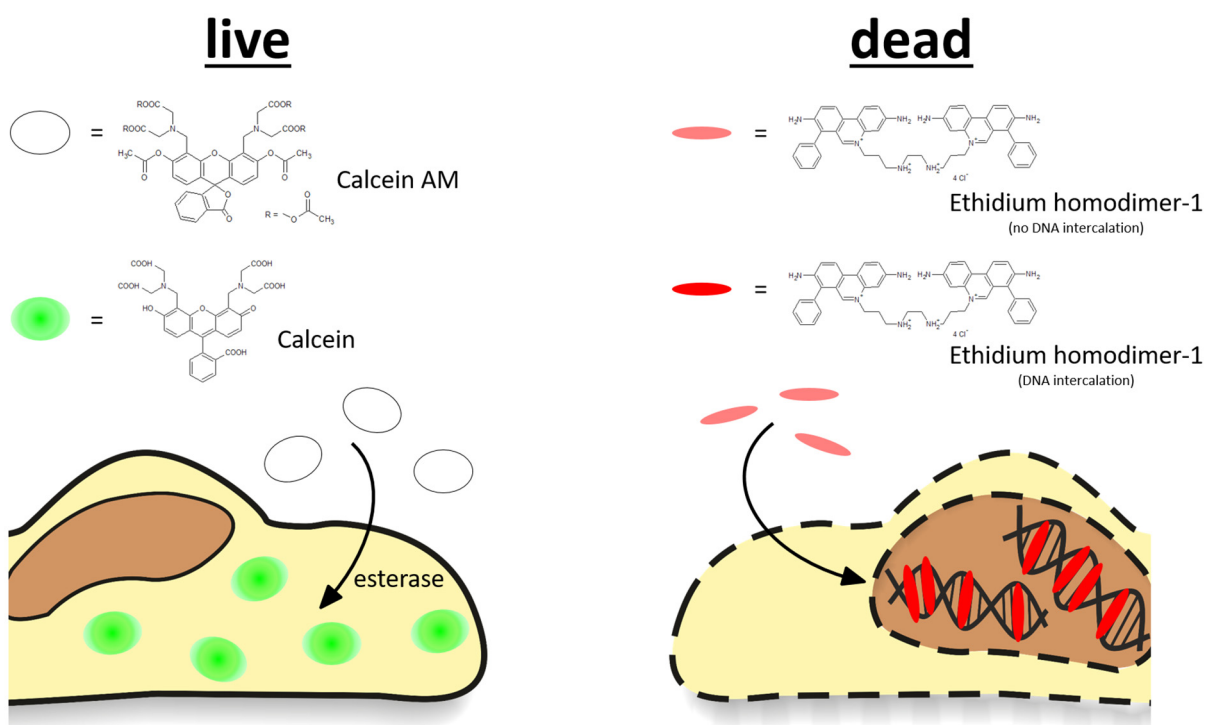


Fig. 3.7 Principle of the live-dead staining with Calcein AM (CaAM) and Ethidium homodimer-1. The non-fluorescent dye CaAM is converted by intracellular esterases of live cells to Calcein. Calcein, which binds Ca^{2+} , is trapped inside the cells and emits strong green fluorescence. When cells are dead, the membrane impermeable dye EthD-1 can pass the damaged cell membrane. The dye intercalates into DNA which leads to a strong red fluorescence of the cell nuclei of dead cells.

Live-dead staining was used to visualize cells and spheroids grown on oxygen sensor foils. First, a 2 mM stock solution of EthD-1 in DMSO was diluted to a working concentration of 4 μM and a 1 mM

stock solution of CaAM in DMSO was diluted to a final working concentration of 2 μM in PBS⁺⁺ buffer. Then, samples were washed twice with 1 ml PBS⁺⁺ buffer solution. Cells were incubated with 1 ml live-dead staining solution containing 2 μM CaAM and 4 μM EthD-1 in PBS⁺⁺ for 30 min in the dark (0 % CO₂, 37 °C). After the staining solution had been removed, fluorescently labelled cells were examined in PBS⁺⁺ buffer using a confocal laser scanning microscope (Nikon Eclipse 90i) with 10x and 60x magnification. CaAM was excited at 488 nm and its green emission was detected using the 515/30 nm detector. Eth-D1 was excited at 543 nm and fluorescence emission was recorded with a 650 LP detector.

Staining of the Cytoskeleton with Alexa Fluor® 488 Phalloidin

Phalloidin is a fungal toxin produced by the death cap (*Amanita phalloides*). It selectively binds to filamentous actin (f-actin). In this work the brightly green emitting conjugate Alexa Fluor® 488 phalloidin was used to label the actin cytoskeleton.

The actin cytoskeleton of cells grown on oxygen sensor foils was stained using the following protocol. Cells were inoculated with a density of 5.0×10^4 c cm⁻² or 4.5×10^5 c cm⁻² in Lab-Tek® 8-well chamber arrays that were glued to the oxygen sensor foils using silicon glue (see chapter 3.2.4). 24 h after cell inoculation, cytochemical staining was performed. For cytoskeleton staining, the Alexa Fluor® 488 phalloidin stock solution (8.7 mg/ml) was diluted 1:100 in PBS⁺⁺ buffer solution to a final working concentration of 87 $\mu\text{g}/\text{ml}$. Cells on oxygen sensitive substrates were washed twice with 400 μl PBS⁺⁺ buffer per well. Then, cells in each well were fixed with 200 μl PFA, 4 % (w/v) in PBS⁺⁺ (10 min, RT), and washed twice with 400 μl PBS⁺⁺. Cell membranes were permeabilized by adding 200 μl 0.5 % (v/v) Triton-X-100 in PBS⁺⁺ to each well (10 min, RT). Prior to addition of Alexa Fluor® 488 phalloidin staining solution (100 $\mu\text{l}/\text{well}$), cells were washed twice with 400 μl PBS⁺⁺ buffer. Cells were incubated with the staining solution for 40 min (0 % CO₂, 37 °C). After removing the staining solution, cells were washed three times with PBS⁺⁺ and analyzed with a Nikon Eclipse 90i confocal laser scanning microscope. Alexa Fluor® 488 phalloidin was excited at 488 nm and the fluorescent signal was recorded at 515 ± 30 nm.

3.4 IMPEDANCE SPECTROSCOPY

3.4.1 PRINCIPLES OF IMPEDANCE SPECTROSCOPY

Impedance spectroscopy is a highly sensitive electrochemical method that provides a large amount of information via the readout of numerous parameters and that is applicable to conductors, semi-conductors and insulators. Impedance spectroscopy has various applications, e.g. it is used as a standard characterization tool of solid materials or for monitoring electrochemical processes of both biological and non-biological systems (Lasia 2014).

Ohm's law states that for a direct current (DC) system, the resistance R is described by the ratio of the applied voltage U to the resulting current I :

$$R = \frac{U}{I} \quad (3.3)$$

Hence, in an electric system with an alternating current (AC) circuit, the impedance Z is described by the ratio of the applied alternating voltage to the resulting alternating current. Impedance spectroscopy applies a sinusoidal AC voltage at an angular frequency ω whose complex dimensions can be described by Euler's formula:

$$U(t) = U_0 e^{i\omega t} \quad (3.4)$$

and:

$$\omega = 2\pi f \quad (3.5)$$

where $U(t)$ is the alternating voltage at a certain time t , U_0 the voltage amplitude, ω the angular frequency, f the AC frequency and $i = \sqrt{-1}$.

Equation 3.6 describes the corresponding sinusoidal alternating current I at a time t with the amplitude I_0 :

$$I(t) = I_0 e^{i(\omega t - \varphi)} \quad (3.6)$$

with φ as the phase difference between $U(t)$ and $I(t)$. φ becomes zero when a system shows ideal resistive behavior.

As mentioned above the complex impedance Z of an AC circuit is given by the ratio of voltage $U(t)$ and current $I(t)$:

$$Z = \frac{U(t)}{I(t)} = \frac{U_0 e^{i\omega t}}{I_0 e^{i(\omega t - \varphi)}} = \frac{U_0}{I_0} e^{i\varphi} = |Z| e^{i\varphi} \quad (3.7)$$

The impedance Z can be expressed as the sum of two components using the Cartesian notation:

$$Z = R + iX \quad (3.8)$$

The first term is named the resistance R and it is the real part deriving from the current that is in-phase with the alternating voltage. The second component is the imaginary part or reactance X . X arises from the phase-shifted current that is caused by inductive and capacitive impedance contributions.

The complex impedance Z can be represented as vector in the Gaussian plane with the imaginary part (y-axis) plotted against the real part. **Fig. 3.8** displays the Gaussian plane with the Cartesian Coordinates R , X and the polar coordinates $|Z|$ and φ . While the magnitude of impedance $|Z|$ is described by the length of the vector, the phase shift φ between voltage and current is the angle between $|Z|$ and $Re(Z)$.

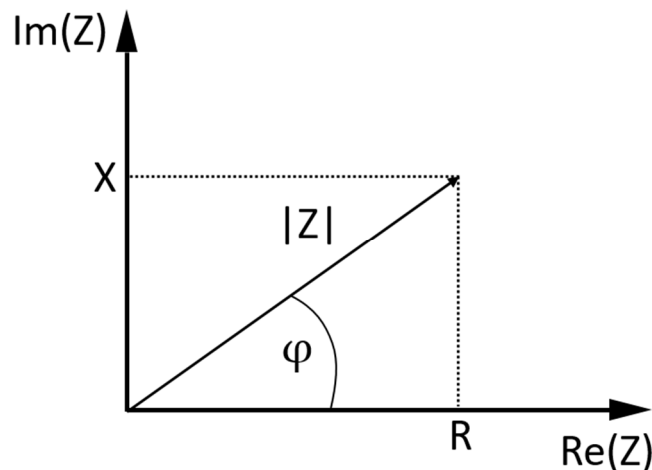


Fig. 3.8 The complex impedance represented as a vector in the Gaussian plane with the imaginary part plotted as a function of the real part.

The polar coordinates $|Z|$ and φ can be converted into the Cartesian coordinates X and R :

$$R = |Z|\cos\varphi = Re(Z) \quad X = |Z|\sin\varphi = Im(Z) \quad (3.9)$$

Vice versa, reactance X and resistance R can be converted into the polar coordinates $|Z|$ and φ :

$$|Z| = \sqrt{R^2 + X^2} \quad \varphi = \arctan\frac{X}{R} \quad (3.10)$$

3.4.2 ELECTRIC CELL-SUBSTRATE IMPEDANCE SENSING (ECIS)

Electric cell-substrate impedance sensing (ECIS) is a technique that allows non-invasive online monitoring of adherent cells with high throughput and good time resolution. The ECIS technique was first described in 1984 by Giaever and Keese who cultivated fibroblasts on biocompatible gold film electrodes and measured the temporal changes of the electrode impedance (Giaever and Keese 1984). The basic principle of ECIS relies on measuring the AC impedance of thin gold film electrodes which are covered with a monolayer of adherent cells (**Fig. 3.9**). The measurement set-up consists of a small working electrode and a significantly bigger counter electrode (about 500 – 1000 times the surface area of the working electrode) which are electrically connected via the bulk cell culture medium. Because impedance is inversely proportional to the electrode surface area, the working electrode contributes the most to the measured impedance magnitude while contributions from the bulk medium and the counter electrode are negligible. Additionally, the small size of the working electrode allows the analysis of a relatively small cell population. The thickness of the gold film electrodes is about 100 nm what makes it possible to visualize the cell population grown on the electrodes via regular light microscopy (Michaelis et al. 2012). When cells are cultivated on the gold film electrodes, the dielectric properties of the plasma membrane cause a significant increase of impedance over a broad frequency range. Thus, cell-covered electrodes exhibit higher impedance values compared partly covered or cell-free electrodes. This model may be condensed to a three-parameter equivalent circuit (**Fig. 3.9, inset**). Within the circuit model, three elements are connected in series which represent the individual impedance contribution from the bulk medium, the cell layer and the electrode. The electrolyte resistance of the bulk phase medium is represented by the ohmic resistance R_{bulk} , while contributions from the electrode-electrolyte interface are described by a constant phase element (*CPE*). When a cell-free electrode is analyzed, only R_{bulk} and the *CPE* contribute to the total impedance. However, when a confluent cell layer covers the electrode, its impedance Z_c additionally contributes to the total impedance. Depending on the monitoring frequency of the measurement, impedance values reveal information about cell morphology changes or electrode coverage. In the low and medium frequency range ($f < 10$ kHz, approximately), the AC current will pass underneath and between neighboring cells via paracellular pathways. Correspondingly, impedance changes in this frequency range correlate to changes in cell morphology. At frequencies higher than approximately 10 kHz, the AC current can pass directly through the cellular plasma membrane by capacitive coupling (transcellular pathway). Thus,

measurements in the high frequency region are most sensitive to monitor changes in electrode coverage, e.g. during wound healing processes (see **chapter 3.5.4**).

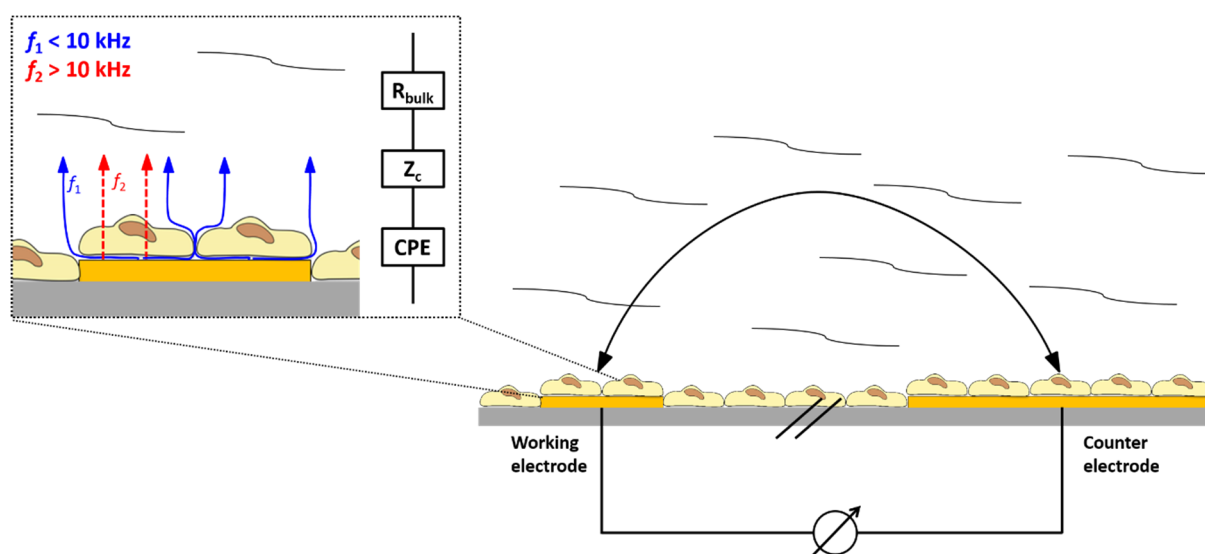


Fig. 3.9 Schematic view of the ECIS principle based on impedance measurements of gold film electrodes. Inset: Cell-covered working electrode with the corresponding equivalent circuit model (right). Depending on the frequency range, the AC current flow is either paracellular (blue arrows) or transcellular (red arrows).

3.4.3 SET-UP FOR OXYGEN SENSING AND IMPEDANCE MEASUREMENTS: ECIS-O₂

One of the objectives of this work was the development of a chip, which allows the cell growth on its surface and enables the readout of multiple cellular parameters. While cell morphology changes, cell-substrate and cell-cell interactions should be detected by impedance measurements via gold electrodes, changes in cellular oxygen consumption should be monitored by ratiometric optical oxygen sensing. Therefore, a chip was fabricated which enables a spatially separated, dual readout of both, impedance and oxygen partial pressure.

3.4.3.1 ELECTRODE LAYOUT AND CHIP FABRICATION

The electrode layout for the dual-sensor chip is shown in **Fig. 3.10, A**. The electrode structures are established upon a standard microscope slide covered by an oxygen sensor foil. As photolithographic electrode patterning would have destroyed the dyes incorporated in the foil, the electrodes, leads and contact pads were created by using a mask during the sputter coating with gold that contained the electrode structures as openings. The mask was prepared by laser beam

milling. The layout consists of four linear electrode pairs with a width of 0.5 mm and a length of 7.3 mm, leads with a thickness of 1.1 mm and eight contact pads.

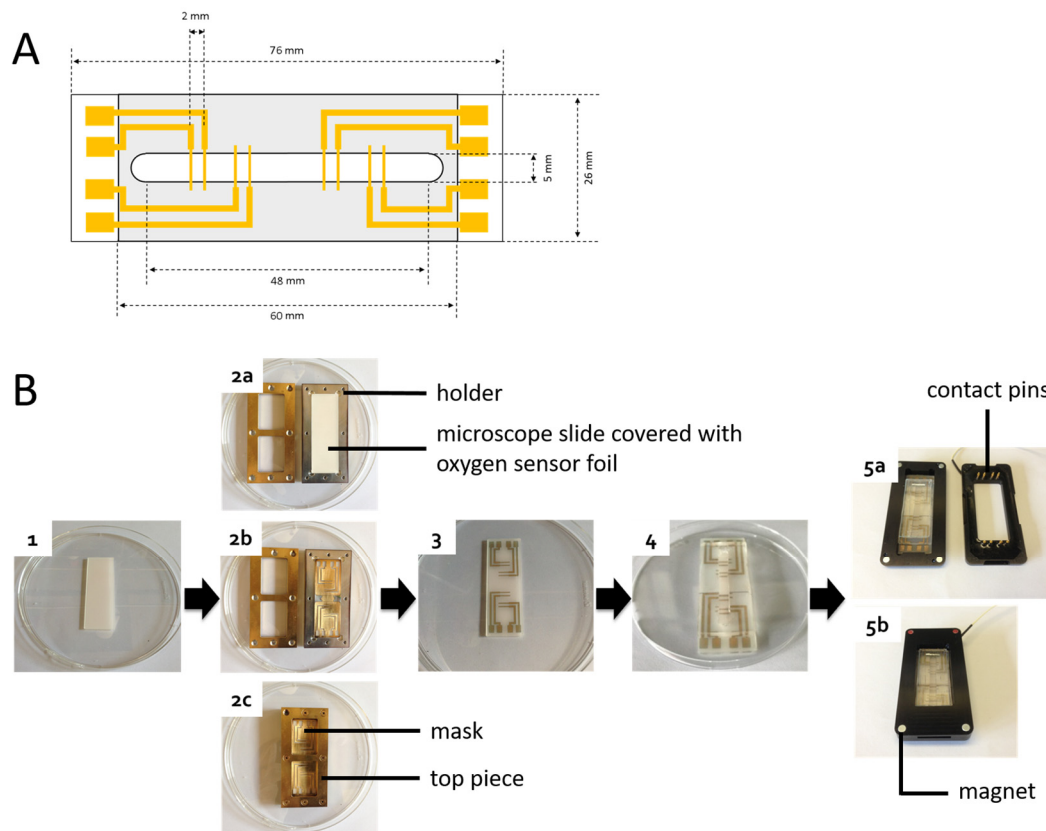


Fig. 3.10 (A) Electrode layout which is established on an oxygen sensor foil immobilized on standard microscope slide. Structures highlighted in yellow show linear electrodes, leads and contact pads, while the dimensions of the PDMS chamber for cell cultivation are highlighted in grey. (B) Individual production steps for the fabrication of the dual chip. (1) Oxygen sensor foil glued on a standard microscope slide. (2) Integration of the microscope slide into a custom-built mask for the deposition of 100 nm gold film electrodes. The microscope slide is put into the holder (2a) and covered with a thin mask (2b). Microscope slide and mask are fixed using a top piece (2c). (3) Sputter coated electrode structures. (4) Adhesive bonding of a PDMS chamber for cell cultivation. (5) Integration of the dual chip into a customized holder (5a). The electrodes are contacted using a top piece with eight pins that is attached to the bottom holder by magnetic force (5b).

First, a piece of oxygen sensor foil (SF-RPSu4) was glued to a standard microscope slide (75 mm x 26 mm) using silicone glue. The foil was attached bubble free to the microscope slide by rolling a glass bar over it. After the glue had dried (24 h, RT), excess foil was removed from the edges of the microscope slide with a scalpel and the protection layer of the sensor foil was removed with tweezers (**Fig. 3.10, B1**). The microscope slide was inserted into a custom-built holder and covered with the sputter mask produced by laser-beam cutting (**Fig. 3.10, B2**). The mask was covered by a top piece and the complete holder was screwed together tightly to prevent the mask from getting out of place. Then, 100 nm thick gold film electrode structures were deposited on the sensor foil using a sputter coater (Sputter Coater Bal-Tec SCD 050) as shown in **Fig. 3.10, B3**. In order to

cultivate cells, either a microchannel (1st layout: ibidi sticky-Slide I^{0.4}luer) or a handmade PDMS chamber (2nd layout: $A_{\text{well}} = 2.5 \text{ cm}^2$, $V_{\text{well}} = 1 \text{ ml}$) was glued on the foil using silicone glue (**Fig. 3.10, B4**). For PDMS chamber fabrication, base and curing agent (Sylgard® 182 Silicone Elastomer Kit, base + curing agent) were mixed in a ratio of 1:10, stirred well, poured in the lid of a petri dish ($d = 9 \text{ cm}$) and was allowed to cure for at least 48 h at 60 °C. A customized holder with a magnetic lid was used to contact the dual chip on both sides (**Fig. 3.10, B5**). The holder has a window frame on the bottom part and in the lid for excitation and observation of the sample. The holder was covered with a lid during measurement to prevent evaporation of the medium in the PDMS chamber.

3.4.3.2 MEASUREMENT SET-UP

Measurements were conducted with the dual-sensor chip, chip holder and imaging camera placed inside a humidified incubator (48 l) at 37 °C, 0 % CO₂. The electrodes were contacted by the customized holder shown in **Fig. 3.10** and connected to the impedance analyzer (SI 1260, Solartron, Farnborough, UK) via a relay that switches between different electrode pairings. Both, relay and impedance analyzer were controlled by a microcontroller connected to a PC (**Fig. 3.11**). The impedance magnitude as well as the corresponding phase angle were recorded in a frequency range from 1 – 10⁵ Hz at a voltage amplitude of 50 mV (rms). All in all, data was recorded at 51 frequencies with an equidistant distribution on a logarithmic scale and a time resolution of 4.3. The impedance measurement was controlled by a customized LabVIEW™ based program written by Prof. J. Wegener (Institute of Analytical Chemistry, Chemo- and Biosensors, University of Regensburg). Impedance data was analyzed using the ECIS viewer software, also LabView based and written by the Wegener lab.

Ratiometric oxygen measurements were conducted using the VisiSens A1 system which is capable to perform measurements in a humidified atmosphere. The bigger field of view allows recording images of both electrode-free sensor foil and electrode structures. The camera system is controlled by the AnalytiCal® 1 software (VA1.12-RC05). The VisiSens A1 camera system with adapter tube 1 was connected via a USB port to a second computer as running the software for ECIS and pO₂ analysis one the same device led to interferences. Prior to the measurement, parameters (exposure time, brightness) were adjusted and kept constant during the measurement and the calibration. The camera was focused on the surface of the oxygen sensor foil. Images were recorded automatically

every 15 min. Subsequent calibration of the sensor foil was carried out as described in **chapter 3.2.5** by choosing an appropriate ROI on the sensor foil that was not covered by electrode structures.

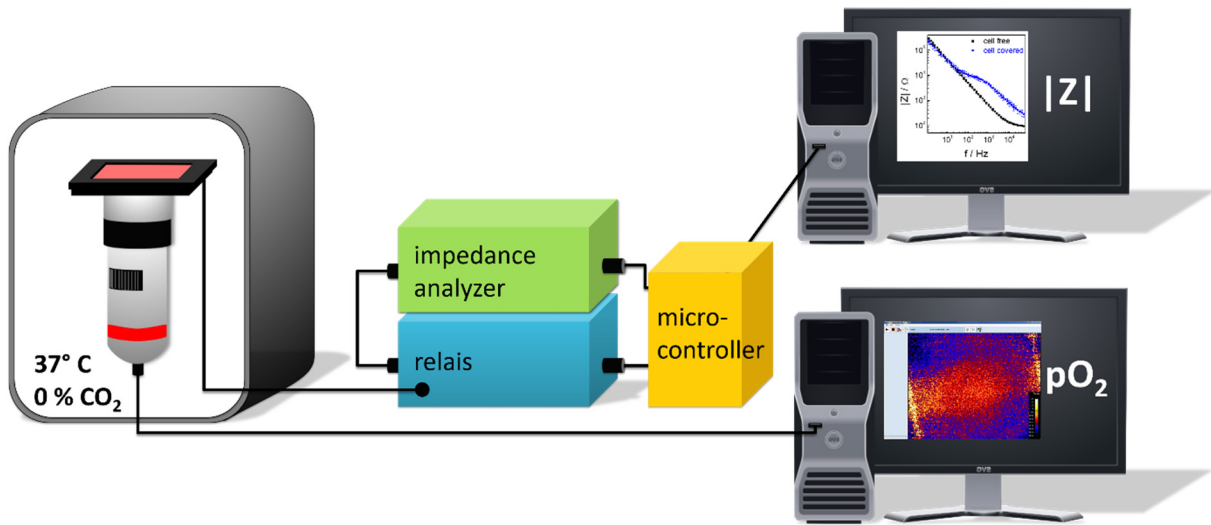


Fig. 3.11 Schematic set-up for dual measurements of oxygen levels and impedance.

3.4.3.3 EXPERIMENTAL PROCEDURE

Before cell seeding, ECIS-O₂ arrays were exposed to an argon plasma for 25 s. MDCK II cells were cultivated in the ECIS-O₂ chip containing 1 ml culture medium according to **Tab. 3.8**.

Tab. 3.8 Experimental conditions for ECIS-O₂ measurements.

Experiment	Seeding density	Beginning of measurement
Cell adhesion	4.5 × 10 ⁵ cells/cm ² resuspended in L-15 medium (+ 5 % FCS, + 1 % P/S)	Immediately after seeding
Influence of drugs on OXPPOS	4.5 × 10 ⁵ cells/cm ² resuspended in culture medium	2 d after seeding

All ECIS-O₂ measurements were conducted in a humidified cell culture incubator at 0 % CO₂, 37 °C. L-15 medium supplemented with 5 % FCS and 1 % P/S was used in all experiments. Before starting the experiment, electrode contact was checked and the VisiSens A1 camera was focused on the surface of the oxygen sensor foil. Camera parameters (exposure time, brightness) were adjusted with settings for the exposure time ranging between 80 and 160, and brightness ranging between 0

and 15 depending on the brightness of the batch of sensor foils. Camera parameters were kept constant over the whole experiment and subsequent calibration.

3.4.3.4 CORRECTION OF SPECTRA

Due to the high resistance of the feeding lines to the active electrode, recorded spectra were shifted to higher impedance at the high frequency end of the spectrum. The obvious nature of this impedance shift allowed for a simple correction. Therefore, resistance of the electrodes was corrected so that a final value of the high frequency impedance was equal to 100 Ω at 10⁴ Hz.

$$R_{corr} = R - x; \quad (3.11)$$

with:

$$R_{corr}(at\ 10^4 Hz) = 100\ \Omega \quad (3.12)$$

The correction resistance due to the feeding lines was determined separately for each electrode and array by recording cell-free spectra, as contributions by lead resistance highly varied. Corrected impedance $|Z|$ was determined using eq. 3.13:

$$|Z|_{corr} = \sqrt{R_{corr}^2 + X^2} \quad (3.13)$$

with:

$$X = Im = \frac{1}{2\pi f C} \quad (3.14)$$

with the monitoring frequency f in Hz and the recorded capacity C in F.

3.5 WOUND HEALING ASSAYS

A wound healing assay is a method commonly used to study cell migration processes *in vitro*. Usually a defect or wound is introduced in a two dimensional cell layer to study wound closure and thus, cell motility and migratory behavior (Riahi et al. 2012).

For all wound healing assays conducted in this work, NRK cells were seeded with a density of 2.5×10^5 cells cm^{-2} to the different culture substrates two days before the experiment was performed. Cells were fed with 2 ml fresh medium 24 h before wounding.

3.5.1 OPTICAL ASSAY

An optical wound healing assay based on the excitation of an oxygen sensitive dye used as a photosensitizer incorporated in a biocompatible polymer matrix was developed in the course of this work (Fig. 3.12). Adherent cells are grown to confluence on functionalized substrates that consist of an oxygen permeable polymer doped with a photosensitizer. The wound is introduced by 408 nm laser excitation of a selected area. Upon irradiation, singlet oxygen is created by quenching the excited state of the photosensitizer. Singlet oxygen induces cell death, thus creating a wound which live cells residing in the periphery of the wound can repopulate by detaching dead cells.

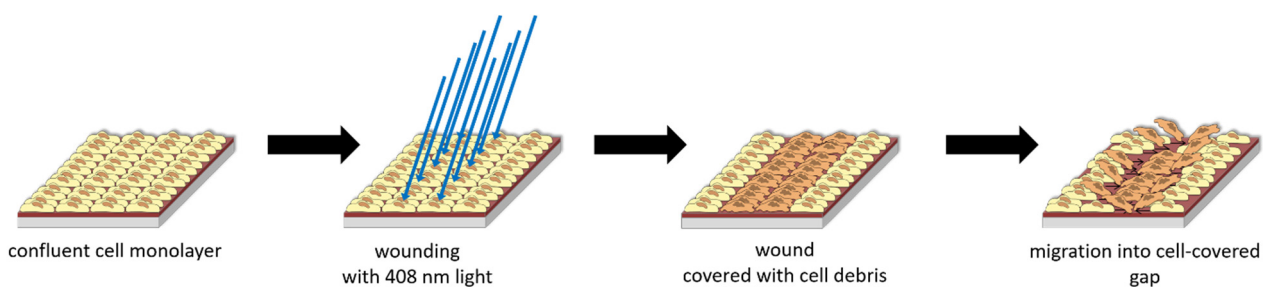


Fig. 3.12 Principle of the newly developed optical wound healing assay. The wound is introduced by excitation of a photosensitizer at 408 nm, that is incorporated in the polymer-based growth substrate.

Fabrication of Substrates for the Optical Wound Healing Assay

Round glass cover slips with a diameter of 12 mm were cleaned in 5% (v/v) Elma Clean solution for 30 min at 70 °C in an ultrasonic bath. Afterwards, the cover slips were rinsed 3 times with deionized water and further sonicated in deionized water at 70 °C for 30 min. The last step was repeated once more to completely remove any remaining cleaning solution. Finally, the clean glass slides were

dried overnight and stored under dry and dust-free conditions until usage. Polymer based films doped with a photosensitizer upon a transparent base substrate were produced by spin coating using a custom-built spin coating device. The polymer cocktail consisted of 10 % (w/v) polystyrene (number average molecular weight $M_n = 140000$ g/mol, weight average molecular weight $M_w = 230000$ g/mol) and 3 % (w/w of PS) 5,10,15,20-Tetrakis(2,3,4,5,6-pentafluorophenyl)-porphyrin-platinum(II) (PtTFPP), a molecule that absorbs visible light and undergoes phosphorescence which is readily quenched by dissolved oxygen. Both components were dissolved in toluene and the solution was stirred overnight at 900 rpm in the dark. Dry glass cover slips were cleaned with acetone and isopropanol and were then dried at 120 °C for 30 min. Then, 50 μ l TI prime[®] solution was spin coated on the slides at 3000 rpm for 20 s for better adhesion of the polymer layer. The adhesive agent was activated for 10 min at 130 °C. The cover slips were then coated with 50 μ l polystyrene cocktail for 1 min at 2000 rpm and dried at room temperature for at least 24 h protected from light before usage. The functionalized substrates were attached to the bottom of small standard cell culture petri dishes with two small patches of silicone glue. After drying of the glue (24 h, RT), the substrates were sterilized for 1 min in an argon plasma before the cell suspension was seeded.

For the control substrates, a mixture with 10 % (w/v) polystyrene in toluene was used without addition of PtTFPP. Polymer cocktail and substrates were handled as described above.

To produce substrates capable of scavenging the 1O_2 by containing different amounts of vitamin E (D- α -tocopherol), a mixture containing 10 % (w/v) polystyrene, 1 – 10 % (w/w of PS) D- α -tocopherol and 3 % (w/w of PS) PtTFPP in toluene was used. The sensor cocktail and the substrates were produced as described above. Substrates were kept in the dark at 4 °C before usage due to low stability of D- α -tocopherol.

Experimental Protocol

As wound healing substrates showed significant batch to batch variations in wound size, probably caused by ageing of the photosensitizer PtTFPP due to oxidation processes, single experiments were conducted using substrates from one batch only.

At the day of the experiment, the petri dish was sealed air tight with a lid covered with a ring of Blu-Tack[®] and was completely filled with culture medium (9.6 ml) to prevent condensation of water on the lid during illumination. Usually, NRK culture medium was used, except when mentioned otherwise. The samples were wounded using the 10x magnification objective of the Nikon Eclipse

90i laser scanning microscope. First, cells growing on the surface of the photosensitizer-doped polymer were focused using standard phase contrast settings. Then, the samples were excited using the 408 nm laser in pulsed line-scan mode with total illumination periods ranging between 0.5 min and a maximum of 2 min which resulted in linear wounds with a length of 1.5 mm – 1.6 mm and a width varying with illumination time. Usually, an ND4 filter was used to decrease the intensity of the laser light unless mentioned otherwise. After the cells had been wounded, the lid was removed, medium was aspirated and the cells were washed twice with 1 ml medium. Wound closure was monitored as a function of time in 2 ml medium. As it took about 10 – 15 min to distinguish wounded from non-wounded areas by light microscopy, the first images were recorded 20 min after wounding the samples. This time point was the starting point of the assay marked as $t = 0$ h. Progress of wound closure was followed by taking phase contrast images every 3 h with an inverted microscope (PLAN / 4x / NA 0.13, Nikon, Diaphot).

3.5.2 SCRATCH ASSAY

The scratch assay is a simple, straightforward and fast method to study the migration of 2D cell monolayers *in vitro*. The cell layer is wounded by scratching, e.g. with the help of a pipet tip, thus removing the cells in the path of the tip. Cells at the edges of the newly created wound can migrate into the cell-free area which will eventually lead to wound closure and re-establishment of cell-cell contacts (Liang et al. 2007). **Fig. 3.13** shows the introduction of a wound in a monolayer of adherent cells using the scratch assay.

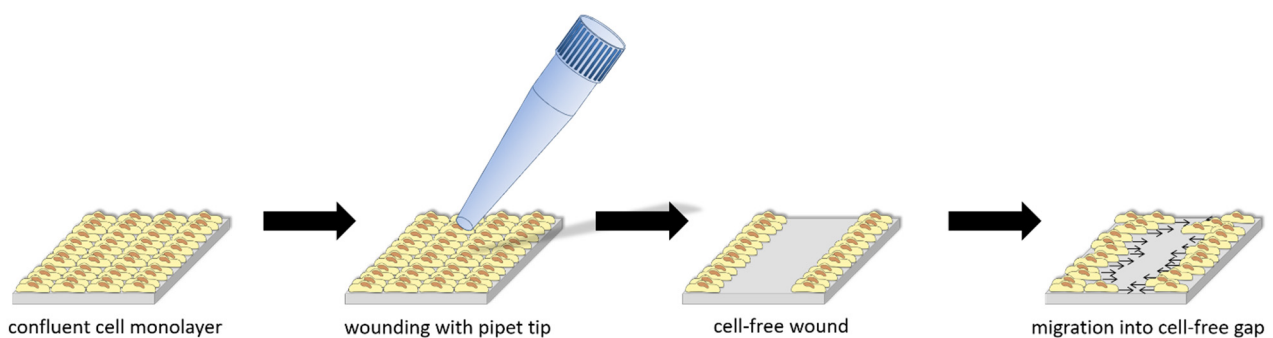


Fig. 3.13 Schematic of the scratch assay based on the introduction of a wound using a pipet tip.

A 1 ml pipet tip was used to manually scratch a linear wound into a confluent NRK cell layer grown on a small cell culture petri dish. For better reproducibility, equidistant lines perpendicular to the scratch were introduced on the outer bottom side of the petri dishes before scratching using a scalpel. Thus, uniform wounds with a length between 1.7 mm – 1.9 mm were created. After introduction of the wound, the cells were washed twice with 1 ml medium to remove dead cells and debris. Cells were then incubated in 2 ml medium at 37 °C, 5 % CO₂ and the wound healing process was followed over time by taking phase contrast images with an inverted microscope (PLAN / 4x / NA 0.13, Nikon, Diaphot) every 3 h.

3.5.3 BARRIER ASSAY

The barrier assay uses a physical barrier – pre-attached to the growth substrate before cell seeding – to retain a cell-free area into which the cells are able to migrate after the barrier was removed (**Fig. 3.14**). Physical barriers must be biocompatible and can be either of liquid character, such as agarose gel, or solid like PDMS or Teflon based barriers (Varani et al. 1978; Pratt et al. 1984). Upon removal of the barrier, migration of cells into the cell-free area is initiated (Riahi et al. 2012).

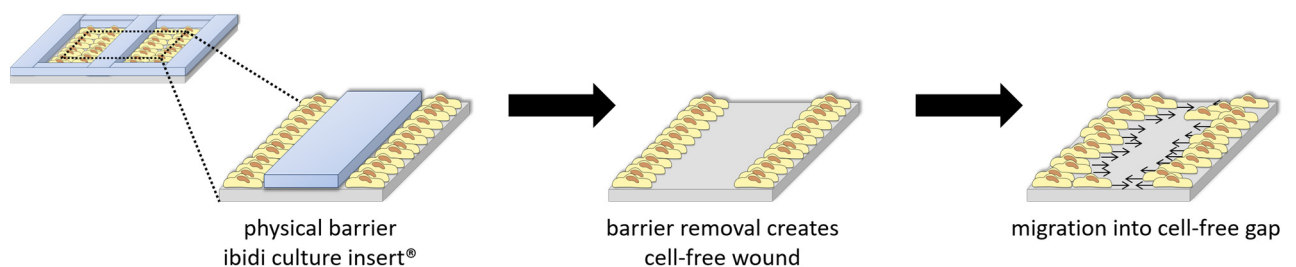


Fig. 3.14 Schematic of the wound healing assay based on a physical barrier, e.g. ibidi culture insert®. After removal of the barrier cells can migrate into the cell-free area.

ibidi two chamber culture inserts® were used for the barrier-based wound healing assay. The culture insert® is biocompatible and it has a special adhesive surface for easy attachment to cell culture substrates such as petri dishes. Cells can be cultivated in both wells of the insert. This results in two growth areas ($A_{\text{well}} = 0.22 \text{ cm}^2$) with a distinct shape of a rounded rectangle. Before inoculation, culture inserts® were sterilized for 1 minute by exposure to an argon plasma. The clean inserts were carefully attached to the surface of a small petri dish ($d = 3.5 \text{ cm}$) using tweezers. 70 μl cell suspension was added to each of the two compartments and cells were allowed to attach. After two

days of cell cultivation at 37 °C and 5 % CO₂, the insert was removed with tweezers creating a cell-free gap of about (500 ± 50) μm between the two growth areas. Cell migration into the cell-free linear gap was monitored by taking phase contrast images with an inverted microscope (PLAN / 4x / NA 0.13, Nikon, Diaphot) every 3 h.

3.5.4 ELECTRICAL ECIS® ASSAY

ECIS® is a method which allows both, electrical wounding and non-invasive online monitoring of cell migration into the wounded area. Therefore, cells are grown to confluence on small planar gold film electrodes (as described in **chapter 3.4.2**) and are wounded by application of an electrical pulse of several volts for 15 to 30 s. Cells growing on the bigger counter electrode and next to the working electrode remain vital as they are not affected by the electrical field (**Fig. 3.15**). The increased electrical voltage during pulse application leads to the lesion of the cellular plasma membrane which eventually results in death of all cells on the electrode which can be followed as a sudden drop of impedance to values of a cell-free electrode. As soon as the wound has been introduced, intact neighboring cells start to migrate. The repopulation of the working electrode can be monitored as an increase in impedance. With complete wound closure impedance values recover to pre-wounding values (Keese et al. 2004).

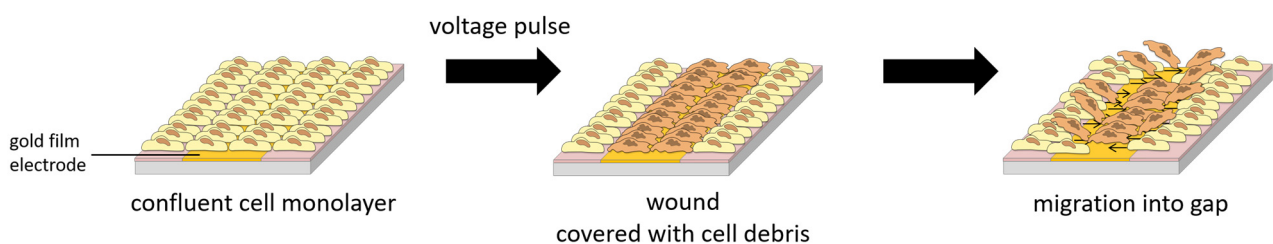


Fig. 3.15 Schematic of the electrical ECIS® wound healing assay. Cells are cultivated on planar gold film electrodes and wounded by application of an invasive electrical pulse. Dead cells are detached from the electrode surface by neighboring cells migrating on the electrode and closing the wound.

For the electrical ECIS® wound healing assay NRK cells were grown to confluence on commercial 8W2LE arrays. Each of the 8 wells comprises a growth area of 0.75 cm² with a working volume of 400 μl and contains two linear gold film electrodes with a size of 667 μm x 150 μm. The linear electrode layout allowed the generation of wounds with similar geometry compared to the optical, scratch and barrier assay. Cells were monitored in MFT (multi-frequency/time) mode. After

recording the baseline signal for at least for 30 min, cells were wounded by application of an invasive voltage pulse of 5 V for 30 s at 40 kHz and the wound healing process was followed for at least 10 h.

3.5.5 DETERMINATION OF WOUND HEALING RATE

All images of wounded cell areas (optical, scratch, barrier assay) were analyzed with the NIH ImageJ software. The wounded area in each picture (4288 x 2848 pixels or 2381 μm x 1582 μm) was expressed in μm^2 using the polygon selection tool. The time-dependent area of wound closure was calculated by subtracting the wounded area value from later time points during wound healing from the wounded area at time zero. Data was analyzed using OriginPro 8 software. Wound healing rates in $\mu\text{m h}^{-1}$ were determined by either linear fitting (eq. 3.15) or logistic fitting (eq. 3.16) of the data using the following functions:

$$y = A + Bt \quad (3.15)$$

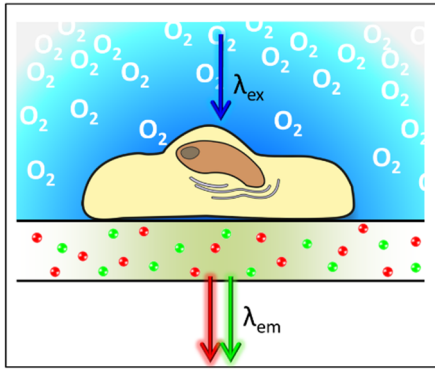
with the time t in h, a slope B representing the average wound healing rate in and an intercept A .

$$y = A_2 + \frac{A_1 - A_2}{1 + \left(\frac{t}{t_0}\right)^p} \quad (3.16)$$

with A_1 as initial value (wound size), A_2 as final value (wound size at $t = \infty$), a center t_0 describing the time point of half closure of the wound and the power p . To calculate the wound healing rate the first order derivative of the logistically fitted data points was determined and parameters such as maximum velocity v_{max} and velocity at time point of half wound closure $v(t_{1/2})$ were computed. Uncertainty of $v(t_{1/2})$ was calculated using an error estimation.

In electrical ECIS[®] wound healing studies, capacitance data at a frequency of 32 kHz was used to determine the amount of the cell-covered electrode area since the capacitance decrease at high frequencies is proportional to increasing electrode surface coverage. The wound closure velocity of impedimetric measurements was expressed as the time-point of half-maximal capacitance decrease after application of the wounding pulse or by logistic fitting of the capacitance decrease (increase in electrode coverage/healed area) over time followed by calculation of the first order derivative to determine v_{max} and $t(v_{max})$. The uncertainties for v_{max} and $t(v_{max})$ were estimated by numerical procedures that determine the maximum and minimum values for both parameters based on the fit results with the logistic transfer function including the standard errors for each parameter.

4 IMAGING THE OXYGEN CONSUMPTION OF ADHERENT CELLS IN MONOLAYERS



Monitoring oxygen concentration by luminescence quenching of sensor dyes has gained much popularity in recent years offering an alternative to electrochemical sensing systems, such as the Clark electrode. Optical oxygen sensors have the advantage to being fully reversible and to not consume oxygen during the measurement (Wolfbeis 2015). Up now a huge number of optical oxygen sensor types has been developed,

ranging from free dyes, to dendrimers, nanoparticles, sensor foils or needle-based sensors. However, when monitoring biological samples, such as cells, particle or microneedle based probes are invasive, while the free dye is rather cytotoxic (Dmitriev and Papkovsky 2012). Planar oxygen sensitive culture substrates offer an alternative, which allows the non-invasive detection of the oxygen partial pressure directly beneath the cell layer.

The aim of this project was to measure oxygen consumption of adherent monolayer cells with the new imaging system VisiSens TD mic which was developed in cooperation with PreSens GmbH, Regensburg. The imaging system fits inside a standard 48 l incubator which allows monitoring of cell samples under standard culture conditions. Ratiometric oxygen sensor foils (SF-RPSu4, PreSens GmbH) were used as culture substrates for adherent mammalian cells. The close proximity of the cells and the sensor layer allows a non-invasive measurement of oxygen concentration directly underneath the adherent cell layer. In order to conduct long term experiments with cells, parameters such as the photostability and the biocompatibility of planar sensor foils had to be analyzed. In proof-of-concept studies cellular oxygen consumption was monitored as a function of seeding density, cell type, medium volume and medium composition. Furthermore, the effects of toxins, such as carbon dots (C-dots) or cadmium chloride, upon cellular respiration were investigated. Cellular oxygen consumption was also manipulated by the addition of blockers and uncouplers of oxidative phosphorylation and the associated changes in oxygen consumption were monitored. Finally, the VisiSens TD mic system was used to image temporal and spatial changes of oxygen gradients caused by a respiring small patch of monolayer cells.

4.1 BIOCOMPATIBILITY AND PHOTOSTABILITY OF OXYGEN SENSITIVE CULTURE SUBSTRATES

4.1.1 PHOTOSTABILITY

To test the photostability of 2D sensor foils, experiments were performed in a cell-free petri dish with an incorporated sensor spot. The culture dish was filled with 9.6 ml L-15 medium and the sensor dyes in the sensor foil were excited every 3 s with measurement parameters set in the range of typical measurements with cells ($U_{LED} = 8$ mV, $t_{exposure} = 250$ ms). In total, 4800 images were recorded over 4 h. Images were split into single RGB files and the intensities of the red channel (sensor dye), the green channel (reference dye) and the corresponding ratiometric signal were analyzed using the NIH ImageJ software. **Fig. 4.1, A** displays the intensities of the oxygen sensor dye, the reference dye and the total ratiometric signal which were averaged over the whole field of view ($\sim 1.2 \times 10^6$ Px) as a function of time. Within the first 50 minutes, both intensities of the red and the green channel show a slight decrease with higher intensity values measured for the green channel.

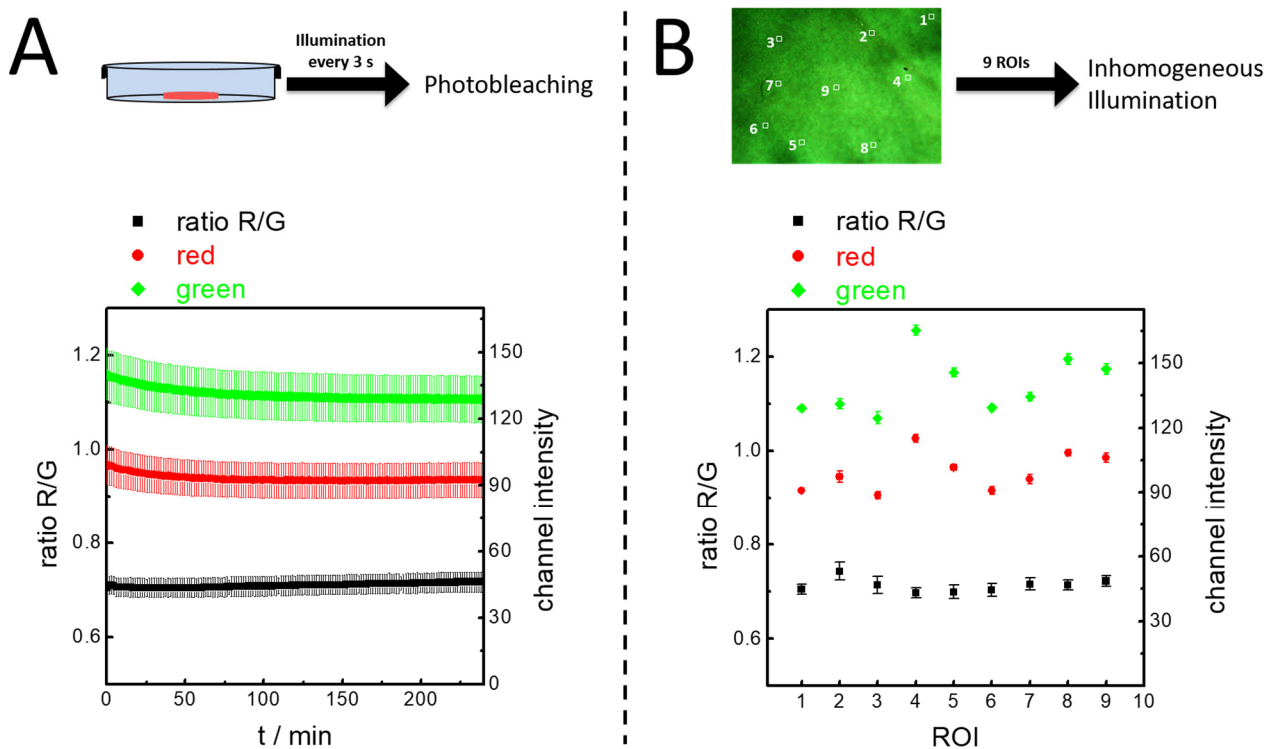


Fig. 4.1 (A) Long-term exposure of the sensor foil under continuous illumination to detect changes in the ratiometric signal caused by photobleaching of the dyes. The oxygen sensor foil incorporated in a cell-free cell culture petri dish was illuminated every 3 s. Recorded images were split into single RGB channels and the intensity changes of the red channel (sensor dye, ●), the green channel (reference dye, ◆), and the intensity ratio of the red and the green channel (■) were plotted as function of time. Photobleaching experiments were repeated twice with different batches of sensor foil. Measurements were conducted at $T = 37$ °C. (B) 9 different ROIs were analyzed to investigate the influence of inhomogeneous illumination.

After this, the intensity values of both channels remain constant until the end of the experiment. Although the intensities of the red and green channel fluctuate, this has only little impact on the ratiometric signal. The ratiometric signal shows a total increase of about 1 % compared to the starting value after 4800 images were recorded. Furthermore, the effect of inhomogeneous illumination caused by imperfect alignment of the LED and the sensor spot within one field of view was analyzed. Local changes of the ratiometric signal that are caused by inhomogeneous illumination or inhomogeneous distribution of the two dyes, could lead to artefacts when imaging spatial distribution of oxygen levels, e.g. during imaging of small cell patches. Therefore, 9 small ROIs with a size of 30 x 30 Px were chosen and the intensities and the ratiometric signals were plotted as illustrated in **Fig. 4.1, B**. While the raw data image shows a broad intensity distribution, the ratiometric false color image is highly homogeneous with values of the nine analyzed ROIs ranging between (0.70 ± 0.01) and (0.74 ± 0.02) . These results indicate, that the sensor foil based on a ratiometric readout is highly photostable and can be used in long-term experiments. The ratiometric readout takes care of local inhomogeneities in illumination or dye concentration.

4.1.2 CYTOCOMPATIBILITY

To employ the oxygen sensor foils in long-term cell experiments, their cytocompatibility was tested. Therefore, parameters such as cell adhesion and potential phototoxicity of the sensor foils were studied.

Cell Adhesion to Oxygen Sensor Foils

To measure oxygen levels directly beneath the cell monolayer, cells needed to successfully attach and spread upon the surface of the oxygen sensor films. To promote cell adhesion, sensor films were coated with different adhesion promoting reagents (see **chapter 3.2.4**), such as FCS, fibronectin, gelatin, culture medium, and poly-L-lysine. Cell adhesion upon the surface of coated sensor foils was compared with uncoated foils and standard cell culture petri dishes. Because sensor films are opaque, monolayer cells cannot be visualized by phase contrast microscopy. Therefore, MDCK II cells were seeded subconfluent (5.0×10^4 cells cm^{-2}) and confluent (4.5×10^5 cells cm^{-2}) on the sensor films. 24 h after seeding the cells were stained with either CaAM and EthD-1 or Alexa Fluor 488 phalloidin. **Fig. 4.2, AI – AIII** shows live-dead stained, subconfluent MDCK II cells adhered to the

control substrates (**AI**), non-coated sensor foil (**AII**) and foil coated with 0.5 % (w/v) gelatin (**AIII**). The green cytoplasmic fluorescence of CaAM shows that cells are vital on all substrates with only a few red fluorescing nuclei of dead cells. Staining of the cellular actin cytoskeleton with Alexa Fluor 488 phalloidin shows that cells are attached and form a stable cytoskeleton (**Fig. 4.2, AIV – AVI**). However, on both coated (**AVI**) and non-coated sensor foils (**AV**), some cells exhibit only weak adhesion to the substrates which is noticeable by the rounded shape of the cells and the number of spread cells is lower compared to control conditions. However, the number of dead cells marked by the red nuclear emission of EthD-1 is not increased when cells are cultivated on coated and non-coated sensor foils.

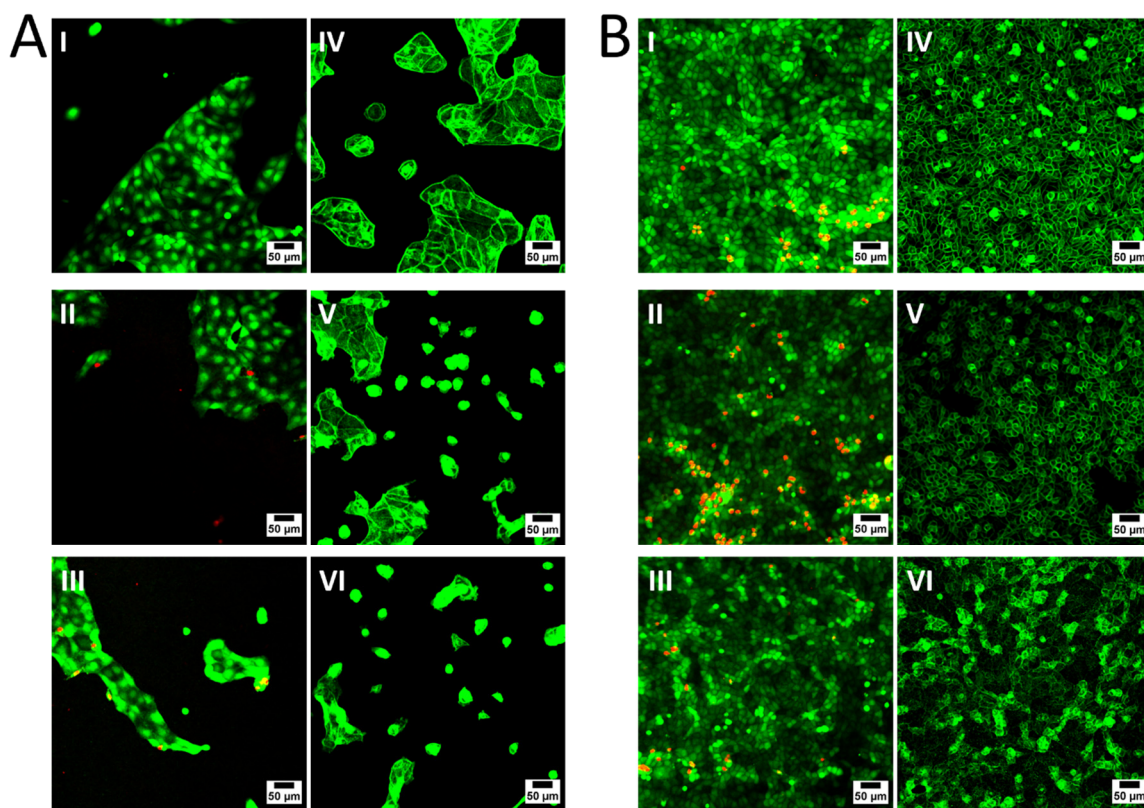


Fig. 4.2 (A) MDCK II cells seeded subconfluently (5.0×10^4 cells cm^{-2}) on a standard cell culture substrate (**AI**, **AIV**), on non-coated oxygen sensor foils (**AII**, **AV**) or on sensor foils coated with 0.5 % (w/v) gelatin (**AIII**, **AVI**). (B) MDCK II cells seeded confluent (4.5×10^5 cells cm^{-2}) on a control substrate (**BI**, **BIV**), on uncoated oxygen sensor foils (**BII**, **BV**) or on sensor foils coated with 0.5 % (w/v) gelatin (**BIII**, **BVI**). Cells were labelled with live-dead staining (**AI – AIII**, **BI – BIII**). Green cytoplasmic fluorescence of CaAM shows viable cells, while the nuclei of dead cells exhibit a bright red fluorescence of EthD-1. Furthermore, cells were stained with Alexa Fluor 488 phalloidin to label the cytoskeleton (**AIV – AVI**, **BIV – BVI**).

Fig. 4.2, B displays the results of both staining methods applied to confluent MDCK II cell layers. Live-dead staining of cells cultivated on non-coated and gelatin coated sensor foils (**BII**, **BIII**) shows vital cells and a similar cell coverage compared to the control (**BI**). However, the number of dead cells on non-coated foils is increased about 50 % compared to the control substrate and gelatin

coated sensor foils. Fluorescent micrographs of MDCK II cells cultivated on sensor foils coated with culture medium, FCS, fibronectin and poly-L-lysine can be found in the supplementary data (see **Fig. 11.1**). Here, no significantly improved adhesion behavior as well as no increased number of dead cells was observed compared to the non-coated sensor foils. Additionally, three other cell lines were analyzed by fluorescent staining yielding similar results. Micrographs of BAEC, NRK and U-373 MG cells labelled with live-dead staining can be found in the supplementary information (see **Fig. 11.2**, **Fig. 11.3** and **Fig. 11.4**). Comparable to results obtained for MDCK II cells, BAEC, NRK and U-373 MG cells do also fully adhere and spread upon non-coated oxygen sensor foils. Compared to standard cell culture substrates, cells cultivated on oxygen sensor foils do fully adhere onto the surface when seeded sub-confluent and confluent. However, a slight increase in the number of dead, rounded-up cells can be observed when cells are cultivated on coated and non-coated oxygen sensor foils. Coating of sensor foils with adhesion promoting agents shows no significant improvement on cell adhesion independent of the analyzed cell line. As cells were inoculated in serum containing cell culture medium, non-coated sensor foils were used for further cell experiments.

Phototoxicity

In the presence of oxygen, oxygen sensor dyes transfer energy in a radiationless manner to oxygen in its triplet state. Triplet oxygen is then converted to singlet oxygen (see **chapter 3.2.1.**) – a molecule which is highly reactive and rapidly induces cell death. When singlet oxygen diffuses out of the sensor foil and reaches the basal cell membrane, it oxidizes biomolecules and eventually kills the cells residing on the foil as depicted in **Fig. 4.3, A** thus making the foils unsuitable for long term cell experiments. To study this potential phototoxic effect, MDCK II cells were cultivated confluent on the SF-RPSu4 sensor foils. Live-dead staining was used to indicate the amount of living and dead cells before and after 4 h of illumination with the blue LED used in oxygen imaging (**Fig. 4.3, B**). As control, cells were grown in a standard cell culture petri dish and were also stained before and after a 4 h illumination period. Control cells show no difference in viability of both, non-illuminated and illuminated samples (**Fig. 4.3, BI, BIII**). Furthermore, 4 h of oxygen imaging does not affect the viability of MDCK II cells cultivated on the oxygen sensor foils (**Fig. 4.3, BIV**). This indicates that singlet oxygen created inside the sensor foil may not be long-lived enough to reach the cells residing on the surface. Moreover, oxygen readings can directly distinguish between sensor films covered with confluent cells and a cell-free sensor foil as shown in **Fig. 4.3, C**. Here, MDCK II cells were grown

with a density of $4.5 \times 10^5 \text{ c cm}^{-2}$ either on petri dish and sensor spot (**Fig. 4.3, CI**) or only on the petri dish surface without covering the sensor spot (**Fig. 4.3, CII**). Oxygen consumption was monitored in L-15 medium. The decrease of pO_2 is faster when cells cover the sensor foil, which allows the direct determination of pO_2 beneath the cells (**Fig. 4.3, C, ■**). Here, the cells become anoxic in about 3.75 h after measurement start. When the sensor is not covered with cells, the oxygen depletion of the medium close to the sensor surface due to the oxygen consuming cells takes longer because of the extra diffusion distance. The sensor reports on a slower decrease of pO_2 reaching hypoxic values in about 7.5 h as seen in **Fig. 4.3, C, ◆**.

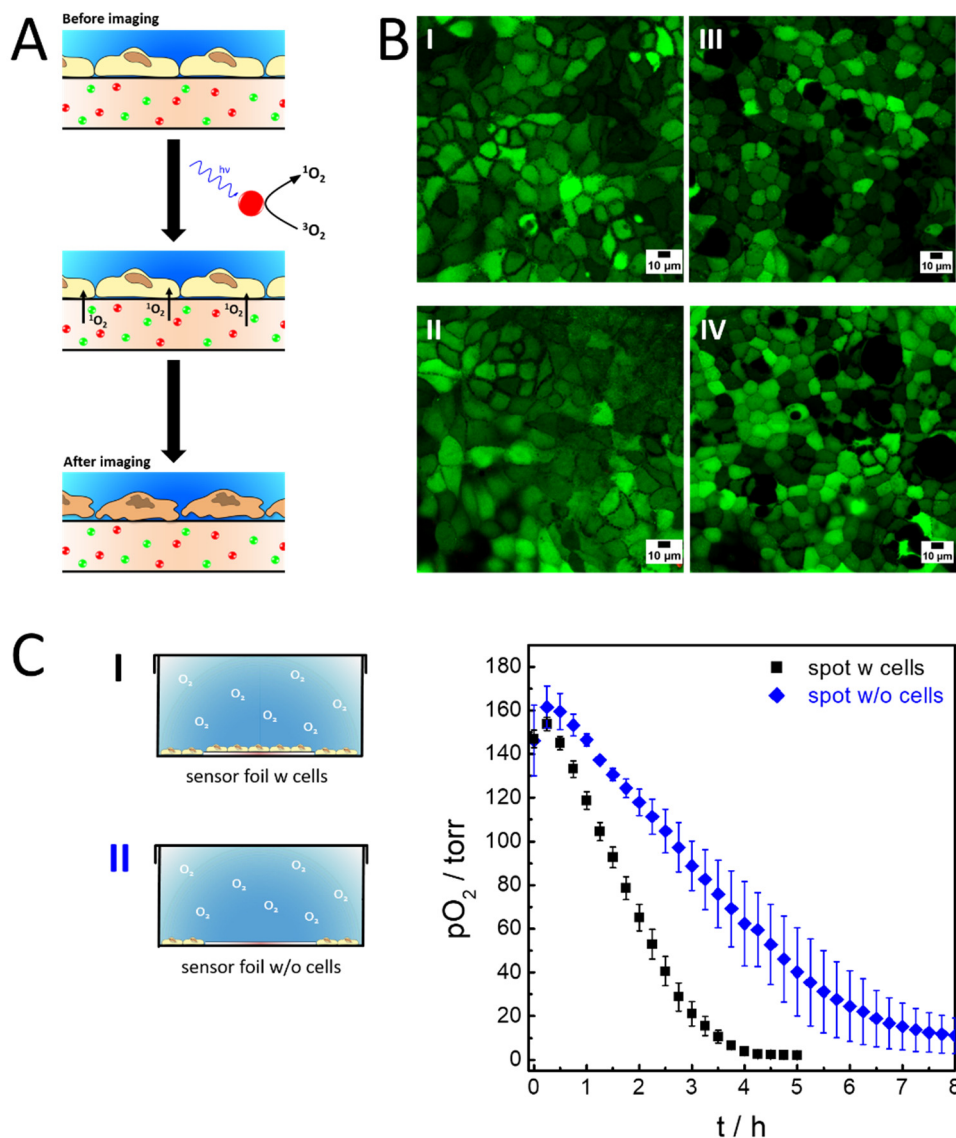


Fig. 4.3 (A) Phototoxic cell damage induced by singlet oxygen. Upon illumination with blue light, energy is transferred from the sensor dye to molecular triplet oxygen which is converted to singlet oxygen. Singlet oxygen may diffuse out of the polymer layer and may induce cell death. (B) Live-dead staining of MDCK II cells cultivated on standard cell culture substrates (BI, BIII) and on oxygen sensor foils (BII, BIV). (BI, BII) Cells before illumination with the blue LED. (BIII, BIV) Cells after 4 h of illumination with the blue LED. (C) Decrease in oxygen partial pressure of a cell-covered and a cell-free sensor spot. Due to diffusional distance between the consuming monolayer and the sensor, the decrease of pO_2 measured on the cell-free sensor (◆) is slower compared to the cell-covered sensor (■). Schematic on the left side is not to scale. Mean \pm SE, $n \geq 2$, $T = 37^\circ\text{C}$.

4.2 OXYGEN CONSUMPTION IN OPEN AND CLOSED SYSTEMS

To ensure that experimental readings of respiration are independent of volume or the presence of an air-liquid interface that enables diffusion of oxygen, measurements of cellular oxygen consumption with the newly developed VisiSens TD mic imaging system were performed in closed systems that were sealed airtight (no oxygen influx) and an open system that allows oxygen to diffuse in from the gas phase to the liquid phase. As closed systems three cultivation chambers with different heights and volumes ranging from 4.8 – 19.2 ml were used (**Fig. 4.4, I – III**). The open system contained a volume of 4.8 ml (**Fig. 4.4, IV**). Both, open and closed system contain an identical growth area of 9.6 cm². MDCK II cells were seeded with a density of 4.5 x 10⁵ c cm⁻² 24 h before oxygen measurements were performed. Oxygen consumption was monitored in L-15 medium. The graph in **Fig. 4.4** shows the decrease of oxygen partial pressure as a function of time for confluent MDCK II cells that were cultivated in open or closed systems. As expected, oxygen partial pressure below the epithelial layer decreases faster with a decreasing medium volume in closed systems. pO₂ reaches (7 ± 3) torr at t = 1.75 h when cells are cultivated in a closed system with a volume of 4.8 ml (▲). If the volume is doubled to 9.6 ml of L-15 culture medium, oxygen partial pressure decreases to (79 ± 5) torr after 1.75 h and finally drops to a value of (7 ± 2) torr after t = 3.75 h (◆). When oxygen consumption of MDCK II cells is measured in 19.2 ml L-15 medium, pO₂ reaches a value of (119 ± 3) torr at t = 1.75 h and (30 ± 2) torr at the end of the observation in time of 5 h (●). In the open system pO₂ first decreases linearly to (97 ± 11) torr, then pO₂ reaches equilibrium with stable values of about 80 torr (■). However, pO₂ readings have a higher standard deviation, probably due to condensation of water on the lid of the culture dish and the resulting scattering of the excitation light. Open and closed systems were compared with regard to cellular oxygen consumption rates (**Tab. 4.1**). Therefore, oxygen profiles of closed systems were fitted linearly (supplementary information, **Fig. 11.5**) and the apparent oxygen consumption rates (AOCRs) were determined. AOCR is the highest for closed systems with a medium volume of 4.8 ml and amounts to a value of (92.1 ± 3.4) torr h⁻¹. With a doubling of volume, AOCR reduces to (50.5 ± 1.6) torr h⁻¹ that corresponds to 55 % of the original value to. When medium volume is quadrupled, AOCR is decreased to 32 % compared to the value recorded in a volume of 4.8 ml reaching a a value of (29.7 ± 1.1) torr h⁻¹. For the open system with a medium volume of 4.8 ml, the pO₂ value after 5 h of measurement was used to calculate the oxygen consumption rate using eq. 3.2 (**chapter 3.2.6**). For a better comparison to the oxygen consumption rate of open systems, AOCR values were

converted into volume independent oxygen consumption rates yielding similar values for open and closed systems with a slightly higher OCR of $(53.3 \pm 3.7) \text{ pmol s}^{-1}$ found for the open system.

To sum it up, both open and closed systems can be used to measure changes of oxygen partial pressure beneath adherent cells yielding similar results for calculated oxygen consumption rates. In this work, the closed system with a medium volume of 9.6 ml was used. First, because the incubator was working in a non-humidified atmosphere as the camera was not perfectly watertight. And second, to prevent evaporation and condensation of medium when samples were monitored over longer periods.

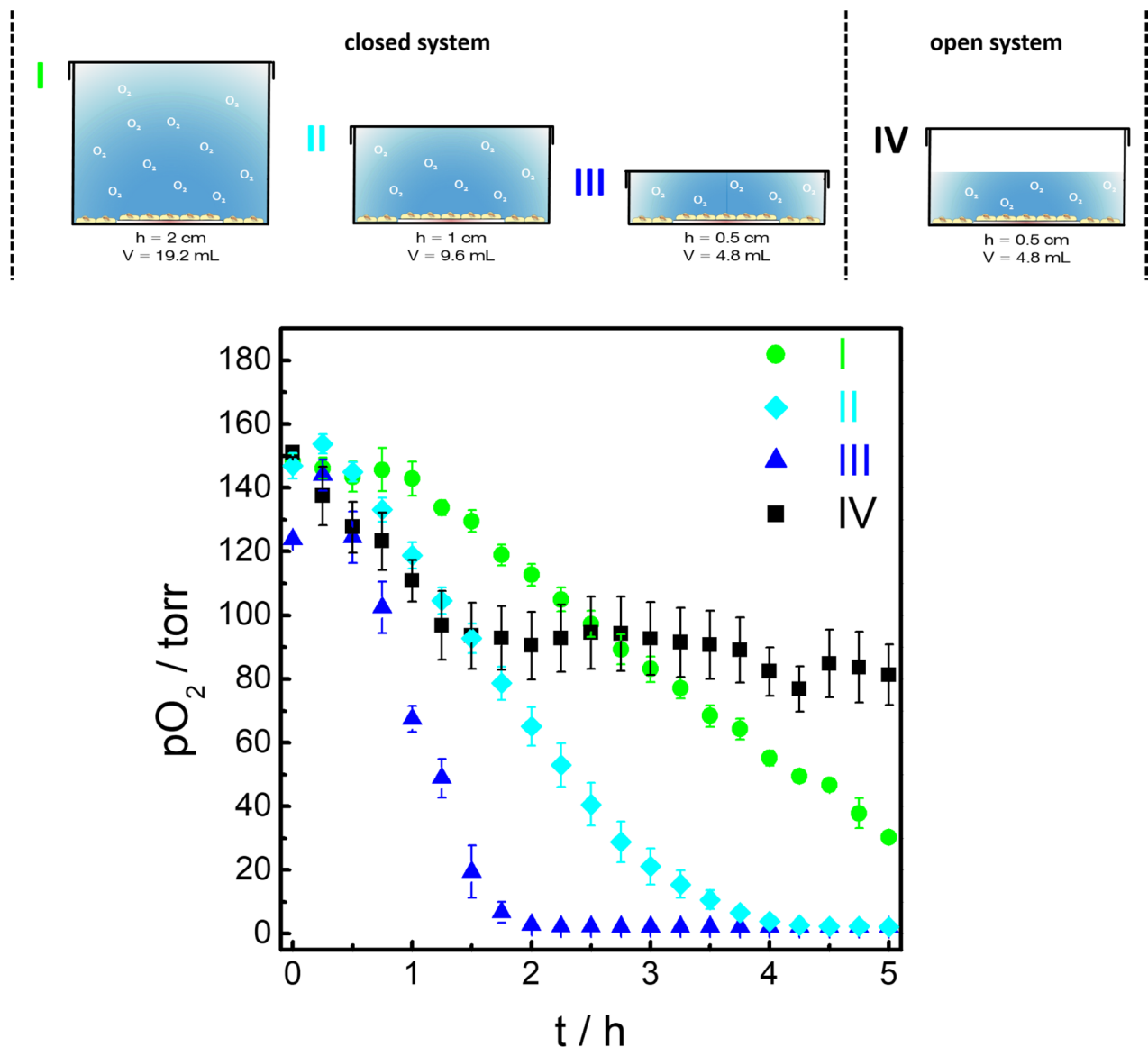


Fig. 4.4 Oxygen measurements conducted in closed (I – III) and open systems (IV). While cultivation area was kept constant (9.6 cm^2), different volumes of L-15 medium were applied to the vessels. Closed systems were filled completely with L-15 medium and sealed air-tight, while open systems still possessed a medium – gas-phase interface. Oxygen partial pressure plotted as function of time for confluent MDCK II cells ($4.5 \times 10^5 \text{ cells cm}^{-2}$) cultivated in closed (I – III) and open (IV) systems. Mean \pm SE, $n \geq 3$, $T = 37 \text{ }^\circ\text{C}$.

Tab. 4.1 Apparent oxygen consumption rates of confluent MDCK II cells measured in closed systems with different volumes at $T = 37\text{ }^{\circ}\text{C}$. Oxygen partial pressure after 5 h measured in an open system containing confluent MDCK II cells. Respective oxygen consumption rates for both closed and open system.

$V_{\text{medium}} / \text{ml}$	$\text{AOCR} \pm \text{SE} / \text{torr h}^{-1}$	$\text{pO}_{2; 5\text{h}} \pm \text{SE} / \text{torr}$	$\text{OCR} \pm \text{SE} / \text{pmol s}^{-1}$
<u>Closed</u>			
4.8	92.1 ± 3.4	2 ± 1	17.3 ± 0.7
9.6	50.5 ± 1.6	2 ± 1	19.0 ± 0.6
19.2	29.7 ± 1.1	30 ± 2	22.3 ± 0.8
<u>Open</u>			
4.8	-	81 ± 10	53.3 ± 3.7

4.3 DEPENDENCY OF OXYGEN CONSUMPTION RATES ON MEDIUM COMPOSITION

Confluent MDCK II monolayers were treated with PBS⁺⁺ buffer containing equal amounts of either galactose (Gal) or glucose (Glc) as substrates for the cells to metabolize in glycolysis and oxidative phosphorylation. **Fig. 4.5** shows the oxygen partial pressure as a function of time for MDCK II cells incubated with the two different buffers. Note that oxygen consumption is slower in both PBS⁺⁺ buffers, compared to measurements conducted in L-15 medium as shown in **chapter 4.2**, because PBS⁺⁺ contains no further nutrients except the monosaccharides glucose and galactose. When MDCK II cells are incubated with 1 g l^{-1} glucose in PBS⁺⁺ (\blacktriangle), the oxygen partial pressure decreases from (159 ± 4) torr, which corresponds to values of air-saturated buffer, to hypoxic values lower than 10 torr. Within 11.75 h, the oxygen partial pressure stabilizes to values of (3 ± 1) torr. However, MDCK II cells incubated with 1 g l^{-1} galactose (\blacksquare) in PBS⁺⁺ show a faster decrease of oxygen partial pressure. Values steadily drop from an initial normoxic level of (153 ± 1) torr to stable values of (4 ± 2) torr within 9.5 h.

Linear fitting was used to determine apparent oxygen consumption rates for MDCK II cells treated with PBS⁺⁺/Glc or PBS⁺⁺/Gal (supplementary information, **Fig. 11.6**). Results are shown in **Tab. 4.2**. Apparently, treatment with galactose enhances cellular oxygen consumption with AOOCR values up to (22.0 ± 0.8) torr h⁻¹. The AOOCR value decreases by about 25 % to (16.2 ± 0.6) torr h⁻¹ for cells treated with glucose.

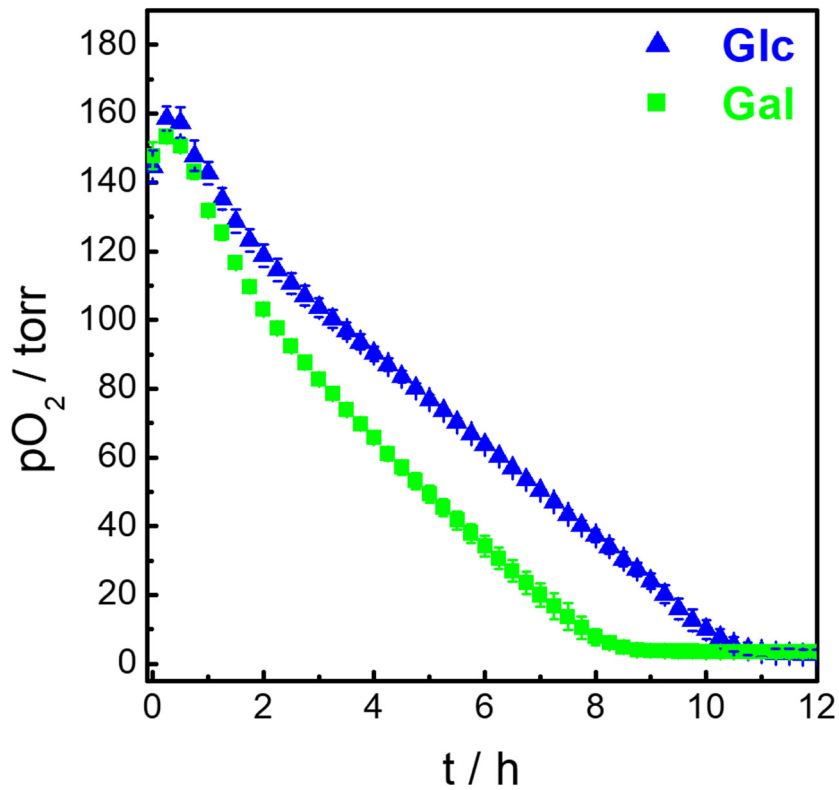


Fig. 4.5 Oxygen partial pressure as a function of time for confluent MDCK II cells (4.5×10^5 cells cm^{-2}) treated with PBS⁺⁺ buffer containing either 1 g/l glucose (\blacktriangle) or 1 g/l galactose (\blacksquare). Mean \pm SE, $n = 3$, $T = 37$ °C.

Tab. 4.2 Apparent oxygen consumption rates (related to a medium volume of 9.6 ml) and oxygen consumption rates of MDCK II cells treated with PBS⁺⁺ buffer supplemented with glucose or galactose at $T = 37$ °C.

Medium	AOCR \pm SE / torr h ⁻¹	OCR \pm SE / pmol s ⁻¹
PBS ⁺⁺ /Glc	16.2 \pm 0.6	6.1 \pm 0.2
PBS ⁺⁺ /Gal	22.0 \pm 0.8	8.3 \pm 0.3

4.4 OXYGEN CONSUMPTION IN DEPENDENCY ON SEEDING DENSITY

Oxygen consumption profiles of two kidney cell lines (MDCK II, NRK) in dependency on the cell inoculation density were recorded.

4.4.1 MDCK II CELLS

MDCK II cells were seeded at five different cell densities upon the oxygen sensor substrates, ranging from confluent to highly subconfluent cell layers. 24 h after cell inoculation, oxygen consumption of MDCK II cells was followed as a function of time in 9.6 ml L-15 medium. **Fig. 4.6** shows the decrease of the oxygen partial pressure in dependency on the initial cell seeding density. Independent of the cell density, the initial oxygen partial pressure increases within the first 0.5 h to normoxic values. However, oxygen partial pressure quickly drops to values below 10 torr for confluent MDCK II cells ($2.0 \times 10^5 \text{ c cm}^{-2}$) after 4.25 h and finally reaches stable values of about 2.5 torr (■) after 5 h. Cells seeded with a density of $1.0 \times 10^5 \text{ c cm}^{-2}$ fall below a value of 10 torr after 7.5 h (●). With a further decreased seeding density, the drop of oxygen partial pressure caused by cellular oxygen consumption is delayed to later time points. Values of (9 ± 6) torr are reached after 14.75 h for an initial seeding density of $5.0 \times 10^4 \text{ c cm}^{-2}$ (▲), values of (10 ± 6) torr are reached after 22.5 h for a cell density of $2.5 \times 10^4 \text{ c cm}^{-2}$ (◆) and values of (10 ± 4) torr are reached after 33.25 h for cells seeded at a density of $1.5 \times 10^4 \text{ c cm}^{-2}$ (▼). In addition, the curve loses its linearity with proceeding time when the three lowest cell densities are analyzed. This could be caused by a continuous increase of respiring cells on the sensor surface due to cell division. This interpretation is supported by the increase on slope with time.

Apparent oxygen consumption rates and corresponding oxygen consumption rates are summarized in **Tab. 4.3** (for corresponding linear fits see supplementary information, **Fig. 11.7**). Values range between (3.4 ± 0.1) torr h^{-1} for highly subconfluent cells ($1.5 \times 10^4 \text{ c cm}^{-2}$) and a maximal AOCR of (43.9 ± 1.1) torr h^{-1} for the highest seeding density. AOCR approximately increases proportional to initial cell density. Volume independent values for the OCR lie between (1.3 ± 0.1) pmol s^{-1} for an initial seeding density of $1.5 \times 10^4 \text{ c cm}^{-2}$ and (16.5 ± 0.4) pmol s^{-1} for an initial seeding density of $2.0 \times 10^5 \text{ c cm}^{-2}$.

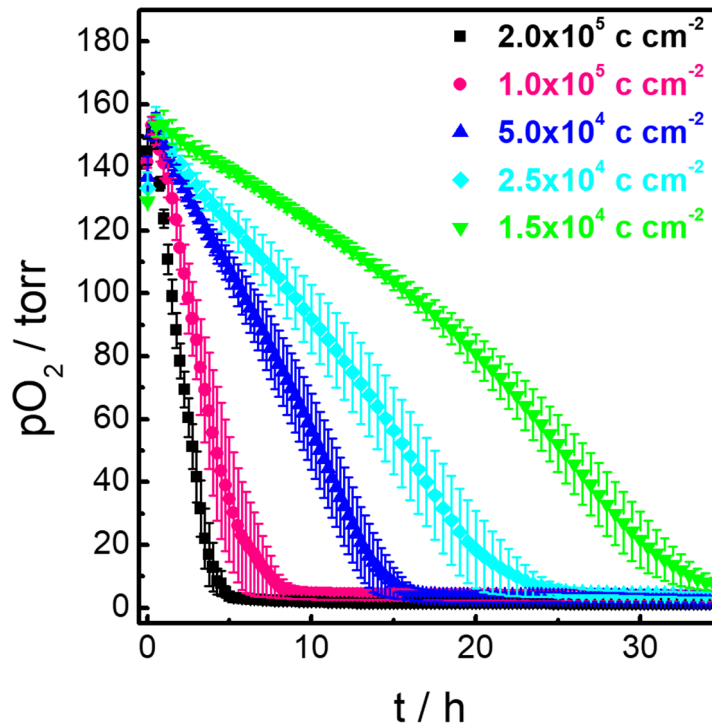


Fig. 4.6 Decrease of oxygen partial pressure plotted as a function of time for different seeding densities of MDCK II cells. Oxygen partial pressure decreases faster from normoxic conditions to anoxic values with increasing seeding density. Mean \pm SE, $n = 3$, $T = 37^\circ\text{C}$.

Tab. 4.3 Apparent oxygen consumption rates (recorded in a volume of 9.6 ml L-15 medium) and volume independent oxygen consumption rates of MDCK II cells seeded with different cell densities for oxygen readings recorded at $T = 37^\circ\text{C}$.

Cell density / c cm^{-2}	AOCR \pm SE / torr h^{-1}	OCR \pm SE / pmol s^{-1}
1.5×10^4	3.4 ± 0.1	1.3 ± 0.1
2.5×10^4	7.8 ± 0.3	2.9 ± 0.1
5.0×10^4	11.0 ± 0.2	4.3 ± 0.1
1.0×10^5	30.9 ± 0.5	11.6 ± 0.2
2.0×10^5	43.9 ± 1.1	16.5 ± 0.4

4.4.2 NRK CELLS

Additionally, oxygen consumption of NRK cells inoculated at different cell densities was followed online. Oxygen consumption of NRK cells was measured in L-15 medium 24 h after seeding. The corresponding changes of oxygen partial pressure beneath the cell layer are plotted as a function of time in **Fig. 4.7**. After an initial increase of oxygen partial pressure to normoxic values of about 150 torr, pO_2 drops beneath 10 torr after 8 h for confluent NRK cells ($2.0 \times 10^5 \text{ c cm}^{-2}$, ■). With decreasing seeding density oxygen consumption of the adherent cell layer is slowed down. When the number of seeded cells is reduced to 50 % (●), twice as much time is needed before pO_2 drops to hypoxic values ($t = 15.25 \text{ h}$; $10 \pm 8 \text{ torr}$). With a further reduction of cell number ($5.0 \times 10^4 \text{ c cm}^{-2}$, ▲), the pO_2 reaches a value of $(10 \pm 1) \text{ torr}$ after 27 h. At an initial seeding density of $2.5 \times 10^4 \text{ c cm}^{-2}$, NRK cells reach a pO_2 of $(10 \pm 7) \text{ torr}$ after 44 h (◆). When seeded at the lowest density ($1.5 \times 10^4 \text{ c cm}^{-2}$), oxygen partial pressure beneath the NRK cell layer does not fall below 10 torr after 62.25 h of imaging (▼).

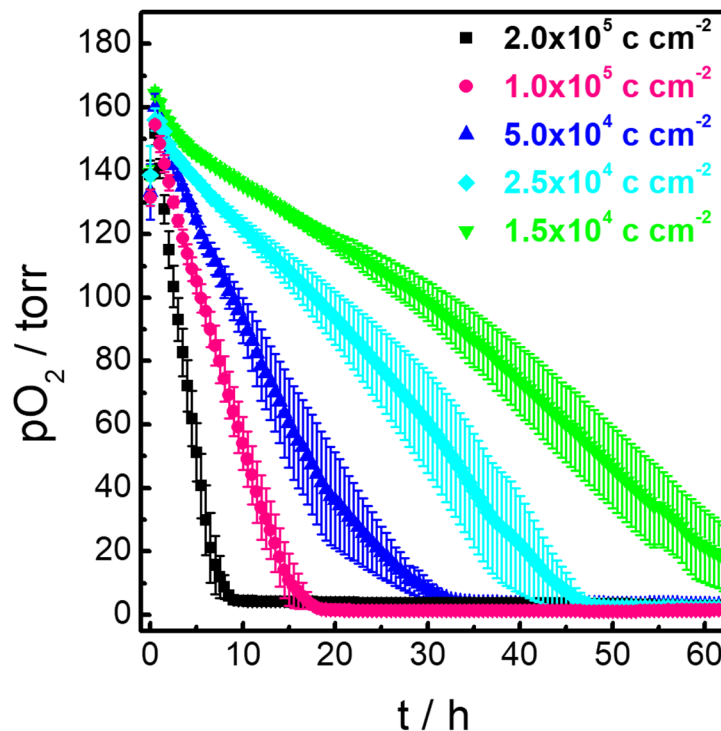


Fig. 4.7 Time dependent oxygen consumption profiles for NRK cells which were inoculated in different cell densities ranging from $2.0 \times 10^5 \text{ c cm}^{-2}$ to $1.5 \times 10^4 \text{ c cm}^{-2}$ 24 h before cellular oxygen consumption was monitored in L-15 medium. With increasing seeding density, the oxygen partial pressure decreases faster from normoxic to anoxic values. Mean \pm SE, $n = 3$, $T = 37 \text{ }^\circ\text{C}$.

Linear fitting was used to determine AOCRs of NRK cells. The corresponding fit functions are summarized in supplementary information, **Fig. 11.8**. The calculated values are shown in **Tab. 4.4** with values ranging from (23.3 ± 0.3) torr h⁻¹ for the highest seeding density to (4.3 ± 0.2) torr h⁻¹ for the lowest seeding density. However, AOCR values for the two lowest seeding densities do not show a significant difference, whereas AOCRs roughly double for higher seeding densities.

Tab. 4.4 Apparent oxygen consumption rates (recorded in a volume of 9.6 ml L-15 medium) and volume-independent oxygen consumption rates of NRK cells inoculated at different cell densities. T = 37 °C.

Cell density / c cm ⁻²	AOCR ± SE / torr h ⁻¹	OCR ± SE / pmol s ⁻¹
1.5 × 10 ⁴	4.3 ± 0.2	1.6 ± 0.1
2.5 × 10 ⁴	5.6 ± 0.2	2.1 ± 0.1
5.0 × 10 ⁴	7.8 ± 0.2	2.9 ± 0.1
1.0 × 10 ⁵	11.8 ± 0.1	4.4 ± 0.1
2.0 × 10 ⁵	23.3 ± 0.3	8.8 ± 0.1

Compared to oxygen consumption rates of MDCK II cells (see **Tab. 4.3**) NRK cells consume oxygen slower. Apparent oxygen consumption rates of MDCK II cells are nearly two-fold higher (43.9 ± 1.1 torr h⁻¹ for an initial seeding density of 2.0×10^5 c cm⁻²) compared to NRK cells seeded with identical cell number (23.3 ± 0.3 torr h⁻¹). AOCR as well as OCR values for highly subconfluent cells are not significantly different for both cell lines.

4.5 OXYGEN CONSUMPTION OF BAEC & U-373 MG CELLS

Changes of oxygen partial pressure as a function of time were determined for two additional cell lines. Therefore, U-373 MG and BAEC cells were seeded confluent (1.5×10^5 c cm⁻²) to cell culture petri dishes with incorporated oxygen sensor foils. 24 h after inoculation, cellular oxygen consumption was monitored in 9.6 ml L-15 medium. The resulting oxygen consumption profiles are displayed in **Fig. 4.8**. U-373 MG cells (▲) show a higher respiratory activity compared to BAEC cells. After an initial increase, the oxygen partial pressure drops from normoxic levels at $t = 0.5$ h to (9 ± 6) torr within 12.5 h and stabilizes to a final value of about 3 torr. Oxygen partial pressure beneath

BAEC layers remains at (86 ± 26) torr after 12.5 h with a slight decrease to (55 ± 43) torr after 24 h of measurement (●). Compared to U-373 MG cells, oxygen consumption profiles of BAECs show a significantly higher scattering of pO_2 values.

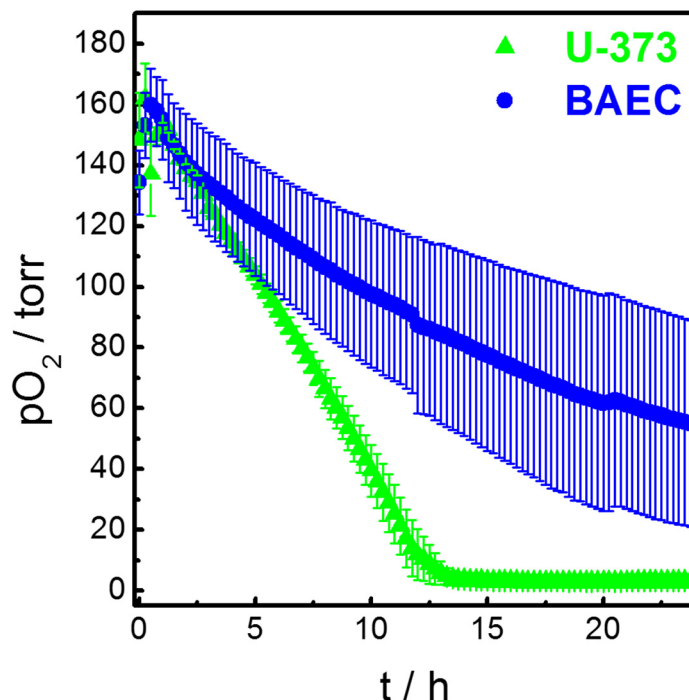


Fig. 4.8 Time dependent oxygen consumption profiles of U-373 MG (▲) and BAEC cells (●). Cells were cultivated with a density of 1.5×10^5 c cm^{-2} . 24 h after inoculation oxygen consumption was monitored in L-15 medium. Oxygen partial pressure beneath U-373 MG cell layers decreases faster compared to BAEC cells. Mean \pm SE, $n = 3$, $T = 37$ °C.

Linear fitting resulted in an apparent oxygen consumption rate of (13.2 ± 0.3) torr h^{-1} for U-373 MG cells (**Tab. 4.5**). Fitting of data for BAEC cells yields a 35 % lower apparent oxygen consumption rate compared to U-373 with a value of (8.6 ± 0.5) torr h^{-1} . Corresponding fit functions can be looked up in supplementary data, **Fig. 11.9**.

Tab. 4.5 Apparent oxygen consumption rates (in a volume of 9.6 ml L-15 medium) and oxygen consumption rates of BAEC and U-373 cells seeded with a density of 1.5×10^5 c cm^{-2} . Oxygen recordings were conducted at $T = 37$ °C.

Cell line	AOCR \pm SE / torr h^{-1}	OCR \pm SE / pmol s^{-1}
BAEC	8.6 ± 0.5	3.2 ± 0.2
U-373	13.2 ± 0.3	4.9 ± 0.1

4.6 INFLUENCE OF pH ON OXYGEN CONSUMPTION

Experiments described in this chapter were conducted in cooperation with L. Sauer (Institute of Analytical Chemistry, Chemo- and Biosensors, University of Regensburg, Germany). NRK cells were grown to confluence (seeding density $2.5 \times 10^5 \text{ c cm}^{-2}$) on oxygen sensor substrates. 24 h after seeding, the culture medium was aspirated and cells were treated with L-15 medium adjusted to pH 6.4, pH 7.2 and pH 7.8. Cellular respiration was measured in dependency on different extracellular pH values (**Fig. 4.9, A**). **Fig. 4.9, B** shows the oxygen consumption profiles of NRK cells incubated with L-15 medium adjusted to different pH. An acidic pH of 6.4 clearly influences the decrease of oxygen partial pressure beneath the epithelial cell layer. Compared to a pH of 7.2, that corresponds to a pH value of standard cell culture medium, NRK cells incubated with L-15 medium with a pH of 6.4 reach low pO_2 values of (9 ± 5) torr about 10.5 h after measurement start (**Fig. 4.9, B, ▲**). When cells are treated with L-15 medium with a pH of 7.2, the pO_2 drops below 10 torr about 2.8 h earlier (**Fig. 4.9, B, ■**). These findings nicely correlate with phase contrast micrographs taken of the NRK monolayer after the oxygen measurement was finished (**Fig. 4.9, C**). The confluent cell layer seems to be altered in morphology at an acidic pH of 6.4. NRK cells exhibit blurry cell-cell contacts and many rounded, detached cells are found in the samples after imaging was finished. While the morphology of cells incubated at pH 7.2 does not change compared to cell morphology before imaging the oxygen consumption. Astonishingly, cells incubated at a slightly basic extracellular pH of 7.8 seem to consume oxygen even faster than under standard culture conditions at pH 7.2. Here, oxygen partial pressure drops below (10 ± 6) torr within 6 h after measurement start (**Fig. 4.9, B, ●**). Also, incubation with basic L-15 medium during the oxygen measurement does not seem to have any negative influence on the morphology of the NRK monolayer (**Fig. 4.9, C**).

Data from oxygen consumption profiles at pH 6.4, 7.2 and 7.8 was fitted linearly to determine AOCRs (for fitting data see **Fig. 11.10**). With an apparent oxygen consumption rate of (14.3 ± 0.2) torr h^{-1} the AOCR of NRK cells measured at an acidic extracellular pH of 6.4 shows a decrease of about 37 % compared to the AOCR at pH 7.2 (**Tab. 4.6**). At a basic pH of 7.8 cells consume oxygen at a rate of (29.4 ± 0.8) torr h^{-1} . This is an increase of 31 % compared to the rate determined for an extracellular pH of 7.2 with an apparent oxygen consumption rate of (22.6 ± 0.2) torr h^{-1} .

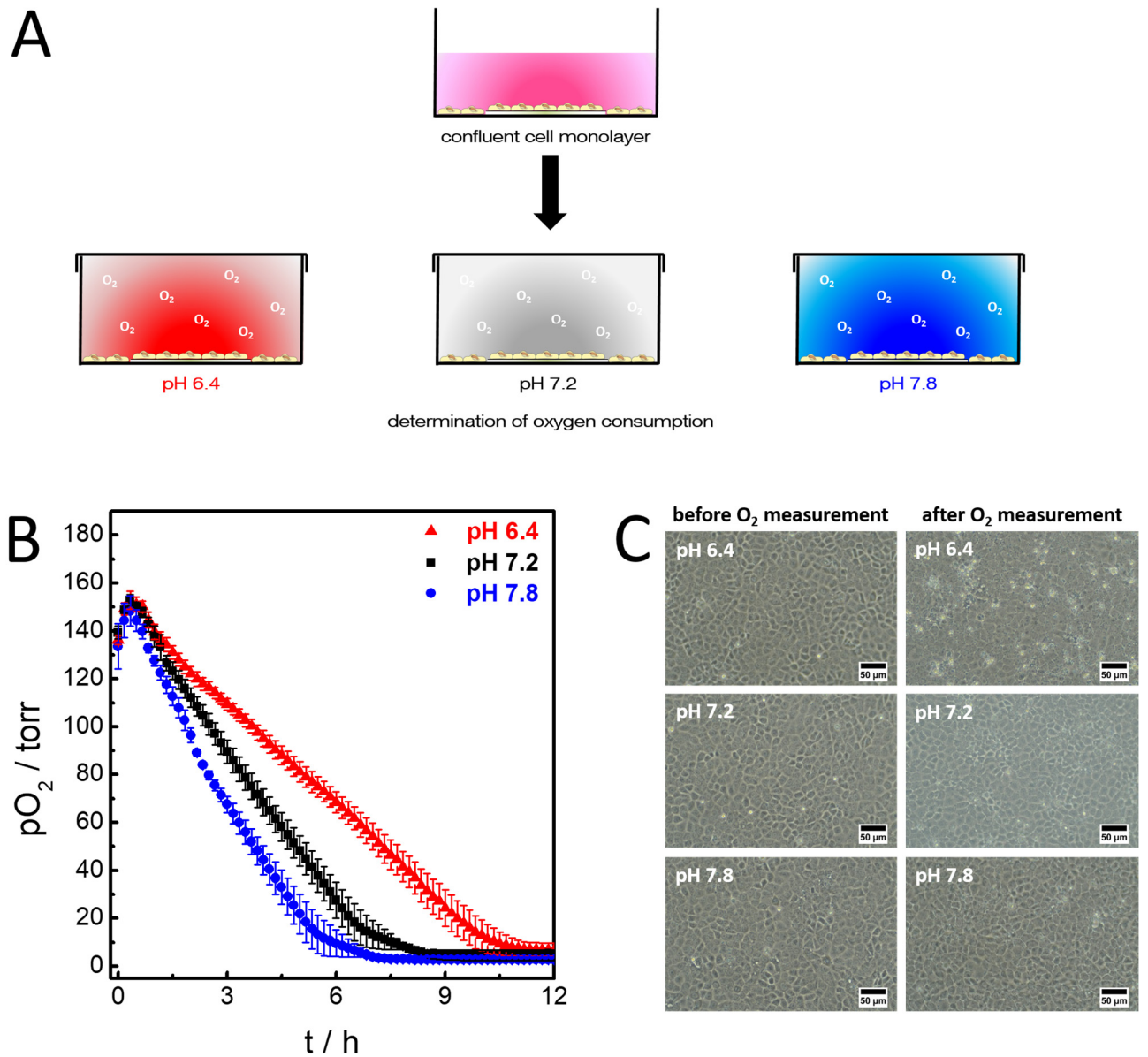


Fig. 4.9 (A) Experimental protocol for measuring the oxygen consumption of NRK cells at different extracellular pH values. (B) Decrease of oxygen partial pressure as a function of time. At a basic pH of 7.8 (●), cells show faster oxygen consumption, while oxygen consumption is reduced at acidic pH of 6.4 (▲) compared to neutral pH of 7.2 (■). (C) Micrographs of NRK cells treated with pH-adjusted L-15 medium before and after the oxygen measurement. Because the oxygen sensor foil is opaque, images show cells grown next to the sensor film on the cell culture petri dish. Mean \pm SE, $n = 3$, $T = 37^\circ\text{C}$.

Tab. 4.6 Apparent oxygen consumption rates (recorded in a volume of 9.6 ml L-15 medium) and volume-independent oxygen consumption rates of NRK cells treated with L-15 medium with pH adjusted to 6.4, 7.2 or 7.8 at $T = 37^\circ\text{C}$.

pH	AOCR \pm SE / torr h^{-1}	OCR \pm SE / pmol s^{-1}
6.4	14.3 ± 0.2	5.4 ± 0.1
7.2	22.6 ± 0.2	8.5 ± 0.1
7.8	29.4 ± 0.8	11.0 ± 0.3

4.7 INFLUENCE OF DRUGS ON OXYGEN CONSUMPTION

Under aerobic conditions, cells consume oxygen to store energy in the form of adenosine triphosphate (ATP) during oxidative phosphorylation inside the mitochondria (**Fig. 4.10**, black inset). In this study, the influence of compounds that intervene with oxidative phosphorylation and the effect on cellular oxygen consumption should be investigated. Therefore, antimycin A (Ant A) and malonoben (Mal) were chosen as model substances. Antimycin A is an antibiotic produced by *Streptomyces kitazawensis* (Nakayama et al. 1956). Antimycin A belongs to a class of compounds that are known to inhibit mitochondrial complex III, the second proton translocating complex residing in the inner mitochondrial membrane. The high affinity of Ant A to bind to complex III effectively blocks the electron transfer at the center Q_i (quinone-reducing center), resulting in a complete breakdown of mitochondrial electron transport (Wallace and Starkov 2000; Xu et al. 2014). Treatment of cells with effective antimycin A concentrations below 5 μM leads to the complete inhibition of complex III, thus reducing cellular oxygen consumption to a minimum (Campo et al. 1992). In contrast to inhibitors, uncouplers of oxidative phosphorylation are compounds which lead to a decrease of mitochondrial ATP production. Addition of uncoupling molecules induces energy dissipating processes that compete with regular mitochondrial processes to store energy in form of ATP (Wallace and Starkov 2000). SF6847 [2,6-di-tert-butyl-4-(2',2'-dicyanovinyl)phenol], also known as malonoben, is a lipophilic weak acid that is considered one of the most potent uncouplers of oxidative phosphorylation. With an effective concentration below 10 nM, malonoben is 1800 times more effective than 2,4-dinitrophenol (Terada 1981). Malonoben is a moderately weak acid that acts as a protonophore, shuttling H^+ across the mitochondrial membrane. This leads to the release of protons into the mitochondrial matrix, thus inducing the short-circuiting of the mitochondrial proton gradient. Upon breakdown of the proton gradient, the ATP synthase loses its driving force. In order to compensate the low gradient, cells react immediately by increasing their oxygen consumption rates (Mclaughlin and Dilger 1980; Wallace and Starkov 2000).

MDCK II cells were inoculated in a density of $4.5 \times 10^5 \text{ c cm}^{-2}$ on oxygen sensor substrates. 24 h after seeding, the oxygen consumption of cells was measured and the influence of the two drugs on oxidative phosphorylation was investigated. **Fig. 4.10** shows the time-resolved oxygen consumption profiles of confluent MDCK II monolayers treated with 2 μM Ant A or 100 nM Mal. First, a baseline was recorded for all conditions. Therefore, oxygen consumption was monitored in L-15 medium for the first 5.25 h. Then, the L-15 medium was exchanged to L-15 medium containing antimycin A or

malonoben. As control condition, fresh L-15 medium was added. Under control conditions, the curve progression is similar for addition of L-15 medium at $t = 0$ h and $t = 5.25$ h. When fresh medium is added, oxygen partial pressure increases to normoxic values followed by a decrease to anoxic values within 2 – 3 h after medium exchange (**Fig. 4.10, ■**). Addition of 100 nM Mal in L-15 medium at $t = 5.25$ h strongly enhances cellular oxygen consumption with a value of (7 ± 3) torr reached within 0.75 h after addition (**Fig. 4.10, ▲**). Treatment of MCDK II cells with 2 μ M Ant A at $t = 5.25$ h leads to a complete inhibition of cellular respiration (**Fig. 4.10, ●**) resulting in stable levels of normoxic pO_2 of about 145 torr. After 10.75 h, all samples were treated with 0.3 % (w/v) saponin (Sap). Cell permeabilization leads to inactivation of cellular respiration and cell death, which can be seen in a permanent reoxygenation to normoxic values to about 150 torr.

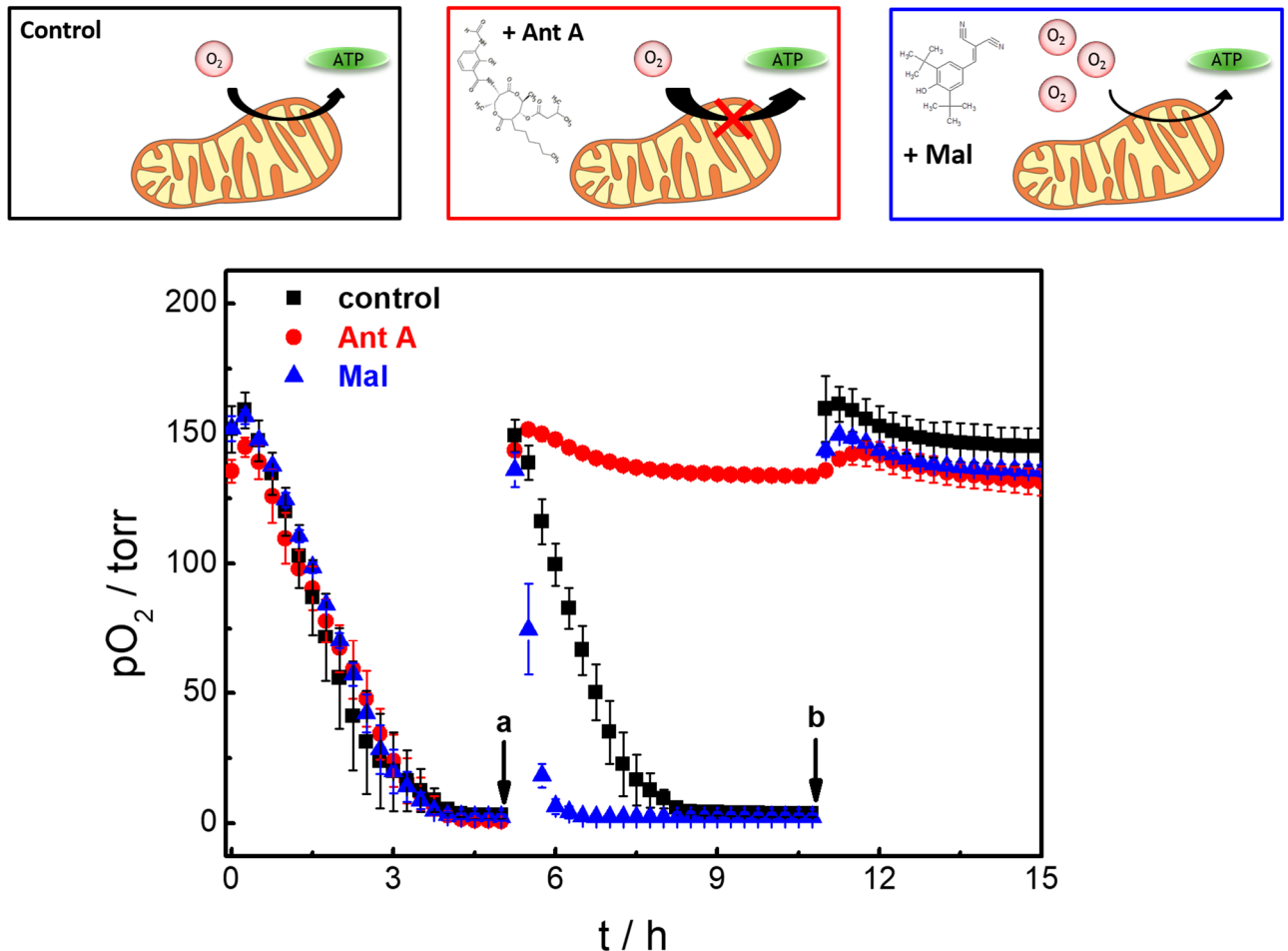


Fig. 4.10 The effect of drugs influencing oxidative phosphorylation on the oxygen consumption of confluent MDCK II layers (seeding density 4.5×10^5 c cm^{-2}). Temporal changes of oxygen partial pressure as a function of time for MDCK II cells treated with L-15 medium as control (■), 100 nM malonoben (▲) or 2 μ M antimycin A (●). First, basal oxygen consumption was recorded in L-15 medium. After 5.25 h (a), MDCK II cells were either treated with 2 μ M Ant A, a blocker of cellular respiration or 100 nM Mal, an uncoupler of mitochondrial oxidative phosphorylation or L-15 medium as control. After 10.75 h, 0.3 % Sap was added (b). Mean \pm SE, $n \geq 3$, $T = 37$ °C.

The influence of antimycin a and malonoben on cellular oxygen consumption is clearly visible in the (apparent) oxygen consumption rates (**Tab. 4.7**). Under control conditions, MDCK II cells exhibit an AOCR of (68.0 ± 2.8) torr h⁻¹. When the respiratory chain is blocked by addition of 2 μM antimycin A, AOCR is drastically reduced to 10 % to a value of (6.9 ± 0.9) torr h⁻¹. Uncoupling oxidative phosphorylation by addition of 100 nM Mal leads to a 3.5fold increase of the AOCR, with cells consuming oxygen at a rate of (235.0 ± 2.2) torr h⁻¹. Linear fits used for the determination of AOCRs can be found in the supplementary data (**Fig. 11.11**). After 10.75 h, the medium was exchanged to L-15 medium containing 0.3 % (w/v) saponin as indicated by arrow b in **Fig. 4.10**. The surfactant saponin (Sap) permeabilizes the cell membrane, which results in cell death and breakdown of metabolic activity. After addition of fresh L-15, pO₂ of control cells, as well as drug treated cells increases to normoxic values of about 150 torr. As cellular respiration is irreversibly impaired by Sap, no cellular oxygen consumption rates can be determined.

Tab. 4.7 Apparent oxygen consumption rates (in a volume of 9.6 ml L-15 medium) and oxygen consumption rates of MDCK II cells treated with compounds blocking (Ant A) or uncoupling (Mal) oxidative phosphorylation. T = 37 °C.

Added compound	AOCR ± SE / torr h ⁻¹	OCR ± SE / pmol s ⁻¹
control (L-15 medium)	68.0 ± 2.8	25.6 ± 1.1
Ant A (2 μM)	6.9 ± 0.9	2.6 ± 0.3
Mal (100 nM)	235.0 ± 2.2	88.3 ± 0.8

4.8 INFLUENCE OF TOXINS ON OXYGEN CONSUMPTION

4.8.1 TREATMENT OF NRK CELLS WITH CARBON DOTS

Carbon dots (C-dots) were first described in 2004 (Xu et al. 2004). These particles have a size of a few nanometers and consist of a graphitic core with a passivated surface that often contains elements such as oxygen, nitrogen or hydrogen which renders them highly hydrophilic. They exhibit a stable fluorescence, are not prone to photobleaching and do not contain any heavy metals which makes them interesting for applications in biological samples (Nandi et al. 2014). For example, C-dots have been used to selectively label live and dead adherent mammalian cells. However, high concentrations reduce cellular viability (Lemberger 2016).

In this work, the influence of C-dots on the cellular oxygen consumption was investigated. Therefore, NRK cells were seeded to confluence to oxygen sensitive culture substrates ($2.5 \times 10^5 \text{ c cm}^{-2}$). 24 h after seeding, cells were incubated for 5 h with 1.0 mg ml^{-1} or 2.5 mg ml^{-1} C-dots in culture medium or pure culture medium as control. Then C-dots were removed by washing the samples twice and the cellular oxygen consumption was measured in L-15 medium (**Fig. 4.11, A**). The time-resolved oxygen consumption profiles are depicted in **Fig. 4.11, B**. Under control conditions, the oxygen partial pressure below the NRK monolayer rapidly drops from normoxic levels to (10 ± 3) torr after 4.5 h (**Fig. 4.11, B, ■**). At the same time, the oxygen partial pressure reaches a value of (90 ± 7) torr when NRK cells have been incubated with 1.0 mg ml^{-1} C-dots (**Fig. 4.11, B, ▲**), while the $p\text{O}_2$ of cells treated with 2.5 mg ml^{-1} C-dots reaches only (104 ± 1) torr (**Fig. 4.11, B, ●**). Furthermore, NRK cells incubated with 1.0 mg ml^{-1} C-dots reach stable $p\text{O}_2$ levels of (11 ± 10) torr after 12 h, while the $p\text{O}_2$ of samples incubated with 2.5 mg ml^{-1} C-dots has a final value of (30 ± 7) torr. Incubation with C-dots seems to affect NRK cell metabolism after a 5 h exposure.

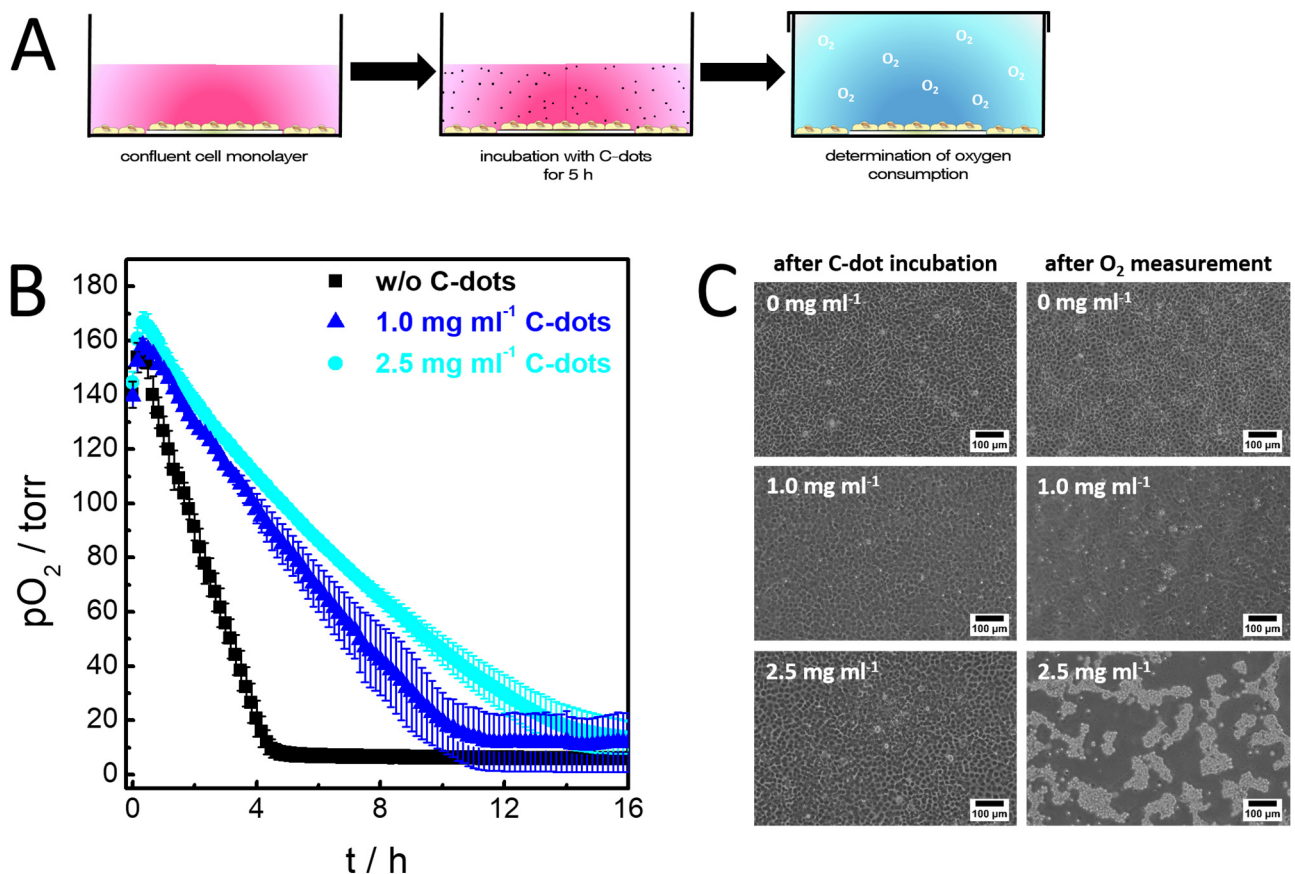


Fig. 4.11 Influence of C-dots on the cellular oxygen consumption. (A) Confluent NRK cells (seeding density $2.5 \times 10^5 \text{ c cm}^{-2}$) were incubated for 5 h with two different concentrations of C-dots before oxygen consumption was measured. (B) The decrease of oxygen partial pressure as a function of time shows a delayed drop of oxygen partial pressure of NRK cells treated with C-dots. (C) Phase contrast images of NRK cells after 5 h incubation with C-dots and after oxygen measurement was finished. Because the oxygen sensor foil is opaque, images show cells grown next to the sensor foil on the cell culture petri dish. Mean \pm SE, $n = 3$, $T = 37^\circ \text{C}$.

Although the cell monolayer is still intact after exposure to C-dots for 5 h, cell morphology is altered with cells starting to round up and expressing blurry cell-cell contacts (**Fig. 4.11, C**). This is most pronounced for cells incubated with the highest C-dot concentration. Furthermore, a clear difference between C-dot treated cells and control cells can be seen after oxygen measurements are finished 16 h later. At a concentration of 1.0 mg ml^{-1} , many dead cells cover the still intact monolayer. However, cell morphology seems changed and cell-cell contacts seem to be weakened compared to the control. Cells treated with the maximum concentration of 2.5 mg ml^{-1} have detached from the growth substrate and appear to have died. Additionally, AOCRs have been determined by linear fitting (supplementary information, **Fig. 11.12**). Values obtained by linear fitting and corresponding volume independent OCRs are shown in **Tab. 4.8**. Incubation with C-dots has a significant impact on cellular oxygen consumption yielding an AOCR value for samples incubated with 1.0 mg ml^{-1} C-dots that is 50 % lower ($17.6 \pm 0.3 \text{ torr h}^{-1}$) than the AOCR value of the control ($35.3 \pm 0.2 \text{ torr h}^{-1}$). When cells are treated with the highest concentration of C-dots, AOCR is further reduced to (14.0 ± 0.2) torr h^{-1} .

Tab. 4.8 Apparent oxygen consumption rates (in a volume of 9.6 ml L-15 medium) and corresponding OCR values of NRK cells incubated with different concentrations of C-dots for 5 h. Oxygen reading were recorded at $T = 37 \text{ }^\circ\text{C}$.

β (C-dots) / mg ml^{-1}	AOCR \pm SE / torr h^{-1}	OCR \pm SE / pmol s^{-1}
0	35.3 ± 0.2	13.3 ± 0.1
1.0	17.6 ± 0.3	6.6 ± 0.1
2.5	14.0 ± 0.2	5.3 ± 0.1

4.8.2 TREATMENT OF NRK CELLS WITH CdCl_2

Cadmium is a heavy transition metal that is known to have carcinogenic, mutagenic and teratogenic effects on organisms (Waalkes 2003). Intoxication with cadmium compounds can lead to severe damage of organs, such as liver, lungs or kidney (Bertin and Averbeck 2006). In vitro studies with monolayer cells showed that μM concentrations of cadmium induce apoptosis, interfere with cell cycle progression, proliferation and DNA repair (Yang et al. 2004; Mao et al. 2007). Long term exposure leads to changes in gene expression levels, resulting in overexpression of protooncogenes

and altered levels of regulatory genes of cell cycle and proliferation (Jin and Ringertz 1990; Vonzglinicki et al. 1992; Misra et al. 2003).

The impact of cadmium on cellular metabolism was tested by measuring the oxygen consumption of NRK cells. NRK cells were seeded with a density of $2.5 \times 10^5 \text{ c cm}^{-2}$. 24 h after seeding, cells were incubated for a period of 2 h with different concentrations of CdCl_2 in NRK culture medium. Afterwards, CdCl_2 was removed by washing the cell layer twice and oxygen consumption was monitored in L-15 medium (Fig. 4.12, A). The impact of different concentrations of CdCl_2 on oxygen consumption is shown in Fig. 4.12, B. pO_2 beneath control cells incubated with medium only rapidly decreases to (10 ± 3) torr within 6.3 h (Fig. 4.12, B, ■). However, when a concentration of $100 \mu\text{M}$ CdCl_2 was added to the cell layer, oxygen partial pressure decreases slower. When compared to control cells oxygen partial pressure lies at (44 ± 10) torr after 6.3 h. Lower values of (10 ± 5) torr are reached after 10.3 h (Fig. 4.12, B, ▲). At a concentration of $300 \mu\text{M}$ CdCl_2 , oxygen partial pressure first decreases till it reaches a minimum of (113 ± 9) torr at $t = 8.8$ h. Then, pO_2 steadily increases

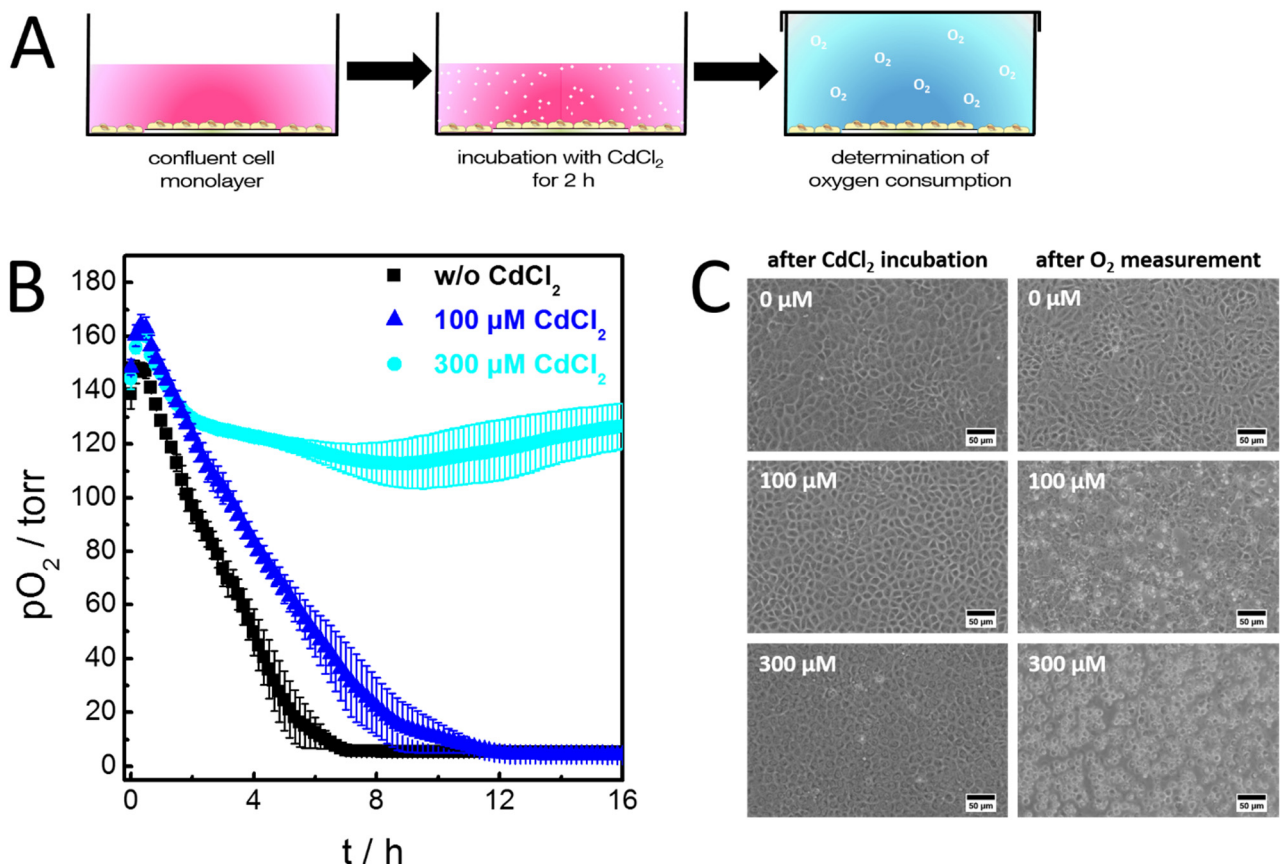


Fig. 4.12 Influence of CdCl_2 on the cellular oxygen consumption of NRK cells. (A) Confluent NRK cells (seeding density $2.5 \times 10^5 \text{ c cm}^{-2}$) were incubated for 2 h with NRK culture medium (■), NRK culture medium containing $100 \mu\text{M}$ (▲) or $300 \mu\text{M}$ CdCl_2 (●) before oxygen consumption was measured. (B) Decrease of the oxygen partial pressure as a function of time shows a delayed decrease of oxygen partial pressure when cells have been incubated with $100 \mu\text{M}$ CdCl_2 . Incubation with $300 \mu\text{M}$ CdCl_2 causes pO_2 levels to return to normoxic values. (C) Phase contrast images of NRK cells 2 h after incubation with CdCl_2 and after the oxygen measurement was finished. Mean \pm SE, $n = 3$, $T = 37^\circ\text{C}$.

to stable values of about 135 torr (**Fig. 4.12, B, ●**). This fast reoxygenation is probably caused by cell death that sets in within a few hours after measurement start. This would prevent the complete depletion of oxygen within the L-15 medium. The cytotoxic effect of CdCl₂ is also visible in phase contrast images taken of samples immediately after incubation with cadmium chloride and after oxygen imaging (**Fig. 4.12, C**). After incubation with 300 μM CdCl₂, NRK cells exhibit a changed morphology with swollen nuclei and blurry cell-cell contacts. When cells are examined after the oxygen measurement, those that were treated with 300 μM CdCl₂ are rounded up and detached from the substrate, while control cells still form an intact cell monolayer. NRK cells incubated for 2 h with 100 μM CdCl₂ do not show changes in morphology compared to control cells incubated with L-15 medium. However, when cells are examined after the oxygen measurement, cells are partly detached and dead with only few cells remaining attached to the surface, compared to the vital, confluent control cell layer.

Apparent oxygen consumption rates show a clear difference between control samples and samples treated with varying concentrations of CdCl₂ (summarized in **Tab. 4.9**, for linear fits see supplementary information **Fig. 11.13**). With an AOCR of (21.3 ± 0.3) torr h⁻¹, NRK cells treated with 100 μM CdCl₂ show a decrease of about 21 % compared to control samples with an AOCR of (27.0 ± 0.4) torr h⁻¹. When monolayers are treated with 300 μM CdCl₂ oxygen consumption rate drops by about 77 % to (6.1 ± 0.7) torr h⁻¹.

Tab. 4.9 Apparent oxygen consumption rates (recorded in a volume of 9.6 ml L-15 medium) and oxygen consumption rates of NRK cells treated with different concentrations of CdCl₂. T = 37 °C.

c(CdCl ₂) / μM	AOCR ± SE / torr h ⁻¹	OCR ± SE / pmol s ⁻¹
0	27.0 ± 0.4	10.1 ± 0.2
100	21.3 ± 0.3	8.0 ± 0.1
300	6.1 ± 0.7	2.3 ± 0.3

4.9 IMAGING OXYGEN GRADIENTS WITHIN AN ISOLATED CELL PATCH

The VisiSens TD mic system was used to monitor oxygen gradients generated within a patch of monolayer cells. Therefore, MDCK II cells were seeded on the oxygen sensor foil with a density of 2.0×10^5 cells cm^{-2} . To create a small patch, cells were seeded in a small insert that served as barrier thus preventing cells from spreading upon the whole sensor surface (see **chapter 3.2.3**). MDCK II cells were cultivated 24 h inside the small chamber to form an adherent monolayer. Then, the PDMS ring was removed so that cells could migrate and spread. The temporal and spatial changes of oxygen levels during migration was monitored in L-15 medium (**Fig. 4.13, A**). **Fig. 4.13, B – D** depicts typical data for one individual cell patch that was studied this way. In total, four independent cell patches were analyzed yielding similar results. The false color oxygen images in **Fig. 4.13, B** nicely show first the formation of an oxygen gradient with smaller oxygen concentrations in the center of the patch caused by the respiring cells. After 10 h, the oxygen consumption caused by the actively respiring cell patch is clearly visible. Within the next 10 h, the pO_2 gradient between cells and surrounding medium further increases in steepness, resulting in a central region with low pO_2 levels. The size of the area with low pO_2 increases during the measurement, probably because the size of the cell patch increases due to cell migration and division. The formation and growth of the oxygen gradient over a period of 60 h is documented by time-lapse video microscopy in **Video 11.1** displayed in false color images with a time resolution of 15 min. The kinetics of the decrease of pO_2 is also dependent on the position of the ROI. **Fig. 4.13, C** shows three different ROIs with a width of 85×80 Px, that are either positioned directly in the center of the MDCK II cell patch (ROI 1: center of cell patch, ROI 2: edge of cell patch) or at the cell-free oxygen sensor (ROI 3). pO_2 values of the cell-covered area can be clearly distinguished from values determined for the cell-free sensor surface. The initial pO_2 levels at $t = 0$ h range from a normoxic value of (142 ± 10) torr for ROI 3 (■), to slightly lower pO_2 levels of (119 ± 9) torr for ROI 1 (●) and (121 ± 10) torr for ROI 2 (▲). Due to cellular oxygen consumption, the pO_2 in the center of the cell spot (ROI 1, ●) decreases by about 90 % to (14 ± 4) torr within 40 h, reaching (1 ± 3) torr after 69 h of imaging. At the edge of the MDCK II patch (ROI 2, ▲), the oxygen partial pressure drops by about 65 % to a value of (44 ± 6) torr after 40 h of imaging. Finally, pO_2 levels reach values of (7 ± 4) torr. This result is similar to ROI 1, which indicates that cells have grown and migrated over the sensor surface during the measurement. This trend is also apparent for the oxygen partial pressure at the cell-free sensor (ROI 3, ■). pO_2 does not stay at the initial constant normoxic values, but slowly decreases with time. It reaches a value of

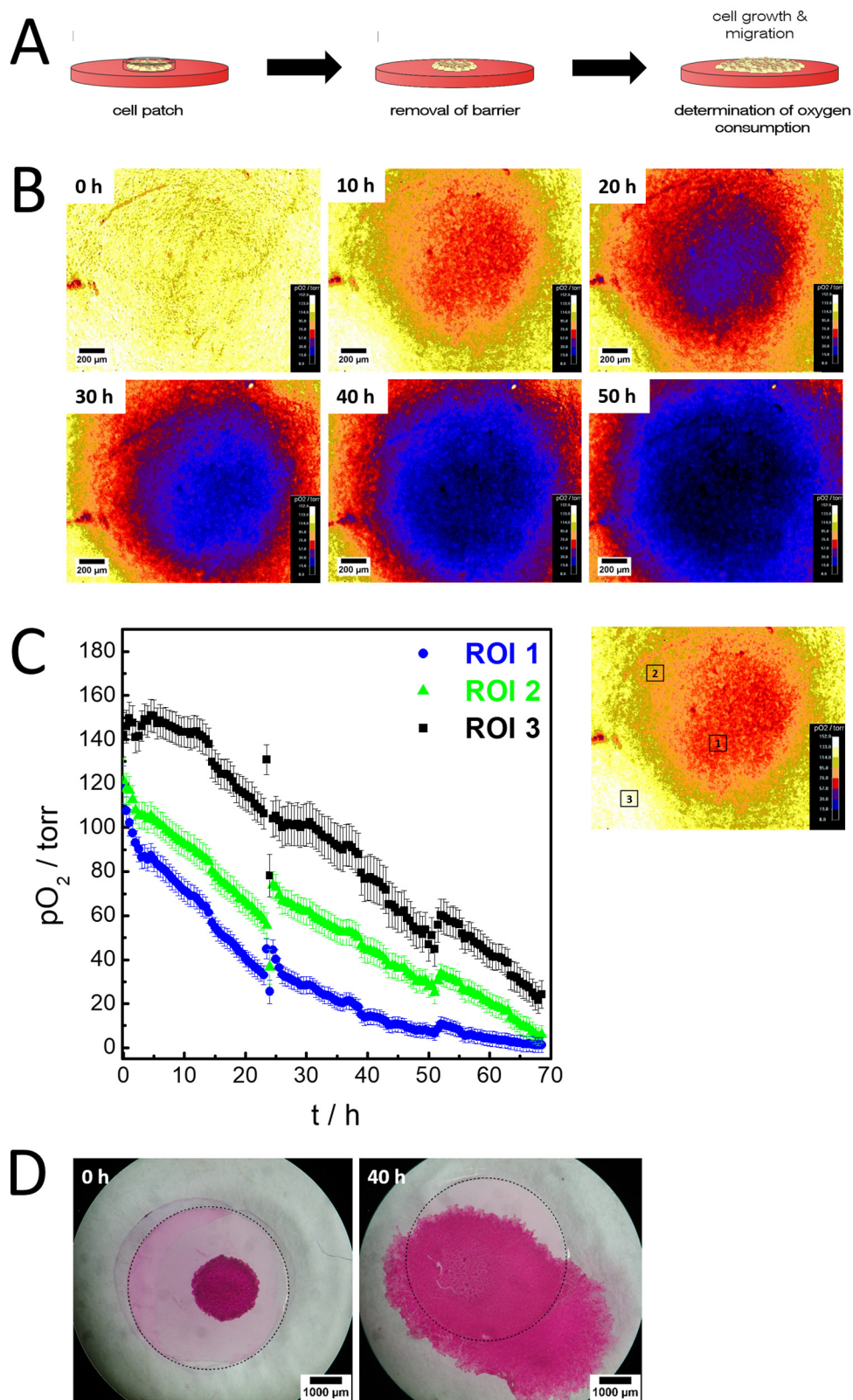


Fig. 4.13 (A) A patch of adherent MDCK II cells growing on oxygen sensitive culture substrates is created by applying a cylindrical barrier. (B) False color oxygen images showing the oxygen gradient formation between center and periphery of the cell patch and the gradient over a period of 50 h. (C) Changes of oxygen partial pressure of different ROIs, representing the cell-covered sensor (ROI 1, ROI 2) and the cell-free sensor (ROI 3) as a function of time. $\text{Mean}_{\text{ROI}} \pm \text{SD}_{\text{ROI}}$. (D) Stereomicroscopic images of a MDCK II cell patch stained with carbolfuchsin after removal of the barrier ($t = 0$ h) and 40 h after barrier removal. After the barrier is removed, cells migrate and spread over the complete substrate. Data show results for one typical cell patch. In total, four individual cell patches were monitored yielding similar results. $T = 37$ °C.

(77 ± 10) torr at $t = 40$ h and further drops to (25 ± 6) torr after 69 h of imaging. Because the sensor spot is not accessible to phase contrast microscopy, MDCK II growth and migration was documented by staining the cell spot with carbofuchsin. The stained cells were analyzed by stereomicroscopy. **Fig. 4.13, D** shows the stained cells immediately after barrier removal at $t = 0$ h and after 40 h of imaging. The initial size of the spot is about 3.3 mm^2 and increases about 8fold in area to 27.3 mm^2 at $t = 40$ h. It can be clearly seen, that cells spread on both oxygen sensor foil and petri dish during the time period of 40 h.

4.10 DISCUSSION

4.10.1 OXYGEN CONSUMPTION IN OPEN AND CLOSED SYSTEMS

When confluent MDCK II cell layers were monitored in closed chambers with different volumes of L-15 culture medium, samples cultivated in smaller volumes showed a faster decrease of $p\text{O}_2$. Volume dependent AOCRs resulted in higher values for smaller volumes, ranging from (92.1 ± 3.4) torr h^{-1} for a volume of 4.8 ml, to (29.7 ± 1.1) torr h^{-1} for a volume of 19.2 ml. However, similar values for the volume independent oxygen consumption rates were obtained, ranging between 17.3 and 22.3 pmol s^{-1} when the same samples are considered. When compared to oxygen measurements conducted with MDCK II cells in an open system, which was in contact with the gas phase of the incubation system, an OCR value of (53.3 ± 3.7) pmol s^{-1} was calculated which lies in the range of the values obtained for the closed chambers.

Usually, measurement of OCRs relies on the use of an airtight chamber system as used in this work. Cells are cultivated inside the chamber either as suspension or adherent cultures and respiration rate is assessed using an electrochemical or luminescent sensor (Jorjani and Ozturk 1999; Kindig et al. 2003). Typically, determination of $p\text{O}_2$ in closed systems yields accurate results and the set-up makes calculation of OCRs easy as there is no need to include oxygen influx in the calculation. Oxygen consumption rates can be directly determined by linear fitting the changes of $p\text{O}_2$ over time, considering the respective volume of the chamber (Ruffieux et al. 1998; Guarino et al. 2004). When a cell monolayer is cultivated under static conditions in an open system, dissolved oxygen reaches the adherent cells only by diffusion. The diffusion of oxygen from the interface between gas phase and medium to the cell layer is described by Fick's second law. Under the assumption that diffusion and respiration come to an equilibrium and the culture vessel is impermeable to oxygen, OCR can

be calculated using eq. 3.2 described in **chapter 3.2.6**. Both methods were used by other labs to determine OCRs of rat alveolar cells cultivated in open and closed systems. Similar to results obtained in this work for confluent layers of MDCK II cells, comparison of alveolar cells yielded similar OCR values independent of cultivation in an open or closed system. The open system is limited, because OCR can only be calculated when the equilibrium state is reached while OCR in closed systems can be determined via the slope of the decrease in pO_2 as soon as the chamber is sealed. The need to wait until an equilibrium state is established takes long when cells with slow metabolism are analyzed, it may negatively affect short-term measurements which monitor fast changes of pO_2 or prevent studies on sequential addition of compounds (Mamchaoui and Saumon 2000). However, this method would enable using open multi-well plates by circumventing a complicated airtight sealing. Combined with a suitable readout system, this could tremendously increase throughput of samples.

4.10.2 INFLUENCE OF MEDIUM COMPOSITION

The influence of medium composition on the oxygen consumption of confluent MDCK II cell layers was investigated using the novel imaging system. Cultivation of MDCK II cells in PBS⁺⁺ buffer containing 1 g l⁻¹ glucose resulted in an about 25 % lower oxygen consumption rate compared to cells cultivated in PBS⁺⁺ buffer containing 1 g l⁻¹ galactose.

An increase of cellular respiration due to the presence of galactose was also found in rat PC12 cells. Upon replacement of glucose by galactose containing medium, oxygenation determined in the adherent cell layer under galactose approached lower pO_2 values compared to cells cultivated in glucose. This result indicates, that replacement of glucose by galactose enhances oxidative phosphorylation and respiration rates (Zhdanov et al. 2010). Moreover, cultivation of myotubes in galactose -containing medium has been shown to enhance aerobic oxidative phosphorylation by an increased cytochrome c activity (Aguer et al. 2011). Further studies showed, that in the absence of Glc but presence of galactose, energy levels can be maintained by an increased mitochondrial respiration. Cellular oxygen consumption rates can be further increased by addition of pyruvate and glutamine to galactose containing medium, which further shifts metabolism from glycolysis to mitochondrial respiration (Zhdanov et al. 2014). These result supports the data measured in this work, where an enhanced oxygen consumption rate of $(8.3 \pm 0.3) \text{ pmol s}^{-1}$ was observed for PBS⁺⁺ buffer containing galactose. OCR was about 25 % lower for cell cultivated in PBS⁺⁺/Glc with a value

of (6.1 ± 0.2) pmol s⁻¹. However, cellular oxygen consumption rate is further increased when the same number of cells is monitored in L-15 medium which also contains pyruvate and glutamine as shown in **chapter 4.2**. Here an OCR of (19.0 ± 0.6) pmol s⁻¹ has been measured. The increased oxygen consumption rates in Gal containing media can be explained by a shift from glycolysis to mitochondrial respiration. Although cells can take up both, Glc and Gal by the superfamily of GLUT transporters located in the plasma membrane, most subtypes exhibit higher affinity for glucose than galactose (Zhao and Keating 2007). Additionally, galactose must be converted into glucose-6-phosphate via Leloir pathway before entering the glycolytic pathway (Berg et al. 2012). Conversion of galactose by galactokinase is often slow, as intracellular galactokinase levels are low (Reitzer et al. 1979). Because the galactose uptake rate are lower and the intracellular conversion processes have slower kinetics compared to glucose metabolism, glycolysis alone is not sufficient to satisfy cellular energy demand. Thus, a shift towards mitochondrial oxidative phosphorylation is necessary in order to maintain sufficiently high ATP levels. In HeLa cells, exposure to medium containing Gal instead of Glc led to a doubling of respiratory rates and long-term adaptations, such as changes in expression levels of mitochondrial proteins and changes in mitochondrial morphology (Rossignol et al. 2004). Furthermore, as uptake and conversion of galactose are slower compared to glucose, cells are forced to metabolize glutamine (glutaminolysis) during mitochondrial energy production in the absence of glucose (Wagner et al. 1991; Kase et al. 2013). This and the availability of pyruvate may also explain the enhanced OCRs found for cells cultivated in L-15 medium compared to values determined in PBS⁺⁺/Gal. Cells rely heavily on oxidative phosphorylation when cultured in Gal containing medium, they become more susceptible to drugs and toxins targeting the mitochondria. This is often exploited in studies which assess drug-induced mitochondrial dysfunction (Marroquin et al. 2007). As oxygen consumption is strongly dependent on metabolite composition of the medium, medium composition should be kept constant to provide a better comparison of OCRs of different cell lines.

4.10.3 INFLUENCE OF CELL SEEDING DENSITY ON OXYGEN CONSUMPTION

Oxygen consumption rates of two different kidney cell lines NRK and MDCK II were analyzed with respect to the initial cell seeding density, while OCRs of two additional cell lines (BAEC, U-373 MG) were monitored for a seeding density of 1.5×10^5 cells cm⁻² for comparison. The respective oxygen consumption rates of the different cell lines are summarized in **Tab. 4.10**. As expected OCRs

increased with increasing cell seeding density. MDCK II cells consumed oxygen faster compared to NRK cells. BAEC cells seeded with the same density as U-373 MG cells exhibit 35 % lower oxygen consumption rates.

Tab. 4.10 Overview of oxygen consumption rates measured in this work and data reported in literature. OCR / pmol s^{-1} was converted into individual cellular OCR / $\text{amol s}^{-1} \text{cell}^{-1}$ by taking the cell seeding density and a growth area of 9.6 cm^2 into account. If possible, literature values were converted into OCR / $\text{amol s}^{-1} \text{cell}^{-1}$ for a better comparison with single cell OCRs determined in this work.

Cell type	Cell density / c cm^{-2}	OCR \pm SE / pmol s^{-1}	OCR \pm SE / $\text{amol s}^{-1} \text{cell}^{-1}$	Literature values OCR / $\text{amol s}^{-1} \text{cell}^{-1}$
MDCK II	1.5×10^4	1.28 ± 0.04	8.9 ± 0.3	20 (Guarino et al. 2004)
	2.5×10^4	2.9 ± 0.1	12.2 ± 0.5	1670 (Doerr et al. 2016)
	5.0×10^4	4.13 ± 0.08	8.6 ± 0.2	
	1.0×10^5	11.6 ± 0.2	12.1 ± 0.2	
	2.0×10^5	16.5 ± 0.4	8.6 ± 0.2	
NRK	1.5×10^4	1.61 ± 0.08	11.2 ± 0.5	40 $\text{pmol min}^{-1} \mu\text{g protein}^{-1}$
	2.5×10^4	2.10 ± 0.08	8.8 ± 0.3	(Oh et al. 2017)
	5.0×10^4	2.93 ± 0.08	6.1 ± 0.1	30 (Ruggiero et al. 2014)
	1.0×10^5	4.44 ± 0.04	4.62 ± 0.04	
	2.0×10^5	8.8 ± 0.1	4.58 ± 0.06	
BAEC	1.5×10^5	3.2 ± 0.2	2.2 ± 0.1	160 (Jones et al. 2008)
				17 (Motterlini et al. 1998)
U-373 MG	1.5×10^5	4.9 ± 0.1	3.43 ± 0.08	Not yet reported
U937	-	-	-	11.0 – 9.9 (Herst and Berridge 2007)
				5 (Guarino et al. 2004)
U-87	-	-	-	57 (Poteet et al. 2013)
A-172	-	-	-	27 (Poteet et al. 2013)

First, oxygen consumption of two kidney cell lines was monitored in dependence of on their individual seeding density. For a better comparison with literature, AOCR values obtained by linear fitting were used to calculate OCR values in pmol s^{-1} . Comparison of NRK and MDCK II cells showed a higher metabolic activity of MDCK II cells as summarized in **Tab. 4.10**. In contrast to NRK cells,

MDCK II cells reach low pO_2 values in the culture medium more quickly. Except for the lowest seeding density of $1.5 \times 10^4 \text{ c cm}^{-2}$, respiratory activity of MDCK II cells nearly doubles when compared with NRK cells inoculated at the same density. Besides, the calculated OCR of a single cell yields slightly higher values for MDCK II cells ranging from 8.6 to 12.2 $\text{amol s}^{-1} \text{ cell}^{-1}$ while single cell OCRs of NRK cells lie between 4.58 – 8.8 $\text{amol s}^{-1} \text{ cell}^{-1}$ except for the lowest seeding density. The fact that oxygen consumption rates increase with increasing cell density has also been shown for other cell lines. A linear relationship between the oxygen consumption rate and the cell density was for example obtained for HL60 cells. This was used as a calibration function to determine an unknown number of cells from the measured OCR (Guarino et al. 2004). Additionally, a nearly linear increase of the respiration rate in dependence on total cell number was obtained for pluripotent stem cells and fibroblasts (Zhang et al. 2012). The oxygen consumption rate of MDCK II cells has been described with a value of 1.25 $\text{fmol min}^{-1} \text{ cell}^{-1}$ (Guarino et al. 2004), which would correspond to 39.9 pmol s^{-1} for a cell density of $2.0 \times 10^5 \text{ cell cm}^{-2}$, a value similar to the OCR measured in this work. However, higher values of about 100 $\text{fmol min}^{-1} \text{ cell}^{-1}$ were also reported (Doerr et al. 2016). For NRK cells, literature studies report values of about 40 $\text{pmol min}^{-1} \mu\text{g protein}^{-1}$ (Oh et al. 2017) or values normalized to basal oxygen consumption without providing absolute values (Marine et al. 2014). This makes a comparison with data obtained in this work difficult or impossible. Another study focuses on the effect of a surplus of albumin and fatty acids on NRK cells, where a basal oxygen consumption rate of about 150 pmol min^{-1} for a cell number of 7.5×10^4 cells is reported (Ruggiero et al. 2014). This would yield slightly higher respiratory rates ranging from 63.9 – 4.8 pmol s^{-1} for 2.0×10^5 – $1.5 \times 10^4 \text{ c cm}^{-2}$, when compared to values obtained in this work. Perhaps different rates were obtained because of different cultivation conditions, as well as different passage numbers. It has been shown that OCRs of HUVEC cells change with increasing passage number (Carlisle et al. 2002).

An OCR of $(3.2 \pm 0.2) \text{ pmol s}^{-1}$ was determined for BAEC cells seeded with a density of 1.5×10^5 cells cm^{-2} in this work yielding a single cell OCR of $(2.2 \pm 0.1) \text{ amol s}^{-1} \text{ cell}^{-1}$. This value is lower compared to values found in literature for endothelial cells from the blood vessels. Here, significantly higher values ranging between 160 pmol s^{-1} and 17 pmol s^{-1} are reported for a total number of 10^6 BAEC cells (Motterlini et al. 1998; Jones et al. 2008) and 50 pmol s^{-1} for HUVEC cells for a total cell number of 10^6 cells. However, these data were obtained using cells in suspension cultures which makes a comparison with detection of pO_2 beneath adherent cells difficult. Newer studies conducted with adherent BAEC cells using using the seahorse XF extracellular flux analyzer

suggest an OCR of $(3.1 \pm 0.2) \text{ pmol s}^{-1}$ (Kajihara et al. 2017) which is highly consistent to the value determined using the VisiSens TD mic system.

Results for U-373 MG cells seeded with the same cell density than BAECs yielded an OCR of $(4.9 \pm 0.1) \text{ pmol s}^{-1}$. So far, no data is found in literature reporting on oxygen consumption of U-373 MG cells. However, other glioblastoma cell lines have been characterized regarding their respiratory activity. OCRs between 11.0 and 9.9 pmol s^{-1} have been determined for U-937 cells inoculated in a total number of 10^6 cells (Herst and Berridge 2007). Other groups report an OCR value of $0.3 \text{ fmol min}^{-1} \text{ cell}^{-1}$, which would correspond to a value of 7.2 pmol s^{-1} for a number of 1.5×10^5 cells (Guarino et al. 2004). Moreover, cellular respiration rates of untransformed astrocytes resulted in a value of about 0.8 pmol s^{-1} , while glioblastoma U-87 cells exhibited slightly higher rates of about 1.7 pmol s^{-1} (Poteet et al. 2013).

In general, the comparison of OCRs of one cell line is difficult, as methods used in literature vary from Clark type oxygen electrode to EPR and luminescence quenching, while cells are either studied as adherent cultures or in suspension (Wagner et al. 2011). Furthermore, one must keep in mind that medium composition often varies, which is a detrimental factor for oxygen consumption as explained in **chapter 4.10.2**. This is especially important when the concentration of carbohydrates such as glucose and galactose and non-carbohydrate compounds such as pyruvate and glutamine vary (Zhdanov et al. 2014). Moreover, many studies report oxygen consumption rates normalized to the protein content. For example oxygen consumption of MDCK cells is reported with a value of $13.0 \pm 0.8 \text{ nmol O}_2 \text{ min}^{-1} \text{ mg cell protein}^{-1}$ (Lynch and Balaban 1987). However, lack of information on protein content of the cells under study complicates the comparison with values obtained for one cell population.

4.10.4 INFLUENCE OF pH ON OXYGEN CONSUMPTION

When confluent NRK cells were monitored in L-15 medium with adjusted extracellular pH using the novel VisiSens TD mic system, it was shown that an acidic extracellular pH of 6.4 decreased the cellular oxygen consumption rate by about 37 % compared to cells cultivated under standard conditions at pH 7.2. Oxygen consumption further increased when the extracellular pH was adjusted to a slightly alkaline value of 7.8.

The effect of variations of extracellular pH on oxygen consumption was also investigated by the group of J. P. Urban. They found in their experiments that oxygen consumption of bovine disc cells

was dependent on extracellular pH. While oxygen consumption rates were highest at a slightly alkaline pH, they decreased when the cells were cultivated at physiological pH. Oxygen consumption was lowest when buffers with an extracellular pH of 6.2 were applied. Moreover, they found an increased glycolytic rate and monosaccharide utilization rate with increasing pH, which they stated could also positively influence oxygen consumption (Bibby et al. 2005). This finding is supported by studies which have shown that alkalization increases nutrient uptake as well as metabolic rates of both glycolysis and glutaminolysis (Ozturk and Palsson 1991). Thus, the levels of metabolites which enter citric acid cycle increases. Furthermore, mitochondrial membrane potential was higher in cells cultivated at alkaline pH which fits to higher ATP levels obtained for a high extracellular pH. This indicates that both elevated citric acid cycle and increased proton motive force lead to increased oxidative phosphorylation rates (Ippolito et al. 2016). This effect may be even more pronounced when cells are cultivated in galactose containing medium, as it additionally shifts metabolism towards oxidative phosphorylation as explained in **chapter 4.10.2**.

4.10.5 INFLUENCE OF DRUGS AND TOXINS ON OXYGEN CONSUMPTION

The VisiSens TD mic system was used to monitor the effect of drugs and toxins on the cellular oxygen consumption. Therefore, cells were treated with C-dots or CdCl₂ to mimic the effect of toxins, and with malonoben and antimycin A to directly influence oxidative phosphorylation. Results showed, that the cellular respiration was efficiently uncoupled by 100 nM malonoben, yielding a 3.5-fold higher AOOCR compared to control conditions. A complete blockage of oxidative phosphorylation was accomplished by using 2 μM antimycin A.

So far, malonoben is mainly used to uncouple isolated mitochondria (Terada 1981) and to study its influence on the mitochondrial membrane potential. Data found in literature studies reports that nanomolar concentrations of Mal lead to the dissipation of mitochondrial membrane potential (Kawamata et al. 2010). Although no studies are available reporting on the effect of malonoben on oxygen consumption of monolayer cells, literature reports on studies using uncoupling agents such as DNP (2,4-dinitrophenol), FCCP (carbonyl cyanide p-trifluoromethoxyphenylhydrazone) or CCCP (carbonyl cyanide 3-chlorophenylhydrazone). These compounds, including malonoben are lipophilic weak acids that possess the ability to shuttle protons across the inner mitochondrial membrane. The release of protons into the slightly more alkaline mitochondrial matrix leads to the breakdown of both, the proton gradient and the membrane potential by short-circuiting which are the driving

force of ATP-synthesis. To compensate the low gradient, cells react by increasing their oxygen consumption rate (Wallace and Starkov 2000). DNP and FCCP were found to increase the respiration of adherent, endothelial umbilical vein cells up to 3.5-fold (Steinlechner-Maran et al. 1996). FCCP has been used to study oxygen consumption rates in fibroblasts and enterocytes. It has been found that uncoupling with 1 μM FCCP resulted in an increase of oxygen consumption of these epithelial cells about a factor 1.75 (Tan et al. 2015). Lower concentrations still increased OCRs of fibroblasts about 100 % compared to basal oxygen consumption (Zhang et al. 2012). Imaging intracellular pO_2 in mouse embryonic fibroblasts (MEF) cells with nanoparticle based sensors showed that 1 μM FCCP effectively uncouples oxidative phosphorylation using fluorescent lifetime imaging (Kondrashina et al. 2012).

Blocking of cellular respiration of MDCK II cells was successfully accomplished using the antibiotic antimycin A. In total, addition of 2 μM Ant A results in a complete reoxygenation and stable pO_2 levels around 150 torr as cellular oxygen consumption is completely suppressed. As already mentioned in **chapter 4.7**, addition of Ant A in the micromolar range leads to a very effective reduction of cellular respiration rates due to the complete inhibition of complex III, resulting in a breakdown of mitochondrial electron transport (Campo et al. 1992). This effect makes Ant A one of the most commonly used compounds to study the inhibition of oxygen consumption of cells and tissues. In literature, the blocking effect of Ant A is also reported for MDCK cells, where micromolar concentrations resulted in a complete inhibition of oxidative phosphorylation (Lynch and Balaban 1987). Studies conducted with intracellularly located, phosphorescence lifetime-based macromolecular probes showed that 10 μM Ant A resulted in a complete reoxygenation of MEF cells due to the efficient blocking of cellular respiration. This was observed as a decreased lifetime of the sensor dye due to quenching by molecular oxygen (Kondrashina et al. 2012; Koren et al. 2012). The immediate effect of Ant A addition on cellular respiration that was observed in studies conducted in this work is also supported by studies found in literature. Adherent cells incubated with Ant A and galactose, which is a metabolite promoting oxidative phosphorylation as mentioned in **chapter 4.10.2**, decrease their oxygen consumption within 15 min to values close to zero (Ashton et al. 2016).

Additionally, the effect of C-dots on the metabolic activity of NRK cells was studied using the novel ratiometric imaging system. It has been found that both C-dot concentrations applied in this work (1.0 and 2.5 mg ml^{-1}) led to a decrease of oxygen consumption rates compared to control conditions. This data is consistent with results from M. Lemberger, who determined an EC_{50} (effective

concentration) value of 1.1 mg ml^{-1} for NRK cells using the PrestoBlue® assay (Lemberger 2016). NRK cells incubated with a concentration higher than the EC_{50} value (2.5 mg ml^{-1}) exhibit an about 60 % lower AOCR compared to control conditions. Light microscopic images show that while cell morphology is still unaffected 5 h after incubation, cells are dead after the oxygen measurement is finished. This was also found in impedimetric measurements conducted by M. Lemberger, where cell death sets in about 6 – 8 h after C-dot addition resulting in a decrease in impedance. However, the oxygen consumption of NRK cells is still impaired when cells are incubated with a concentration of 1.0 mg ml^{-1} resulting in an about 50 % lower AOCR value compared to control conditions. Here, oxygen measurements yield additional information to the ECIS data recorded by M. Lemberger, as the incubation with a critical concentration of 1.0 mg ml^{-1} C-dots did not induce cell death. However, although microscopic images show no altered cell morphology after 5 h incubation with C-dots, oxygen readings indicate that cellular metabolic activity is already impaired. Impairment of cellular metabolism by C-dots is also described in literature, where C-dots synthesized from citric acid and urea negatively influence the metabolic rates of ST-cells in concentrations higher than 0.4 mg ml^{-1} (Zholobak et al. 2016). Furthermore, a cell line dependent decrease of metabolic activity was seen for C-dots synthesized from ginger. While metabolic activity of HepG2 cells was significantly reduced by about 80 % upon incubation with 1.4 mg ml^{-1} C-dots, metabolism of MDA-MB-231 cells was not affected up to concentration of 2.8 mg ml^{-1} (Li et al. 2014). However, these studies rely on measurement of metabolic activity by MTT or Alamar Blue Assays. Up to now, no studies have been published reporting on the impact of C-dots on cellular respiration as indicator of metabolic activity. Furthermore, studies conducted with NRK cells exposed to different concentrations of $CdCl_2$ for 2 h revealed a concentration dependent decrease of cellular oxygen consumption rates with increasing concentrations of $CdCl_2$. Incubation with $100 \text{ } \mu\text{M}$ $CdCl_2$ led to a decrease of the AOCR by about 21 % with part of the cells being dead after the measurement. Treatment with a higher dose of $300 \text{ } \mu\text{M}$ $CdCl_2$ drastically decreased the AOCR by about 77 % compared to control conditions within the first hours of the measurement and resulted in a subsequent phase of reoxygenation, probably caused by rapid cell death and medium convection. So far, no data is known in literature that reports on the effects of $CdCl_2$ on cellular respiration. $CdCl_2$ is known to be highly nephrotoxic by inducing cell death, DNA damage and by suppressing proliferation. Exposure to $CdCl_2$ quickly leads to apoptosis when applied at lower dosage, while high doses are known to effectively induce necrosis (Mao et al. 2007). ECIS® studies conducted by J. Stolwijk showed an acute toxicity setting in 1 – 2 h after incubation of NRK cells with concentrations of $300 \text{ } \mu\text{M}$ $CdCl_2$ and above which is comparable with

the results obtained in this work. Incubation with 100 μM CdCl_2 resulted in a delayed decrease of the impedance signal due to the delayed incidence of cell death. In this study, an EC_{50} value of 60 – 100 μM was found by dose-response analysis (Stolwijk et al. 2012). Additionally, *in vitro* nephrotoxicity was studied by incubation of kidney cells with low doses of CdCl_2 . Here, analysis by morphological appearance and cytotoxicity assays revealed that low concentrations of 10 μM induced cell death by apoptosis after 24 h of incubation with CdCl_2 (Tokumoto et al. 2011; L'Azou et al. 2014).

Therefore, it would be interesting to perform oxygen measurements with a higher number of different concentrations in order to obtain EC_{50} values for CdCl_2 and C-dots by measuring changes in respiratory activity. However, due to the low throughput of the system, screening more than two different concentrations was not practicable.

4.11 OUTLOOK

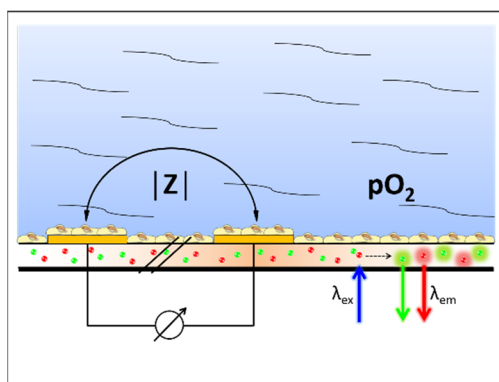
The VisiSens TD mic system allows imaging the temporal and spatial changes in oxygen consumption of adherent cell monolayers online. The system is based on the ratiometric readout of planar, biocompatible, highly photostable oxygen sensor foils which are used as growth substrates for adherent cells. This allows the determination of pO_2 directly beneath the cells. The system has been applied successfully in proof of principle experiments to determine the oxygen consumption rates of different cell lines and the effects of drugs and toxins on cellular respiration. Additionally, the set-up was used to image the metabolic activity of a small cell patch residing on the sensor foil.

Up to now, the VisiSens TD mic system has a low throughput which allows measuring only one sample in one run. This is of course disadvantageous, especially when studying the effect of multiple parameters and different compound concentrations, because completing one measurement series is highly time-consuming. Regarding this kind of problem, it would be better to enhance the throughput at the expense of the imaging resolution. The field of view could for example be enlarged by using a camera with a wide field objective. This would allow online monitoring of one multi-well plate in one run. Reliable data could be produced when multiple concentrations at the same time on the same cell population could be analyzed. Thus, similar to ECIS[®] or SPR (surface plasmon resonance) analysis, monitoring of cell respiration could enable a non-invasive, online determination of EC_{50} values. A similar approach has been used by the group around J. B. Pitner, who used 96-well plates coated with an oxygen sensitive dye. They used the intensity changes of

the oxygen sensor dye as indicator for metabolic activity of different cell lines exposed to anticancer drugs to calculate IC_{50} values and compared them with the commonly used end-point based MTT assay (Wodnicka et al. 2000).

Furthermore, replacing the opaque, ratiometric oxygen sensor foils by transparent, lifetime based foils would make them accessible to standard transmission light microscopy and reduce errors by effects such as light scattering (Quaranta et al. 2012). This would allow the control of cell morphology and adhesion as well as the colocalization of cellular structures and oxygen gradients e.g. when monitoring a cell patch. Moreover, the system could be easily adapted from sensing pO_2 to pH by using a suitable illumination source, emission filters and pH sensitive foils as growth substrates for adherent cells.

5 ECIS-O₂ – A DUAL TRANSDUCER FOR ELECTRICAL AND LUMINESCENT READOUT



Simultaneous recording of two or more parameters is a powerful approach that allows obtaining multiple information about complex living biological samples in one measurement. For both, impedimetric and optical sensing, numerous dual sensors have been developed. To measure photosynthetic activity in cyanobacteria, a double optical thin film sensor for the ratiometric determination of pH and

pO₂ has been developed (Lu et al. 2011). Metabolic activity of two different mammalian cell lines was addressed with multi-well plates with integrated pH and oxygen sensor spots over several days (Naciri et al. 2008). Furthermore, impedimetric analysis has been combined with SPR to study morphology changes and dynamic mass redistribution in adherent kidney cells (Michaelis et al. 2013). Although a multiparametric chip platform with incorporated interdigitated electrodes for impedimetric monitoring as well as electrodes for electrochemical determination of pH and oxygen in cell culture was developed (Wiest et al. 2005), no multiparametric sensor is known for optical detection of oxygen and simultaneous recording of impedance.

In this project, impedimetric and optical readout concepts were combined on one sensor substrate in order to gain multiparametric information about cell behavior and the cellular response upon exposure to different stimuli. The planar sensor consists of an oxygen sensitive commercial sensor foil (RPSu4) which simultaneously serves as support for coplanar gold film electrodes which have been prepared on top of the sensor foil. The dual sensor allows simultaneous, non-invasive online recording of impedance and pO₂. A commercial oxygen imaging system (VisiSens A1) was used for the ratiometric determination of oxygen content. The dual sensor is biocompatible and provides information about changes in cell morphology and electrode coverage via impedance measurements, while changes in oxygen concentration report on the cellular oxygen consumption rate. The sensor was characterized regarding biocompatibility and signal stability and used to investigate cell adhesion and the influence of uncouplers and blockers of oxidative phosphorylation on adherent cells.

5.1 CHARACTERIZATION OF THE DUAL SENSOR SET-UP

5.1.1 1ST GENERATION SENSOR LAYOUT

The first-generation dual sensor layout is depicted in **Fig. 5.1, A**. The planar sensor consists of a standard microscope slide, ratiometric oxygen sensor foil (RPSu4) and 100 nm thin gold film electrodes that were sputtered on top of the sensor foil (for fabrication process see **chapter 3.4.3.1**). As cultivation chamber, a self-adhesive microchannel (ibidi sticky-Slide I^{0.4}luer) was applied. The self-adhesive microchannel has a height of 450 μm , a channel volume of 113 μl and a growth area of 2.5 cm^2 . The four linear gold film electrode pairs with an average electrode area of about 2 mm^2 and an interelectrode gap of 2 mm, are located inside the microchannel. Instead of insulating photoresist, the adhesive part of the sticky-Slide is used to cover the feed lines. The dual sensor is electrically contacted by eight contact pads. MDCK II cells were cultivated under static conditions according to the manufacturer's recommendations with a cell density of 1.0×10^5 cells cm^{-2} inside the microchannel. Oxygen consumption recordings of cells cultivated in L-15 medium under static conditions were started 24 h after seeding, taking images every 5 min using the VisiSens A1 system. The medium was exchanged manually after the start of the oxygen measurement at $t = 0$ h, $t = 2.58$ h and $t = 5.25$ h by slowly adding 1 ml fresh L-15 medium to the channel using a syringe. Oxygen consumption profiles of MDCK II cells cultivated inside the microchannel, recorded in three individual measurements, are shown in **Fig. 5.1, B**. Upon addition of fresh L-15 medium, $p\text{O}_2$ underneath the epithelial cell layer increases to normoxic values of around 150 torr. As cells in the channel consume oxygen, a 50 % decrease of $p\text{O}_2$ is observed within (0.3 ± 0.1) h after addition of fresh L-15 medium. $p\text{O}_2$ rapidly drops to hypoxic values below 10 torr within (1.5 ± 0.2) h after medium addition. Changes in 2D spatial oxygen distribution are also depicted as false color images in **Fig. 5.1, C**. The 2D oxygen images were recorded by adjusting the field of view of the Visisens A1 system to cover the whole channel width. This bigger field of view leads to a decrease in image resolution. Additionally, the epi-illumination of the sample by several individual LEDs arranged in a circular geometry inside the camera system leads to a partial reflection of the excitation light by the objective glass slide. This mirror effect is visible as circular shaped area in the 2D oxygen distribution image. Apart from the variances created by this epi-illumination, a homogeneous distribution of oxygen inside the microchannel has been observed that rapidly drops to levels of deoxygenated solutions. Addition of medium at 0 h, 2.58 h and 5.25 h leads to a complete and homogeneous

reoxygenation of the channel solution to normoxic values. The complete time series of one typical oxygen measurement inside the microchannel is available in **Video 11.2**.

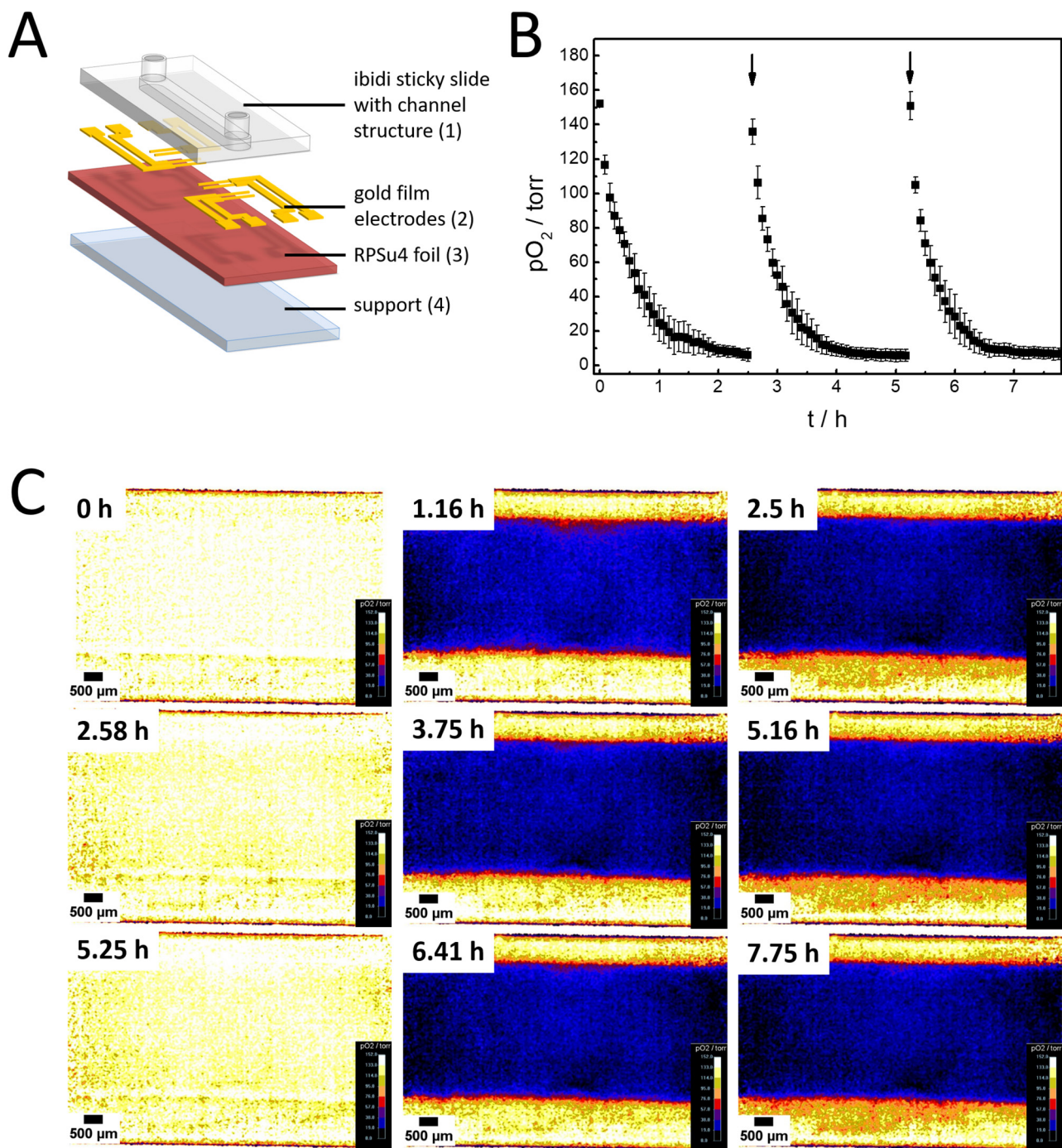


Fig. 5.1 (A) Schematic view illustrating different components of the 1st generation dual sensor layout. The chip is composed of a standard microscope slide as support (4), a RPSu4 oxygen sensor foil (3), thin Au film electrodes (2) and a self-adhesive microchannel ((1) ibidi sticky-Slide I^{0.4}uer). (B) Decrease of oxygen partial pressure as a function of time for MDCK II cells cultivated under static conditions in a microchannel with a height of 450 μ m. As indicated by the arrows, fresh L-15 medium was pumped through the channel after 0 h, 2.58 h and 5.25 h causing a return of solution pO_2 from hypoxic to normoxic values. Mean \pm SE, $n = 3$. (C) Typical false color oxygen images showing changes in oxygenation as a function of time. $T = 37$ $^{\circ}$ C.

According to the manufacturer's instructions, the self-adhesive channel allows static cultivation of cells inside the channel. However, when the channel is applied on the oxygen sensor foil, that possesses an oxygen impermeable bottom polyester support layer, oxygen supply is insufficient and cells quickly become hypoxic as shown by the ratiometric oxygen measurements. This also influences viability and proliferation of the cultivated cells. Under static conditions cells did not grow to confluence – which is a necessary requirement for stable impedimetric measurements (for fluorescence micrographs, see **Fig. 11.14**). Therefore, the dual sensor layout was changed to a layout containing an open cultivation chamber to meet the requirements necessary for the dual measurement and to provide sufficient oxygen supply.

5.1.2 2ND GENERATION SENSOR LAYOUT

The 2nd generation sensor layout is illustrated in **Fig. 5.2, A**. Here, the microchannel of the 1st layout is replaced by an open PDMS cultivation chamber. Instead of insulating photoresist or the adhesive sticky-Slide, the bonded PDMS chamber is used to cover the feed lines. The PDMS cultivation chamber and to provide a growth area of 2.5 cm² and a volume of 1 ml. A lid is used to cover hosting the chamber to prevent medium evaporation. The dual sensor is fabricated as described in **chapter 3.4.3.1** with a completed version shown in **Fig. 5.2, B**. The ECIS-O₂ chip fits into a specified holder which allows optical access to the oxygen sensor foils as described in **chapter 3.4.3.1**. First, cell adhesion and viability were studied. **Fig. 5.2, C** shows fluorescence images of MDCK II cells stained with the live-dead stains CaAM and EthD-1 48 h after confluent inoculation. Cells adhere to both, the oxygen sensor foil (**Fig. 5.2, C, II**) and the gold film electrodes (**Fig. 5.2, C, III**). Compared to control cells grown on a standard petri dish (**Fig. 5.2, C, I**) cells cultivated on the dual sensor exhibit similar viability as indicated by the green fluorescent signal of CaAM. Cells cultivated in the open chamber system form a confluent monolayer with characteristic cobble-stone-like morphology and blisters. Thus, the second layout was used for the dual measurement of impedance and oxygen levels, as presented in the following chapters.

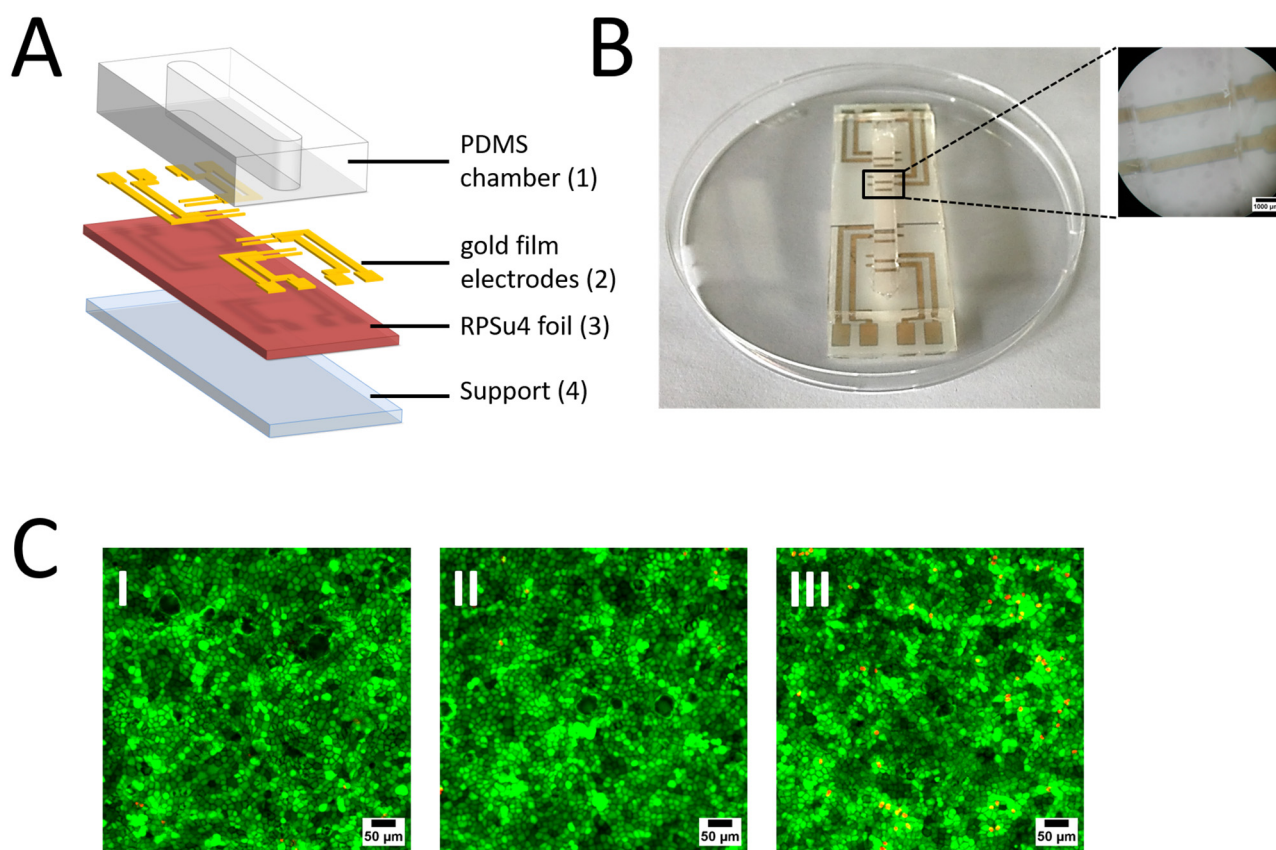


Fig. 5.2 Final layout for the dual measurement of impedance and pO₂. (A) Schematic view illustrating the different components. The chip is composed of a PDMS cultivation chamber (1), 100 nm thin Au film electrodes (2), a RPSu4 oxygen sensor foil (3) and a microscope slide as support (4). (B) Completed ECIS-O₂ chip. The magnified stereomicroscopic image shows one pair of electrodes. (C) Live-dead staining of MDCK II cells seeded to confluence ($4.5 \times 10^5 \text{ c cm}^{-2}$) on a standard cell culture petri dish (I) or in the ECIS-O₂ chip, where cells grow on the RPSu4 oxygen sensor foil (II) and on the gold film electrodes (III). Green fluorescence indicates live cells stained with $2 \mu\text{M}$ CaAM and red fluorescence shows dead cells stained with $4 \mu\text{M}$ EthD-1.

5.1.3 ELECTRODE CHARACTERIZATION AND BASELINE MEASUREMENTS

The novel ECIS-O₂ chip was analyzed impedimetrically. Therefore, frequency spectra of cell-free electrodes and of electrodes confluent covered with MDCK II cells were recorded. Cell-covered spectra were recorded 24 h after seeding to guarantee a fully established cell monolayer formation and adhesion. Spectra were corrected for the ohmic resistance of the feed lines as described in **chapter 3.4.3.4** to enhance sensitivity. Spectral correction led to an increase of signal difference between cell-free and cell-covered electrodes of a factor of about 2.2. **Fig. 5.3, A – C** shows frequency-dependent changes in impedance $|Z|$, resistance R and capacitance C of cell-free (■) and cell-covered (●) electrodes. The impedance of the system significantly increases between $10^2 - 10^4$ Hz when a confluent cell layer covers the electrodes. A plateau value of about 5500Ω is reached at $100 - 400$ Hz before the impedance of cell-covered electrodes decreases with

frequency. The resistance for cell-covered electrodes exceeds the resistance of the cell-free electrode in the range of $10^1 - 10^4$ Hz with a plateau value of about 6000Ω between $10^1 - 10^2$ Hz. Capacitance spectra show a decrease in C from $10^2 - 10^5$ Hz for cell-covered electrodes reaching an absolute value of about 50 nF in the plateau region between $10^3 - 10^4$ Hz. Normalization of impedance, resistance and capacitance spectra was used to determine the most sensitive frequencies for each parameter, as illustrated in **Fig. 5.3, D – F**. A peak maximum at around 1 kHz was found for $|Z|$, while the most sensitive frequency for resistance monitoring of MDCK II cells lies at 0.3 kHz. Normalization of capacitance data reveals the most sensitive frequency at approximately 1.6 kHz.

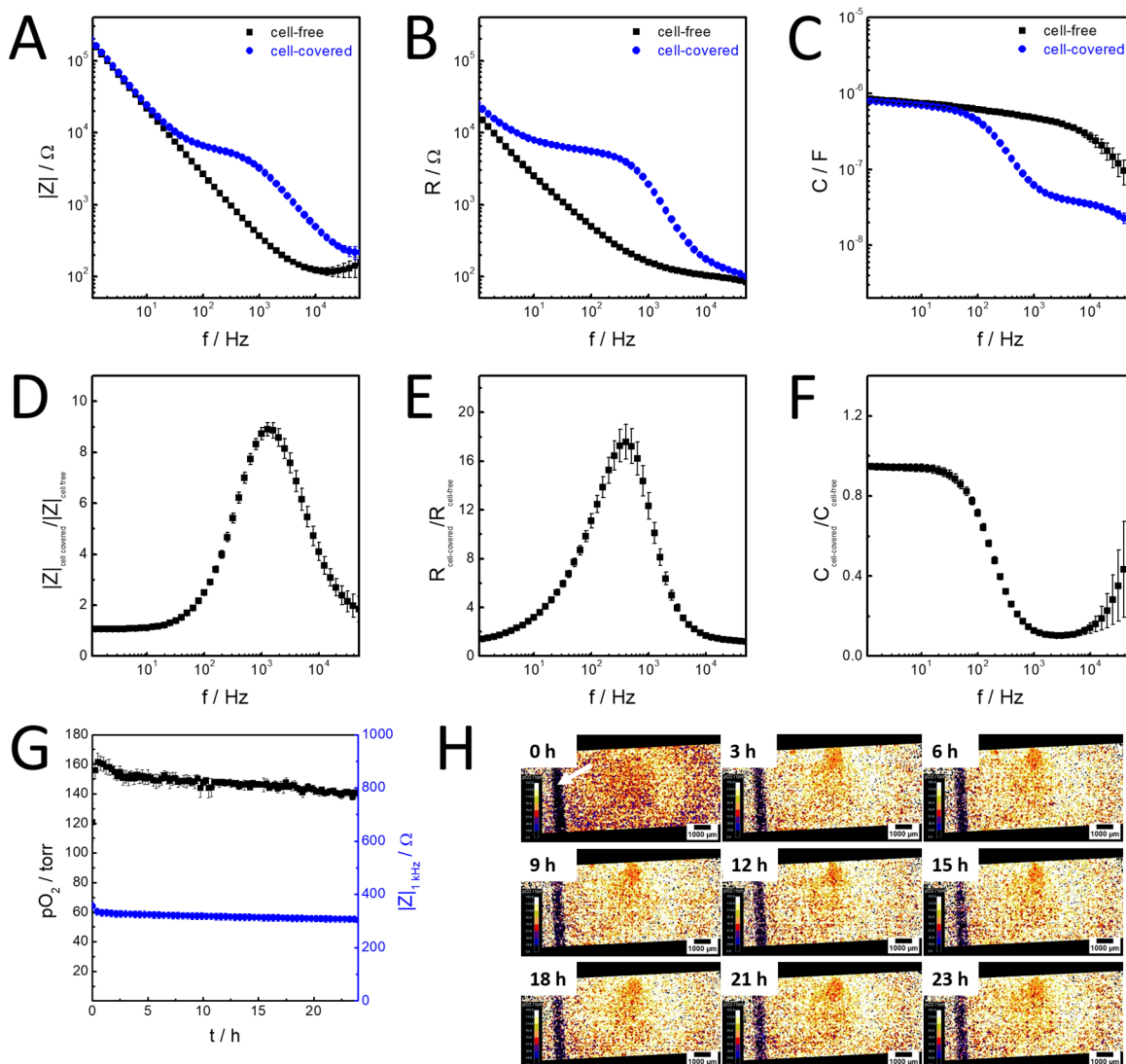


Fig. 5.3 (A – F) Typical spectra of frequency-dependent parameters of the ECIS-O₂ chip. (A) Impedance $|Z|$, (B) resistance R and (C) capacitance C for cell-free (■) and cell-covered (●) electrodes. Normalized spectra of (A), (B) and (C) show sensitive frequencies (peak maxima/minimum) for (D) impedance at 1 kHz, (E) resistance at 0.3 kHz and (F) capacitance at 1.6 kHz. Mean \pm SE; $n = 4$. Monitoring impedance and pO_2 in dual mode for a cell-free ECIS-O₂ chip in L-15 medium. (G) Impedance and corresponding oxygen levels determined by dual measurements over a period of 24 h conducted at $T = 37^\circ C$. Mean \pm SE; $n = 3$. (H) Typical false color images depicting a stable 2D spatial oxygen distribution in the ECIS-O₂ chip. The white arrow indicates the position of one linear gold film electrode. For better visualization of the culture well, the edges of the PDMS chamber were outlined in black using the NIH ImageJ software.

Dual online monitoring with the ECIS-O₂ chip was performed in L-15 medium under cell-free conditions for a period of 24 h to check for stability of the electrochemical signal and photobleaching of the oxygen sensor film. Oxygen partial pressure was determined every 15 min with camera settings similar to those used in cell experiments. pO₂ beneath gold film electrodes could not be determined, probably due to low oxygen permeability of the gold-films. Therefore, ROIs for determination of pO₂ were chosen next to the electrode structures. Results of 3 independent measurements are depicted in **Fig. 5.3, G** which shows absolute values of impedance at 1 kHz (●) and oxygen partial pressure (■) for a cell-free chip in L-15 medium over a period of 24 h. pO₂ fluctuates around values of air saturated solutions with a maximum value of (162 ± 6) torr measured at t = 0.5 h. A total signal change of about 10 % from an initial value of (156 ± 5) torr to (141 ± 1) torr after 24 h is observed. The impedance changes from an initial value of (340 ± 10) Ω to a final value of (300 ± 10) Ω after 24 h. Although the chip is covered with a lid, this decrease can be explained by evaporation of water over 24 h of monitoring, which leads to an increase of ions in the bulk phase medium, resulting in a decrease in the total impedance. **Fig. 5.3, H** shows typical false color images of the spatial oxygen distribution inside a cell-free culture well recorded within one dual measurement run. As mentioned above, due to low permeability of gold, imaging of pO₂ below the gold film electrodes yields constant low and artificial values, which do not allow a simultaneous readout of impedance and pO₂ on the electrodes but requires the spatial separation of the two readout locations. In total, 2D spatial distribution of oxygen partial pressure does not significantly change over 24 h of the measurement. However, compared to the novel imaging system VisiSens TD mic, 2D images have a poorer spatial resolution with additional circular artifacts caused by the circular excitation source of the camera system, as already shown in **chapter 5.1.1**.

5.2 MONITORING OF CELL ADHESION

The dual sensor chip was used for online monitoring of cell adhesion. Thus, impedimetric and luminescent monitoring was started immediately after inoculation of MDCK II cells in L-15 medium at a density of $4.5 \times 10^5 \text{ c cm}^{-2}$. Oxygen images were recorded every 15 min using the VisiSens A1 system. Results of four independent experiments measured with the dual ECIS-O₂ chip are displayed in **Fig. 5.4**. Changes in impedance at a monitoring frequency of 1 kHz are shown in **Fig. 5.4, A**. Shortly after cell inoculation at time zero, the impedance amounts to values of a cell-free electrode of about 400 Ω . $|Z|$ starts to increase about 8.5 h after inoculation reaching half-maximum signal change within about 13.9 h after cell seeding. The impedance reaches stable values at $t = 22.5$ h with a final value of $(4100 \pm 500) \Omega$ within 24 h after inoculation. The corresponding time course of the resistance at 0.3 kHz is shown in **Fig. 5.4, B**. The resistance remains at its starting value of $(200 \pm 20) \Omega$ within the first 6 h of the measurement before reaching the half-maximum signal change at 14.6 h. R reaches a final value of $(4900 \pm 600) \Omega$ at $t = 24$ h. Additionally, cell adhesion and spreading on the linear gold film electrodes can be analyzed by monitoring changes in capacitance at 1.6 kHz as shown in **Fig. 5.4, C**. The capacitance remains at its starting levels of (500 ± 20) nF for about 5 h and decreases as MDCK II cells start to attach and spread on the electrode surface, forming establishing a confluent monolayer with time. The capacitance decreases within 10.5 h to about 50 % of the initial value and reaches (70 ± 9) nF after 24 h of the measurement. In contrast to impedance/capacitance data, which exhibit a delayed increase/decrease of the signal, oxygen partial pressure decreases more than 50 % from its initial value of (153 ± 5) torr to (74 ± 2) torr within 2.75 h, simply because the inoculated, metabolically active cells reside close to the surface. Stable values are reached within 10 h, as shown in the time-dependent oxygen profile displayed in **Fig. 5.4, D**. Oxygen consumption rate at equilibrium was determined using eq. 3.2, yielding a value of $(20.8 \pm 0.3) \text{ pmol s}^{-1}$. This is in a similar range to OCR values determined for MDCK II cells of the same cell density as described in **chapter 4.2**. Changes in the spatial oxygen distribution within the ECIS-O₂ chip after cell seeding for one typical measurement are highlighted in **Fig. 5.4, E**. Fast deoxygenation due to active cell metabolism is seen in the heterogeneous 2D spatial oxygen distribution within 3 h after cell inoculation. Areas of low pO₂ increase in size within 9 – 12 h after seeding, reaching a homogeneous distribution of pO₂ inside the culture well till the end of the measurement ($t = 24$ h).

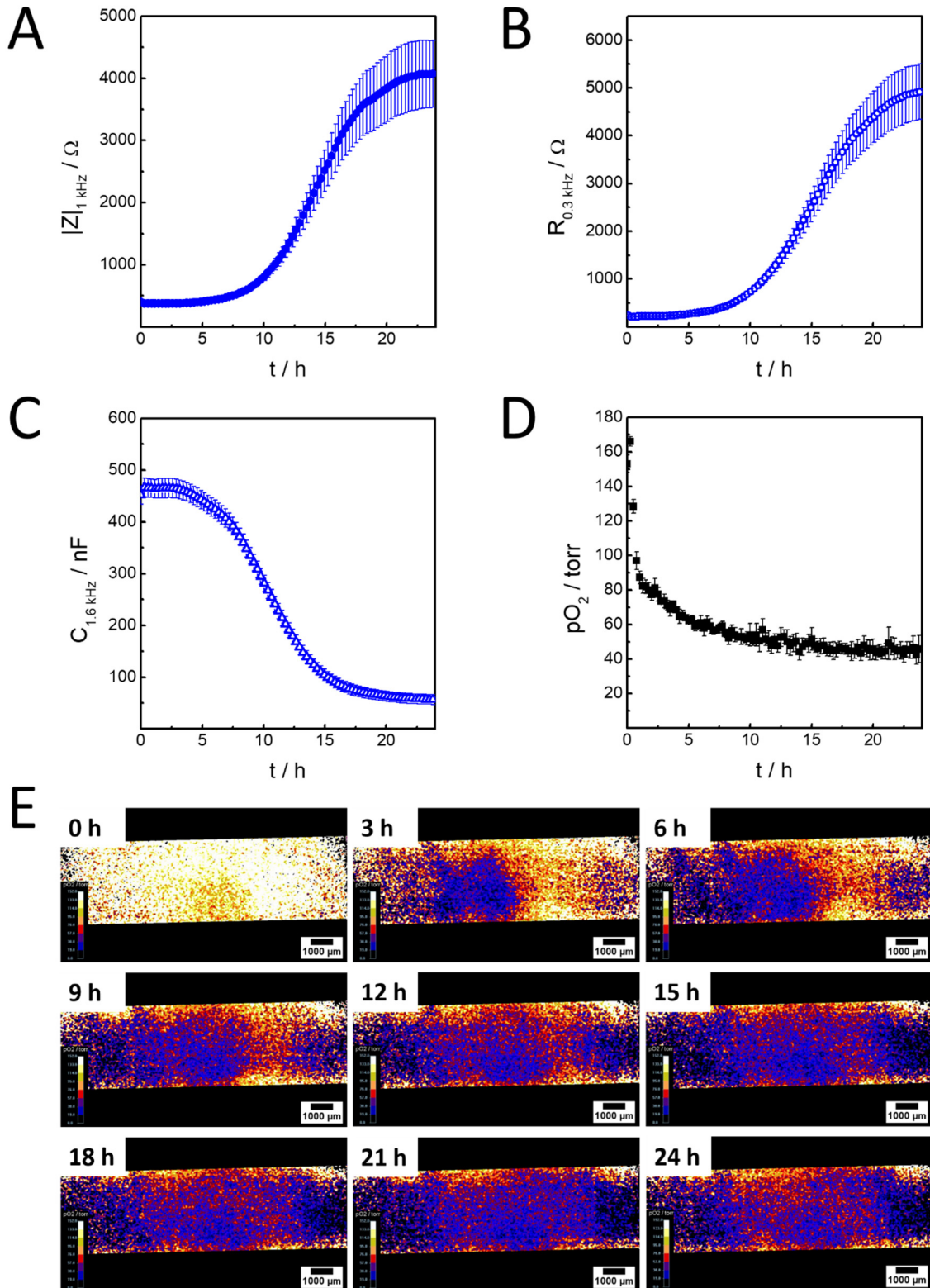


Fig. 5.4 Monitoring of adhesion of MDCK II cells inoculated with a density of $4.5 \times 10^5 \text{ c cm}^{-2}$ using the dual ECIS- O_2 sensor. Cells were inoculated at $t = 0$ h. (A) Changes in impedance monitored at 1 kHz as a function of time, (B) corresponding changes in resistance at 0.3 kHz and (C) capacitance at 1.6 kHz. Decrease of oxygen partial pressure due to cell respiration. Mean \pm SE; $n = 4$. (D) Typical false color oxygen distribution maps illustrating the decrease of $p\text{O}_2$ due to cellular oxygen consumption as a function of time. Areas outside the culture well were outlined in black using the NIH ImageJ software for better visualization. $T = 37^\circ \text{C}$.

5.3 MONITORING OF DRUG EXPOSURE

Similar to studies presented in **chapter 4.7**, the dual impedimetric and luminescent readout was used for online monitoring of the influence of drugs, such as malonoben and antimycin A, on confluent layers of adherent MDCK II cells.

5.3.1 INFLUENCE OF UNCOUPLERS OF OXIDATIVE PHOSPHORYLATION

The ECIS-O₂ sensor was used to monitor the effect of malonoben, an uncoupler of oxidative phosphorylation, on adherent cells. Therefore, MDCK II cells were grown to confluence in the ECIS-O₂ chip as described in **chapter 3.4.3.3**. Cellular oxygen consumption and impedance was recorded in L-15 medium. Oxygen images were recorded every 15 min. The time course of impedance (1 kHz) and pO₂ is shown in **Fig. 5.5, A**. First, baseline impedance and pO₂ values were recorded in L-15 medium. pO₂ decreases due to cellular oxygen consumption to values below 20 torr within about 0.75 h after starting the measurement (**Fig. 5.5, A, ■**), while impedance signal decreases about 10 % from an initial value of (2800 ± 300) Ω to (2500 ± 300) Ω after 5 h, probably triggered by the change from culture medium to L-15 medium (**Fig. 5.5, A, ●**). After 5 h, 1 ml fresh L-15 medium containing 100 nM malonoben (Mal) was added to the chip, as marked in **Fig. 5.5, A, arrow a**. Medium addition leads to an immediate reoxygenation to a value of (124 ± 5) torr. Within 0.25 h pO₂ decreases to values below 20 torr due to the increased oxygen consumption caused by the uncoupling effect of Mal. Addition of Mal does not lead to changes in |Z| except for a slight increase probably caused by medium exchange, reaching a value of (2400 ± 300) Ω after 10.75 h. This data indicates that uncoupling of oxidative phosphorylation does not seem to have an immediate negative effect on cell viability. After 10.75 h, the medium was exchanged to 1 ml L-15 medium containing 0.3 % (w/v) saponin, as indicated by arrow b in **Fig. 5.5, A**. Saponin permeabilizes the cell membrane, thus inducing break-down of cell metabolism and cell death. The immediate effect of saponin on MDCK II cells can be seen in a change in impedance as well as pO₂. pO₂ increases to (138 ± 2) torr after addition and gradually approaches levels of normoxic solutions of around 150 torr. Simultaneously, a steep decrease of |Z| of about 88 % from (2400 ± 300) Ω to a value of (300 ± 20) Ω upon addition of 0.3 % saponin was observed. The final impedance values correlate with |Z| of cell-free electrodes and are explained by the membrane permeabilization caused by saponin that facilitates the

electrical current flow into the bulk phase medium. As permeabilization is an irreversible process, both signals for pO_2 and $|Z|$ do not show recovery.

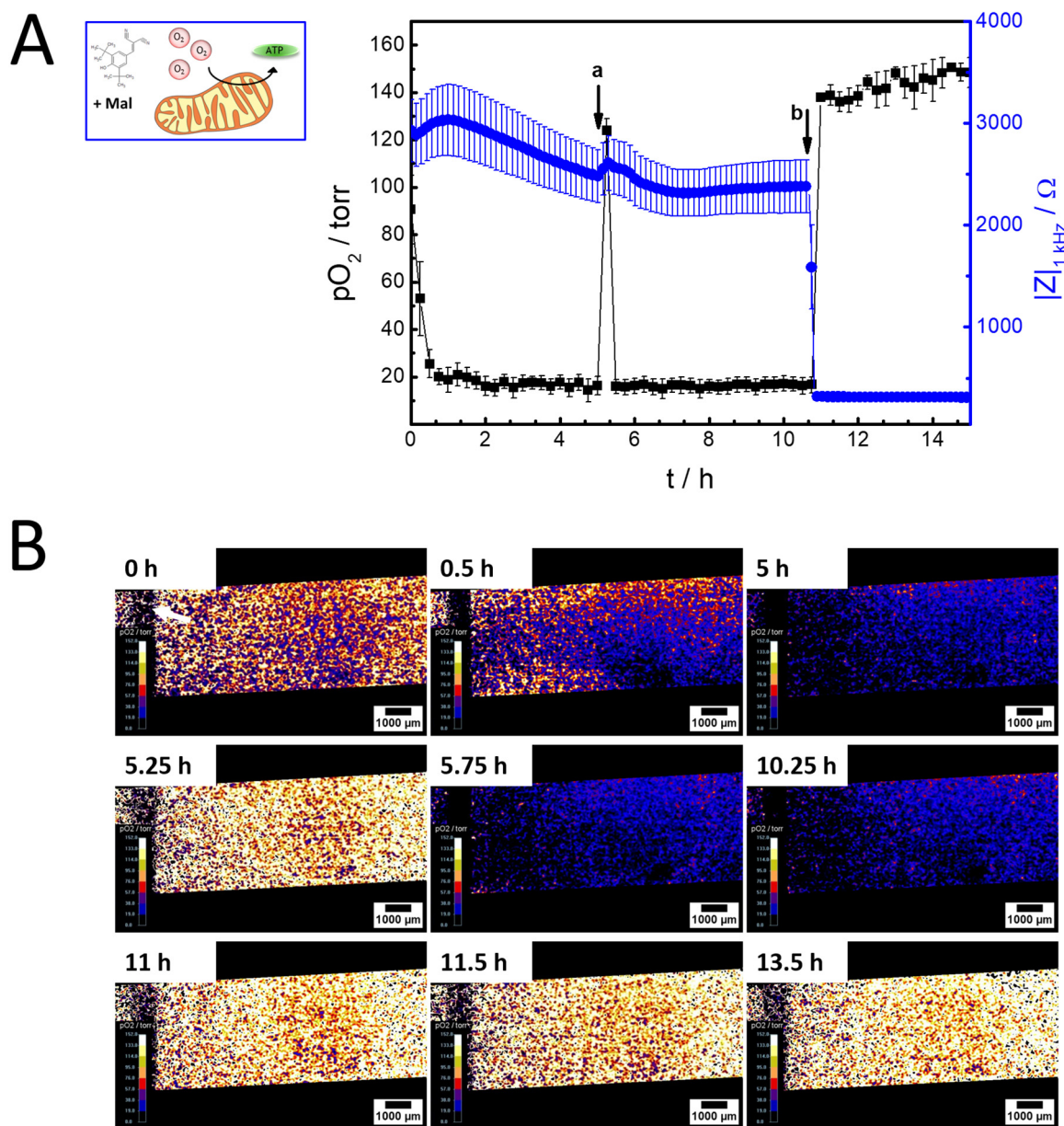


Fig. 5.5 Online monitoring the effect of the uncoupler malonoben (Mal) on confluent MDCK II cells. (A) Dual measurement of impedance (●) and oxygen consumption (■) with the ECIS- O_2 chip. After baseline recording in L-15 medium, fresh L-15 medium containing 100 nM Mal was added after 5 h (a). At $t = 10.75$ h, fresh L-15 medium containing 0.3 % (w/v) saponin (Sap) was added (b). Mean \pm SE; $n = 3$. (B) Typical false color images highlighting the oxygen distribution beneath MDCK II cells at selected time points. The arrow (0 h) indicates the position of one linear gold film electrode. For better visualization of the culture well, areas in the periphery of the growth surface were outlined in black using the NIH ImageJ software. $T = 37$ °C.

Oxygen consumption rates of the adherent cell layer in the open well were calculated using eq. 3.2. Oxygen consumption was determined to be (26.9 ± 0.2) pmol s^{-1} in L-15 medium. A slightly higher value of (27.2 ± 0.1) pmol s^{-1} was obtained for samples treated with 100 nM Mal and a basal rate of

$(0.5 \pm 0.3) \text{ pmol s}^{-1}$ was determined after addition of 0.3 % Sap, which leads to a break-down of oxygen consumption. 2D false color images recorded on the chip surface show spatial and temporal changes in oxygenation, as depicted in **Fig. 5.5, B**. False color images illustrate the deoxygenation under standard conditions within 5 h. After addition of fresh L-15 medium containing 100 nM Mal, a momentary reoxygenation was observed. Uncoupling leads to a quick deoxygenation which is too fast to be resolved by the current setup. Addition of 0.3 % Sap in L-15 medium at $t = 11 \text{ h}$ leads to an irreversible reoxygenation of the culture chamber. For one typical complete time series of oxygen imaging see **Video 11.3** on the attached DVD.

5.3.2 INFLUENCE OF BLOCKERS OF OXIDATIVE PHOSPHORYLATION

Furthermore, the dual sensor was used for impedimetric and luminescent monitoring of the effect of the blocking agent antimycin A (Ant A) on confluent MDCK II cells. **Fig. 5.6, A** shows changes in impedance at 1 kHz (●) and pO_2 (■) as a function of time. First, MDCK II cells were monitored in L-15 medium to record a baseline signal. As expected, deoxygenation by actively respiring cells is rapid, reaching stable pO_2 values below 10 torr within $t = 0.75 \text{ h}$ with an oxygen consumption rate of $(28.3 \pm 0.1) \text{ pmol s}^{-1}$. The impedance slightly decreases from $(3300 \pm 200) \Omega$ at $t = 0 \text{ h}$ to $(3000 \pm 200) \Omega$ at 5 h. After 5 h medium was exchanged to 1 ml fresh L-15 medium containing 2 μM Ant A (**Fig. 5.6, A, arrow a**), resulting in an immediate reoxygenation to $(159 \pm 9) \text{ torr}$ due to liquid exchange. Oxidative phosphorylation is irreversibly blocked by Ant A indicated by the fact that pO_2 remains at the level of oxygenated solutions during the complete incubation period, yielding a minimal OCR of $(4.1 \pm 5.2) 10^{-2} \text{ pmol s}^{-1}$. Impedance data shows that Ant A seems to exhibit a cytotoxic effect when applied to cells for several hours. Addition of Ant A is followed by a continuous decrease of $|Z|$ at 1 kHz, resulting in a total signal decrease of nearly 60 % to a value of $(1400 \pm 100) \Omega$ at $t = 10.75 \text{ h}$. As indicated in **Fig. 5.6, A** by arrow b, 1 ml fresh L-15 medium containing 0.3 % (w/v) saponin was added. Permeabilization and detachment of cells leads to a return of impedance values to levels of a cell-free electrode of about $(500 \pm 100) \Omega$, while oxygenation values continue to fluctuate around values of air saturated medium with a low OCR of $(0.3 \pm 0.2) \text{ pmol s}^{-1}$. The effects of Ant A and Sap are also clearly visible in the 2D spatial oxygen maps depicted in **Fig. 5.6, B** (for the complete time series see **Video 11.4** on the attached DVD). False color images show the basal oxygen consumption within the first 5 h of the measurement. Complete reoxygenation of the culture chamber due to liquid exchange, as well as blockage of cellular oxygen

consumption is observed after addition of L-15 medium containing 2 μM Ant A. Addition of 0.3 % Sap after 10.45 h does not alter the 2D spatial and temporal distribution of normoxic pO_2 anymore.

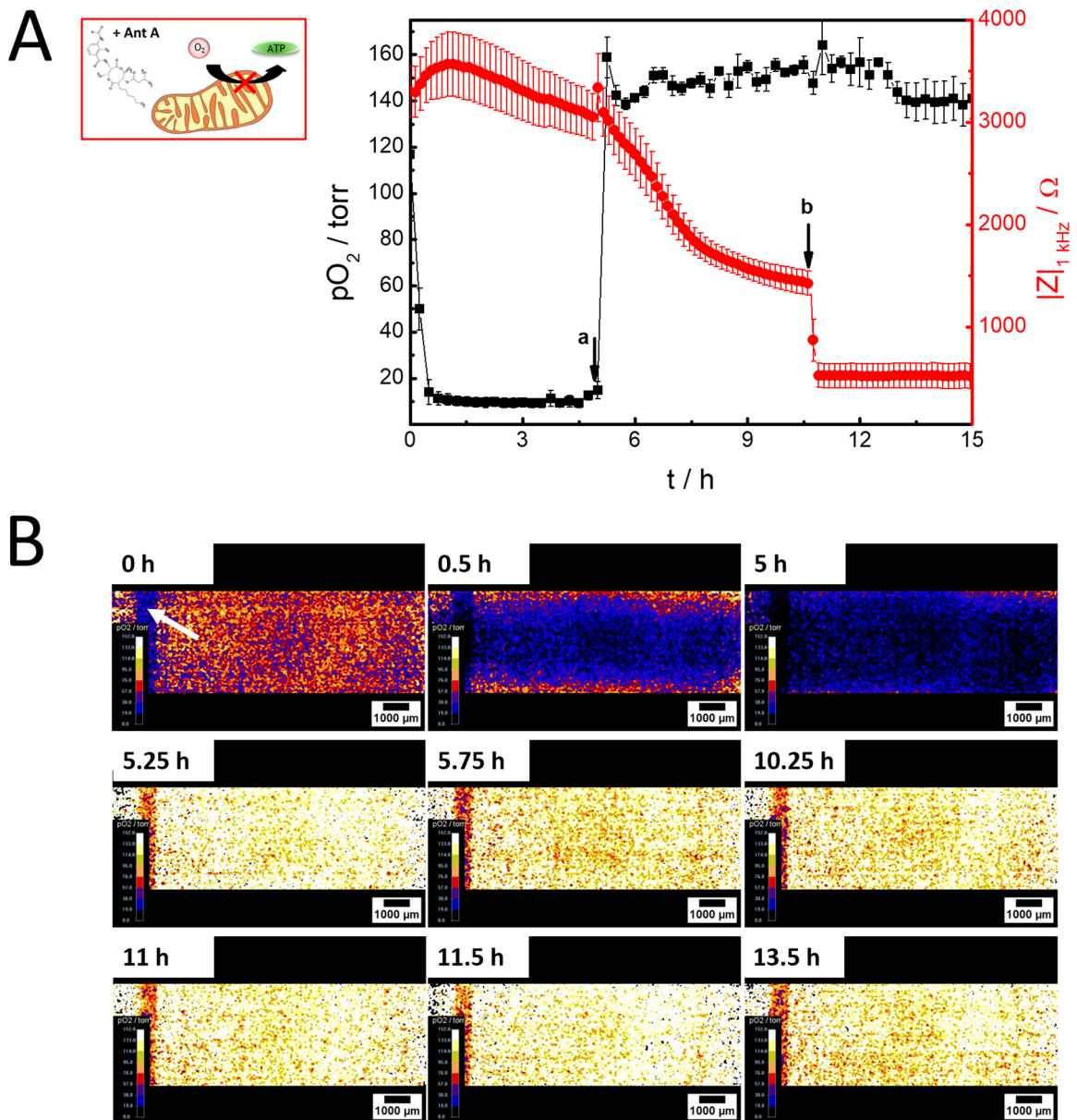


Fig. 5.6 Online monitoring the effect of the blocker antimycin A (Ant A) on confluent MDCK II cells. (A) Dual measurement of impedance (●) and oxygen consumption (■) with the ECIS- O_2 chip. After baseline recording in L-15 medium, fresh L-15 medium containing 2 μM Ant A was added after 5 h (a). At $t = 10.75$ h, fresh L-15 medium containing 0.3 % (w/v) Sap was added (b). Mean \pm SE; $n = 3$. (B) Typical false color images mapping the 2D spatial distribution of oxygen partial pressure beneath MDCK II cells at selected time points. The arrow (0 h) indicates the position of one linear gold film electrode. For better visualization of the culture well, peripheral areas were outlined in black using the NIH ImageJ software. $T = 37^\circ\text{C}$.

5.4 DISCUSSION

A dual sensor system combining an impedimetric and optical readout was developed. Therefore, a dual chip was designed that holds the technical requirements for both measurement modalities, i.e. an oxygen sensor foil was used as support for eight linear gold film electrodes. Layout optimization of the chip allowed the cultivation of confluent, adherent cells inside a customized culture well that was open to the atmosphere. A customized holder enabled contacting the gold film electrodes, while the integrated window allowed imaging of pO₂ beneath cells on the sensor foil. The ECIS-O₂ chip was used for the online measurement of changes in impedance and pO₂ during the adhesion of confluent MDCK II cells. Furthermore, the influence of drugs, such as Ant A and Mal, on confluent layers of MDCK II cells was investigated.

Although the ECIS-O₂ chip allows simultaneous monitoring of pO₂ and impedance, the set-up has certain drawbacks. First, an open culture chamber should be used for monitoring. Closed structures such as microchannels which might reduce operating costs due to smaller volume, did not allow the cells to grow to confluence probably due to poor oxygen permeability of the base substrate and the polymer microchannel. The use of an open culture chamber needs detection systems which are compatible with humidified incubators. Therefore, the commercial water-tight VisiSens A1 imaging system had to be used for oxygen measurements as the novel imaging system VisiSens TD mic was built for a non-humidified atmosphere. Due to its bigger field of view that allowed for a signal integration over a large area of the culture chamber, images recorded by VisiSens A1 showed lower lateral resolution and bigger pixel to pixel variation. Additionally, the epi-illumination using a circular arrangement of the several LEDs led to scattering and reflection effects at the glass interface of the chip which was noticeable as circular patches exhibiting an artificially lower pO₂ in the false color oxygen images. In comparison with data obtained by the VisiSens TD mic system presented in **chapter 4.1.1**, excitation of oxygen sensor foils with the VisiSens A1 system led to a 10fold higher signal loss when imaging the cell-free sensor foil.

Nevertheless, the dual sensor system was successfully used for an online monitoring of cell adhesion and the influence of drugs on confluent MDCK II cells. Cells successfully attached on the dual sensor surface which was followed online by an increase in impedance and resistance and a decrease in capacitance due to cell adhesion, spreading and the establishment of cell-cell contacts (Wegener et al. 2000). Cells were metabolically active during adhesion and spreading, as was shown by the decrease in pO₂ during cell adhesion and maturation of the cell monolayer. Adhesion kinetics of

MDCK II cells on the ECIS-O₂ chip seem to be slower compared to measurements with standard ECIS electrodes, resulting nevertheless in confluent monolayers. It is known that adhesion behavior strongly depends on surface properties. Pre-coating surfaces with adhesion promoting proteins has been shown to accelerate cell spreading and adhesion upon gold film electrodes (Wegener et al. 2000). Additionally, nanotopography of gold surfaces has a huge impact on cell adhesion. It has been demonstrated that gold surfaces with increased roughness negatively influence adhesion behavior (Brunetti et al. 2010). A rougher surface topography could also be the reason for a slower adhesion of MDCK II cells to the gold film electrodes of the ECIS-O₂ chip. As the underlying substrate (RPSu4 sensor foil) has a rougher surface compared to standard polymer supports used for ECIS electrodes, such as polycarbonate or polyethylene terephthalate, vacuum deposition of gold probably results in rougher electrode structures. To confirm this assumption further investigations on topography using for example atomic force microscopy need to be done.

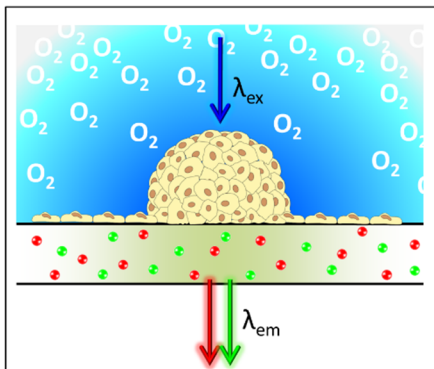
Online monitoring of impedance and pO₂ of confluent MDCK II cells treated with uncouplers and blockers of oxidative phosphorylation yielded results similar to data obtained for oxygen measurements conducted with the VisiSens TD mic system as presented in **chapter 4.7**. Dual monitoring of cells treated with the uncoupler Mal showed a rapid decrease of pO₂, while impedimetric analysis indicated that cell morphology and viability remained unchanged. However, this result cannot be supported by literature as no source is known that reports on toxicity of malonoben. On the other hand, treatment of MDCK II cells with 2 μM Ant A, a concentration which is typically used in literature studies reporting on strategies to uncouple oxidative phosphorylation, did not only lead to respiratory inhibition, resulting in a reoxygenation of the extracellular buffer to normoxic levels. Simultaneous impedimetric measurements revealed that exposure to 2 μM Ant A drastically affects cell health and morphology, resulting in a rapid decrease in impedance. The negative impact of antimycin A on cells was also found in studies conducted with PC12 and HL-60 tumor cell lines, where Ant A induced morphological changes and apoptosis (King and Radicchi-Mastroianni 2002; Xu et al. 2014). Treatment of MDCK II cells with Ant A quickly induced cell death after a few hours of incubation (Pan et al. 2005). This may be caused by an increased production of reactive oxygen species by one electron reduction of molecular oxygen at the Q₀ center of complex III upon blocking by Ant A (Turrens 1997). Furthermore, blocking of oxidative phosphorylation results in a breakdown of the mitochondrial membrane potential and a depletion of ATP, which has been shown to disrupt membrane functionality and to activate apoptotic pathways (Feldenberg et al. 1999). Additionally, lower EC₅₀ values were obtained for cells exposed to Ant A in galactose

containing medium (Kamalian et al. 2015), probably due to metabolic shift towards oxidative phosphorylation as already explained in **chapter 4.10.2**. This could also explain the high susceptibility of MDCK II cells cultivated in Gal containing L-15 towards Ant A. Usually, the applied concentration of 2 μM is in the range of concentrations typically used for blocking oxidative phosphorylation of cells in proof-of-concept studies. However, studies in literature focus mainly on the impact of Ant A on oxygen consumption, thus focussing on metabolic activity only without testing of long-term cytotoxicity (Dmitriev et al. 2015; Tan et al. 2015). Here, the dual ECIS-O₂ chip provides additional information on cell viability and morphology, which is not taken into account by oxygen monitoring that solely focusses on metabolic activity.

5.5 OUTLOOK

The ECIS-O₂ sensor enables a non-invasive, online measurement of impedance and pO₂ of adherent cells, thus providing simultaneous information about cell metabolism and morphology. For future studies, the dual set-up could be combined with microfluidic pumps to enable successful cultivation of confluent monolayers and monitoring under flow conditions. This would allow measurements inside a non-humidified incubator with the VisiSens TD mic system, resulting in lower photobleaching and a better resolution. Alternatively, throughput could be enhanced by increasing the number of culture wells to four with one electrode pair per well. However, this would require a different imaging set-up with a larger field of view to monitor the oxygenation of four wells simultaneously. Exchange of the oxygen sensitive RPSu4 foil to, for example, a pH sensor foil would allow the dual monitoring of impedance and pH. Exchanging the non-transparent RPSu4 oxygen sensor foil by thin, transparent and lifetime based sensor films would make the determination of oxygen content less prone to errors, caused by fluctuations of the illumination source or photobleaching, and the dual chip is accessible by to light microscopy to check cell morphology before and during the measurement. Using sensor films doped with multiple dyes in combination with suitable excitation sources, emission filters and camera systems would enable a simultaneous, multiparametric readout of parameters such as pO₂, pH or CO₂ while monitoring impedance via gold film electrodes deposited on the sensor film. Additionally, embedding oxygen sensitive dyes or sensor particles in conducting polymers, such as the oxygen permeable, transparent PEDOT:PSS (Seemann et al. 2009), would enable the simultaneous readout of impedance and pO₂ over one cell population residing directly on the electrode/optrode surface.

6 IMAGING OXYGEN GRADIENTS IN MCF-7 SPHEROIDS



3D tissue models are considered as useful *in vitro* models in biomedical and clinical research. Due to their 3D structure, they close the gap between simple 2D monolayer cell culture and regular tissue structures. 3D models such as multicellular tumor spheroids consist of aggregates of cells. They mimic physiological conditions normally found in tissue more closely compared to standard 2D cell culture. Multicellular tumor spheroids are currently used in many cancer studies. They are an attractive model system in studies on (chemotherapeutic) drug efficacy and delivery, cell responses to radiotherapy, angiogenesis, tumor growth and proliferation, as well as invasion and migration processes (Weiswald et al. 2015). Because 2D cell monolayers behave differently compared to cells in a 3D environment, spheroids possess a more complex network of extracellular matrix and cell-cell contacts. Their 3D structure usually comprises an outer region of viable, proliferating cells followed by an intermediate quiescent cell layer. Depending on the spheroid size, deprivation of nutrients leads to the formation of an inner necrotic core. This structure with different isocentric layers leads to the formation of metabolic gradients from the inside to the outside of the spheroid which also occur in tissue. Due to diffusion limits and metabolic activity of the outer cell layers, metabolic waste products accumulate in the inner spheroid region, where levels of nutrients and oxygen are low (Hirschhaeuser et al. 2010). However, studies about oxygenation and hypoxia in live 3D spheroids are scarce because of the lack of biocompatible measurement techniques. Standard methods, such as the Clark type oxygen electrode allow online monitoring, but perturb the samples by insertion injection of the microneedle and they consume oxygen during the measurement, while immunohistochemical detection with markers such as misonidazole allows only an end-point, semi-quantitative determination of oxygenation (Gross et al. 1995). Nanoparticle-based detection of oxygen inside spheroids can overcome these drawbacks to a certain extent. However, incorporation of highly oxygen permeable particles inside spheroids can alter spheroid structure or physiology, thus influencing oxygen values or physiological relevance (Papkovsky and Dmitriev 2013). The following chapter gives an overview of the application of the novel imaging system VisiSens TD mic for quantitative monitoring of oxygenation levels in live MCF-7 tumor spheroids under standard

growth conditions with good spatio-temporal resolution. Furthermore, the set-up was used to image the influence of drugs on oxygen gradients formed by metabolically active spheroids.

6.1 CYTOCOMPATIBILITY OF SENSOR FOILS AND SPHEROID ADHESION

To enable stable long term ratiometric oxygen monitoring with the novel imaging system VisiSens TD mic, spheroids need to attach to the surface of the oxygen sensor foils. In previous studies, the adhesion of MCF-7 monolayer cells to the oxygen sensitive culture substrates was successfully tested. Confluent and subconfluent MCF-7 cells were seeded onto uncoated and protein coated RPSu4 oxygen sensor foils and cellular viability was confirmed by life-dead staining (see supplementary information **Fig. 11.15**). Because viability and adhesion behavior of cells on uncoated sensor foils was not significantly different compared to standard cell culture dishes or coated sensor

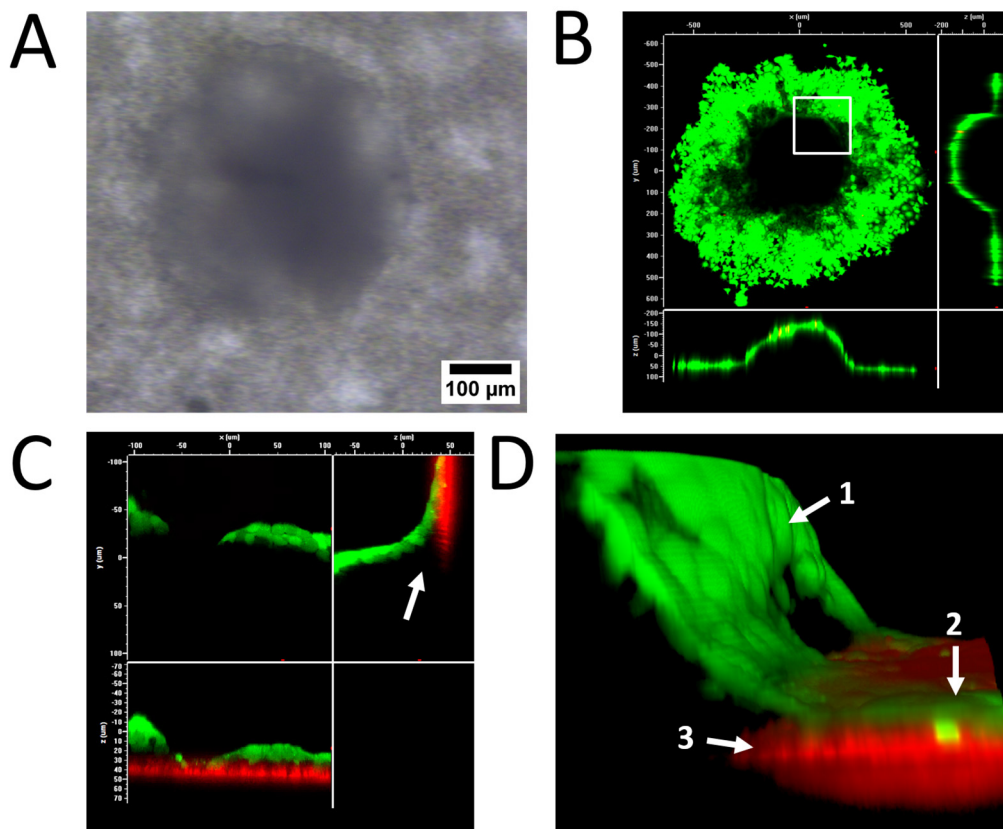


Fig. 6.1 (A) Phase contrast image of a spheroid 24 h after seeding on the oxygen sensor foil. (B) CLSM image of (A) stained with CaAM and EthD-1 to mark live and dead cells, showing the adhered spheroid that consists of a semi-spherical part and an outgrowing cell monolayer. Image shows fluorescent signals from the spheroid only, fluorescent signal from the oxygen sensor foil was not monitored. (C) Zoom-in of the white inset shown in (B) displaying the transition from the spherical part to the monolayer in xy-, xz- and yz-axis (indicated by the white arrow). Green cytoplasmic fluorescence marks live MCF-7 cells, red fluorescence marks the subjacent sensor foil and the nuclei of dead cells. (D) 3D image of CLSM z-stacks including the stack from (C) illustrating the transition from the spherical part (1) to the monolayer (2) and the subjacent oxygen sensor foil (3).

foils, MCF-7 spheroids were cultivated also on uncoated oxygen sensor foils. Since phase contrast microscopy does not allow visualization of the 3D structure of the spheroid (**Fig. 6.1, A**), CaAM/EthD-1 staining was used to verify adhesion and viability of MCF-7 spheroids. 24 h after seeding, MCF-7 spheroids have attached to the surface of the sensor foil which leads to the formation of a live central, half spherical 3D structure that is surrounded by a base of outgrowing monolayer cells, as depicted in **Fig. 6.1, B**. A closer view of the transition zone from the half sphere to the monolayer base is shown in **Fig. 6.1, C and D**. Green cytoplasmic fluorescence indicates live MCF-7 cells while red fluorescence is emitted from the nuclei of dead cells and the subjacent oxygen sensor foil. Due to limited diffusion of the fluorescent dyes and limited penetration depth of the laser light only the outer cell layers of the spherical part can be visualized by confocal laser scanning microscopy.

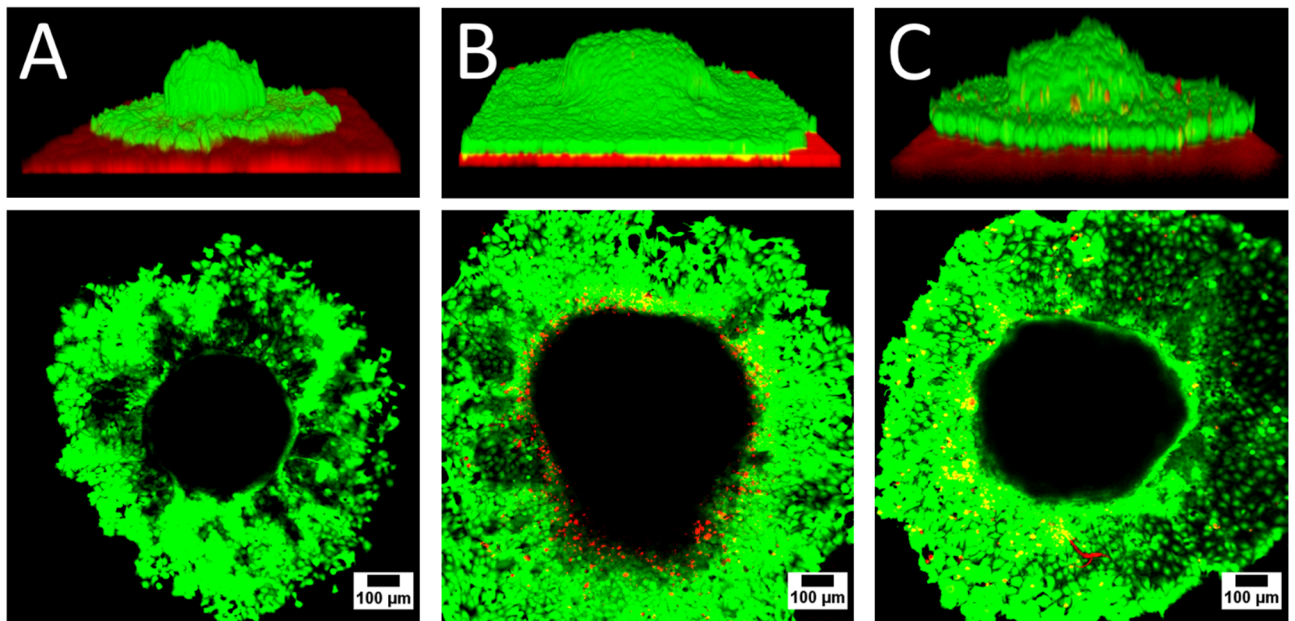


Fig. 6.2 Fluorescence micrographs of MCF-7 spheroids adhered to the oxygen sensor foil and stained with 2 μM CaAM and 4 μM EthD-1. Green cytoplasmic fluorescence indicates live cells, red fluorescence dead cells/sensor foil. (A) Upper panel: 3D reconstruction of a viable MCF-7 spheroid 24 h after inoculation before oxygen imaging. Lower panel: xy-image of the base of the attached spheroid. (B) Upper panel: 3D reconstruction of a control spheroid cultivated under imaging conditions for 3.5 d but without illumination of the sample. Lower panel: corresponding xy-image of the spheroid base. (C) Upper panel: 3D image of a spheroid after 3.5 d of oxygen imaging and corresponding xy-image (lower panel). The sample was illuminated every 15 min for 3.5 d without inducing phototoxic damage to the spheroid by singlet oxygen production.

In order to ensure long time measurements, a potential phototoxic effect on the spheroids needed to be excluded. Triplet oxygen quenches the luminescence of the sensor dye and is converted to singlet oxygen which can severely damage biological samples during the imaging process. 9 d old MCF-7 spheroids were cultivated for 24 h on oxygen sensor foils. Then, the viability of the samples was checked either immediately or after 3.5 d under oxygen imaging conditions as shown in **Fig. 6.2**.

Before imaging is started the viable spheroid nicely attaches to the sensor foil forming a half spherical shape as illustrated in **Fig. 6.2, A**. After another 3.5 d of cultivation under imaging conditions, the sample residing on the unexposed sensor foil is still viable. Due to cell division and spreading, both, the 3D central structure and surrounding monolayer base increased in size (**Fig. 6.2, B**). Compared to control conditions, the spheroid used for a 3.5 d period of oxygen imaging does not show any significant differences in viability (**Fig. 6.2, C**). Illumination of the sample with blue light every 15 min does neither induce cell death nor prevent cell division and spreading due to irradiation of the oxygen sensor dye and generation of singlet oxygen, indicating low phototoxicity of the sensor foils. These results clearly show, that RPSu4 oxygen sensor foils are both, compatible with long-time cultivation of MCF-7 spheroids and oxygen imaging.

6.2 IMAGING OXYGEN GRADIENTS IN MCF-7 SPHEROIDS

6.2.1 GRADIENT FORMATION

The novel imaging system was used to visualize oxygen consumption and oxygen gradients caused by metabolically active multicellular spheroids. Thus, MCF-7 spheroids were cultivated on the oxygen sensor foils and oxygen consumption was monitored in L-15 medium. **Fig. 6.3** depicts typical data of oxygen imaging of an 8 d old MCF-7 spheroid. Raw data images show the spherical structure of the spheroid adhered to the foil, while false color images clearly show differences of pO_2 between spheroid center and surrounding culture medium. Alpha blending which superimposes raw data and false color oxygen images reveals colocalization of areas with low pO_2 and the position of the 3D spheroid as shown in **Fig. 6.3, A**. Alpha blending was done using the customized version of the AnalytiCal[®] software to create an overlay of the raw data and the false color oxygen image. Gradient formation in MCF-7 spheroids due to active metabolism was imaged over a period of 9.5 h with an interval of 10 min between each recorded image. In **Fig. 6.3, B** a typical time series of 2D false color oxygen images is illustrated. After addition of fresh L-15 medium at $t = 0$ h a lateral oxygen gradient is established with pO_2 in the spheroid center steadily dropping until $t \sim 4$ h and remaining stable for the rest of the measurement. A more detailed and vivid view of gradient formation and oxygen consumption with better time resolution is provided by **Video 11.5** in the attached DVD. Ratiometric imaging of MCF-7 spheroids grown on planar oxygen sensor foils allows detailed, spatio-temporal analysis of the oxygen consumption pattern. By freely choosing different ROIs, oxygenation data can

be either plotted as a function of time or distance. **Fig. 6.3, C** displays differences in pO_2 of three ROIs (spheroid center, spheroid edge and the surrounding medium) as a function of time.

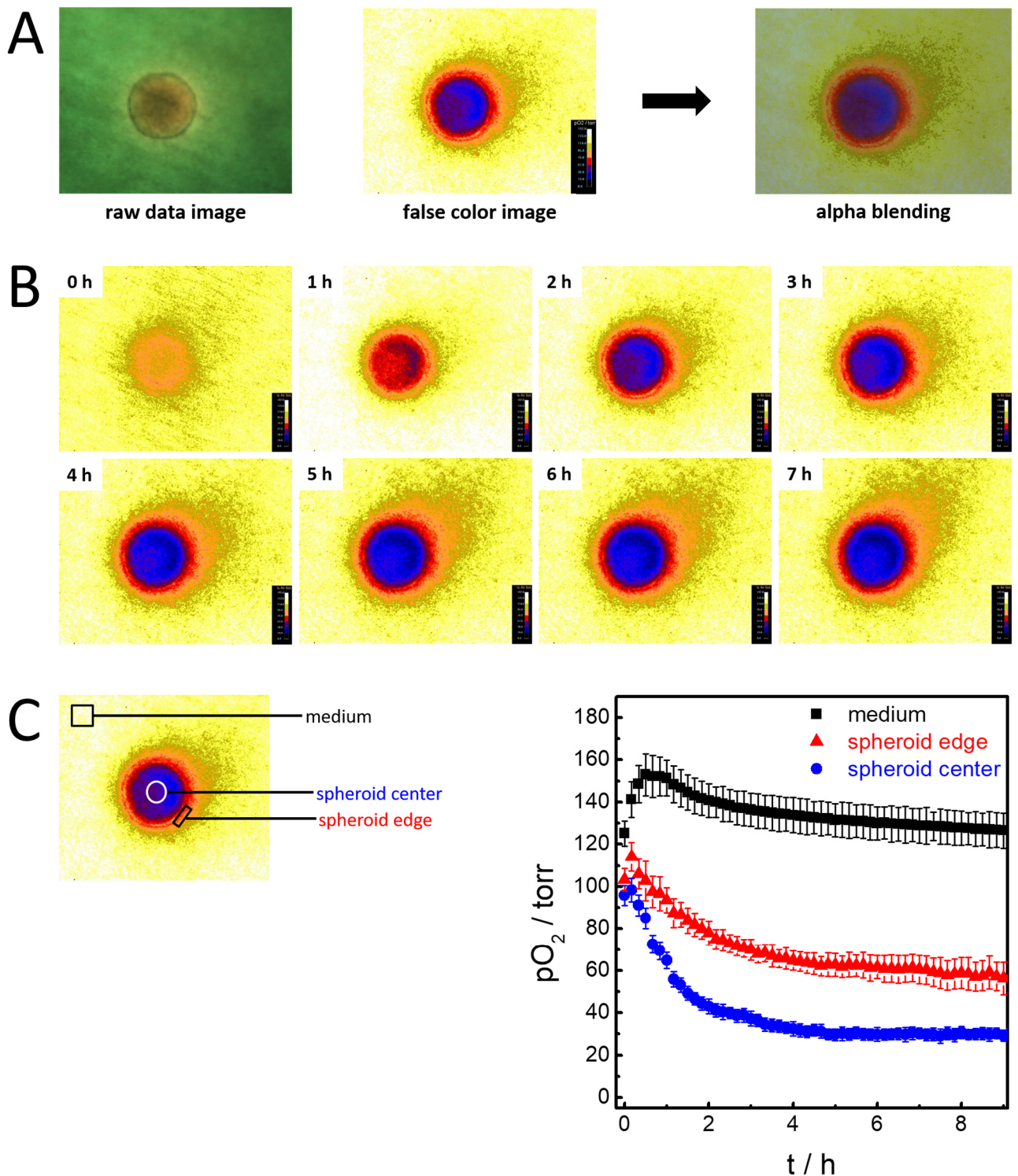


Fig. 6.3 (A) Alpha blending of raw data image and false color oxygen image allows colocalization of oxygen gradient and spheroid structure. (B) Time series of 2D false color oxygen images, illustrating the oxygen consumption and the formation of a lateral oxygen gradient caused by a metabolically active spheroid. (C) Oxygen partial pressure was analyzed for different ROIs as a function of time. Low pO_2 values can be measured at the spheroid center (●) and edge region (▲), while oxygen levels of medium (■) correspond to pO_2 of an air saturated solution. $T = 37^\circ C$.

After addition of fresh L-15 medium at $t = 0$ h, pO_2 at the center area reaches a value of (95.8 ± 4.7) torr. Then, pO_2 level decreases to about 45 % of the initial value and it reaches (43.0 ± 3.5) torr at $t = 2$ h. Afterwards, oxygen levels in the spheroid center decrease only slowly, yielding a value of (29.3 ± 2.6) torr after 9 h (see **Fig. 6.3, C, ●**). Oxygenation of the spheroid edge region is slightly higher compared to the central area, with an initial value of (103.3 ± 5.4) torr as shown in **Fig. 6.3, C, ▲**. Compared to the fast decrease of pO_2 in the inner region, oxygen levels in the edge region decrease more slowly reaching a pO_2 of (78.0 ± 5.8) torr at $t = 2$ h. However, oxygen levels further drop to a final value of (56.2 ± 7.7) torr at $t = 9$ h with pO_2 values slightly higher compared to the values from the spheroid center. Compared to the metabolically active spheroid, oxygen levels of the surrounding culture medium increase during the first 30 min and then fluctuate around values of air saturated solutions (see **Fig. 6.3, C, ■**).

6.2.2 OXYGEN GRADIENTS IN MCF-7 SPHEROIDS OF DIFFERENT AGE

It is known that due to their spherical structure and diffusion limitations, oxygenation within multicellular spheroids is not homogeneous. While higher pO_2 values are found in the viable outer layer, oxygenation continually decreases from outer layers to the center. Depending on the size and age, the lack of both oxygenation and nutrients in the inner part of the spheroid leads to necrotic zones that are highly hypoxic with pO_2 levels below 10 torr (Mueller-Klieser and Sutherland 1982). Therefore, the novel imaging set-up was used to image oxygen gradients of MCF-7 spheroids of different ages to record age related differences in pO_2 distribution.

Oxygen imaging was done with 7 to 9 d old MCF-7 spheroids that were monitored for 9 h in L-15 medium. **Fig. 6.4, A** shows raw data RGB images and corresponding false color oxygen images of three MFC-7 spheroids of different ages after oxygen gradient formation at $t = 4$ h after seeding. Independent of age, oxygen gradients caused by the respiring spheroids are clearly visible. The transition from normoxic values to low pO_2 is even better visible in the histograms depicted in **Fig. 6.4, B**, representing cross sections through the false color oxygen image including both, spheroid and medium at $t = 4$ h (see corresponding small insets in **Fig. 6.4, B**). pO_2 first steeply decreases from normoxic values of the surrounding medium in the spheroid edge region, reaching stable values below 40 torr in the spheroid center. Analysis of minimal values yields similar results between 29.2 torr and 31.0 torr for the three individual spheroids as shown in **Tab. 6.1**. pO_2 of the MCF-7 spheroids does not seem to be strongly hypoxic with a pO_2 of < 10 torr as often reported in literature

for many spheroid cell lines (Mueller-Klieser and Sutherland 1982; Mueller-Klieser 2000). No areas with pO_2 below 10 torr were detected within the MCF-7 spheroids. However, the size of areas with pO_2 below 59 torr increases by about 45 % with increasing age from 79600 μm^2 for the 7 d old spheroid to 140300 μm^2 for the 9 d old spheroid. However, **Tab. 6.1** also shows that after analysis of three individual samples for each age, size of the area with minimum pO_2 and minimum pO_2 do not significantly increase with age, but are strongly dependent on the cell batch and passage number. Taken together, MCF-7 spheroids do not seem to possess a hypoxic center with oxygen partial pressure below 10 torr except for two samples. Analysis of pO_2 from ROIs representing medium, spheroid edge and spheroid center as a function of time are shown in **Fig. 6.4, C**. 7 d, 8 d and 9 d old spheroids show similar kinetics of pO_2 change for the individual ROIs. Medium oxygenation increases within the first hour to values of an air saturated solution (**Fig. 6.4, C, ■**). Then, measured values in ROIs representing medium show a slight decrease within the next 8 h. Oxygen levels under the central part of the spheroid quickly decrease within the first 2 h reaching stable values with a mean pO_2 of (32.6 ± 3.7) torr for the 7 d old spheroid. Mean pO_2 of the 8 d old spheroid amounts to (35.9 ± 2.8) torr and to (34.9 ± 2.7) torr for the 9 d old spheroid (**Fig. 6.4, C, ●**). Oxygenation of the spheroid edges decreases slower with final values of (30.2 ± 4.9) torr, (30.1 ± 2.9) torr and (24.2 ± 2.2) torr which are similar compared to values obtained for the central spheroid area as shown in **Fig. 6.4, C, ▲**.

Tab. 6.1 Oxygenation data at $t = 4$ h of those MCF-7 spheroids shown in **Fig. 6.4**. The lower panel summarizes the statistics of three independent measurements, including data from **Fig. 6.4**. $T = 37$ °C.

	7 d	8 d	9 d
area _{< 59 torr} / μm^2	79600	123700	140300
area _{< 10 torr} / μm^2	0	0	0
Minimum / torr	29.2	29.3	31.0
	7 d (n = 3)	8 d (n = 3)	9 d (n = 3)
area _{< 59 torr} / μm^2	85700 \pm 8600	115500 \pm 79800	149000 \pm 89700
area _{< 10 torr} / μm^2	927.8	0	104.2
Minimum / torr	41.9 \pm 24.8	30.0 \pm 13.0	27.1 \pm 12.2

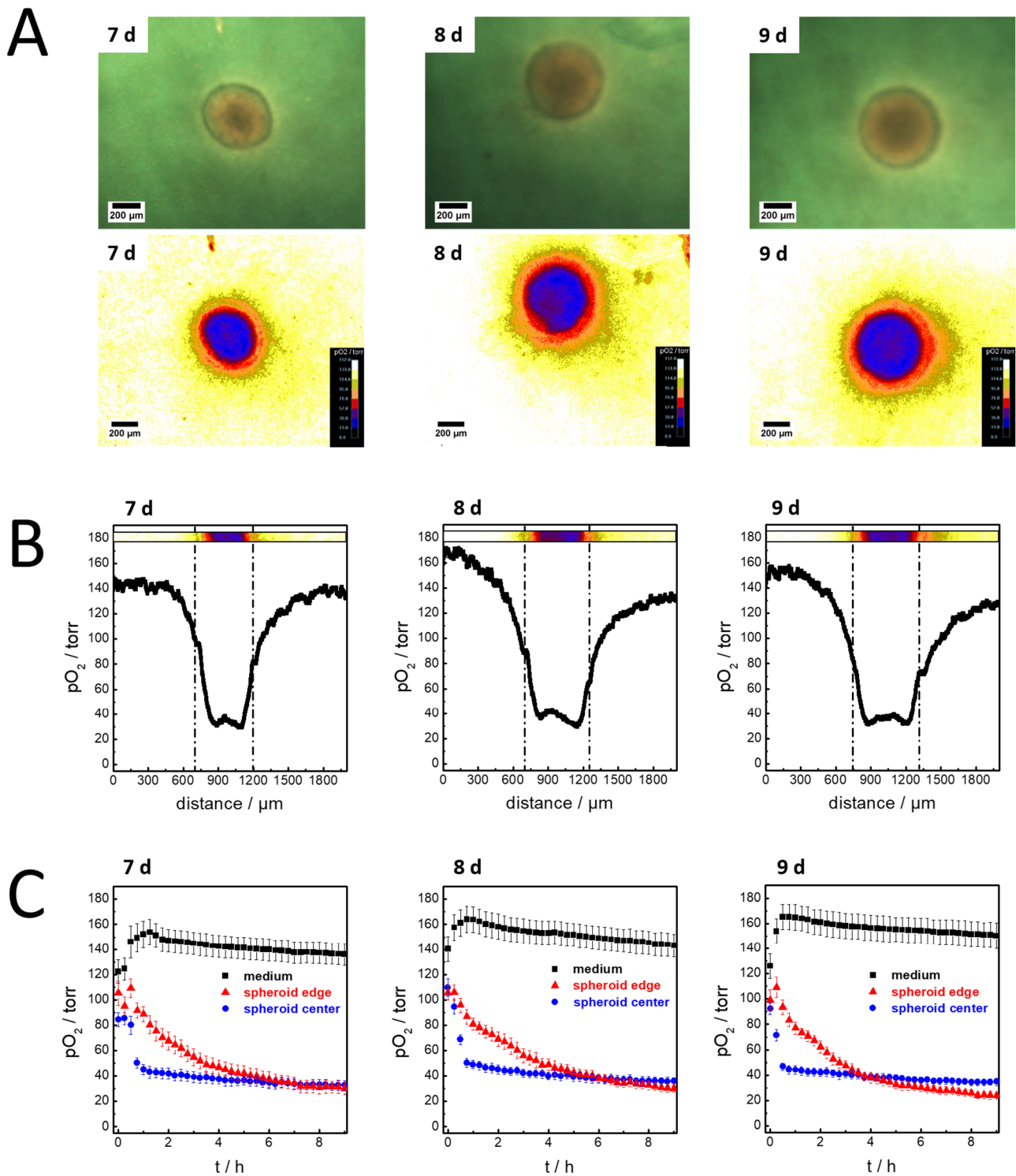


Fig. 6.4 (A) Raw data and corresponding false color oxygen images of 7 – 9 d old MCF-7 spheroids bathed in L-15 medium recorded 4 h after start of the imaging experiment. (B) Cross sections through medium and spheroid displaying lateral pO_2 gradients at $t = 4$ h. Dashed lines indicate the transition from the spherical part to the section of an outgrowing monolayer. (C) Changes in oxygenation for three different ROIs as a function of time for 7 – 9 d old spheroids. While pO_2 of medium (\blacksquare) remains constant during the measurement period, oxygenation of the spheroid edge (\blacktriangle) and the center (\bullet) decreases to values below 50 torr. Data plots represent one 7d, one 8d and one 9d old spheroid. $\text{Mean}_{\text{ROI}} \pm \text{SD}_{\text{ROI}}$. In total, three individual spheroids were monitored for each age at $T = 37^\circ\text{C}$.

6.2.3 COMPARISON OF VISISENS TD MIC PERFORMANCE WITH VISISENS A1

Unlike macroscopic structures such as tissue slides, organs or whole organisms where oxygenation has already been monitored with commercially available imaging systems (Meier et al. 2012; Hofmann et al. 2013; Zhu et al. 2015), multicellular spheroids are microscopically small structures. Thus, detailed information about oxygen consumption and oxygen gradients can only be gained with a suitable measurement system providing sufficiently high spatial resolution.

The novel microscopic imaging system was compared to the commercially available camera system VisiSens A1 regarding its lateral resolution. Therefore, 9 d old MCF-7 spheroids were cultivated on RPSu4 oxygen sensor foils and the gradient formation and oxygen consumption was monitored for 24 h using the VisiSens TD mic or the VisiSens A1 system. Two different adapters yielding a pixel size of about 9 μm (tube 1) and 6 μm (tube 2) were used for oxygen measurements with the VisiSens A1 system as described in **chapter 3.2.2.1**. Oxygen measurements were recorded in L-15 medium for one day. **Fig. 6.5, A** shows a typical color image recorded with the VisiSens A1 system and tube 1. With a field of view of 11728 x 9383 μm^2 , this set-up is capable of monitoring the whole sensor spot inside one cell culture petri dish, thus three spheroids residing on the sensor foil are easily be visualized. For a better view, the surrounding background signal from the petri dish was replaced by a homogeneous black background using the ImageJ software. Two different ROIs were chosen to extract oxygenation of the spheroid center or the bulk medium as a function of time, as displayed in the corresponding graph. Mean values of medium ROI resemble normoxic values of about 150 torr and slightly decrease during the measurement (**Fig. 6.5, B, ■**). Oxygenation of the spheroid center decreases from an initial value of (80 ± 7) torr after medium exchange at $t = 0$ h, to (51 ± 7) torr after 2 h and to (28 ± 6) torr after 23.75 h (**Fig. 6.5, B, ●**). A complete time series showing the oxygen distribution in false color images can be seen in **Video 11.6**. With adapter tube 2, a field of view of 7131 x 5705 μm^2 can be monitored with the VisiSens A1 system. **Fig. 6.5, C** shows the false color oxygen image of one MCF-7 spheroid adhered to the sensor foil 2 h after measurement start. The complete time series over a measurement period of 24 h is shown in **Video 11.7**. The corresponding time series data shows a curve progression for both ROIs which is similar to imaging data recorded with the VisiSens A1 system and tube 1. While medium oxygenation fluctuates around values of 150 torr (**Fig. 6.5, D, ■**), pO_2 underneath the spheroid quickly decreases from a starting value of (83 ± 10) torr at $t = 0$ h, to (46 ± 10) torr at $t = 2$ h. Then, spheroid oxygenation does only change slightly with a final value of (51 ± 10) torr (**Fig. 6.5, D, ●**).

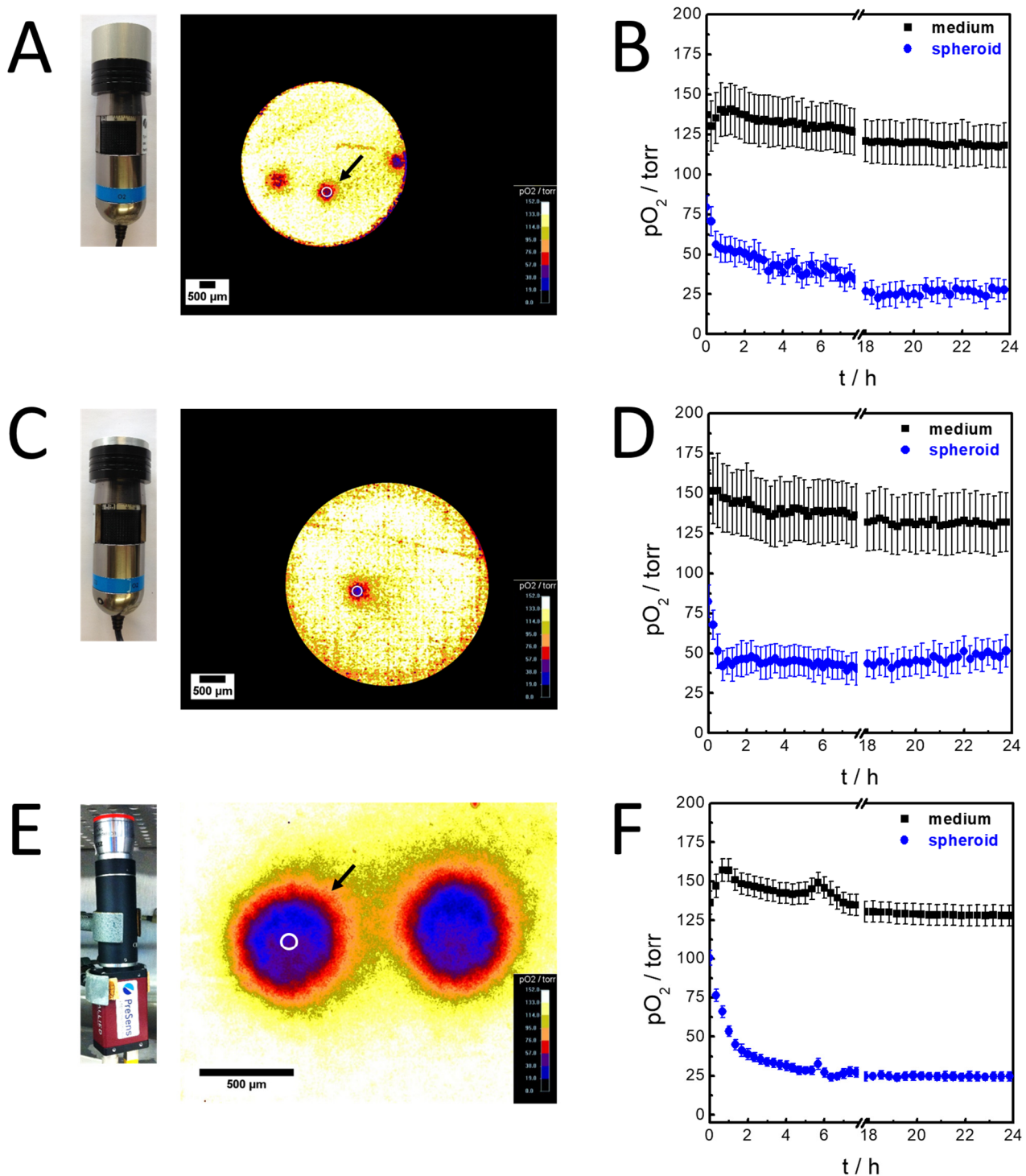


Fig. 6.5 Comparison of the commercially available, optical oxygen imaging system VisiSens A1 and the VisiSens TD mic system developed in this work. Both systems were used to image oxygen gradients and consumption of 9 d old MCF-7 spheroids in L-15 medium. (A) False color oxygen image at $t = 2$ h of three MCF-7 spheroids recorded with VisiSens A1 and a 2.5 cm tube (tube 1) and (B) corresponding changes in mean pO_2 of two different ROIs over 24 h. A circular region (white circle) covering the inner spheroid area and a rectangular region covering the surrounding medium were chosen as ROIs. The black arrow indicates the spheroid used for the determination of inner pO_2 . (C) False color oxygen image of one spheroid recorded with VisiSens A1 and a 1.2 cm tube (tube 2) after 2 h. (D) The corresponding graph shows changes in oxygen levels of medium and spheroid center as a function of time. (E) False color oxygen image of two MCF-7 spheroids at $t = 2$ h monitored with the VisiSens TD mic system. Central pO_2 of the left spheroid was used for detailed analysis (indicated by the black arrow). (F) The corresponding graph shows mean pO_2 of medium and inner spheroid ROIs over a measurement period of 24 h. All measurements were repeated twice yielding similar results. $T = 37$ °C.

Oxygen consumption of MCF-7 spheroids was monitored with the VisiSens TD mic system as depicted in **Fig. 6.5, E**. Compared to VisiSens A1, the novel imaging system has a much smaller field of view of 2064 x 1540 μm yielding a pixel size of 1.6 μm . This allows a more detailed recording of oxygen gradients formed by the spheroid with better resolution of the transition from inner spheroid to the edges to the surrounding medium. The inner spheroid area with a pO_2 between 19 and 57 torr can be clearly distinguished from the edge regions, with oxygen levels gradually increasing concentrically from median values ranging between 57.0 – 76.0 torr to 76.0 – 95.0 torr, with a final transition to oxygen levels of air saturated solutions. Kinetics of oxygen gradient formation is similar to measurements conducted with the VisiSens A1 system as depicted in **Fig. 6.5, F**. However, mean pO_2 of the ROIs under study are more homogeneous, exhibiting a lower standard deviation compared to the commercial systems. pO_2 determined for medium lies at normoxic values. Mean oxygenation measured in the right spheroid drops from (102 ± 6) torr at $t = 0$ h to (36 ± 3) torr at $t = 2$ h due to oxygen gradient formation, reaching (25 ± 2) torr after 23.75 h of the measurement (**Fig. 6.5, F, ●**). The complete time lapse video of oxygen gradient formation and oxygenation changes in the two MCF-7 spheroids is shown in **Video 11.8**. To sum up, the novel imaging system VisiSens TD mic clearly outperforms the commercial system yielding a better spatial resolution and lower pixel to pixel variations.

6.3 EXPOSURE TO DRUGS INFLUENCING OXIDATIVE PHOSPHORYLATION

Spheroids are a versatile tool commonly used for drug screening and cytotoxicity tests of pharmaceutical compounds (Wenzel et al. 2014; Sabhachandani et al. 2016). Usually, analysis addresses morphology changes documented by microscopic techniques or metabolic activity (Mehta et al. 2012). However, most assays are either invasive and end-point based, such as immunostaining of sectioned slices, viability assays or analysis of protein/DNA/RNA content, while label free microscopic time-lapse imaging only yields information on the outer morphology. To overcome these drawbacks, the novel imaging system was used for non-invasive, online monitoring of drug effects on spheroid oxygenation and oxygen gradient formation as indicator for metabolic status.

Analogous to studies conducted with monolayer cells as described in **chapter 4.7**, the effect of drugs influencing oxidative phosphorylation was studied. Therefore, MCF-7 spheroids were first monitored in L-15 medium. After gradient formation, the cell aggregates were either treated with

antimycin A, a blocker of cellular respiration or malonoben, one of the most potent uncouplers of oxidative phosphorylation. Fresh L-15 culture medium was used as a vehicle control. For better comparison of the three measurement conditions, the sizes of the ROIs used to determine bulk medium and inner spheroid pO_2 were kept constant. **Fig. 6.6, A** shows results of changes in oxygenation of a spheroid imaged under control conditions over a measurement period of 13 h. An oxygen gradient is formed with the initial mean pO_2 in the spheroid center of (84 ± 8) torr decreasing by about 35 % to (57 ± 4) torr (**Fig. 6.6, A, ●**) after 2 h while medium oxygenation slightly increases from (128 ± 12) torr at $t = 0$ h to (159 ± 9) torr (**Fig. 6.6, A, ■**) at $t = 2$ h. Directly before addition of fresh L-15 medium at $t = 8$ h, oxygen partial pressure in the spheroid center yields values of (41 ± 4) torr. pO_2 of bulk medium is in the range of normoxic solutions with a pO_2 of (149 ± 8) torr. After addition of fresh L-15 medium, pO_2 immediately approaches oxygenation levels measured at $t = 0$ h for the spheroid sample, with a measured value of (76 ± 5) torr, then decreases to (62 ± 4) torr within 0.5 h after addition and approaches a 35 % lower value of (49 ± 4) torr at $t = 10.25$ h. This result closely resembles kinetics of initial gradient formation, indicating that medium addition does not influence the metabolism of the spheroid. Addition of fresh L-15 medium leads to a slight initial decrease of medium pO_2 to (135 ± 8) torr, quickly recovering to values of air saturated solutions. Changes in the lateral oxygen gradient formed by the spheroid before and after addition of fresh L-15 medium are also clearly visible in the sensor response at $t = 8$ h and $t = 8.5$ h, shown in the raw data and corresponding false color oxygen images in **Fig. 6.6, B**. The images also indicate that medium exchange does not alter the position of the spheroid or detach the spheroid. After 8 h, a stable oxygen gradient is established (a), while addition of fresh L-15 medium leads to a temporary reoxygenation of the inner part (b). The complete time series of false color oxygen imaging data is provided by **Video 11.9**. Cross sections through the central parts of the 2D false color oxygen images recorded at $t = 8$ h and $t = 8.5$ h depicted in **Fig. 6.6, C** show differences in the steepness of the oxygen gradient and central oxygenation levels, while oxygenation of the bulk phase is only slightly influenced by medium exchange and subsequent equilibration. pO_2 measured at the left and right edge of the spheroid yields similar values of 70 torr and 70 torr before and 87 torr and 85 torr after addition of fresh L-15 medium (dashed lines in **Fig. 6.6, C**). Diameter of areas below an oxygen partial pressure of 59 torr decrease by about 80 % from 440 μm at $t = 8$ h to 90 μm at $t = 8.5$ h. However, the diameter of low pO_2 approaches dimensions equivalent to basic values of about 450 μm within 13 h.

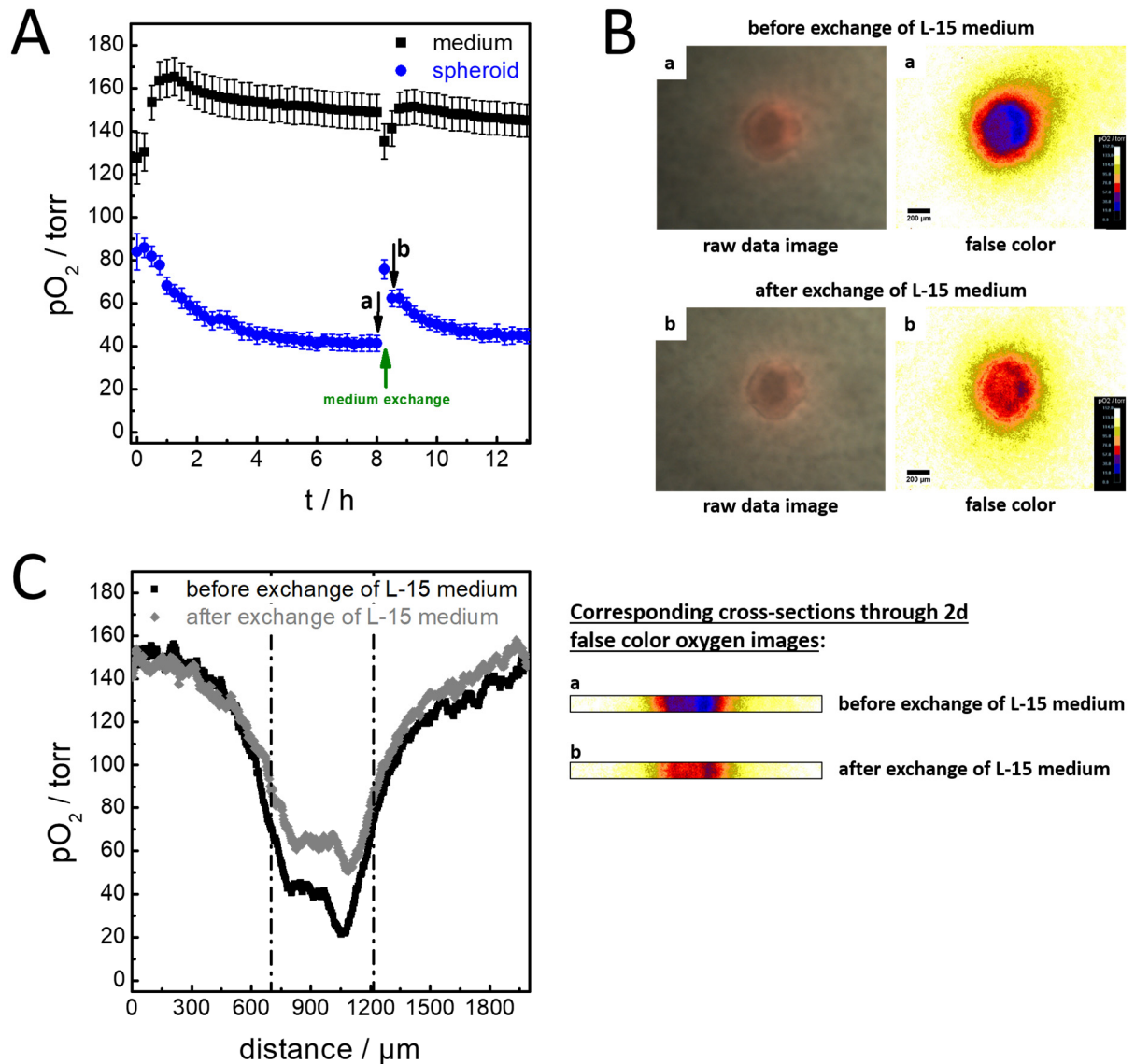


Fig. 6.6 MCF-7 spheroid imaged under control conditions. (A) Changes in oxygen levels in the bulk phase and spheroid center, respectively, over a measurement period of 12 h. After monitoring gradient formation in L-15 medium, fresh L-15 medium was added at $t = 8$ h. Black arrows indicate time points directly before (a) and 0.5 h after addition (b) of fresh L-15 medium, while the green arrow marks the time point of medium exchange. (B) Raw data images and corresponding false color oxygen images recorded directly before (a) and 0.5 h after (b) addition of fresh L-15 medium. (C) Cross sections the spheroid at $t = 8$ h (■) and $t = 8.5$ h (◆) and the corresponding sections through the 2D false color oxygen images, showing lateral pO_2 of bulk phase and spheroid. Dashed lines indicate the transition from the spherical part of the spheroid to the monolayer. Measurements were repeated twice with similar results ($n = 2$). $T = 37$ °C.

Fig. 6.7 shows oxygen imaging results of one MCF-7 spheroid treated with the uncoupler malonoben (100 nM) which strongly enhances cellular oxygen consumption by uncoupling oxidative phosphorylation. **Fig. 6.7, A** illustrates the temporal changes in pO_2 of two ROIs located in the bulk phase or the inner spheroid. After the start of the measurement, average pO_2 in the center of the spheroid is (96 ± 4) torr. Oxygenation values decrease within 2 h to (68 ± 4) torr, finally reaching (47 ± 5) torr at $t = 8$ h (**Fig. 6.7, A, ●**). After addition of 100 nM Mal in L-15 medium, central spheroid

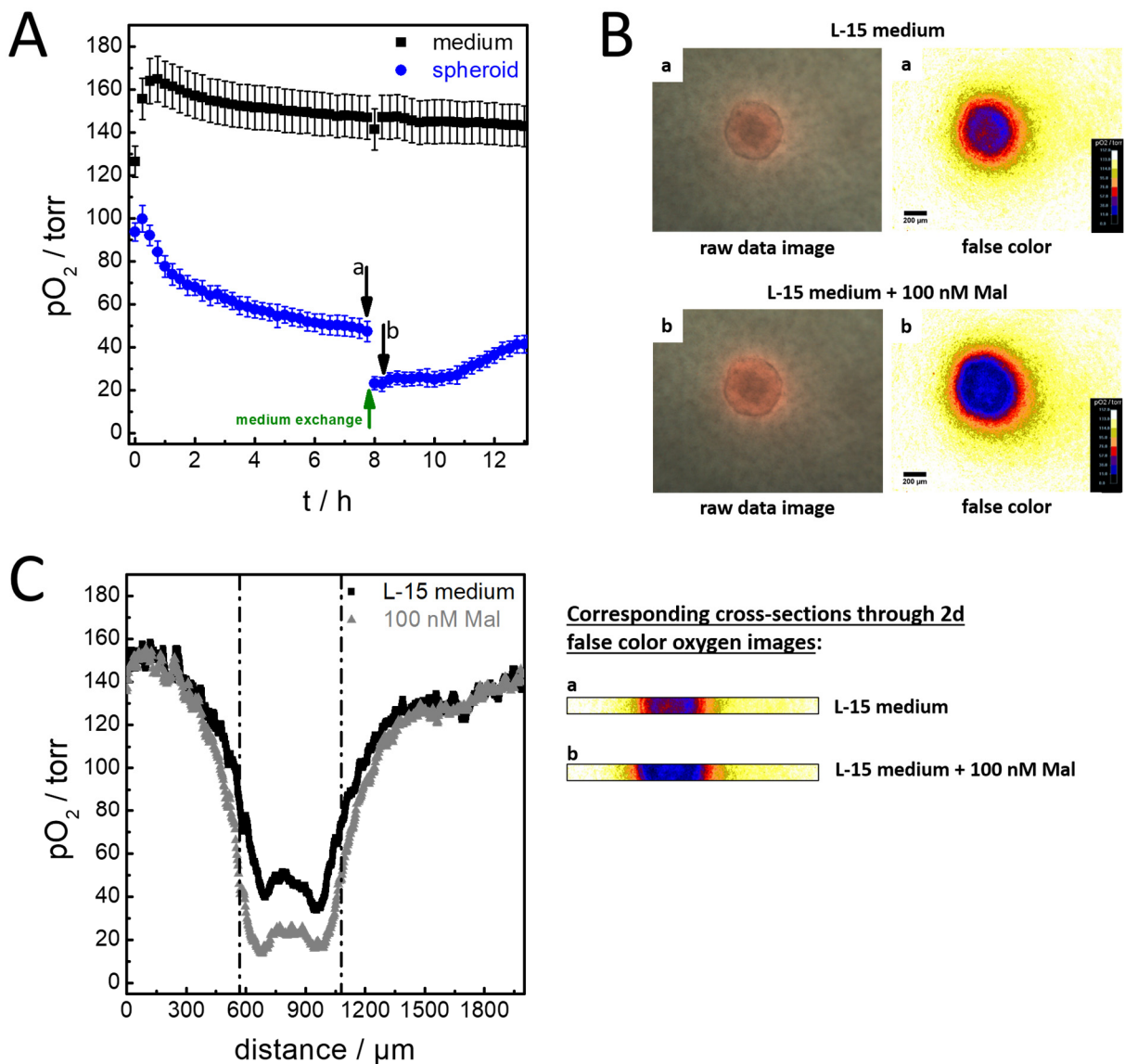


Fig. 6.7 MCF-7 spheroids treated with 100 nM malonoben in L15 medium. (A) Changes in pO_2 of two different ROIs as a function of time. Gradient formation was first monitored in L-15 medium. After 8 h fresh L-15 medium containing 100 nM Mal was added. Black arrows indicate time points directly before (a) and 0.5 h after addition (b) of 100 nM Mal, while the green arrow indicates the time point of medium exchange. (B) Corresponding raw data and false color images captured before (a) and 0.5 h after addition (b) of the uncoupler. (C) Histograms showing lateral changes in spheroid oxygenation before (■) and 0.5 h (▲) after addition of 100 nM malonoben. Dashed lines indicate edges of the spherical part. Data represents results of one typical measurement. Imaging experiments were conducted with three individual samples, yielding similar results ($n = 3$). $T = 37^\circ\text{C}$.

oxygenation immediately drops by about 50 % to a value of (23 ± 3) torr, staying constantly below values determined in L-15 medium. However, reoxygenation of central areas approximately 3 h after addition of Mal reach (42 ± 4) torr at $t = 13$ h, a level which is equivalent to basic values measured before addition. Changes in bulk phase show a similar curve progression as in the control measurement described in **Fig. 6.6, A** with oxygen levels resembling normoxic conditions. The effect of the uncoupler on spheroid oxygenation is even more pronounced when looking at the raw data

and false color oxygen images (**Fig. 6.7, B**). Upon addition of 100 nM Mal, the sensor response raw data below the spherical part of the spheroid is clearly shifted to a more intense and brighter red emission of the oxygen sensor dye. This corresponds to an increased area of low pO_2 and a steepening of the oxygen gradient by uncoupling the cellular respiration. **Video 11.10** stored on the supplementary DVD animates the complete time series of false color oxygen images. This trend is also visible in the corresponding histograms (**Fig. 6.7, C**). pO_2 determined at the transition region from the monolayer to the spherical part (dashed lines) decreases from 79 torr to 41 torr on the left side and from 73 torr to 47 torr on the right side of the attached spheroid. The cross sections show, that the width of the part below an oxygen partial pressure of 59 torr increases by about 30 % from about 400 μm at $t = 8$ h to about 540 μm at $t = 8.5$ h with an overall a drop of the average pO_2 . However, minimal values of 34 torr to 14 torr before and after addition of 100 nM Mal do not reach complete hypoxia which is reported to show pO_2 values below 10 torr.

When MCF-7 spheroids are treated with antimycin A, the blocking effect completely inhibits cellular respiration, leading to a breakdown of the oxygen gradient as depicted in **Fig. 6.8**. Bulk phase and inner spheroid oxygenation is plotted as function of time in **Fig. 6.8, A**, showing the typical curve progression from initial lower pO_2 of (133 ± 9) torr to normoxic levels around 150 torr. Addition of 2 μM Ant A after $t = 8.5$ h does not influence the measured oxygen levels in L-15 medium yielding stable values around 150 torr (**Fig. 6.8, A, ■**). The ROI representing the inner spheroid oxygenation yields an initial value of (100 ± 5) torr for a MCF-7 spheroid in L-15 medium at $t = 0$ h (**Fig. 6.8, A, ●**). After 2 h, central pO_2 decreases by about 45 % to (55 ± 4) torr. Immediately before addition of 2 μM Ant A at $t = 8.5$ h, mean pO_2 has further decreased to (31.6 ± 3.2) torr. Medium exchange leads to a rapid reoxygenation. No subsequent decrease of pO_2 is observed due to the exposure to 2 μM Ant A. A pO_2 value of (156.6 ± 6.8) torr is measured 0.5 h after addition of the blocking agent. No further deoxygenation is recorded probably due to the irreversible inhibition of oxidative phosphorylation. Breakdown of the oxygen gradient is clearly visible in **Fig. 6.8, B** depicting raw data and corresponding false color images showing 2D oxygen distribution at $t = 8.5$ h (a) and $t = 9$ h (b). Before addition of Ant A, the oxygen gradient created by the actively respiring spheroid in L-15 medium is clearly visible in the false color oxygen image. Although the spherical part of the spheroid is still visible on the raw data image after addition of Ant A, the false color oxygen image shows a homogeneous distribution of P_x values in the normoxic range of 150 torr (for the complete time series, see **Video 11.11**). This is also visible in the histograms in **Fig. 6.8, C**. The inner area with pO_2 values below 59 torr of the MCF-7 spheroid in L-15 medium is about 450 μm in diameter, with

a minimal oxygen partial pressure of 21 torr and values of 64 torr and 70 torr measured at the transition region. 2 μM Ant A leads to a complete reoxygenation not only at the edges with 159 torr on the left side and 149 torr on the right side, but also in the central part with pO_2 levels between 154 torr and 174 torr, matching values of the surrounding medium. Additionally, longer exposure to 2 μM Ant A seems to influence spheroid morphology. Comparison of spheroid outlines of raw data images reveals an increase in size by about 15 % 2 h after addition of Ant A as shown in supplementary information, **Fig. 11.16**.

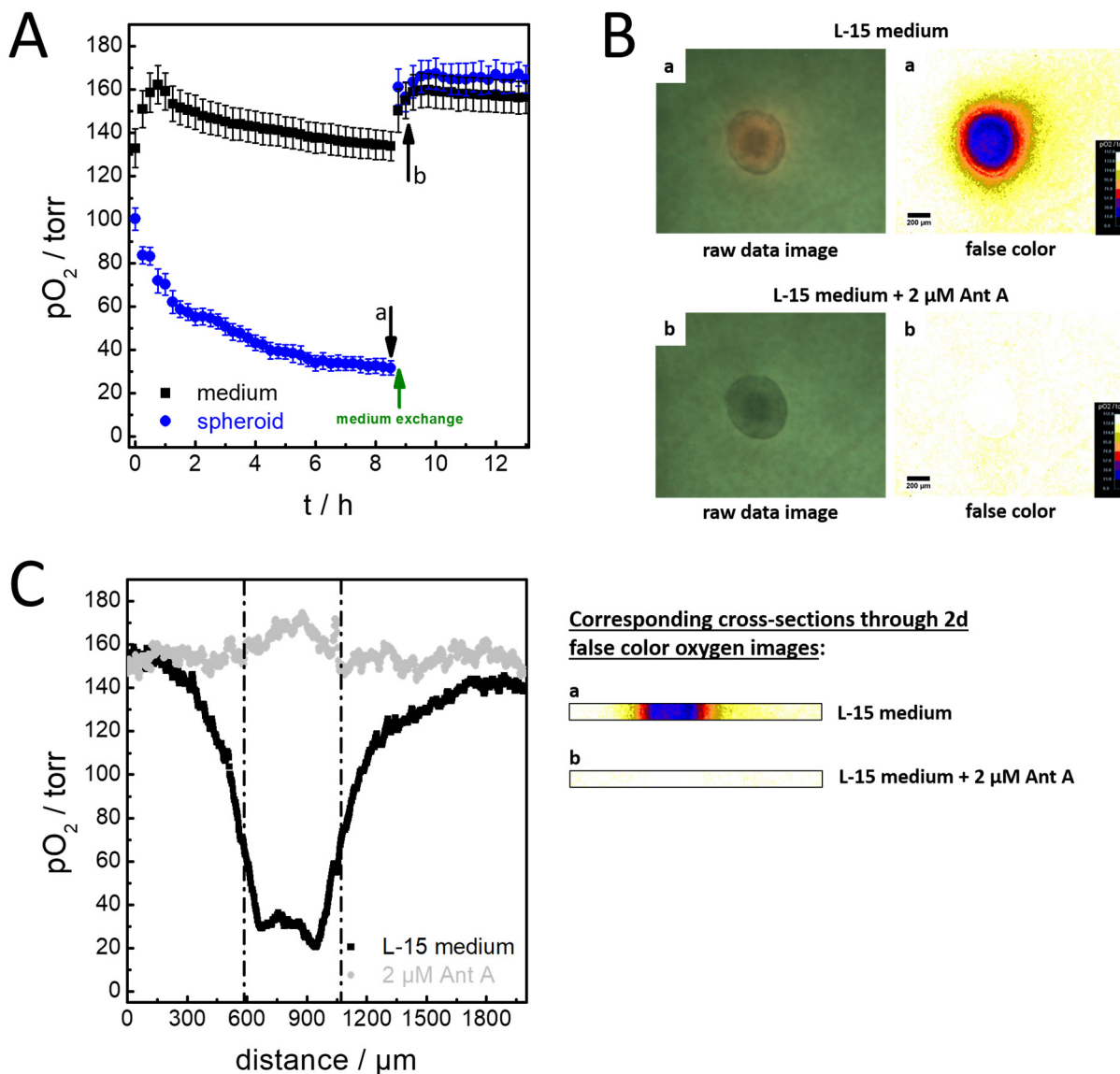


Fig. 6.8 MCF-7 spheroids treated with 2 μM antimycin A to block oxidative phosphorylation. (A) Changes in pO_2 of two different ROIs as a function of time. Gradient formation was first monitored in L-15 medium. After 8.5 h, fresh L-15 medium containing 2 μM Ant A was added. Black arrows indicate time points directly before (a) and 0.5 h after addition (b) of 2 μM Ant A, while the green arrow indicates the time point of medium exchange. (B) Raw data and corresponding false color images captured before (a) and 0.5 h after addition (b) of Ant A. (C) Cross sections showing lateral changes in spheroid oxygenation before (■) and 0.5 h (●) after addition of 2 μM Ant A. Dashed lines indicate transition from the spherical part to the monolayer. The data represents results of one typical experiment. Imaging experiments were repeated twice yielding similar results ($n = 2$). $T = 37^\circ\text{C}$.

6.4 DISCUSSION

6.4.1 IMAGING OXYGEN GRADIENTS IN MCF-7 SPHEROIDS

The VisiSens TD mic system was used for non-invasive monitoring of oxygen gradient formation in MCF-7 spheroids. The planar oxygen sensor foil was found to exhibit excellent cytocompatibility. Additionally, planar oxygen sensor foils did not induce phototoxicity. This allowed long-term cultivation and oxygen monitoring of MCF-7 spheroids on the oxygen sensitive foils. As described in **chapter 6.2.1**, oxygen gradient formation was monitored online with a time resolution of 10 min. 2D false color oxygen images showed the formation of a stable gradient within a few hours with low pO_2 in the center underneath the spheroid, a steep increase towards the edges and oxygen levels similar to air saturated medium outside the spheroid. Although so far no data is available in literature on the kinetics of oxygen gradient formation beneath spheroids, a number of studies have been conducted to determine spatial distribution of oxygen within spheroids. Mueller-Klieser and Sutherland used microelectrodes to measure oxygen gradients within EMT6/Ro spheroids. They observed asymmetric oxygen gradients in spheroids with non-spherical geometry, while oxygen gradients were symmetric in spheroids with spherical geometry. The group measured characteristic pO_2 profiles with a normoxic pO_2 in the bulk phase, a slightly lower pO_2 at the surface of the spheroids, followed by a steep decrease of pO_2 within the rim regions and a plateau in the center (Mueller-Klieser and Sutherland 1982). Similar observations were made in this work. Compared to oxygen measurements conducted with microelectrodes, imaging pO_2 with planar sensor foils allows not only spatial mapping but also temporal mapping of changes in pO_2 . After formation of the oxygen gradient, imaging data showed a symmetric gradient with a steep decrease of oxygenation from the bulk phase towards a homogeneous oxygenation in the center within half spherical MCF-7 spheroids. However, a direct comparison to data found in literature is difficult, as the measurement used in this work set-up detects pO_2 beneath the adhered half-spherical spheroid and not directly inside the spherical cell aggregates.

Monitoring the oxygenation of spheroids of different ages (7 – 9 d) as described in **chapter 6.2.2**, showed no strongly hypoxic areas with a pO_2 below 10 torr that are probably linked to a necrotic core. This result is in agreement with observations made by C. Hupf who could not detect a necrotic core in TEM sections of MCF-7 spheroids up to an age of 9 d (Hupf 2016). It has been found that the onset of necrosis in spheroids is specific for the observed spheroid cell type, spheroid age and

spheroid size (Freyer 1988; Khaitan et al. 2006; Venkatasubramanian et al. 2006). As found by Groebe and Mueller-Klieser, inner pO_2 of WiDr human colon carcinoma spheroids does not reach levels around 0 torr until they reach a certain diameter larger than 500 – 600 μm where they develop a necrotic core (Groebe and Mueller-Klieser 1996; Mueller-Klieser 2000). Jeong et al. observed that only MCF-7 spheroids with a diameter > 700 μm start to exhibit a necrotic core (Jeong et al. 2010). Additionally, mathematical models have been developed that describe oxygenation within spheroids and predict hypoxic, necrotic and proliferating regions. Data modelled for DLD1 spheroids showed that spheroids with a diameter of 400 μm do not exhibit strong hypoxia, but their central pO_2 is at a value of about 30 torr, while pO_2 at the edge is about 100 torr (Grimes et al. 2014). These findings are similar to observations described in this work, where MCF-7 spheroids with a size between 400 and 600 μm were monitored, yielding a mean inner pO_2 between 20 and 50 torr, depending on passage number and age. However, the comparison between data found in literature and data from this work relies on the assumption that the oxygenation of spherical and surface-attached half-spherical spheroids is the same even though diffusion from below is inhibited by the oxygen impermeable layer of the sensor foil. Reports on oxygenation in half spherical structures have not yet been published. Additionally, imaging data showed a general but not significant tendency that the inner area with a pO_2 below 59 torr increased with increasing age of the MCF-7 spheroids probably due to increasing size of the cell aggregates. However, size of the area was strongly dependent on passage number of cells used to form the spheroids. Although nothing is known about age dependent oxygenation in spheroids, results from literature state that oxygen levels in spheroids strongly depend on the cell type, spheroid size, ambient oxygen content and cultivation conditions. It was found that V-79 spheroids cultivated in spinner flasks exhibit lower inner pO_2 compared to samples cultivated under static conditions (Carlsson et al. 1979; Kaufman et al. 1981). Oxygenation profiles of EMT6/Ro and V-79 spheroids were found to be significantly different when samples of similar size were compared. Compared to EMT6/Ro spheroids V-79 Chinese hamster lung fibroblast aggregates had a steeper decrease of pO_2 in the rim and considerably lower inner oxygen partial pressure (Mueller-Klieser and Sutherland 1982). Newer studies suggest that oxygenation of E18 neurospheres depend on the size of the sample. Intracellular oxygenation was measured by lifetime imaging of small molecular phosphorescent probes. While smaller samples of about 60 μm diameter showed no lateral oxygen gradient but a homogeneous 2D spatial oxygen distribution, spheres larger than 250 μm exhibited symmetric

oxygen gradients with a plateau of about 35 torr in the central area and a pO_2 of about 100 torr at the edge facing the bulk phase (Dmitriev et al. 2014).

As shown in **chapter 6.2.3**, imaging experiments conducted with the novel imaging system VisiSens TD mic generated highly detailed false color oxygen images with a better resolution compared to commercial oxygen imaging systems. With a resolution of $1.6 \mu\text{m}/\text{Px}$, images depicting lateral oxygen gradients caused by MCF-7 spheroids were recorded, showing in detail central areas with low pO_2 and transition zones from the center to the surrounding medium. Therefore, the novel imaging set-up clearly outperforms the commercial system where rim regions could not be distinguished from the central regions due to poor spatial resolution. As mentioned above, detailed oxygen gradients were recorded in neurospheres using phosphorescence lifetime imaging microscopy. Compared to measurements done with the VisiSens TD mic system, PLIM possesses higher resolution as the system is equipped with a 20x magnification objective. However, this set-up is mainly used for recording snapshots and not for long-term online monitoring. As already mentioned in **chapter 1.2**, sensor particles are introduced into the spherical aggregates for PLIM analysis. This method is invasive and may affect spheroid morphology and integrity. Additionally, particle stability and photobleaching may also be problematic (Papkovsky and Dmitriev 2013) and no studies have been conducted that report on phototoxicity in long term PLIM analysis. In contrast to PLIM, VisiSens TD mic allows online monitoring of spheroid oxygenation with good spatial and temporal resolution. As spheroid size is a few hundred μm , an objective with 5x magnification is sufficient to image the whole spheroid. The ratiometric oxygen sensor foils are biocompatible and highly photostable. Besides, the set-up can be used to conduct long-term measurements as no phototoxic damage to spheroids was detected after an continuous imaging period of 3.5 d.

6.4.2 EXPOSURE TO DRUGS INFLUENCING OXIDATIVE PHOSPHORYLATION

Oxygen imaging of MCF-7 spheroids treated with drugs influencing oxidative phosphorylation showed that oxygenation within control spheroids treated with culture medium is not influenced by medium exchange. As the results in **chapter 6.3** show, kinetics of gradient formation is similar each time fresh culture medium is added, with similar oxygen values measured in the rim and center region.

Results for MCF-7 spheroids treated with the protonophore malonoben show a similar trend compared to oxygenation data reported on other spheroid types. Though, no data is available

reporting on uncoupling of multicellular spheroids with malonoben, studies have been conducted with uncouplers that have the same mode of action such as CCCP, FCCP or DNP. However, most studies rely on the pimonidazole staining method to determine regions of low pO_2 – a method which is known to be highly prone to errors – while studies using optical oxygen sensors are scarce. Experiments conducted with pimonidazole stained HCT116 spheroids treated with the uncoupler CCCP show an increase in area of low pO_2 compared to control spheroids cultivated in medium (Zhang et al. 2014). Furthermore, after 24 h incubation with the protonophore, reoxygenation of the hypoxic region was observed by pimonidazole staining of spheroid sections. This phenomenon was explained by upregulation of glycolytic rates and downregulation of oxidative phosphorylation (Senkowski et al. 2015). Deep, continuous deoxygenation for a few hours followed by reoxygenation was also monitored in medium containing galactose, pyruvate and glutamine (Zhdanov et al. 2014). This is consistent with observations made in MCF-7 spheroids that were monitored in L-15 medium/Mal that also contains galactose, pyruvate and glutamine. There, deep deoxygenation was observed for about 3 h followed by reoxygenation to baseline levels. Furthermore, PLIM experiments performed with neurospheres led to increased phosphorescence lifetime of the incorporated sensor probes when cell aggregates were treated with 2 μ M FCCP. While resting spheres exhibited oxygenation levels of about 100 torr, uncoupling caused a pO_2 decrease of about 65 % to 35 torr (Dmitriev et al. 2015). This is similar to a decrease in oxygenation of about 50 % measured in this work.

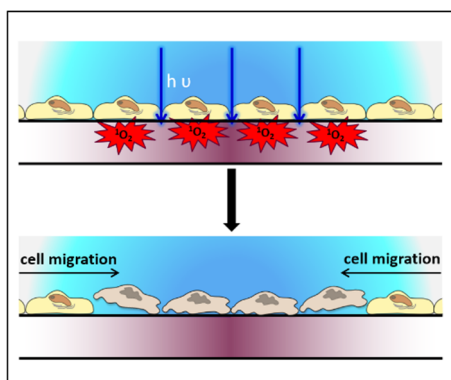
The breakdown of oxygen consumption caused by antimycin A is consistent with results published in literature. Although no data reports on the effects of Ant A in MCF-7 spheroids, complete reoxygenation was detected in pimonidazole stained cryosections of HTC116 spheroids (Klutznny et al. 2017) and FaDu spheroids (Ashton et al. 2016) that had been treated with 0.2 – 1 μ M antimycin. Analysis of spheroid oxygenation by phosphorescent lifetime imaging showed an immediate response after Ant A addition. Neurospheres treated with the inhibitor modulate intracellular pO_2 measured through the whole spheroid to air-saturated levels within a few minutes (Dmitriev et al. 2015). The immediate response to Ant A is consistent to imaging data of MCF-7 spheroids where inhibition of complex III leads to reoxygenation to air-saturated levels within 15 min. Furthermore, it has been shown that mitochondrial health of HCT116 spheroids is negatively affected by Ant A with concentrations above 200 nM inducing cell death (Sirenko 2016). The cytotoxic effect of Ant A may also trigger the volume increase of MCF-7 spheroids caused by swelling and disruption of the cell aggregates.

However, all data reported so far on the effects of drugs on 3D tissue models, such as blockers and uncouplers of oxidative phosphorylation rely on end-point assays, such as immunofluorescent labeling of spheroid sections. Studies conducted by phosphorescent lifetime imaging are not to be laid out for continuously monitoring of samples but rely on snapshots from one defined time point. This gap of lacking information on long-term online monitoring of oxygen gradients and oxygen consumption of spheroids exposed to drugs is now closed, as shown by optical ratiometric imaging with 2D oxygen sensor foils and the microscopic imaging system VisiSens TD mic.

6.5 OUTLOOK

The VisiSens TD mic system enables detailed imaging of oxygen gradients within tissue models. Optical imaging is non-invasive and its good cytocompatibility allows long term monitoring of spatial changes in oxygenation with good temporal resolution. To study kinetics of drug actions on oxygen gradients temporal resolution can be further improved by adjustment of the software and increase of computational storage capacity. For monitoring spheroids with smaller size, the lateral resolution can be enhanced by changing the magnification of the objective from 5x to a higher magnification. However, the system is still limited regarding its low throughput. Up to now, obtaining reproducible measurement data is time-consuming, as a maximum of two samples can be measured per day. To make the imaging system a promising candidate for pharmacological screening studies, future efforts should be undertaken to image multiple samples simultaneously. This could be for example done by using a combination of multiwell-plates equipped with planar sensor spots and a motorized xy-stage for plate movement without suffering the loss of high resolution. Coordinated image recording and plate movement would for example allow for parallel, long-term imaging of dose-response relationships within one experiment.

7 DEVELOPMENT OF AN OPTICAL WOUND HEALING ASSAY



Luminescence collisional quenching of sensor dyes by triplet oxygen leads to the production of singlet oxygen that is highly cytotoxic. Although its lifetime is short, direct exposition to singlet oxygen leads to oxidation of biomolecules, such as proteins, lipids or nucleic acids. Exposure to high concentrations of 1O_2 ultimately results in apoptotic and/or necrotic cell death (Klotz et al. 2003). This damaging effect is

for example exploited in photodynamic therapy, that uses oxygen sensitive dyes as photosensitizers to systematically target and destroy cancer tissue (Chandra et al. 2000). Additionally, oxygen sensor dyes are also used in photodynamic inactivation of a broad spectrum of clinical relevant pathogens. The highly efficient production of 1O_2 by photosensitizers is applied to treat local inflammations in patients caused by pathogens, such as viruses, fungi or antibiotic resistant, biofilm-forming bacteria (Hamblin 2016).

Wound healing assays are a useful approach to study physiological processes *in vitro* related to coordinated cell migration as occurring during embryogenesis, metastasis and regeneration (Riahi et al. 2012). In this project, the production of 1O_2 by oxygen sensor dyes and its ability to efficiently kill cells is used to develop a novel optical wound healing assay for probing collective cell migration. By spatially confined illumination of oxygen sensitive culture substrates, wounds in a confluent cell layer should be created to study the migration behavior of cells in the periphery of the wound. Therefore, a thin polymer film with an incorporated oxygen sensor dye were deposited upon cover glasses by spin coating. These oxygen sensitive substrates are the basis of the wound healing assay and they were analyzed regarding their biocompatibility. The influence of parameters such as different light sources, microscope filter settings and culture medium used for wounding on the wound healing process of confluent NRK cell layers was investigated. The novel wound healing assay was compared to commonly used wound healing assays such as the scratch, barrier or electrical ECIS[®] assay. Furthermore, initial proof-of-concept studies were performed to study wound healing under various conditions, such as serum starvation or differences in extracellular pH, to show the potential of the novel optical assay.

7.1 CHARACTERIZATION OF OXYGEN SENSITIVE SUBSTRATES DESIGNED FOR WOUND HEALING

7.1.1 BIOCOMPATIBILITY AND WOUND GEOMETRY

Oxygen sensitive substrates designed for wound healing were produced by doping the biocompatible polymer polystyrene (PS) with the oxygen sensor dye PtTFPP and subsequent deposition on a glass coverslip by spin coating as described in **chapter 3.5.1**. For application in an optical wound healing assay, PS/PtTFPP substrates must not induce cytotoxicity during cell cultivation. Therefore, NRK cells were seeded subconfluently on standard cell culture petri dishes or PS/PtTFPP substrates and cell adhesion and proliferation was monitored over 96 h as depicted in **Fig. 7.1**. Cell morphology is evaluated by standard light microscopy as the functionalized substrates are optically transparent due to a mean thickness of the polymer layer of about $(1.40 \pm 0.02) \mu\text{m}$ (thickness was determined via profilometry by J. Sondhauß, nanoAnalytics GmbH, Münster). Phase contrast micrographs recorded 24 h after cell inoculation show that NRK cells are adhered to PS/PtTFPP. Cells on PS/PtTFPP substrates showed similar proliferation behavior compared to cells cultivated on control substrates confluent covering the substrates 96 h after cell inoculation. These results indicate that biocompatibility of PS/PtTFPP substrates is similar to standard cell culture substrates.

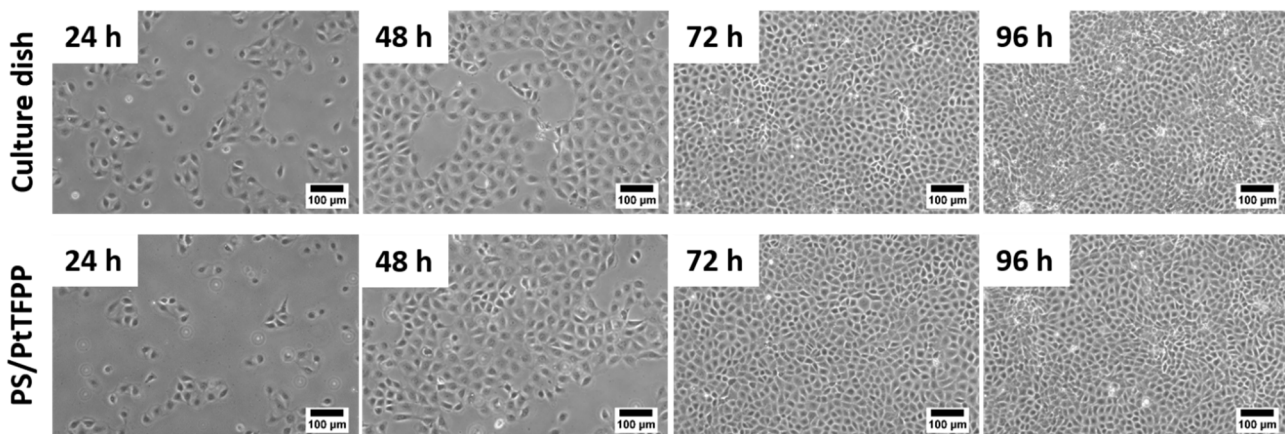


Fig. 7.1 Phase contrast images of NRK cells seeded subconfluently ($2.5 \times 10^4 \text{ c cm}^{-2}$) to the PS/PtTFPP coated substrate and a standard cell culture dish. Micrographs show adhesion and proliferation behavior as a function of time. NRK cells grown on the novel substrate designed for wound healing do not exhibit differences in spreading and proliferation characteristics compared to control conditions.

For successful creation of a wound, the substrates needed to be highly phototoxic upon illumination. For quantifying cellular wound healing processes reproducibly, the wounds need to exhibit a consistent geometry with a defined boundary separating live and dead cells created by illuminated and non-illuminated parts of the oxygen sensitive culture substrate. Depending on the illumination set-up, the wound geometry in confluent NRK cell layers can be defined as shown in **Fig. 7.2**. A linear wound of about 1500 μm in length and 100 μm in width is created when using the 408 nm confocal laser in line scan mode and an objective with 10x magnification as depicted in **Fig. 7.2, A**. Here, the sample was illuminated for 0.5 min. Cell death is initiated rapidly after wounding, with changes in cell morphology visible within 10 – 15 min. Phase contrast images recorded after illumination show a clear morphological difference between cells exposed to laser light and those that were not. In contrast to cells in the periphery of the field of illumination, exposed NRK cells exhibit volume shrinkage with small, condensed nuclei, but remain settled on the wounded areas. The difference in cell viability was also checked by live-dead staining verifying the observations made by phase contrast microscopy. Cells growing in the area exposed to laser light were completely killed by the emerging $^1\text{O}_2$, exhibiting a bright red nuclear fluorescence of EthD-1, while non-illuminated cells remained vital, as marked by the strong green cytoplasmic fluorescence of CaAMin a live-dead assay. **Fig. 7.2, B** illustrates samples illuminated for 0.5 min with a mercury arc lamp through a UV-2A filter block ($\lambda_{\text{ex}} = 380 \text{ nm}$, $\lambda_{\text{em}} \geq 420 \text{ nm}$) and a 4x objective. Equivalent to the circular field of view, a roughly circular wound with a diameter of about 400 μm is created. Analogous to the exposure to laser light, irradiated cells die, while non-illuminated cells remain unaffected as depicted in the corresponding phase contrast and fluorescence micrographs. Wound geometry can also be altered to create wounds with custom-made shape using inkjet printed masks as shown in **Fig. 7.2, C**. By placing the mask in front of the sample, the circular shape of the incident light beam is modified, for example, to display the logo of the University of Regensburg. To create the wound, samples were irradiated with a mercury arc lamp through a UV-2A filter block and a 4x objective. Due to the bigger size of the mask compared to the field of view, the objective was manually moved repeatedly back and forth to ensure uniform illumination. In total, the sample was illuminated for 5 min to cover the whole mask and a wound with a length of about 5 mm and a height of about 4 mm is created. The generated wound clearly corresponds to the emblem of the University of Regensburg showing illuminated, dead cells surrounded by vital cells. These results show that the novel substrates designed for wound healing can be used in combination with different illumination set-ups. Wound geometry can be flexibly tailored to any pattern required by the application with

the help of optical masks. Wounding takes place independent of the selected light source (laser, mercury arc lamp) as long as the emitted wavelength matches the absorption spectrum of the oxygen sensor dye PtTFPP. As linear wounding produced the most homogeneous wounds, all studies presented in the subsequent chapters were done using linear wounding by a 408 nm confocal laser in line scan mode.

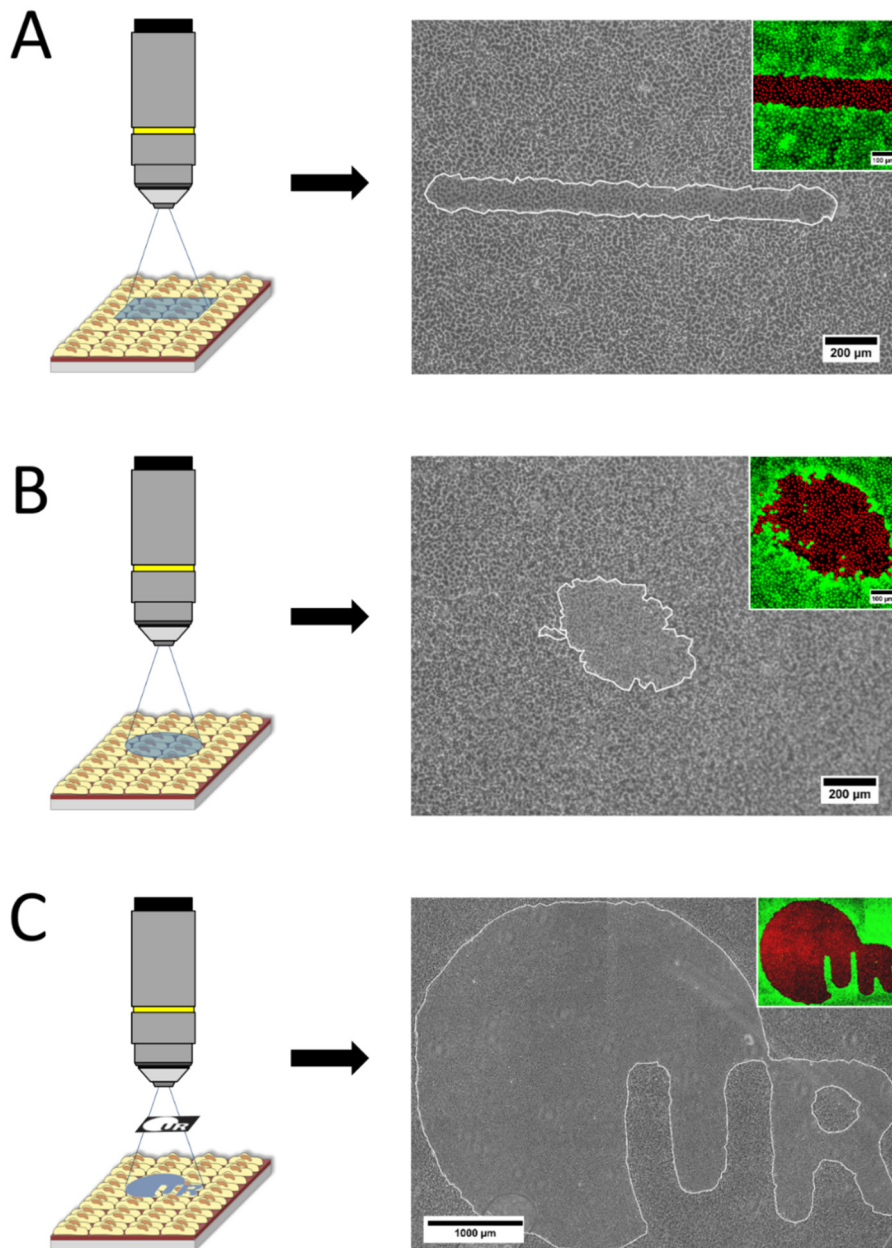


Fig. 7.2 Differences in wound geometry in confluent NRK cell layers. Wound geometry is defined by the geometry of the incident light beam. (A) Linear wounding is accomplished by using the line scan mode of a 408 nm confocal scanning laser that irradiates the substrate through a 10x objective. Phase contrast image of the linear wound. The small inset shows live dead staining of the wound region with live cells exhibiting green cytoplasmic fluorescence and dead cells showing red fluorescing nuclei. (B) A circular wound can be created by illumination of the samples using a 4x objective and a standard mercury arc lamp. Phase contrast image and corresponding live-dead staining of the circular wound. (C) Cell wound corresponding to the emblem of the University of Regensburg is created by illuminating the samples through an inkjet printed mask with a 4x objective. Phase contrast image with corresponding live-dead staining. For better visualization of phase contrast images, wound edges were accentuated by white outlines using the NIH ImageJ software.

7.1.2 DEPENDENCY ON EXCITATION WAVELENGTH

To show that wounding of cells is mediated through $^1\text{O}_2$ generated by phosphorescence quenching of PtTFPP and not caused by direct laser irradiation of cells and/or the polystyrene substrate, confluent NRK cell layers were grown on PS/PtTFPP coated substrates, while control cells were grown on self-made substrates coated with polystyrene without PtTFPP. Both samples were irradiated for 2 min with three different confocal lasers in line scan mode without decreasing the intensity of the laser light by using neutral density filters as described in **chapter 7.1.4**. Cell viability was checked 1 h after illumination microscopically using the live-dead stain. Because PtTFPP has a sharp excitation peak at around 400 nm, only illumination with a 408 nm laser should introduce wounds due to $^1\text{O}_2$ generation by collisional quenching of the dye and $^3\text{O}_2$ (for corresponding excitation and emission spectra of PtTFPP, see supplementary information, **Fig. 11.17**).

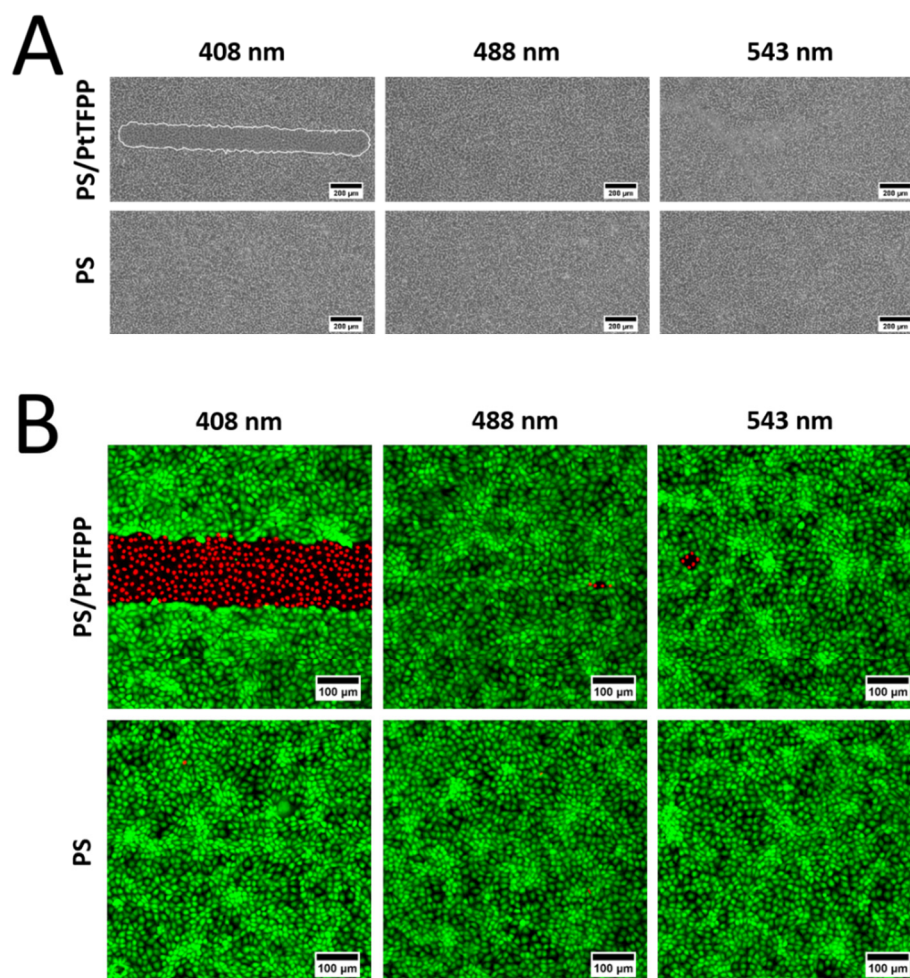


Fig. 7.3 (A) Phase contrast images of NRK cells grown on PS/PtTFPP or PS coated substrates that were illuminated for 2 min with 408 nm, 488 nm or 543 nm laser light. Wounds are only generated when PS/PtTFPP is excited with the adequate wavelength of 408 nm. Illumination of control substrates with both, adequate and non-adequate wavelengths does not introduce wounds into the cell layer. (B) Corresponding fluorescence micrographs of NRK cells stained with 2 μM CaAM and 4 μM EthD-1 with dead cells exhibiting red fluorescing nuclei and vital cells emitting a green cytoplasmic fluorescence.

Excitation of the functionalized substrates for 2 min with 408 nm introduced a linear wound into the monolayer, while excitation of polystyrene substrates with the same wavelength did not harm the cells at all as shown in **Fig. 7.3, A**. The same samples were fluorescently labeled with 2 μM CaAM and 4 μM EthD-1 to mark live and dead cells (**Fig. 7.3, B**). No wounding occurs after 2 min excitation of PS/PtTFPP substrates with 488 nm or 543 nm because the laser light does not match the excitation spectrum of PtTFPP. Here, the fluorescence micrographs show a vital monolayer. Moreover, no wounding of NRK cells grown on PS substrates occurs when samples are illuminated for 2 min with 408 nm, 488 nm or 543 nm. CLSM images depict that all samples show vital cells without any indication of cell wounding, with live NRK cells emitting green cytoplasmic fluorescence of CaAM. However, the energy output of the three different lasers varies as summarized in **chapter 3.3.3**. The energy output of the 408 nm laser is about 10 – 100 times higher compared to the 488 nm and 543 nm laser. Thus, to fully compensate the differences in energy output it would be necessary to increase illumination time about the factor 10 to 100. This approach wasn't pursued further as it would have yielded unreasonable long illumination times.

Nevertheless, these results indicate that a 2 min illumination with laser light does not induce a damage of the monolayer per se when cells are grown on PS substrates. Wounds can be selectively generated by excitation of the oxygen sensitive dye PtTFPP with 408 nm and the resulting singlet oxygen generation.

7.1.3 DEPENDENCY ON CULTURE MEDIUM

Different cell lines require different culture media containing different additives, such as vitamins that could act as scavengers or the indicator phenol red that could partially absorb the light used for excitation of the photosensitizer. However, the novel wound healing assay should be applicable to different cell lines and medium compositions.

To study the influence of different media on wounding efficacy, confluent NRK cells were cultivated on PS/PtTFPP substrates and illuminated in three different culture media (L-15 medium, PBS⁺⁺ and NRK culture medium). Wounding was done by a 408 nm laser in line scan mode that illuminated the samples for 0.5 – 2 min through a neutral density (ND 4) filter. Exemplary phase contrast images of linear wounds generated in NRK monolayers that were cultivated in three different media are illustrated in **Fig. 7.4, A**. No change in linear wound geometry due to different media is observed. While the wounded area increases with increasing exposure time to the laser light, the size of the

wounds at one fixed exposure time is similar for samples wounded in L-15 medium, PBS⁺⁺ or NRK culture medium as shown in **Fig. 7.4, B**. Wound sizes of samples illuminated for 0.5 min were recorded 20 min after wounding and are between a minimum of $(113000 \pm 12000) \mu\text{m}^2$ for NRK cells cultivated in L-15 medium and a maximum of $(141000 \pm 12000) \mu\text{m}^2$ in culture medium. Wound sizes of samples irradiated for 1 min show minimum values of $(152000 \pm 12000) \mu\text{m}^2$ in PBS⁺⁺ and maximum values of $(187000 \pm 14000) \mu\text{m}^2$ in culture medium. After 2 min illumination, the size of the wounded areas varies between $(188200 \pm 9000) \mu\text{m}^2$ in L-15 medium and $(222000 \pm 17000) \mu\text{m}^2$ in culture medium. These results indicate, that efficient wounding with a 408 nm laser light can be accomplished in different culture media, yielding similar sizes of wounded areas if exposure time is kept constant. Thus, wounding of cells in experiments described in this work was usually done in culture medium if not mentioned otherwise.

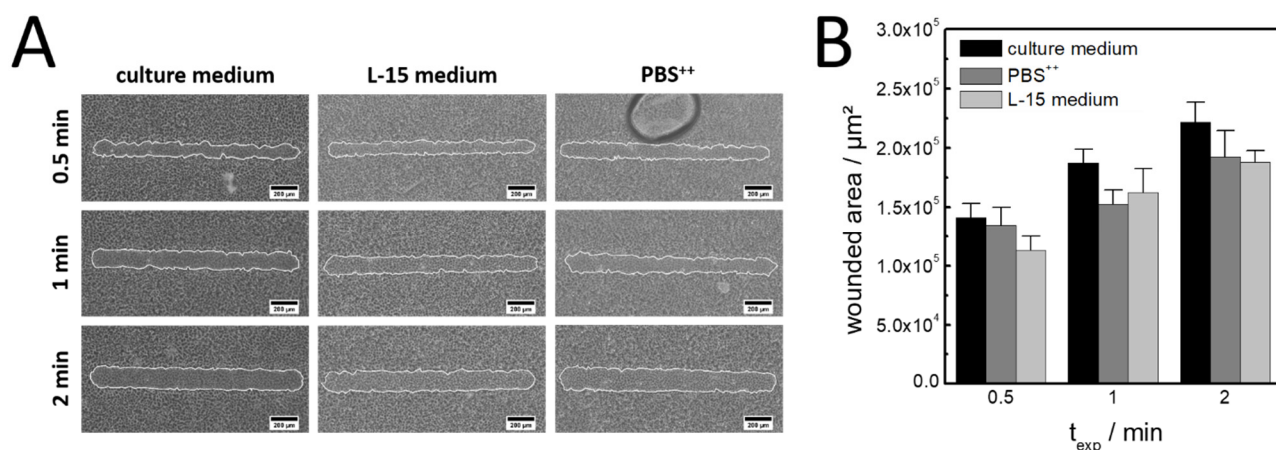


Fig. 7.4 Dependency of wound size on the incubation buffer. Confluent NRK cells inoculated at a density of $2.5 \times 10^5 \text{ c cm}^{-2}$ in petri dishes containing different incubation buffers were exposed to a 408 nm confocal laser in line scan mode. For better visualization of phase contrast images, wound edges were accentuated by white outlines using the NIH ImageJ software. (A) Phase contrast images of the generated wounds in dependency on incubation buffer and illumination time t_{exp} . (B) Changes in wounded area depending on culture medium and illumination time. Mean \pm SE; $n = 4$, $T = 37 \text{ }^\circ\text{C}$.

7.1.4 DEPENDENCY ON LIGHT INTENSITY

Wounding efficacy of the confocal laser light was investigated by regulating the intensity of the laser light by filters. To decrease incident light intensity, neutral density (ND) filters were used, that allow the reduction of light intensity without altering the relative spectral distribution of energy. NRK cells were grown to confluence on PS/PtTFPP substrates and wounded with a 408 nm confocal laser. Cells were exposed for 0.5 min, 1 min or 2 min to the laser beam. The intensity of the incident laser light was regulated by using a ND 8 (12.5 % transmittance), ND 4 (25 % transmittance) or no filter. After

wounding, cells were examined using phase contrast microscopy as presented in **Fig. 7.5, A**. As already shown above, the created wound size strongly depends on exposure time, with 2 min illumination generating the largest wounds as depicted in **Fig. 7.5, B**. The use of ND filters results in smaller, linear wounds compared to non-filtered laser light at the same exposure time. When using an ND 4 filter that has a transmittance of 25 %, wound size is reduced to (65 ± 8) % compared to the non-filtered samples exposed for 0.5 min. The shrinkage in wound size is even more prominent when light is passing through a ND 8 filter with 12.5 % transmittance. Here, the size of the wounded areas for samples exposed for 0.5 min decreases to (43 ± 13) % of the non-filtered values. For samples exposed for 1 min to 408 nm laser light, sizes of the wounds reduce from (269000 ± 2000) μm^2 for wounds generated without filter to (165000 ± 12000) μm^2 for wounds created with the ND 4 filter, corresponding to (61 ± 8) % of the area wounded without filtering. Wound size decreases further to (141000 ± 13000) μm^2 when a ND 8 filter is used, reaching (51 ± 8) % of the original wound size. 2 min excitation of PtTFPP generates the largest wounds with a mean wounded area of (325000 ± 30000) μm^2 while illumination through the ND 4 filter provides wounds (59 ± 9) % of the original size. Filtering through the ND 8 filter produces a mean wound size of (183000 ± 16000) μm^2 which corresponds to (57 ± 10) % of the area wounded without filter. To sum up, wound size can be controlled either by controlling the incident light intensity or by tuning exposure periods.

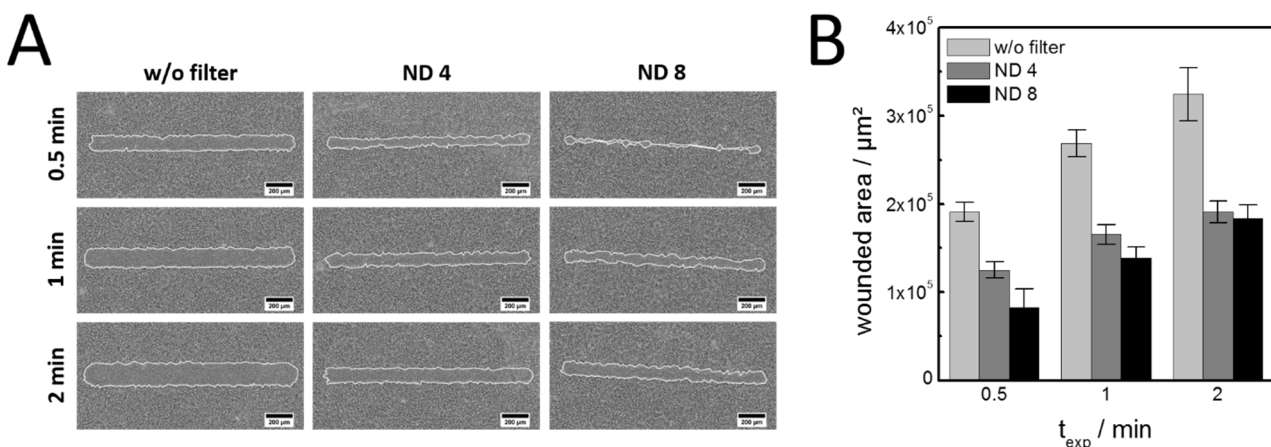


Fig. 7.5 Effect of neutral density emission filters on wound size in confluent NRK monolayers exposed to 408 nm laser light in line scan mode. (A) Typical phase contrast images of wounded cell monolayers in dependency on the neutral density filters used to control light intensity and on exposure times. For better visualization of phase contrast images, wound edges were accentuated by white outlines using the NIH ImageJ software. (B) Changes in the size of the wounded areas in dependency on the light intensity and illumination time. Mean \pm SEM; $n = 8$, $T = 37$ °C.

7.1.5 BLOCKING THE CYTOTOXIC INFLUENCE OF SINGLET OXYGEN BY VITAMIN E

The term vitamin E describes a class of hydrophobic potent antioxidants that protect cells and tissues against a wide variety of damaging effects and pathological conditions caused by $^1\text{O}_2$ and other reactive oxygen species (Ricciarelli et al. 2001). It has eight forms with D- α -tocopherol being the most potent one (Di Mascio et al. 1990). Vitamin E is known to efficiently scavenge $^1\text{O}_2$. Deactivation of $^1\text{O}_2$ to $^3\text{O}_2$ by vitamin E is mainly achieved by physical quenching via radiationless charge-transfer deactivation. One molecule of vitamin E is known to scavenge 40 – 120 molecules of $^1\text{O}_2$ before its scavenging ability is lost (Kamal-Eldin and Appelqvist 1996). However, irreversible oxidation of vitamin E by chemical quenching is also possible (Kaiser et al. 1990). Due to its hydrophobic nature, vitamin E is soluble and stable in nonpolar solvents (Preedy and Watson 2007) and can be incorporated into polymer matrices. This has been used for example in food packaging or orthopedic implants as its antioxidative characteristics enhance shelf-life of products and increase oxidation resistance (Noronha et al. 2014; Bellare et al. 2016).

To prevent $^1\text{O}_2$ induced cell death of cells exposed to 408 nm light, substrates designed for wound healing were doped with the scavenger (D- α -tocopherol) as described in **chapter 3.5.1**. For simplification, D- α -tocopherol used in this work is named vitamin E (Vit E). Confluent NRK monolayers were cultivated on PS/PtTFPP containing different amounts of Vit E. The samples were exposed to 408 nm laser light passing through a ND 4 filter and the scavenging effect of Vit E was studied. The Vit E mediated scavenging scheme of $^1\text{O}_2$ is depicted in **Fig. 7.6, A**. Upon excitation of PtTFPP incorporated into the polystyrene matrix, $^3\text{O}_2$ is converted into cytotoxic $^1\text{O}_2$ by collisional quenching. Emerging $^1\text{O}_2$ is deactivated before reaching the cells via physical or chemical quenching by Vit E that is incorporated into the polystyrene matrix as well. **Fig. 7.6, B** shows phase contrast images of wounded NRK monolayers in dependency on illumination time and Vit E content of the functionalized substrates. 0.5 h after illumination, the samples were stained with 2 μM CaAM and 4 μM EthD-1 to distinguish between live and dead cells, as illustrated in the fluorescence micrographs in **Fig. 7.6, C**. Less $^1\text{O}_2$ is produced when PtTFPP is excited for a shorter time, resulting in smaller wounds. Wound size is reduced by about 95 % from $(112000 \pm 13000) \mu\text{m}^2$ to $(6000 \pm 6000) \mu\text{m}^2$ when cells are illuminated for 0.5 min with 408 nm laser light on PS/PtTFPP containing 1 % (w/w of PS) Vit E as depicted in **Fig. 7.6, D**. A content of 2 % (w/w of PS) Vit E is sufficient to scavenge the amount of singlet oxygen produced during 0.5 min illumination completely, leaving the monolayer intact. When the coated substrates are excited for 1 min, 2 % Vit

E is not sufficient to prevent wounding of cells, although wound size is reduced by about 90 % from $(156000 \pm 12000) \mu\text{m}^2$ on PS/PtTFPP substrates without Vit E to $(17000 \pm 4000) \mu\text{m}^2$. Higher concentrations of Vit E scavenge emerging $^1\text{O}_2$ efficiently which results in vital, undamaged cell layers. When increasing illumination time to 2 min, no wounding of NRK monolayers grown on PS/PtTFPP containing 5 % or 10 % (w/w of PS) Vit E is observed. For lower Vit E doping wound sizes increase from $(49000 \pm 6000) \mu\text{m}^2$ for PS/PtTFPP + 2 % Vit E to $(134000 \pm 8000) \mu\text{m}^2$ for PS/PtTFPP + 1 % Vit E and $(208000 \pm 12000) \mu\text{m}^2$ for PS/PtTFPP containing no Vit E.

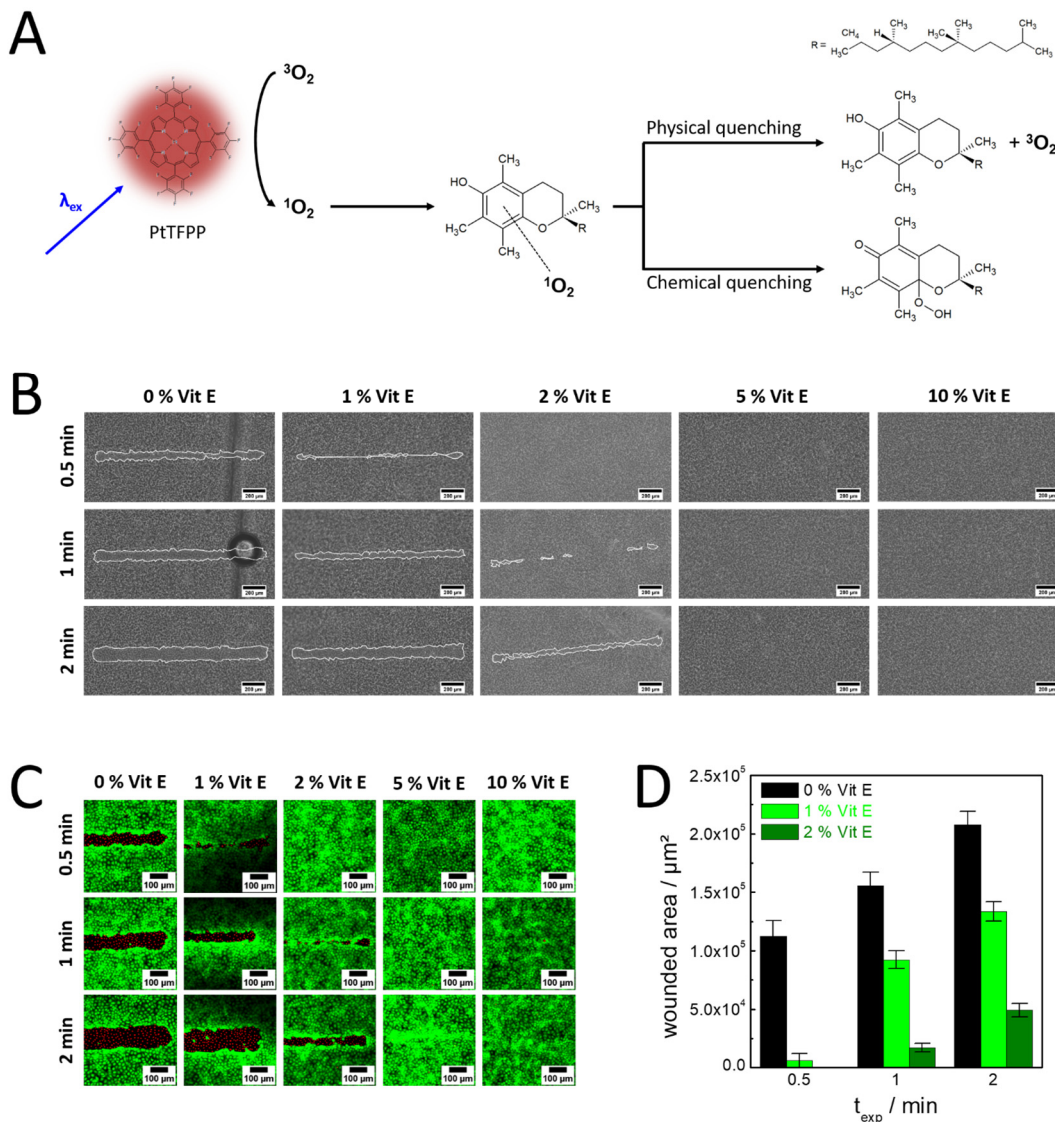


Fig. 7.6 Wounding of NRK cells cultivated on PS/PtTFPP substrates containing different amounts of vitamin E (D- α -tocopherol), a physical scavenger of $^1\text{O}_2$, upon exposure to 408 nm laser light. (A) Deactivation of $^1\text{O}_2$, generated by collisional quenching of $^3\text{O}_2$ and PtTFPP, by D- α -tocopherol via physical or chemical quenching. Scheme modified after (Kamal-Eldin and Appelqvist 1996). (B) Phase contrast images of typical substrates illuminated for 0.5 – 2 min with 408 nm laser light in line scan mode. Wounding can be prevented using increasing amounts of Vit E (w/w of PS). For better visualization of phase contrast images, wound edges were accentuated by white outlines using the NIH ImageJ software. (C) Corresponding fluorescence images showing green cytoplasmic fluorescence of live cells stained with 2 μM CaAM and red fluorescence of dead cell nuclei stained with 4 μM EthD-1. (D) Size of the wounded areas as a function of Vit E content (w/w of PS) and illumination time t_{exp} . Mean \pm SE; $n = 3$, $T = 37^\circ\text{C}$.

7.2 COMPARISON OF DIFFERENT WOUND HEALING ASSAYS

The novel optical wound healing assay based on oxygen sensitive PS/PtTFPP culture substrates was compared to typical wound healing assays used to study cell migration, such as the scratch, the barrier and the electrical ECIS[®] assay regarding wound healing rates, wound geometry, throughput and data evaluation. All assays were performed using NRK cells as described in **chapter 3.4.3.4**.

7.2.1 OXYGEN-BASED OPTICAL WOUND HEALING ASSAY

The novel functionalized substrates should not only allow the optical introduction of wounds, but neighboring, non-wounded cells should also be able to migrate into the wounded area and close it. The wound closure process of NRK cells was followed over 24 h after successful introduction of wounds on PS/PtTFPP substrates with 408 nm laser light. Intensity of the laser light was decreased by an ND 4 filter. **Fig. 7.7, A** shows phase contrast images of linear wounds 0 h, 3 h, 6 h, 9 h and 24 h after wounding. Live-dead staining was used to mark live and dead cells at each time point for a better visualization of the wound healing process, as depicted in the fluorescent micrographs in **Fig. 7.7, B**. As expected, wound size increases with increasing exposure time to the 408 nm laser light. Migration of cells into the wounded area is observed microscopically starting at $t = 3$ h. Wound closure becomes even more distinct 6 h and 9 h after wounding with dead cells being detached and replaced by migrating intact neighboring cells. Wound closure is completed after 24 h independent of illumination time. Due to linear cell migration into the wound, a linear scar-like bulge is left after wound healing is completed. Often, the distance between the two wounded edges is used to quantify wound healing. However, determination of the wounded area has been found to reduce errors in sampling (Reinhart-King 2008). Therefore, the area was used to determine wound healing rates. Changes in wound size (**Fig. 7.7, C**) were recorded over time by measuring the size of the wounded area using the NIH ImageJ software. The wound size after 0.5 min exposure to 408 nm laser light decreases by about 92 % from $(174000 \pm 8000) \mu\text{m}^2$ at $t = 0$ h to $(13000 \pm 3000) \mu\text{m}^2$ within 9 h. Bigger wounds generated by 1 min illumination time decrease by about 82 % in size within 9 h, while wounded areas on substrates exposed for 2 min to 408 nm laser light decreases by about 71 % from $(249000 \pm 3000) \mu\text{m}^2$ to $(71000 \pm 12000) \mu\text{m}^2$. **Fig. 7.7, D** shows the corresponding increase of the healed area as function of time. After 24 h, wounds are completely repopulated by living cells.

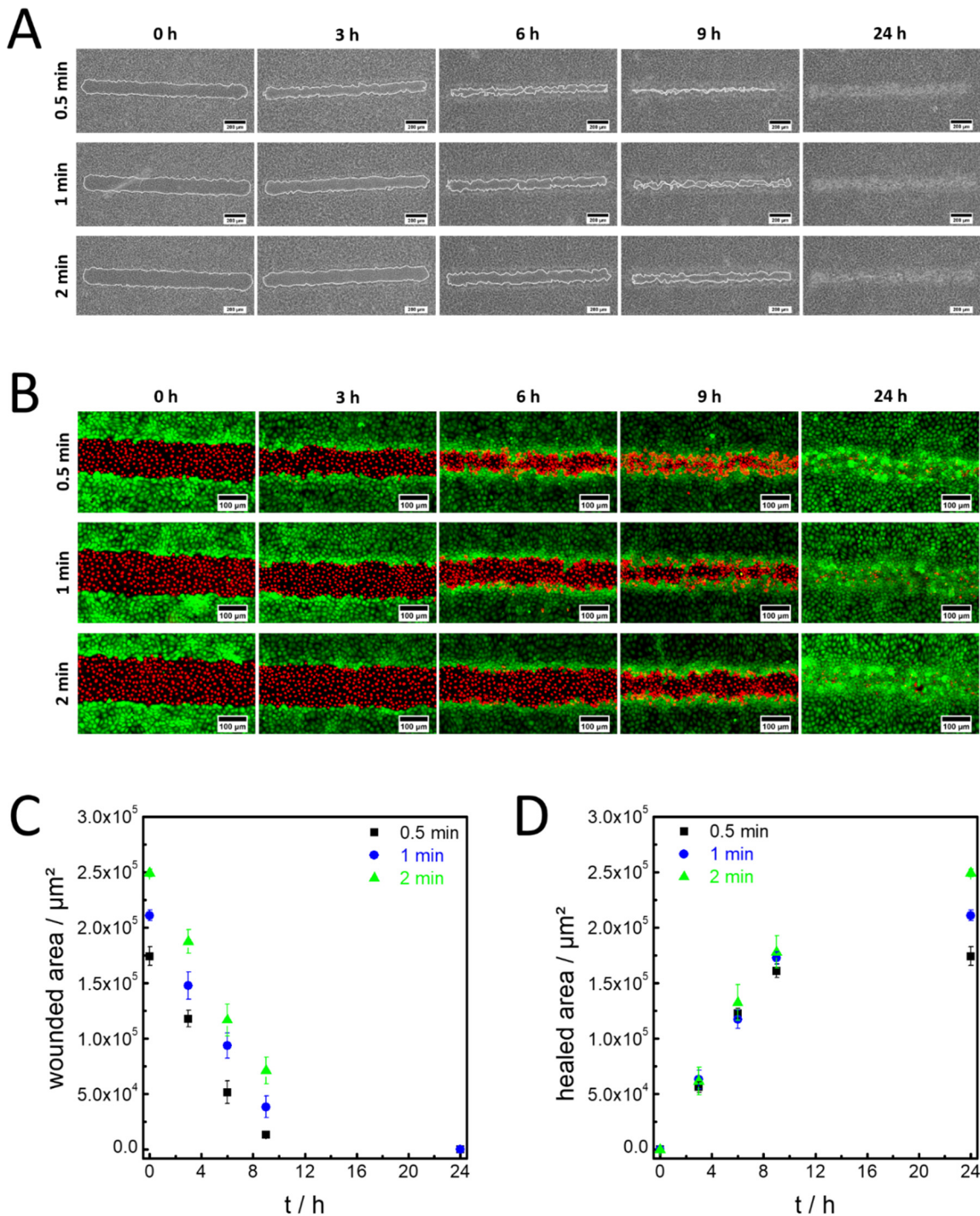


Fig. 7.7 Wound closure process of NRK cells monitored over 24 h. Confluent cell layers were wounded with 408 nm laser light in line scan mode for 0.5 – 2 min using an ND 4 filter in the incident light path. (A) Typical phase contrast images showing the wound healing process in dependency on illumination time at different time points after wounding. Wounds are closed after 24 h. For better visualization wounds in of phase contrast images, wound edges were accentuated by white outlines using the NIH ImageJ software. (B) Corresponding fluorescence micrographs of live-dead stained wounds shown in (A). Wounded cells exhibit strong red fluorescence of EthD-1 intercalated in nuclear DNA, while neighboring live cells emit green cytoplasmic fluorescence of CaAM. During wound healing, live cells migrate into the wound, replacing dead cells. (C) Graph showing changes in wounded area size as a function of time and exposure time to laser light. (D) Corresponding increase of healed area due to cell migration over a period of 24 h. Healed area was calculated by subtracting the wounded area at the respective time point t from the initial wounded area at $t = 0$ h. mean \pm SEM; $n = 6$, $T = 37$ °C.

Although linear regression analysis of data as shown in **Fig. 7.7, D** is often used to determine wound healing rates, this approach assumes that wound healing rates are constant over time (Jonkman et al. 2014; Masuzzo et al. 2016). However, it is also thought that wound healing behavior of cell monolayers resembles migratory behavior found *in vivo*. Here, wound closure is dependent on the respective phase of wound healing and not linear (Zhao et al. 2003). Thus, migration rates can also be determined in a rather unbiased way using logistic fitting (Topman et al. 2012). Therefore, in this work wound healing rates were determined by both, linear and logistic fitting of data shown in **Fig. 7.7, D** (for the corresponding fit functions, see supplementary information, **Fig. 11.18**). Resulting wound healing rates are listed in **Tab. 7.1**. Linear fits result in wound healing rates that are similar for all exposure times. The trend that wound healing rates are not dependent on exposure time is also visible from the results of logistic data analysis with cells reaching similar v_{\max} between 27000 – 30000 $\mu\text{m}^2 \text{h}^{-1}$ between 2.7 – 2.9 h after introduction of the wound. Due to the increase of wound size by prolonged illumination time, the time of half closure of the wound is shifted to later time points for samples illuminated for 1 min and 2 min. However, wound healing rates at $t_{1/2}$ yields similar values independent of illumination time. The uncertainties for v_{\max} and $t(v_{\max})$ have been estimated by numerical procedures that determine the maximum and minimum values for both parameters based on the fit results with the logistic transfer function including the standard errors for each parameter. The uncertainties as given in **Tab. 7.1** represent the full interval of values covered by the logistic parameter estimates and their individual standard errors.

Tab. 7.1 Wound healing rates determined for the optical assay conducted with confluent NRK cells cultivated on PS/PtTFPP substrates designed for wound healing. Results are shown for linear and logistic analysis of the raw data.

	0.5 min	1 min	2 min
Linear fitting			
$v / \mu\text{m}^2 \text{h}^{-1}$	19000 ± 900	19000 ± 300	20000 ± 700
$t_{1/2} / \text{h}$	4.6 ± 0.5	5.5 ± 0.3	6.1 ± 0.3
Logistic fitting			
$t_{1/2} / \text{h}$	4.3 ± 0.4	5.1 ± 0.6	6.3 ± 0.1
$v(t_{1/2}) / \mu\text{m}^2 \text{h}^{-1}$	25000 ± 4000	21000 ± 5000	18000 ± 600
$v_{\max} / \mu\text{m}^2 \text{h}^{-1}$	30000 ± 8000	28000 ± 8000	27000 ± 40
$t(v_{\max}) / \text{h}$	2.9 ± 0.6	2.9 ± 1.3	2.77 ± 0.01

7.2.2 SCRATCH ASSAY

Wound healing behavior of NRK cells was also studied using the scratch assay. As illustrated in **Fig. 7.8, A**, a linear wound is introduced into the confluent monolayer by scratching a pipet tip over the cell sheet. The complete removal of cells in the path of the tip generates an artificial, cell-free gap that will be closed over time by cells migrating in from the periphery. First, a confluent NRK monolayer grown on cell culture petri dishes was wounded by scratching. The wound healing process was monitored by recording phase contrast images at selected time points. **Fig. 7.8, B** shows typical microscopic images recorded during the migration of the NRK cell sheet over 9 h. After wounding, NRK cells start to migrate into the cell-free gap, closing more than 77 % of the wounded area within 9 h and 100 % after 24 h, resulting in a healed area of $(1203000 \pm 63000) \mu\text{m}^2$. The healed area was plotted as a function of time as shown in **Fig. 7.8, E**. To determine the wound healing rate, data shown in **Fig. 7.8, E** was either fitted linearly or logistically (for corresponding fits see supplementary information, **Fig. 11.19, A - C**). Results are listed in **Tab. 7.2**. Linear fitting results in an uniform migration rate of $(88000 \pm 2000) \mu\text{m}^2 \text{h}^{-1}$, while logistic fitting yields a maximum value of $111000 \mu\text{m}^2 \text{h}^{-1}$ at $t = 3.4$ h. Compared to values obtained for the optical wound healing assay in **chapter 7.2.1**, cellular migration rates provided by the scratch assay are generally higher. It was necessary to ensure that the decelerated wound healing rates observed in optical wounding were caused by the differences in wound morphology (scratch: cell-free wound, optical: cell debris on wound) and not by the growth substrate (petri dish or PS/PtTFPP) itself. Thus, wound healing behavior of confluent NRK monolayers was investigated for cells cultivated on PS/PtTFPP substrates but wounded by scratching (**Fig. 7.8, C**). PS/PtTFPP substrates designed for wound healing behaved similar to standard culture dishes during the wounding process. A cell-free artificial wound was introduced by carefully scratching without damaging the polymer layer. Cells migrated into the cell-free gap as illustrated in the phase contrast images in **Fig. 7.8, D**. Continuous cell migration resulted in a more than 81 % reduction of the cell-free area within 9 h after wounding. Cells completely covered the wounded area of $(956000 \pm 73000) \mu\text{m}^2$ after 24 h. The healed area was plotted as a function of time as depicted in **Fig. 7.8, F** and the wound healing rate was determined by fitting. Fitted curves and parameter estimates are summarized in supplementary information, **Fig. 11.19, D - F**. Linear fitting yielded a value of $(82000 \pm 5000) \mu\text{m}^2 \text{h}^{-1}$ as listed in **Tab. 7.2**. Cells reached half coverage of the wound about 2 h earlier compared to cells on control substrates. However, logistic

fitting yielded a maximum rate similar to values determined for cells cultivated on standard petri dishes.

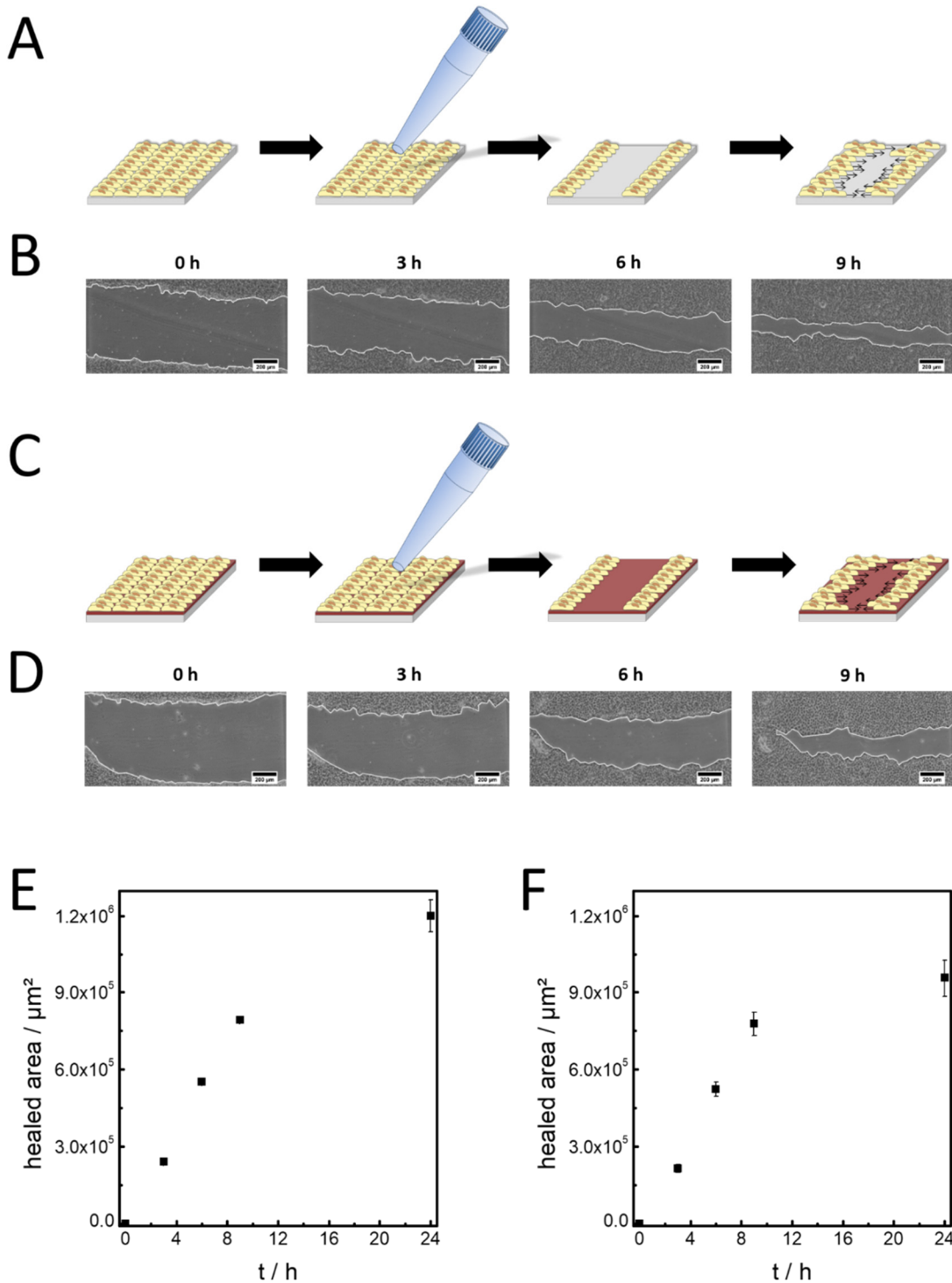


Fig. 7.8 (A) Scheme illustrating the workflow of introducing wounds in a confluent cell sheet by scratching. (B) Phase contrast images of a wounded confluent layer of NRK cells at $t = 0$ h and subsequent wound closure by migrating cells. The healed areas was determined as a function of time over a period of 9 h. (C) Schematic illustrating the introduction of a wound into a confluent cell layer grown on PS/PtTFPP coated substrates by scratching with a pipet tip. (D) Typical phase contrast images showing the wound healing process of NRK cells over a period of 9 h. (E) Change of healed area as a function of time for NRK cells wounded on cell culture petri dishes. Mean \pm SE; $n = 15$. (F) Change of healed area as a function of time for NRK cells wounded on PS/PtTFPP substrates. Mean \pm SE; $n = 13$. For better visualization of phase contrast images, wound edges were accentuated by white outlines using the NIH ImageJ software. $T = 37$ °C.

Tab. 7.2 Wound healing rates determined by the scratch assay conducted with confluent NRK cells cultivated on standard cell culture petri dishes or on PS/PtTFPP substrates designed for wound healing. Results are shown for linear and logistic fitting of data shown in **Fig. 7.8, E** and **F**. The uncertainties for v_{\max} and $t(v_{\max})$ have been estimated by numerical procedures that determine the maximum and minimum values for both parameters based on the fit results with the logistic transfer function including the standard errors for each parameter. They represent the full interval of values covered by the logistic parameter estimates and their individual standard errors.

	NRK on petri dish	NRK on PS/PtTFPP
Linear fitting		
$v / \mu\text{m}^2 \text{ h}^{-1}$	88000 ± 2000	82000 ± 5000
$t_{1/2} / \text{h}$	6.8 ± 0.2	5.8 ± 0.9
Logistic fitting		
$t_{1/2} / \text{h}$	7.7 ± 0.5	5.7 ± 0.7
$v(t_{1/2}) / \mu\text{m}^2 \text{ h}^{-1}$	76000 ± 1000	94000 ± 22000
$v_{\max} / \mu\text{m}^2 \text{ h}^{-1}$	111000 ± 6000	119000 ± 34000
$t(v_{\max}) / \text{h}$	3.4 ± 0.5	3.5 ± 0.9

7.2.3 BARRIER ASSAY

Next to the scratch assay, the barrier assay is another wound healing assay that is used to study the migration of cells into a cell-free gap. Here, a physical barrier is placed on the growth substrate before cell seeding leaving a gap which cells cannot populate. After removal of the physical barrier, cells can migrate into the artificial cell-free gap. The barrier assay was conducted with confluent NRK cells as described in **chapter 3.5.3**. First migration of NRK cells cultivated on standard cell culture petri dishes was examined (**Fig. 7.9, A**). After removal of the silicone barrier, cells start to close the rectangular cell-free gap by collective migration, as shown in the phase contrast images in **Fig. 7.9, B**. The size of the cell-free gap is reduced by about 15 % after 3 h, 37 % after 6 h and more than 60 % within 9 h after barrier removal. 24 h after barrier removal, the wound is completely covered with cells, yielding a healed area of $(987000 \pm 35000) \mu\text{m}^2$. Changes in healed area as a function of time are shown in **Fig. 7.9, E**. For comparison, the barrier assay was also conducted with NRK cells grown on PS/PtTFPP coated substrates, as illustrated in **Fig. 7.9, C**. Removal of the silicone insert leaves a clean, cell-free gap on the PS/PtTFPP substrate surface without removing the polymer. Cells start to populate the artificial gap shortly after barrier removal, as depicted in phase contrast images in **Fig. 7.9, D**. Changes of the healed area as a function of time are shown in **Fig.**

7.9, F. Within 3 h, about 19 % of the cell-free gap is populated. Coverage steadily increases to about 44 % after 6 h and to about 73 % after 9 h. Full coverage by cells is reached within 24 h.

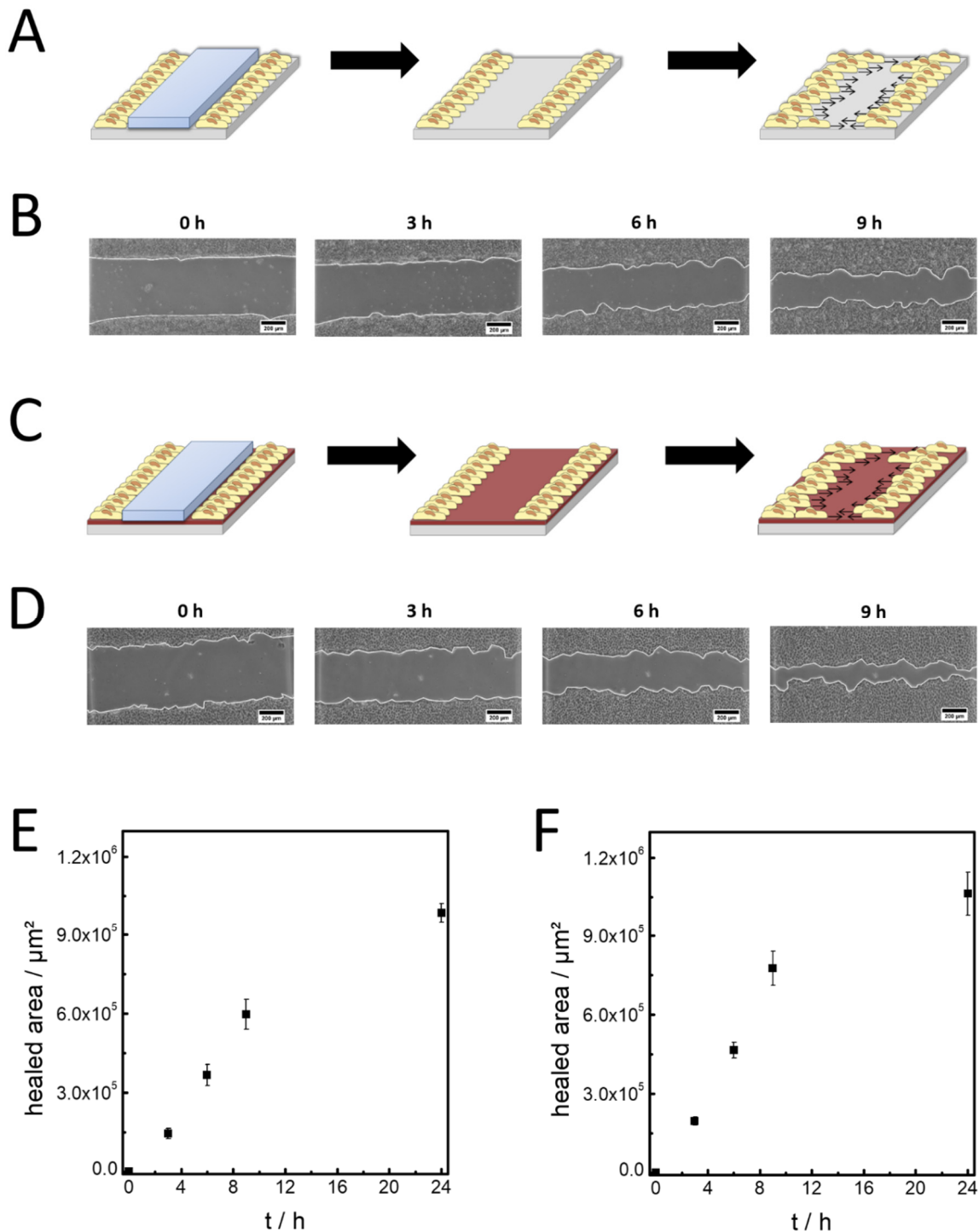


Fig. 7.9 (A) Scheme illustrating the barrier assay. A cell-free gap is created within a layer of NRK cells grown on cell culture petri dishes by removal of a cytocompatible physical barrier. (B) Phase contrast images illustrating the migration of NRK cells into the wound. (C) Illustration of the barrier assay conducted on PS/PtTFPP coated substrate. (D) Typical phase contrast images showing the wound healing process of NRK cells over a period of 9 h. (E) Change of the healed area as a function of time for NRK cells wounded on cell culture petri dishes. Mean \pm SE; $n = 7$. (F) Change of healed area as function of time for NRK cells wounded on PS/PtTFPP coated substrates. Mean \pm SE; $n = 10$. For better visualization of phase contrast images, wound edges were accentuated by white outlines using the NIH ImageJ software. $T = 37^\circ\text{C}$.

Data for both assay conditions was fitted linearly and logistically to determine wound healing rates. Corresponding fit functions and parameter estimates can be found in supplementary information, **Fig. 11.20**. Fitting results for NRK cells grown on petri dishes and on PS/PtTFPP coated substrates are listed in **Tab. 7.3**. Migration rates determined with the barrier assay are in the range of values determined with the scratch assay. Linear fitting yielded values of $(59000 \pm 5000) \mu\text{m}^2 \text{h}^{-1}$ for NRK cell cultivated on culture dishes and a slightly higher value of $(75000 \pm 6000) \mu\text{m}^2 \text{h}^{-1}$ for cells cultivated on PS/PtTFPP. Further, v_{max} determined for NRK cells on PS/PtTFPP substrates was about 25 % higher compared to values for cells grown on cell culture petri dishes. Similar values obtained for both culture substrates indicate, that PS/PtTFPP substrates per se do not negatively influence cell migration, but higher migration rates are observed when cells can migrate into cell-free areas.

Tab. 7.3 Wound healing rates determined for the barrier assay conducted with confluent NRK cells cultivated on standard cell culture petri dishes or on PS/PtTFPP substrates designed for wound healing. Results are shown for linear and logistic fitting of data (**Fig. 7.9, E, F**). The uncertainties for v_{max} and $t(v_{\text{max}})$ have been estimated by numerical procedures that determine the maximum and minimum values for both parameters based on the fit results with the logistic transfer function including the standard errors for each parameter. They represent the full interval of values covered by the logistic parameter estimates and their individual standard errors.

	NRK on petri dish	NRK on PS/PtTFPP
<u>Linear fitting</u>		
$v / \mu\text{m}^2 \text{h}^{-1}$	59000 ± 5000	75000 ± 6000
$t_{1/2} / \text{h}$	8.4 ± 1.0	7.2 ± 1.2
<u>Logistic fitting</u>		
$t_{1/2} / \text{h}$	9.0 ± 0.7	7.5 ± 1.6
$v(t_{1/2}) / \mu\text{m}^2 \text{h}^{-1}$	58000 ± 9000	74000 ± 30000
$v_{\text{max}} / \mu\text{m}^2 \text{h}^{-1}$	80000 ± 12000	101000 ± 45000
$t(v_{\text{max}}) / \text{h}$	4.4 ± 0.8	3.9 ± 1.75

7.2.4 ELECTRICAL ECIS[®] ASSAY

As third assay for comparison with the novel optical wound healing assay, the electrical ECIS[®] wound healing assay was conducted. As depicted in **Fig. 7.10, A**, NRK cells were grown to confluence on 8W2LE electrode arrays. A linear wound is introduced by application of a short invasive voltage pulse that permeabilizes the membrane of the cells residing on the linear working electrode, while neighboring cells around the electrode remain unharmed. Dead cells are replaced by cells migrating in from the periphery of the electrode repopulating the electrode. Wound healing is followed online by monitoring the capacitance, resistance or impedance time course. Results of wounding NRK cells are shown in **Fig. 7.10, B** where the normalized capacitance at 32 kHz is plotted as a function of time. After recording baseline values, a wounding pulse of 5 V amplitude was applied at $t = 0$ h for 30 s at 40 kHz. Successful wounding is indicated immediately by an increase of the normalized C by a factor of 4.2 (●), reaching values of a cell-free electrode, while C_{norm} for the non-wounded control population (■) stays on baseline values. Repopulation of the electrode is monitored online by the decrease of C_{norm} which reaches the baseline level around 4 h after wounding. Because the decrease in capacitance is proportional to increasing electrode coverage, the measured capacitance is converted into fractional electrode area that is recovered by migrating cells as shown in the graph in **Fig. 7.10, C**. Directly after application of the voltage pulse the healed area is zero by definition, as wounding kills cells all over the electrode. Within 1 h after wounding, cells start repopulating the electrode which is visible as an increase in healed area. Confluency is reached within about 4 h as vital cells have repopulated the complete electrode surface. Non-wounded samples do not show a change in capacitance and, thus in electrode surface coverage during the measurement. Logistic fitting of the healed area plotted versus time and subsequent differentiation was used to determine of the wound healing rate of NRK cells on 8W2LE electrode arrays with results listed in **Tab. 7.4**. For logistic fitting, corresponding differentiation and impedance data see supplementary information, **Fig. 11.21**. NRK cells reach a maximum wound healing rate of $(58000 \pm 700) \mu\text{m}^2 \text{h}^{-1}$ about 1.6 h after wounding. A velocity of $(55000 \pm 200) \mu\text{m}^2 \text{h}^{-1}$ is determined at (1.794 ± 0.003) h which corresponds to the time of half-maximal electrode coverage. These results are similar to data obtained from scratch and barrier assay. However, when wound healing rates are calculated using the time-point of the half-maximal capacitance decrease, a lower migration rate of about $(35000 \pm 4000) \mu\text{m}^2 \text{h}^{-1}$ is obtained. This value is in a similar range with results obtained by the novel optical wound healing assay.

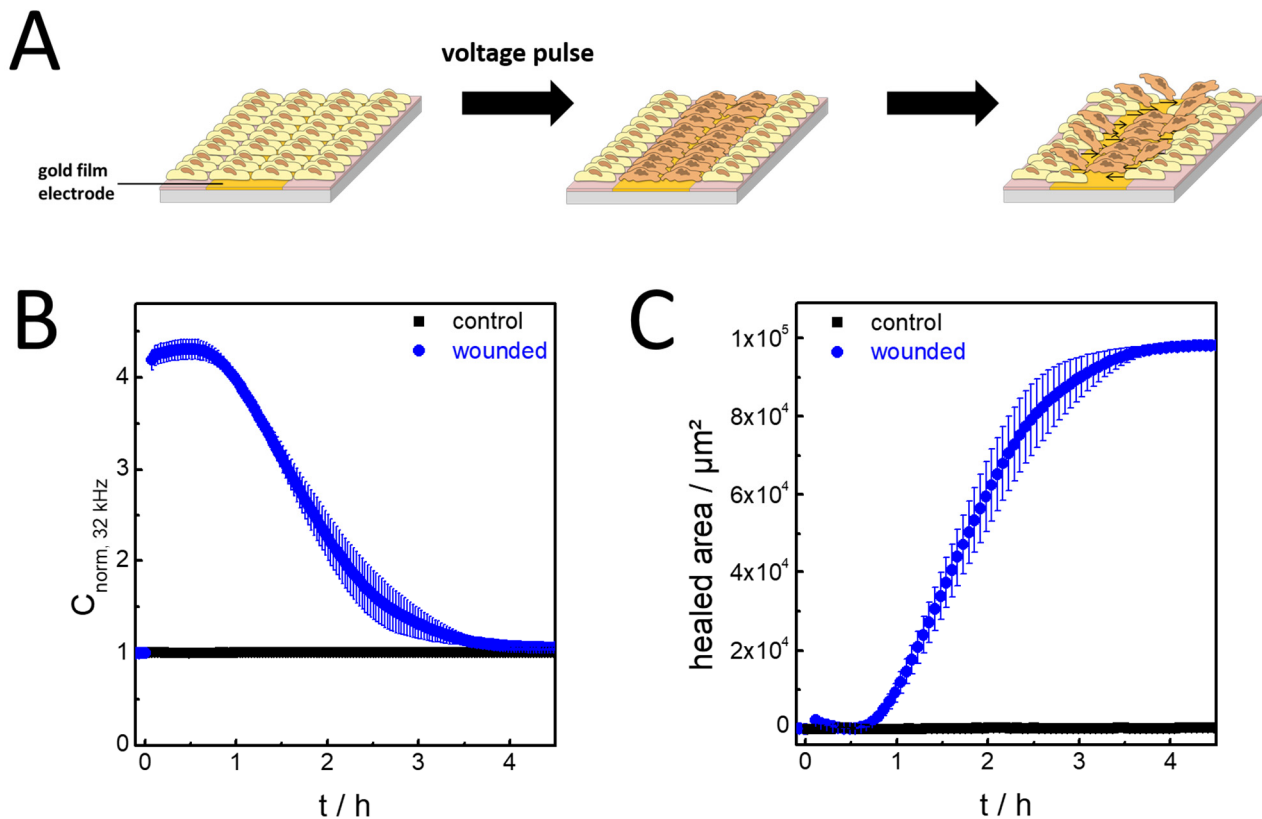


Fig. 7.10 (A) Scheme illustrating the electrical ECIS[®] wound healing assay. Confluent cells cultivated on a gold film working electrode are killed by application of an invasive voltage pulse of 5 V amplitude for 30 s at 40 kHz (●). Dead cells remain on the electrode and are replaced by cells migrating in from the area next to the electrode. No voltage pulse was applied under control conditions (■). (B) Normalized capacitance as a function of time for NRK cells on 8W2LE electrode arrays. The wounding pulse was applied at $t = 0$ h. (C) Respective change in healed electrode area as a function of time. Mean \pm SE; $n \geq 2$, $T = 37$ °C.

Tab. 7.4 Wound healing rates determined for the electrical ECIS[®] assay conducted with confluent NRK cells cultivated on 8W2LE ECIS[®] arrays. Results are shown for the half maximum capacitance change and logistic fitting of data. The uncertainties for v_{max} and $t(v_{\text{max}})$ were estimated by numerical procedures that determine the maximum and minimum values for both parameters based on the fit results with the logistic transfer function including the standard errors for each parameter. They represent the full interval of values covered by the logistic parameter estimates and their individual standard errors.

NRK on 8W2LE	
Half maximum	
$v / \mu\text{m}^2 \text{ h}^{-1}$	35000 ± 4000
$t_{1/2} / \text{h}$	1.4 ± 0.2
Logistic fitting	
$t_{1/2} / \text{h}$	1.794 ± 0.003
$v(t_{1/2}) / \mu\text{m}^2 \text{ h}^{-1}$	55000 ± 200
$v_{\text{max}} / \mu\text{m}^2 \text{ h}^{-1}$	58000 ± 700
$t(v_{\text{max}}) / \text{h}$	1.56 ± 0.01

7.3 PROOF-OF-CONCEPT STUDIES

7.3.1 INFLUENCE OF SERUM STARVATION ON THE WOUND HEALING RATE

Many studies on cell migration and wound healing deprive cells of serum before migration behavior is monitored. This step is necessary when wound healing behavior of highly proliferative cells such as cancer cells is studied to prevent that wound closure by migration is superposed by cell division (Jonkman et al. 2014). Thus, migration of NRK cells in dependency on previous serum starvation was studied using the novel optical wound healing assay. NRK cells were cultivated on PS/PtTFPP coated substrates as described in **chapter 3.4.3.4**. Cells were deprived of serum by exchanging standard culture medium to 2 ml serum free culture medium 24 h before wounding. Then, wounds were introduced by illuminating the samples for 1 min with 408 nm laser light in line scan mode (ND 4 filter) and wound closure was monitored in serum containing standard NRK cell culture medium by phase contrast microscopy. Typical phase contrast images of samples after wounding and the consecutive wound closure process of control and serum deprived NRK monolayers are shown in **Fig. 7.11, A**. Compared to control cells, wound closure of cells that underwent serum starvation is delayed. 3 h after wounding, serum deprived cells cover only 2 % of the wounded area as illustrated in **Fig. 7.11, B, ●**, while about 24 % of the wounded area is covered by cells under control conditions. However, serum deprived cells start to migrate into the wound, reaching about 25 % coverage rate after 6 h and about 56 % coverage rate after 9 h. Control samples cover 49 % of the wounded area after 6 h, increasing to a coverage of 83 % after 9 h (**Fig. 7.11, B, ■**). 24 h after wounding, wounds are completely closed. The obtained data was fitted using linear fitting as described in literature (Jonkman et al. 2014), and using the logistic fit function. The fit parameters are summarized in supplementary information, **Fig. 11.22**. Changes in wound healing rate are displayed as a function of time in **Fig. 7.11, C** with important parameters highlighted in **Tab. 7.5**. Linear fitting yields a wound healing rate which is reduced by about 50 % compared to control conditions. Serum starved cells migrate with a velocity of $(9000 \pm 2000) \mu\text{m}^2 \text{h}^{-1}$ with a time-point of half-coverage of the wounded area delayed to $(8.9 \pm 1.9) \text{h}$ compared to $(5.9 \pm 0.9) \text{h}$ under control conditions. Logistic fitting shows a delayed wound healing of serum deprived cells, that results in a similar, but time-delayed v_{max} value as well as a similar but time delayed $v(t_{1/2})$ values compared to control conditions. While control cells reach a v_{max} value of $(19000 \pm 13000) \mu\text{m}^2 \text{h}^{-1}$ about 3.2 h after wounding, serum deprived NRK cells reach a v_{max} value of $(17000 \pm 2000) \mu\text{m}^2 \text{h}^{-1}$ after 7 h. Half-coverage of the wounded area by serum deprived cells was reached about 2 h later compared to cells that were not

serum deprived. To sum up, migration rates of serum deprived and control cells are similar. However, serum deprived NRK cells show a delayed onset of migration.

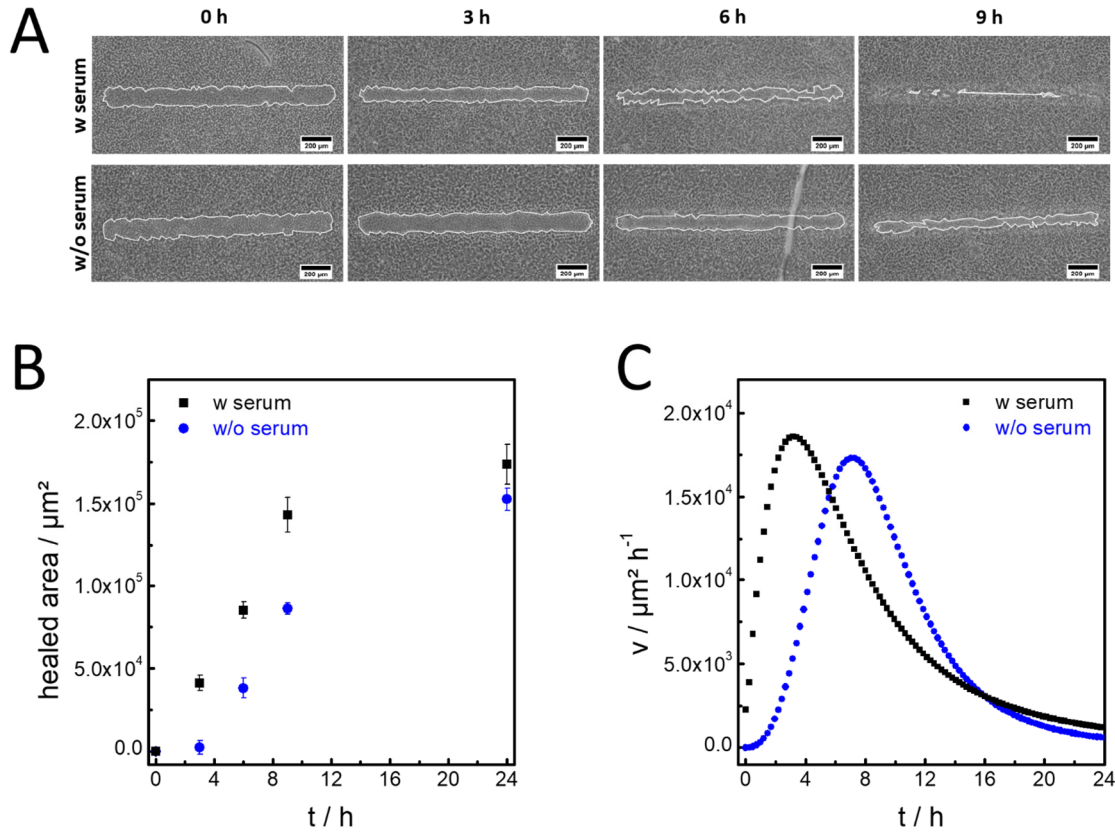


Fig. 7.11 Studies on wound healing dynamics of NRK cells deprived of serum using the novel wound healing assay based on oxygen sensitive culture substrates. (A) Typical phase contrast images of control cells and cells deprived of serum for 24 h, illustrating wound closure over a period of 9 h. For better visualization, wound edges were accentuated by white outlines using the NIH ImageJ software. (B) Increase of healed area due to migration of NRK cells cultivated with (■) or without serum (●) 24 h before wounding as a function of time. Mean \pm SE; $n = 17$, $T = 37$ °C. (C) Wound healing rate of control and serum deprived cells determined by logistic fitting and subsequent differentiation.

Tab. 7.5 Wound healing rates and characteristic time points obtained for serum deprived and control cells using the optical wound healing assay. Table shows data obtained for linear and logistic fitting of healed area as a function of time. The uncertainties for v_{\max} and $t(v_{\max})$ were estimated by numerical procedures determining the maximum and minimum values for both parameters based on the fit results with the logistic transfer function.

	w serum	w/o serum
Linear fitting		
$v / \mu\text{m}^2 \text{h}^{-1}$	15000 ± 600	9000 ± 2000
$t_{1/2} / \text{h}$	5.9 ± 0.9	8.9 ± 1.9
Logistic fitting		
$t_{1/2} / \text{h}$	6.5 ± 0.1	8.5 ± 0.2
$v(t_{1/2}) / \mu\text{m}^2 \text{h}^{-1}$	17000 ± 8000	16000 ± 700
$v_{\max} / \mu\text{m}^2 \text{h}^{-1}$	19000 ± 13000	17000 ± 2000
$t(v_{\max}) / \text{h}$	3.2 ± 2.7	7.0 ± 0.4

7.3.2 INFLUENCE OF CYTOCHALASIN D ON THE WOUND HEALING RATE

Cytochalasin D (Cyt D) is a membrane-permeable metabolite produced by fungi and is known to effectively bind actin filaments within mammalian cells. Binding to actin prevents actin polymerization but leaves depolymerization unchanged leading to a net reduction of the actin filament length, corresponding changes in cell morphology and severe restrictions of cellular motility (Goddette and Frieden 1986; Cooper 1987). The negative effect on motility of NRK cells was studied using the novel optical wound healing assay. Therefore, NRK cells cultivated on PS/PtTFPP substrates were illuminated for 1 min with 408 nm laser light in line scan mode using the ND 4 filter. After wound generation, cell migration was microscopically monitored in NRK culture medium containing either no Cyt D or 0.1 μM Cyt D. **Fig. 7.12, A** shows typical phase contrast images of wounded NRK monolayers at different time points during wound healing. A clear difference in wound healing behavior of control and Cyt D treated cells is visible. While cells under control condition exhibit a fast repopulation of the wounded area, cells treated with 0.1 μM Cyt D show a significantly slower migration into the wounded areas with incomplete wound closure 24 h after wounding. Additionally, NRK cells treated with 0.1 μM Cyt D show a change in morphology characterized by rounding up. Changes in the healed area as a function of time of 17 independently generated wounds are plotted in **Fig. 7.12, B**. Cells treated with 0.1 μM Cyt D (●) close only about 10 % of the wounded area within 3 h after wounding due to the negative influence of Cyt D on cell motility. Migration and wound closure increases over time, however, wound coverage by migrating cells is less than 78 % 24 h after wound generation. Under control conditions (**Fig. 7.12, B, ■**), NRK cells repopulate about 30 % of the wounded area 3 h after wounding. Fractional repopulation increases to about 50 % after 6 h and 91 % after 9 h. 24 h after wounding, live cells have completely replaced dead cells forming the characteristic linear scar-like bulge. Raw data was fitted using the linear and logistic fit function and successive differentiation was applied. For details on the fit function and parameter estimates, see supplementary information, **Fig. 11.23**. Fitted parameters are highlighted in **Tab. 7.6**. Linear fitting yields a wound healing rate which is reduced by about 50 % by exposure to 0.1 μM CD compared to control. NRK cells treated with 0.1 μM Cyt D migrate at a rate of $(9000 \pm 700) \mu\text{m}^2 \text{h}^{-1}$, while control cells exhibit a velocity of $(18000 \pm 300) \mu\text{m}^2 \text{h}^{-1}$. Changes in wound healing rate determined by logistic fitting and differentiation are displayed as function of time in **Fig. 7.12, C**. The uncertainties for v_{max} and $t(v_{\text{max}})$ were estimated by numerical procedures that determine the maximum and minimum values for both parameters based on the fit results with

the logistic transfer function including the standard errors for each parameter. The uncertainties as given in **Tab. 7.6** represent the full interval of values covered by the logistic parameter estimates and their individual standard errors. NRK cells treated with 0.1 μM Cyt D show a significantly lower v_{max} value of $(12000 \pm 2000) \mu\text{m}^2 \text{h}^{-1}$ compared to control cells with a v_{max} value of $(26000 \pm 11000) \mu\text{m}^2 \text{h}^{-1}$. While control cells reach half-coverage of the wounded area in about $(5.1 \pm 0.9) \text{h}$ after wounding with a $v(t_{1/2})$ of $(20000 \pm 700) \mu\text{m}^2 \text{h}^{-1}$, half-coverage upon addition of 0.1 μM Cyt D is reached within about 9.9 h after wounding with a rate $v(t_{1/2})$ of $(9000 \pm 2000) \mu\text{m}^2 \text{h}^{-1}$. In contrast to serum starvation, Cyt D treatment does not only delay the onset of cell migration but it is also slowed down.

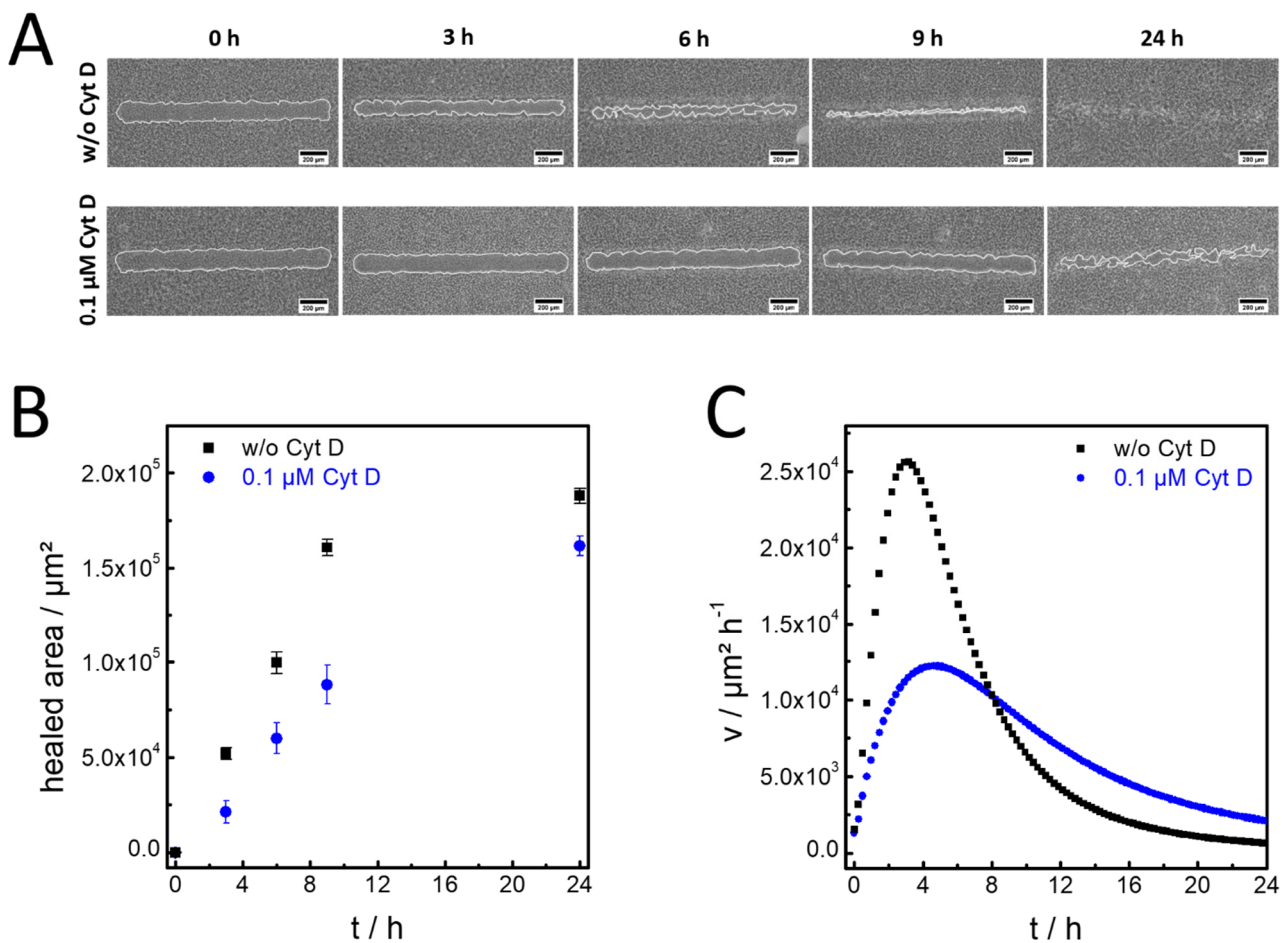


Fig. 7.12 Studies on wound healing dynamics of NRK cells treated with Cyt D using the novel wound healing assay based on oxygen sensitive culture substrates. (A) Typical phase contrast images of control cells and cells treated with 0.1 μM Cyt D illustrating wound closure over a period of 24 h. For better visualization, wound edges were accentuated by white outlines using the NIH ImageJ software. (B) Change in healed area of control (■) and Cyt D (●) treated cells over a period of 24 h as a function of time. Mean \pm SE; $n = 17$, $T = 37^\circ\text{C}$. (C) Wound healing rates of control and Cyt D treated cells determined by logistic fitting and subsequent differentiation.

Tab. 7.6 Wound healing rates and characteristic time points obtained for NRK cells treated w/o or with 0.1 μM Cyt D using the optical wound healing assay.

	w/o Cyt D	0.1 μM Cyt D
<u>Linear fitting</u>		
$v / \mu\text{m}^2 \text{ h}^{-1}$	18000 ± 300	9000 ± 700
$t_{1/2} / \text{h}$	4.6 ± 0.3	10.0 ± 0.9
<u>Logistic fitting</u>		
$t_{1/2} / \text{h}$	5.1 ± 0.9	9.9 ± 0.9
$v(t_{1/2}) / \mu\text{m}^2 \text{ h}^{-1}$	20000 ± 700	9000 ± 2000
$v_{\text{max}} / \mu\text{m}^2 \text{ h}^{-1}$	26000 ± 11000	12000 ± 2000
$t(v_{\text{max}}) / \text{h}$	3.2 ± 1.6	4.6 ± 1.1

7.3.3 INFLUENCE OF EXTRACELLULAR pH ON THE WOUND HEALING RATE

Cells need a tightly regulated pH in their microenvironment. Changes of extracellular pH are known to influence cell behavior. Studies have shown, that acidic pH can induce migration and enhances invasive potential of cancer cells (Martinez-Zaguilan et al. 1996; Hanahan and Weinberg 2011) whereas acidosis negatively affects migration behavior in non-transformed cells (de Valliere et al. 2015). Furthermore, wound reepithelization is strongly dependent on extracellular pH (Kruse et al. 2017). Wound healing assays are a useful tool to study the influence of the extracellular environment on the migratory behavior of adherent cells.

The novel optical wound healing assay was used to monitor the impact of changes in extracellular pH on wound healing of adherent cells. Therefore, confluent NRK cells were cultivated on PS/PtTFPP coated substrates and wounded for 1 min with 408 nm laser light in line scan mode with ND 4 filter. Wounded cell layers were washed twice with pH-adjusted serum-free L-15 medium and wound healing was monitored in this medium. Three different extracellular pH values were established. L-15 medium was adjusted to pH 6.4 to mimic an acidic extracellular milieu, to pH 7.2 which lies in the near neutral pH range of normal buffered culture medium and to pH 7.8 resembling a slightly alkaline extracellular environment. As shown in the typical phase contrast images in **Fig. 7.13, A** changing the extracellular pH has a deep impact on wound closure behavior. NRK cells monitored at pH 7.2 and at the slightly basic pH 7.8 can close the wounds within 24 h. Consistent with findings in literature, cellular motility seems to be heavily impaired resulting in only minor wound closure at an acidic pH of 6.4. Changes of the healed area in dependence on extracellular pH of eight individual samples were plotted as a function of time as depicted in **Fig. 7.13, B**. NRK cells

cultivated at pH 7.8 repopulate $(103000 \pm 9000) \mu\text{m}^2$ within 9 h which corresponds to about 70 % of the initial wounded area (●). Migration of NRK cells at pH 7.2 is slightly slower. Here, about 63 % of the initial wound is repopulated by cells after 9 h and full coverage was reached after 24 h (■). When cells are kept in an acidic environment, significantly lower migration rates are obtained. At pH 6.4 about 28 % of the wounded area is closed 9 h after wounding. Closure only slightly increases after 24 h to about 43 % of the total wound size (▲). The wound healing rate was determined by linear and logistic fitting and differentiation as shown in supplementary information, **Fig. 11.24**. However, results obtained at pH 6.4 did not permit successful logistic fitting of data. Thus, only changes in wound healing rates for cells at pH 7.2 (■) and pH 7.8 (●) are depicted in **Fig. 7.13, C** with distinct parameters summarized in **Tab. 7.7**. Logistic fitting shows that cells with an extracellular milieu of pH 7.8 reach half-coverage within (6.7 ± 0.2) h with a $v(t_{1/2})$ value of $(11000 \pm 700) \mu\text{m}^2 \text{h}^{-1}$. The time of half-coverage is slightly delayed at pH 7.2 to (7.6 ± 1.6) h with a lower $v(t_{1/2})$ value of $(7000 \pm 3000) \mu\text{m}^2 \text{h}^{-1}$. The tendency of faster wound closure at a slightly basic pH is also visible in v_{max} . At pH 7.8, a v_{max} value of $(15000 \pm 1000) \mu\text{m}^2 \text{h}^{-1}$ is about one third higher compared to a recorded v_{max} value of $(11000 \pm 5000) \mu\text{m}^2 \text{h}^{-1}$ at pH 7.2. Linear fitting results in a wound healing rate which is increased by about 36 % at an extracellular pH of 7.8 compared to cells monitored at pH 7.2. However, the time point of half-coverage is similar for both pH values. When cells are monitored in an acidic environment the migration rate drops to $(4000 \pm 2000) \mu\text{m}^2 \text{h}^{-1}$ and a shifted time point of half-coverage towards 15.6 ± 7.1 h. To sum up, changes in extracellular pH, that affect cell migration have been successfully monitored using the optical wound healing assay.

Tab. 7.7 Wound healing rates and characteristic time points obtained for extracellular pH values of 6.4, 7.2 and 7.8. Data obtained for an extracellular pH of 6.4 did not allow successful fitting using the logistic fit function. The uncertainties for v_{max} and $t(v_{\text{max}})$ were estimated by numerical procedures that determine the maximum and minimum values for both parameters based on the fit results with the logistic transfer function including the standard errors for each parameter. The uncertainties represent the full interval of values covered by the logistic parameter estimates and their individual standard errors.

	pH 6.4	pH 7.2	pH 7.8
Linear fitting			
$v / \mu\text{m}^2 \text{h}^{-1}$	4000 ± 2000	8000 ± 400	11000 ± 700
$t_{1/2} / \text{h}$	15.6 ± 7.1	6.8 ± 1.6	6.4 ± 1.9
Logistic fitting			
$t_{1/2} / \text{h}$	-	7.6 ± 1.6	6.7 ± 0.2
$v(t_{1/2}) / \mu\text{m}^2 \text{h}^{-1}$	-	7000 ± 3000	11000 ± 700
$v_{\text{max}} / \mu\text{m}^2 \text{h}^{-1}$	-	11000 ± 5000	15000 ± 1000
$t(v_{\text{max}}) / \text{h}$	-	3.4 ± 2.2	3.1 ± 0.7

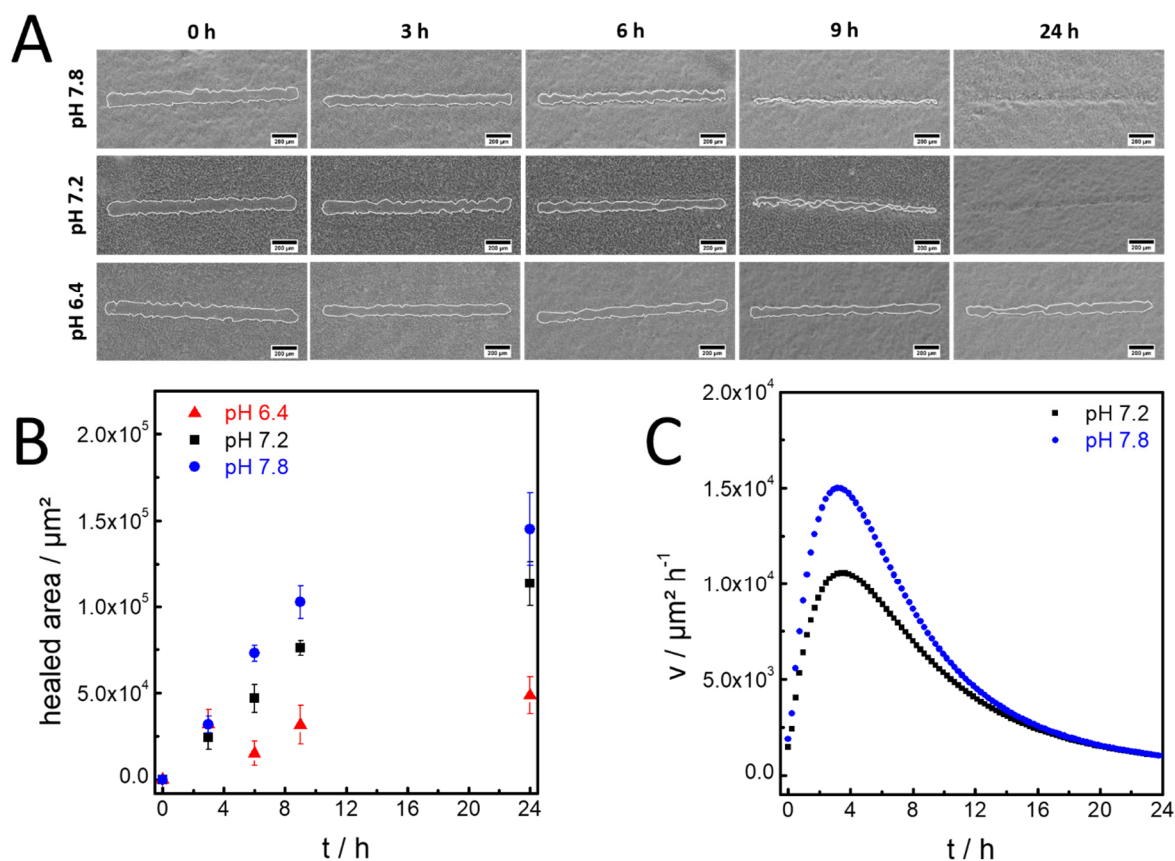


Fig. 7.13 pH dependent wound healing dynamics of NRK cells studied with the novel optical wound healing assay. (A) Typical phase contrast images of the wound closure process of NRK cells pH adjusted L-15 medium. Wounds are completely repopulated at pH 7.2 and pH 7.8, while wounds remain unclosed 24 h after wounding at a pH of 6.4. For better visualization, wound edges were accentuated by white outlines using the NIH ImageJ software. (B) Change in healed area as a function of time in dependence on the extracellular pH. Mean \pm SE; $n = 8$, $T = 37$ °C. (C) Wound healing rate of NRK cells monitored in L-15 medium at pH 7.2 (■) and pH 7.8 (●) determined by logistic fitting and subsequent differentiation.

7.4 DISCUSSION

7.4.1 CHARACTERIZATION OF FUNCTIONALIZED SUBSTRATES DESIGNED FOR WOUND HEALING

In this study, a novel optical wound healing assay based on the oxygen sensor dye PtTFPP embedded in a polystyrene polymer matrix was developed. The thin functional layers are easy to fabricate by spin coating on glass and are optically transparent, which allows monitoring of wound healing processes with a standard microscope. The novel functional substrates exhibited excellent biocompatibility during long term culture of adherent mammalian cells. Wounds were easily generated by illuminating samples with an adequate wavelength around 400 nm, while wavelengths that did not cover the excitation spectrum of the oxygen sensor dye PtTFPP did not introduce

wounds. Wounding was accomplished in different media. Further, the wound geometry was easily tuned by introduction of a photomask or by changing the illumination mode from standard circular illumination to line scan. The wounding mechanism of the novel optical wound healing assay is based on the generation of highly cytotoxic singlet oxygen by luminescence quenching. Illumination of the PS/PtTFPP substrates with a wavelength range (488 nm, 543 nm) that did not excite the porphyrin dye did not result in wounding the cell layer. Additionally, scavenging singlet oxygen by embedding the antioxidant vitamin E into the polymer matrix of the functional coating reduces or even prevents phototoxicity after illumination. Furthermore, no light-induced photodamage of NRK cells cultured on PS substrates without sensor dye was observed for illumination periods up to 2 min with a laser power output in the mW range. As the inherent lifetime of singlet oxygen is about 4 μ s in water, a maximum diffusion radius of about 125 nm is accessible within one lifetime (Redmond and Kochevar 2006). This indicates that cells cultured on PS/PtTFPP substrates are probably killed by diffusion of singlet oxygen from the upper layers of the polymer substrates into the extracellular matrix and the basal membrane where it can react with cellular biomolecules. Singlet oxygen can effectively induce oxidation of membrane lipids producing peroxidation products that can act as precursors for other reactive oxygen species. Furthermore, singlet oxygen reacts with amino acids that can result in protein damage and inactivation (Klotz et al. 2003). Although its lifetime is rather short, singlet oxygen is known to be a potent oxidizing agent that can induce necrotic or apoptotic pathways leading to cell death (Castano et al. 2005). Exposure to high doses of extracellular $^1\text{O}_2$ has been shown to lead to membrane damage by formation of vacuoles, externalization of phosphatidylserine and lipid peroxidation products and membrane rupture (Thorpe et al. 1995; Pimenta et al. 2012). Studies conducted with an extracellularly located palladium porphyrin dendrimer resulted in necrosis of HeLa cells. 10 min after irradiation of the samples, cells exhibited morphological changes typical for necrotic cells (Pedersen et al. 2011). Furthermore, a palladium porphyrin induced necrosis in A-549 cells characterized by a pyknotic nucleus and membrane disintegration (Canete et al. 2004). Similar morphological changes were seen after wounding cells cultivated on PS/PtTFPP coated substrates. However, a clear distinction between necrosis and apoptosis cannot be made by microscopic observation and would require additional methods, such as fluorescence labelling of annexin V – a marker of apoptosis. To sum up, PS/PtTFPP coated substrates are suitable for the application in an optical wound healing assay as they are biocompatible, transparent and illumination leads to a fast and defined generation of wounds.

7.4.2 COMPARISON OF DIFFERENT WOUND HEALING ASSAYS

The novel optical wound healing assay was compared to established wound healing assays, such as the scratch, the barrier and the electrical ECIS[®] assay. An overview of differences and common features is listed in **Tab. 7.8**. In general, the novel optical wound healing assay is more similar to the electrical ECIS[®] wound healing assay regarding wound morphology and wound healing rates. Analog to electrical wounding, excitation of the oxygen sensitive dye generated wounds, where killed cells remained as debris on the substrate surface (Keese et al. 2004), whereas barrier and scratch assay resulted in a debris-free gap. Thus, neighboring vital cells need to detach dead cells before they can

Tab. 7.8 Overview of characteristics of the four different wound healing assays used in this work.

	Optical	Scratch	Barrier	ECIS[®]
Geometry	Linear, round (depends on incident light)	Linear	Linear, round (depends on insert)	Linear, round (depends on electrode geometry)
Reproducibility	High (in one batch)	Poor	Medium	High
Costs	Cheap	Cheap	Cheap	High
Throughput	Medium (~ 15 wounds/substrate)	Medium (several per dish)	Medium (several per dish)	High (8 – 96 independent wells)
Wound morphology	Cell-covered	Cell-free	Cell-free	Cell-covered
Wound monitoring	Microscopic images	Microscopic images	Microscopic images	Electrical (Impedance)
Data analysis	Image based, slow	Image based, fast	Image based, fast	Fast

migrate into the wound. This reflects also conditions found in tissue, where cells do not move to cell-free gaps, but need to modify the surrounding environment. For a successful collective movement, migrating cells need to degrade and remodel their own and the surrounding extracellular matrix (ECM) and clear perturbing cell debris. This includes production and secretion of matrix metalloproteinases (MMPs) which can degrade parts of the ECM, e.g. collagens, laminins or fibrin (Itoh and Nagase 2002). Cells migrate as multicellular sheets maintaining their cell-cell-contacts with leading cells remodeling the ECM and extending cytoplasmic extrusions in the direction of migration (Biname et al. 2010). This process could also be responsible for the overall lower but similar wound healing rates determined for NRK cells with both, optical and electrical wound healing assays. At the time-point of half-coverage of the wounded area, optical wounding yields $v(t_{1/2})$ values between $18000 - 25000 \mu\text{m}^2 \text{h}^{-1}$, while a $v(t_{1/2})$ value of $(55000 \pm 200) \mu\text{m}^2 \text{h}^{-1}$ is obtained for electrically wounded NRK cells. Additionally, determination of the maximum wound healing rate v_{max} resulted in a value of $(58000 \pm 700) \mu\text{m}^2 \text{h}^{-1}$ for the electrical ECIS[®] wound healing assay and slightly lower value ranging between $27000 - 30000 \mu\text{m}^2 \text{h}^{-1}$ for the optical wound healing assay depending on the illumination time. The lower $v(t_{1/2})$ and v_{max} values obtained for optical wounding may be caused by a temperature drop during wounding. To introduce wounds on the cell layer, the functionalized substrates are excited with the 408 nm laser at room temperature, while both, electrical wounding and subsequent monitoring is conducted at a constant temperature of 37°C . The electrical ECIS[®] and the optical wound healing assay reflect physiological conditions better compared to the scratch and the barrier assay, as cell migration during wound healing is coupled with matrix remodeling and clearing of debris. Higher wound healing rates were measured with both barrier and scratch assay probably due to the fact that migrating cells were not hindered by dead cells and surrounding ECM. At the time-point of half-coverage of the wounded area, NRK cells migrated with rates between $76000 - 94000 \mu\text{m}^2 \text{h}^{-1}$ in the scratch assay and rates between $58000 - 74000 \mu\text{m}^2 \text{h}^{-1}$ in the barrier wound healing assay. Compared to the electrical and optical assay, significantly higher v_{max} values maximum rates ranging between $111000 - 119000 \mu\text{m}^2 \text{h}^{-1}$ (scratch assay) and between $80000 - 101000 \mu\text{m}^2 \text{h}^{-1}$ (barrier assay) were measured.

Besides, optical and electrical ECIS[®] assay allow the generation of wounds with a highly reproducible geometry and size defined either by illumination time and shape of the incident light cone or the size of the electrode. However, it has to be admitted that although PS/PtTFPP substrates yielded highly uniform results in one batch, there were still batch to batch variations resulting in variations in wound size, probably caused by ageing of the sensitizer dye PtTFPP. Scratch and barrier assay

yielded rather poor results regarding reproducibility. The introduction of identical wounds was rather difficult by manual scratching and removal of small silicone inserts often led to disruption of the cell layer resulting in non-linear wounds and injuries of the cell sheet. While electrical wound healing assays allowed automated online monitoring of cell migration on the electrode with a good temporal resolution of about 2 min (dependent on the number of samples studied in parallel), wound closure studied with the novel optical wound healing assay as well as with the scratch and barrier assay was dependent on manual recording of microscopic images. Without a suitable microscopy system capable of time lapse microscopy and sample heating, the latter three assays possess a rather poor temporal resolution, as manually capturing images quickly becomes tedious and keeping track of the same field-of-view for each wound is difficult. Additionally, data analysis of microscopic images requires knowledge about image evaluation software such as NIH ImageJ to determine the size of wounded areas. Because barrier and scratch assay produce cell-free gaps, image analysis of huge data sets can be automated by applying thresholding algorithms which are able to distinguish between cell-free and cell-covered areas. This makes the determination of the wound area relatively fast (Bindschadler and McGrath 2007; Sottile et al. 2007). However, no suitable thresholding or filter function was found that could distinguish between dead cells and live neighboring cells in images obtained for the optical wound healing assay. Therefore, area size had to be determined manually for each image using a polygon selection tool. This made data analysis tedious and prone to errors by subjective evaluation of wound edges. This is particularly disadvantageous when producing multiple wounds on one or more substrates, resulting in time consuming analysis of huge data sets. Similar to scratch and barrier assay, the novel optical wound healing assay is relatively cheap with a calculated cost of production of about 10 cent/substrate, a capacity of ~ 15 wounds/substrate (applies for 10x objective, CLSM line scan mode). In contrast, electrical wound healing is generally more expensive because of the sophisticated measurement set-up and electrode arrays. Additionally, the optical wound healing assay could be easily applied as standard assay in biological research as it needs only a suitable light source such as a fluorescence or confocal microscope – standard equipment found in nearly every laboratory. Although some parameters still need to be optimized (e.g. batch to batch variation, throughput, data analysis), the novel optical wound healing assay is an attractive alternative to common wound healing assays regarding its cost effectiveness, reproducible wound geometry and wound morphology.

7.4.3 PROOF-OF-CONCEPT STUDIES

The novel optical wound healing assay based on oxygen sensitive culture substrates was used to monitor cell migration in proof-of-concept studies. First, wound healing behavior of serum starved NRK cells was analyzed. A delayed onset of repopulation of wounds of about 3 h by serum deprived cells was observed. Wound healing rate profiles showed a similar but temporally delayed curve progression for serum deprived cells. This trend was also evident as control and serum starved cells exhibited similar rates for $v(t_{1/2})$, as well as for v_{max} , while serum starved cells reached the time point of half coverage of the wound ($t_{1/2}$) about 2 h later compared to control cells. Usually, cells will migrate into the gap produced during the wound healing assay. However, migration is a process that takes hours to days. Depending on the cell line and wound size, cells cultivated in standard medium will not only migrate, but also proliferate (Jonkman et al. 2014). The additional contribution by proliferation is often undesirable, particularly when migration of highly proliferative (cancer) cells is monitored. Thus, addition of drugs such as actinomycin C to arrest mitosis or serum deprivation is used to minimize proliferative contributions (Davis et al. 2001; Reinhart-King 2008). Although a delayed onset of migration into the wounds was observed with the optical wound healing assay for serum deprived cells, no reduced wound healing rate was recorded.

Furthermore, the influence of the alkaloid Cytochalasin D was studied with NRK cells wounded on PS/PtTFPP coated substrates. The novel optical wound healing assay allowed a clear differentiation of control and Cyt D treated samples regarding wound healing dynamics. 24 h after wounding Cytochalasin D treated NRK cells could only repopulate about 78 % of the wounded area, while control cells reached full wound coverage. Morphological changes upon addition of Cyt D were clearly visible in the microscopic images, showing the wound surrounded by spherical neighboring cells. Cyt D treated cells exhibited a lower wound healing rate with a more than 50 % lower v_{max} value of $(12000 \pm 2000) \mu\text{m}^2 \text{h}^{-1}$ compared to control conditions where a v_{max} of $(26000 \pm 11000) \mu\text{m}^2 \text{h}^{-1}$ was obtained. The drastic decrease in wound healing rates of Cyt D treated cells is caused by the binding of Cyt D to the actin filaments which inhibits their polymerization and disrupts their organization. As actin filaments are an integral part of the eukaryotic cytoskeleton, binding of Cyt D leads to morphological changes, a breakdown of mechanical stability, inhibition of endo- and exocytosis as well as mitosis and cell migration (Blanchoin et al. 2014). Disruption of the actin filaments also influences cell-cell and cell-matrix interactions, resulting in a heavily impairment of collective movement of cell layers (Treat et al. 2012). Although wounds were closed incompletely

24 h after optical wounding, migration was observed in samples treated with Cyt D. This is probably caused by an incomplete inhibition of actin polymerization, as higher doses up to 20 μM are necessary to completely inhibit actin treadmilling (Yahara et al. 1982).

Finally, migration behavior of NRK cells in dependence on the extracellular pH was analyzed with the novel optical wound healing assay. Acidifying the extracellular medium led to a dramatic decrease of wound healing rates in NRK cells with only about 43 % of the wounded area repopulated after 24 h. In contrast to literature data, cells cultivated at a standard pH of 7.2 exhibited lower wound healing rates ($v_{t(1/2)}$ (7000 ± 3000) $\mu\text{m}^2 \text{h}^{-1}$; v_{max} (11000 ± 5000) $\mu\text{m}^2 \text{h}^{-1}$) compared to cells monitored at a slightly alkaline pH of 7.8 ($v_{t(1/2)}$ (11000 ± 700) $\mu\text{m}^2 \text{h}^{-1}$; v_{max} (15000 ± 1000) $\mu\text{m}^2 \text{h}^{-1}$). This observation was also made by L. Sauer, who studied the pH dependent migration of NRK cells using the electrical ECIS[®] wound healing assay (Sauer 2016). Usually, extra- and intracellular pH is tightly regulated. While differentiated cells have an extracellular pH of 7.3 – 7.4, their intracellular pH is generally lower, showing pH values of about 7.2 (Webb et al. 2011). Due to the electrical membrane potential and the metabolic activity, the cytosol tends to acidify even at a normal pH of 7.2. To prevent acidosis and maintain cellular function, cells express ion carriers such as NHE that are located in the plasma membrane and pump protons to the extracellular space (Casey et al. 2010). Although many groups report that a slightly acidic extracellular pH of about 6.8 increases migration and invasion, especially in cancer cells (Hanahan and Weinberg 2011), a highly acidic environment of about 6.4 – 6.6 has been found to reduce cell migration (Stock et al. 2005; de Valliere et al. 2015) similar to results determined for NRK cells at pH 6.4 in this work. Unfortunately, no studies are known that report on wound healing behavior of epithelial cells at slightly alkaline extracellular pH which could explain and support the faster wound healing rates obtained for a pH of 7.8. As shown in **chapter 4.6** and discussed in **chapter 4.10.4**, a decreased extracellular pH reduces cellular oxygen consumption, while an elevated pH increases oxygen consumption. It may be, that the cells have an higher energy demand due to faster migration that leads to an increase in ATP production and to higher oxygen consumption rates.

7.5 OUTLOOK

The novel optical wound healing assay enables a fast, light induced generation of wounds on transparent, biocompatible oxygen sensitive culture substrates by using standard laboratory microscopes. Future work should focus on a facilitated data analysis, as manual evaluation of images makes the assay still tedious due to the lacking contrast between wounded and non-wounded cells. Better visualization and discrimination between wounded and intact parts of the cell layer could be for example reached by using cells expressing fluorescent markers such as the green fluorescent protein (GFP). The wound area could be minimized by using an objective with higher magnification, allowing monitoring of the whole wound within a smaller field of view with better resolution to visualize the boundary between live and dead cells. Furthermore, changing the format of PS/PtTFPP substrates to PS/PtTFPP coated multi-well plates in combination with a LED array and a suitable mask could enhance throughput by simultaneous generation of multiple wounds. The combination of PS/PtTFPP substrates with transparent multichannel microfluidics could also enable studying wound healing behavior under flow conditions and sheer stress – conditions usually found in the body. Doping the novel functionalized substrates with the physical scavenger Vit E led to a complete inhibition of singlet oxygen induced cytotoxicity. This layout could be used to generate culture substrates which possess a low phototoxicity and are at the same time addressable to both light microscopy and lifetime dependent oxygen determination. This constellation would allow long-term monitoring of oxygen consumption without killing cells on the sensor surface. It could also be used to produce a distinct overlay of 2D oxygen distribution maps and the cells grown on the substrates during the experiment which is not possible with opaque substrates such as the ratiometric oxygen sensor foils used in this work. As shown in **chapter 4.9**, oxygen gradients within a cell patch can be monitored using the opaque, ratiometric sensor foils. However, to ensure that the changes in the spatial oxygen distribution are caused by the cell patch the sample needs to get stained at the end of the measurement. This would become redundant when using optical transparent substrates.

8 SUMMARY

Eukaryotic cells need oxygen to sustainably produce the metabolite ATP as their main source of energy. Next to glucose, oxygen is one of the key metabolites which can give us insight into cellular processes and conveys important information of parameters like cellular viability, metabolic activity and physiology. Thus, knowledge about cellular oxygen consumption is an essential parameter not only when studying pathophysiological conditions, such as metabolic disease, cancer or stroke, but also in drug and cytotoxicity screening. Methods to assess oxygenation levels and oxygen consumption of cells, spheroids and tissue range from electrochemical detection to the use of magnetic resonance and radioisotope techniques. However, in recent years the detection of oxygen by luminescence quenching of indicator dyes has emerged as a useful technique to study oxygenation of eukaryotic cells. Thus, one of the main projects in this work was to use planar oxygen sensitive culture substrates based on luminescence quenching as a novel means to estimate and image the oxygen consumption in 2D and 3D cell culture models. The substrates allowed the cultivation of adherent mammalian cells directly on the surface which provides the possibility to measure oxygen content directly beneath the cell monolayer. The combination of planar oxygen sensor foils with a suitable camera system enabled non-invasive, online monitoring of the spatial and the temporal oxygen distribution beneath the cell layer.

The first project addressed the measurement of the oxygen consumption rate of adherent mammalian monolayer cells. Therefore, an imaging system based on microscopy optics (VisiSens TD mic) was developed in cooperation with PreSens GmbH, Regensburg. The system fits inside a standard cell incubator (48 l) and allows imaging the spatial and temporal distribution of oxygen with high resolution. Planar, polymer based oxygen sensitive foils (SF-RPSu4, PreSens GmbH) for a ratiometric fluorescence readout were used as growth substrates which allowed monitoring the oxygen content directly underneath the adherent cells. The sensor foils exhibited high photostability and biocompatibility which allowed their usage for long term cell experiments. The novel imaging system was used for first proof-of-concept studies to assess oxygen consumption rates in dependence on culture vessel volume and cell seeding density yielding highly reproducible results. Additionally, the novel ratiometric imaging system allowed the successful monitoring of the influence of medium composition, extracellular pH, drugs and toxins on respiratory activity of adherent cells. The high spatial resolution of the camera was used for long term imaging of oxygen gradients caused by a metabolically active spot of monolayer cells.

Multiparametric monitoring of cells is a useful approach to obtain multiple information in one measurement. Thus, the second project focused on combining the optical oxygen sensing with impedimetric monitoring to obtain information about cell metabolic activity and cell morphology changes. Therefore, gold film electrodes were sputtered on planar, ratiometric oxygen sensor foils using a laser cut mask. A PDMS chamber was glued on top of the foil that served as cultivation chamber for the adherent mammalian cells. The dual ECIS-O₂ sensor allowed simultaneous, non-invasive online recording of impedance and pO₂ using a standard impedance analyzer and a commercial oxygen imaging system (VisiSens A1). Impedance changes were monitored for the cell population residing on the linear gold film electrodes, while oxygen levels were measured for those cells on the electrode-free sensor film. The dual sensor was characterized regarding its biocompatibility, signal stability and most sensitive impedimetric monitoring frequency. First studies conducted with the dual chip allowed simultaneous monitoring of the oxygen consumption and the impedance during cell adhesion. Moreover, the ECIS-O₂ chip was used to investigate the influence of uncouplers and blockers of oxidative phosphorylation with impedance measurements providing information about changes in cell morphology and electrode coverage, while the ratiometric fluorescence readout reports on the cellular oxygen consumption rate.

3D tissue models such as multicellular tumor spheroids are considered useful *in vitro* tools in biomedical and clinical research. Due to their 3D structure, they close the gap between simple 2D monolayer cell culture and native tissue structures. Multicellular spheroids mimic physiological conditions found in tissue more closely compared to standard 2D cell culture, while handling and cultivation is easier compared to tissue. This makes multicellular tumor spheroids an attractive means in biomedical research and drug screening. Long-term studies on oxygenation in live spheroids are scarce because most assays are either endpoint-based or invasive such as microneedle or particle based approaches. Thus, the third project applied the novel imaging system VisiSens TD mic for quantitative monitoring of oxygenation levels within live MCF-7 tumor spheroids under standard growth conditions. Originally spherical spheroids were allowed to attach and spread on planar, biocompatible oxygen sensor foils forming half-spherical cell aggregates and oxygen content beneath the spheroid was monitored online with high spatio-temporal resolution. The imaging set-up allowed recording the detailed 2D distribution of oxygen gradients caused by metabolically active spheroids with higher resolution compared to commercially available imaging systems. Further studies were conducted investigating the effect of drugs blocking or uncoupling

oxidative phosphorylation on oxygen gradients established in live and metabolically active MCF-7 spheroids.

Wound healing assays are often used to study collective cell migration *in vitro*. The general concept of such assays is to introduce an artificial wound into a confluent layer of adherent cells and to study the migration of non-wounded cells from the periphery into the wound. The aim of the fourth project was the development of a novel wound healing assay based on oxygen sensitive culture substrates. The assay uses planar, polymer-based culture substrates with an embedded oxygen sensor dye as culture substrates for adherent cells. The functional layer was deposited on coverslips by spin-coating providing a transparent composite substrate that is addressable by light microscopy. Upon illumination with a suitable wavelength the dye molecules were excited. The $^1\text{O}_2$ produced by luminescence quenching was used to selectively kill cells residing on areas of the functional coating that were exposed to the illumination light generating wounds with a highly reproducible geometry. The oxygen sensitive substrates designed for wound healing were analyzed regarding their biocompatibility and the influence of parameters such as light source, microscope filter settings and medium composition on wounding efficacy was tested. The novel wound healing assay was used to probe collective cell migration under various experimental conditions and it was compared to other wound healing assays such as scratch, barrier and ECIS[®] assay regarding parameters such as cost, throughput, reproducibility or wound morphology. Similar to the ECIS[®] assay, wounds produced by the novel optical wound healing assay mimic the physiological conditions more closely, as dead cells remain as debris in the wound. Additional studies were performed investigating wound healing behavior of epithelial cells exposed to different extracellular pH values which resulted in reduced wound healing rates at low pH. Furthermore, it was shown that serum starvation and cytochalasin C reduced wound closure rate as well.

9 ZUSAMMENFASSUNG

Eukaryotische Zellen benötigen Sauerstoff, um nachhaltig Energie in Form von ATP zu erzeugen. Daher ist Sauerstoff neben Glukose der Schlüssel-Analyt, mit dessen Hilfe sich Aussagen über wichtige zelluläre Parameter, wie Vitalität, metabolische Aktivität oder Physiologie treffen lässt. Ein veränderter zellulärer Sauerstoffverbrauch ist unter anderem ein wichtiger Indikator um pathophysiologische Zustände wie Krebs, Stoffwechselerkrankungen oder Schlaganfall zu identifizieren. Zudem können unterschiedliche Respirationsraten Aufschluss über die anaerobe Stoffwechselaktivität geben, was insbesondere bei Arzneimitteltests und Zytotoxizitätsscreenings von Interesse ist. Neben der elektrochemischen Bestimmung mittels Clark Elektrode, kann der Sauerstoffverbrauch von Zellen, Gewebemodellen und Geweben auch durch Magnetresonanz- oder Radioisotopentechniken ermittelt werden. Mittlerweile gewinnt die Detektion des zellulären Sauerstoffverbrauchs basierend auf der Lumineszenzlöschung von Indikatorfarbstoffen immer mehr an Bedeutung. Daher befasste sich diese Arbeit mit der Verwendung von planaren Substraten, die mit einer sauerstoffsensitiven Schicht überzogen sind und die eine Bestimmung des Sauerstoffgehalts über die Lumineszenzlöschung erlauben. Adhärenente Säugetierzellen wurden direkt auf der Sensoroberfläche kultiviert, um eine Bestimmung des Sauerstoffgehalts direkt unter der Zellschicht zu ermöglichen. Durch die Kombination der planaren Sauerstoffsensorfolien mit einem geeigneten Kamerasystem wurde die räumliche und zeitliche Änderung des Sauerstoffgehalts unterhalb der Zellschicht nicht-invasiv und mit guter Zeitauflösung untersucht.

Das erste Projekt befasste sich mit der Detektion des Sauerstoffverbrauchs von adhärenenten Säugetierzellmonoschichten. Zur Bearbeitung dieser Problemstellung wurde in Zusammenarbeit mit der Firma PreSens GmbH, Regensburg, ein auf einer Mikroskopoptik basierendes Kamerasystem (VisiSens TD mic) entwickelt. Das Messsystem lässt sich in ein normales Zellkulturinkubationssystem (48 l) integrieren und ermöglicht die Bildgebung der räumlichen und zeitlichen Sauerstoffverteilung mit hoher Auflösung. Als Wachstumssubstrate wurden polymer-basierte, sauerstoffempfindliche Folien (SF-RPSu4, PreSens GmbH) verwendet, die eine ratiometrische Quantifizierung des Sauerstoffgehalts unterhalb der Zellschicht ermöglichen. Eine Nutzung der Sensorfolien für Langzeitstudien an Zellen war aufgrund der hohen Photostabilität, der geringen Phototoxizität und einer guten Biokompatibilität möglich. Das neu entwickelte Messsystem wurde für erste Beispielstudien verwendet. Versuche zur Abhängigkeit der Sauerstoffverbrauchsraten in Abhängigkeit vom Mediumvolumen und der Zellaussaatdichte zeigten reproduzierbare Ergebnisse.

Darüber hinaus konnte der Einfluss des extrazellulären pH-Werts, sowie der Effekt von Toxinen und pharmakologischen Substanzen auf den Sauerstoffverbrauch von NRK und MDCK II Zellen erfolgreich nachgewiesen werden. Zudem wurde die hohe räumliche Auflösung der Kamera für die Abbildung eines Sauerstoffgradienten verwendet, der durch einen isolierten Patch metabolisch aktiver Zellen verursacht wurde.

Die zeitgleiche Erfassung von mehreren Parametern mit Hilfe eines dualen Sensors ist ein nützlicher Ansatz, um den Informationsgewinn einer Messung zu erhöhen. Daher fokussierte sich das zweite Projekt auf die Kombination von optischen Sauerstoffsensoren und Impedanzanalyse (ECIS-O₂) zur Vermessung von adhären Zellschichten. Hierfür wurden lineare Goldfilmelektroden mit Hilfe einer Maske auf planare, sauerstoffsensitive Substrate abgeschieden. Eine auf den Sensor aufgeklebte PDMS Kammer diente zur Zellkultivierung. Der duale Sensor ermöglicht eine gleichzeitige, zeitaufgelöste Messung der Impedanz zur Untersuchung der Zellmorphologie und der ratiometrischen Fluoreszenz-Emission zur Bestimmung des Sauerstoffverbrauchs. Die Kombination der ratiometrischen Sauerstoffbestimmung mit dem impedimetrischen Ausleseverfahren ermöglichte die Korrelation von Zellstoffwechselaktivität und Änderungen der Zellmorphologie. Der duale ECIS-O₂ Sensor wurde hinsichtlich von Parametern wie Biokompatibilität, Signalstabilität und der sensitiven Frequenzen zur Impedanzmessung charakterisiert. Erste Studien ermöglichten das simultane Auslesen des Sauerstoffverbrauchs und der Impedanz während der Adhäsion von MDCK II Zellen. Darüber hinaus wurde der duale Sensor verwendet, um den Einfluss von Entkopplern und Blockern der Zellatmung zu untersuchen.

Multizelluläre Tumorsphäroide sind 3D Gewebemodelle, die als nützliche Werkzeuge für *in vitro* Studien in der klinischen Forschung angesehen werden. Aufgrund ihrer dreidimensionalen Struktur bilden sie den Brückenschlag zwischen 2D Zellmonoschichten und nativem Gewebe. Durch ihren Aufbau entspricht die Physiologie von multizellulären Sphäroiden mehr der von Geweben, während ihre Kultivierung wesentlich einfacher ist als die von Gewebe. Es gibt nur wenige Studien, die über den Sauerstoffgehalt in lebenden Sphäroiden berichten. Gängige Methoden zur Untersuchung des Sauerstoffgehalts sind zumeist endpunktbasierend, führen zum Absterben Zellen während der Messung oder sind struktur-invasiv, wie beispielsweise das Einbringen von Mikroelektroden oder Nanopartikeln in das Sphäroid. Aus diesem Grund wurde im Rahmen des dritten Projekts der Sauerstoffverbrauch von MCF-7 Tumorsphäroiden mit Hilfe des neu entwickelten, mikroskopoptikbasierten Detektionssystems quantitativ untersucht. Hierfür wurden die Sphäroide auf planaren, biokompatiblen Sauerstoffsensorfolien kultiviert. Die zunächst sphärischen Sphäroide bilden nach

Adhäsion auf den Folien semi-sphärische Strukturen, deren Sauerstoffgehalt mit hoher räumlicher und zeitlicher Auflösung nachverfolgt werden konnte. Der Messaufbau erlaubte eine wesentlich detailliertere Darstellung der räumlichen Sauerstoffverteilung, im Vergleich zu etablierten, bildgebenden Sauerstoffdetektionssystemen. So konnten Sauerstoffgradienten innerhalb der Sphäroide, verursacht durch die metabolisch aktiven Zellen im Sphäroid, über Stunden bis Tage vermessen werden. Des Weiteren konnten mit Hilfe des neuen Messsystems die Wirkung verschiedener Testsubstanzen auf die zeitliche und räumliche Sauerstoffverteilung untersucht werden. Hierfür wurde beispielhaft die oxidative Phosphorylierung der Sphäroide mit Pharmaka entkoppelt oder blockiert, was zu einem Anstieg oder Zusammenbruch des Sauerstoffgradienten zwischen Peripherie und Zentrum des Sphäroids führte.

Wundheilungsassays sind ein beliebtes Mittel zur Untersuchung von kollektiver Zellmigration unter *in vitro* Bedingungen. Hierfür wird eine künstliche Wunde in eine Zellmonoschicht eingebracht und die Migration von benachbarten Zellen in die Wunde untersucht. Im Rahmen des vierten Projekts wurde ein neuer Wundheilungsassay basierend auf sauerstoffempfindlichen Kultursubstraten entwickelt. Planare, polymer-basierte Schichten mit eingebetteten, sauerstoffsensitiven Farbstoffen wurde mittels Schleuderbelackung auf Deckgläschen hergestellt. Die so hergestellten transparenten Komposit-Substrate erlauben sowohl eine direkte Kultivierung von adhären Zellen an der Oberfläche, als auch lichtmikroskopische Studien. Die Verwundung erfolgt durch eine gezielte Anregung der Farbstoffmoleküle im Substrat. Durch das Prinzip der Lumineszenzlöschung wird Singulett-Sauerstoff erzeugt, der die Zellen im belichteten Bereich gezielt abtötet. Die funktionalisierten Substrate wurden hinsichtlich ihrer Biokompatibilität analysiert und der Einfluss von Parametern wie Lichtquelle, Belichtungsdauer, Belichtungsintensität oder Art des Kulturmediums wurde untersucht. Der neue optische Assay wurde mit etablierten Methoden wie dem Scratch, Barriere oder ECIS[®] Assay hinsichtlich Kosten, Durchsatz, Reproduzierbarkeit oder Wundmorphologie verglichen. Der neuartige Assay wurde zudem verwendet, um das Wundheilungsverhalten von Epithelzellen unter Einfluss von Faktoren wie verändertem extrazellulärem pH-Wert oder Serumentzug, sowie unter Einwirkung des Mycotoxins Cytochalasin D zu untersuchen.

10 REFERENCES

Aguer, C., Gambarotta, D., Mailloux, R. J., Moffat, C., Dent, R., McPherson, R. and Harper, M. E. (2011) Galactose enhances oxidative metabolism and reveals mitochondrial dysfunction in human primary muscle cells. *Plos One* **6** (12): e28536.

Ahmad, R. and Kuppusamy, P. (2010) Theory, instrumentation, and applications of electron paramagnetic resonance oximetry. *Chemical Reviews* **110** (5): 3212-3236.

Amao, Y. (2003) Probes and polymers for optical sensing of oxygen. *Microchimica Acta* **143** (1): 1-12.

Amesz, J. and Hoff, A. J. (2006). *Biophysical techniques in photosynthesis*. Dordrecht ;, Boston : Kluwer Academic Publishers.

Andreux, P. A., Mouchiroud, L., Wang, X., Jovaisaite, V., Mottis, A., Bichet, S., Moullan, N., Houtkooper, R. H. and Auwerx, J. (2014) A method to identify and validate mitochondrial modulators using mammalian cells and the worm *C. elegans*. *Sci Rep* **4**: 5285.

Ashton, T. M., Fokas, E., Kunz-Schughart, L. A., Folkes, L. K., Anbalagan, S., Huether, M., Kelly, C. J., Pirovano, G., Buffa, F. M., Hammond, E. M., Stratford, M., Muschel, R. J., Higgins, G. S. and McKenna, W. G. (2016) The anti-malarial atovaquone increases radiosensitivity by alleviating tumour hypoxia. *Nat Commun* **7**: 12308.

Ast, C., Schmalzlin, E., Lohmannsroben, H. G. and van Dongen, J. T. (2012) Optical Oxygen Micro- and Nanosensors for Plant Applications. *Sensors* **12** (6): 7015-7032.

Baldini, F., Bacci, M., Cosi, F. and Delbianco, A. (1992) Absorption-Based Optical-Fiber Oxygen Sensor. *Sensors and Actuators B-Chemical* **7** (1-3): 752-757.

Barcroft, J. and Haldane, J. S. (1902) A method of estimating the oxygen and carbonic acid in small quantities of blood. *J Physiol* **28** (3): 232-240.

Bellare, A., D'angelo, F., Ngo, H. D. and Thornhill, T. S. (2016) Oxidation resistance and abrasive wear resistance of vitamin E stabilized radiation crosslinked ultra-high molecular weight polyethylene. *Journal of Applied Polymer Science* **133** (43).

Berg, J. M., Tymoczko, J. L. and Stryer, L. (2012). *Biochemistry*. New York, W.H. Freeman.

- Bertin, G. and Averbeck, D. (2006) Cadmium: cellular effects, modifications of biomolecules, modulation of DNA repair and genotoxic consequences (a review). *Biochimie* **88** (11): 1549-1559.
- Bibby, S. R., Jones, D. A., Ripley, R. M. and Urban, J. P. (2005) Metabolism of the intervertebral disc: effects of low levels of oxygen, glucose, and pH on rates of energy metabolism of bovine nucleus pulposus cells. *Spine (Phila Pa 1976)* **30** (5): 487-496.
- Biname, F., Pawlak, G., Roux, P. and Hibner, U. (2010) What makes cells move: requirements and obstacles for spontaneous cell motility. *Molecular Biosystems* **6** (4): 648-661.
- Bindschadler, M. and McGrath, J. L. (2007) Sheet migration by wounded monolayers as an emergent property of single-cell dynamics. *J Cell Sci* **120** (5): 876-884.
- Blanchoin, L., Boujemaa-Paterski, R., Sykes, C. and Plastino, J. (2014) Actin Dynamics, Architecture, and Mechanics in Cell Motility. *Physiological Reviews* **94** (1): 235-263.
- Boyce, M. W., Kenney, R. M., Truong, A. S. and Lockett, M. R. (2016) Quantifying oxygen in paper-based cell cultures with luminescent thin film sensors. *Analytical and Bioanalytical Chemistry* **408** (11): 2985-2992.
- Brand, M. D. and Nicholls, D. G. (2011) Assessing mitochondrial dysfunction in cells. *Biochemical Journal* **435**: 297-312.
- Braun, R. D., Lanzen, J. L., Snyder, S. A. and Dewhirst, M. W. (2001) Comparison of tumor and normal tissue oxygen tension measurements using OxyLite or microelectrodes in rodents. *American Journal of Physiology-Heart and Circulatory Physiology* **280** (6): H2533-H2544.
- Brunetti, V., Maiorano, G., Rizzello, L., Sorce, B., Sabella, S., Cingolani, R. and Pompa, P. P. (2010) Neurons sense nanoscale roughness with nanometer sensitivity. *Proceedings of the National Academy of Sciences of the United States of America* **107** (14): 6264-6269.
- Campo, M. L., Kinnally, K. W. and Tedeschi, H. (1992) The Effect of Antimycin-a on Mouse-Liver Inner Mitochondrial-Membrane Channel Activity. *Journal of Biological Chemistry* **267** (12): 8123-8127.
- Canete, M., Ortega, C., Gavalda, A., Cristobal, J., Juarranz, A., Nonell, S., Teixido, J., Borrell, J. I., Villanueva, A., Rello, S. and Stockert, J. C. (2004) Necrotic cell death induced by photodynamic treatment of human lung adenocarcinoma A-549 cells with palladium(II)-tetraphenylporphycene. *International Journal of Oncology* **24** (5): 1221-1228.
- Carlisle, R., Rhoads, C. A., Aw, T. Y. and Harrison, L. (2002) Endothelial cells maintain a reduced redox environment even as mitochondrial function declines. *American Journal of Physiology-Cell Physiology* **283** (6): C1675-C1686.

Carlsson, J., Stalnacke, C. G., Acker, H., Haji-Karim, M., Nilsson, S. and Larsson, B. (1979) The influence of oxygen on viability and proliferation in cellular spheroids. *Int J Radiat Oncol Biol Phys* **5** (11-12): 2011-2020.

Carreau, A., El Hafny-Rahbi, B., Matejuk, A., Grillon, C. and Kieda, C. (2011) Why is the partial oxygen pressure of human tissues a crucial parameter? Small molecules and hypoxia. *Journal of Cellular and Molecular Medicine* **15** (6): 1239-1253.

Casey, J. R., Grinstein, S. and Orlowski, J. (2010) Sensors and regulators of intracellular pH. *Nat Rev Mol Cell Biol* **11** (1): 50-61.

Castano, A. P., Demidova, T. N. and Hamblin, M. R. (2005) Mechanisms in photodynamic therapy: part two-cellular signaling, cell metabolism and modes of cell death. *Photodiagnosis and Photodynamic Therapy* **2** (1): 1-23.

Catling, D. C., Glein, C. R., Zahnle, K. J. and McKay, C. P. (2005) Why O₂ is required by complex life on habitable planets and the concept of planetary "oxygenation time". *Astrobiology* **5** (3): 415-438.

Ceroni, P., Lebedev, A. Y., Marchi, E., Yuan, M., Esipova, T. V., Bergamini, G., Wilson, D. F., Busch, T. M. and Vinogradov, S. A. (2011) Evaluation of phototoxicity of dendritic porphyrin-based phosphorescent oxygen probes: an in vitro study. *Photochemical & Photobiological Sciences* **10** (6): 1056-1065.

Chandra, R., Tiwari, M., Kaur, P., Sharma, M., Jain, R. and Dass, S. (2000) Metalloporphyrins—Applications and clinical significance. *Indian Journal of Clinical Biochemistry* **15** (Suppl 1): 183-199.

Chipman, L., Huettel, M., Berg, P., Meyer, V., Klimant, I., Glud, R. and Wenzhoefer, F. (2012) Oxygen optodes as fast sensors for eddy correlation measurements in aquatic systems. *Limnology and Oceanography-Methods* **10**: 304-316.

Chung, K. E., Lan, E. H., Davidson, M. S., Dunn, B. S., Valentine, J. S. and Zink, J. I. (1995) Measurement of Dissolved-Oxygen in Water Using Glass-Encapsulated Myoglobin. *Analytical Chemistry* **67** (9): 1505-1509.

Clark, L. C., Jr., Wolf, R., Granger, D. and Taylor, Z. (1953) Continuous recording of blood oxygen tensions by polarography. *J Appl Physiol* **6** (3): 189-193.

Cooper, J. A. (1987) Effects of Cytochalasin and Phalloidin on Actin. *Journal of Cell Biology* **105** (4): 1473-1478.

- Cui, H. Z. and Yang, X. M. (2010) In vivo imaging and treatment of solid tumor using integrated photoacoustic imaging and high intensity focused ultrasound system. *Medical Physics* **37** (9): 4777-4781.
- Cywinski, P. J., Moro, A. J., Stanca, S. E., Biskup, C. and Mohr, G. J. (2009) Ratiometric porphyrin-based layers and nanoparticles for measuring oxygen in biosamples. *Sensors and Actuators B-Chemical* **135** (2): 472-477.
- Davis, P. K., Ho, A. and Dowdy, S. F. (2001) Biological methods for cell-cycle synchronization of mammalian cells. *Biotechniques* **30** (6): 1322-+.
- de Valliere, C., Vidal, S., Clay, I., Jurisic, G., Tcymbarevich, I., Lang, S., Ludwig, M. G., Okoniewski, M., Eloranta, J. J., Kullak-Ublick, G. A., Wagner, C. A., Rogler, G. and Seuwen, K. (2015) The pH-sensing receptor OGR1 improves barrier function of epithelial cells and inhibits migration in an acidic environment. *Am J Physiol Gastrointest Liver Physiol* **309** (6): G475-490.
- Delarco, J. E. and Todaro, G. J. (1978) Epithelioid and Fibroblastic Rat-Kidney Cell Clones - Epidermal Growth-Factor (Egf) Receptors and Effect of Mouse Sarcoma-Virus Transformation. *J Cell Physiol* **94** (3): 335-342.
- Desmet, C. M., Lafosse, A., Veriter, S., Porporato, P. E., Sonveaux, P., Dufrane, D., Leveque, P. and Gallez, B. (2015) Application of Electron Paramagnetic Resonance (EPR) Oximetry to Monitor Oxygen in Wounds in Diabetic Models. *Plos One* **10** (12).
- Di Mascio, P., Devasagayam, T. P. A., Kaiser, S. and Sies, H. (1990) Carotenoids, Tocopherols and Thiols as Biological Singlet Molecular-Oxygen Quenchers. *Biochemical Society Transactions* **18** (6): 1054-1056.
- Dierckx, R. A. J. O., Otte, A. P., Vries, E. F. J. d. and Waarde, A. v. (2014). *PET and SPECT of neurobiological systems*.
- Dmitriev, R. I., Borisov, S. M., Kondrashina, A. V., Pakan, J. M. P., Anilkumar, U., Prehn, J. H. M., Zhdanov, A. V., McDermott, K. W., Klimant, I. and Papkovsky, D. B. (2015) Imaging oxygen in neural cell and tissue models by means of anionic cell-permeable phosphorescent nanoparticles. *Cellular and Molecular Life Sciences* **72** (2): 367-381.
- Dmitriev, R. I., Kondrashina, A. V., Koren, K., Klimant, I., Zhdanov, A. V., Pakan, J. M. P., McDermott, K. W. and Papkovsky, D. B. (2014) Small molecule phosphorescent probes for O₂ imaging in 3D tissue models. *Biomaterials Science* **2** (6): 853-866.
- Dmitriev, R. I. and Papkovsky, D. B. (2012) Optical probes and techniques for O₂ measurement in live cells and tissue. *Cell Mol Life Sci* **69** (12): 2025-2039.

- Doerr, N., Wang, Y. D., Kipp, K. R., Liu, G. Y., Benza, J. J., Pletnev, V., Pavlov, T. S., Staruschenko, A., Mohieldin, A. M., Takahashi, M., Nauli, S. M. and Weimbs, T. (2016) Regulation of Polycystin-1 Function by Calmodulin Binding. *Plos One* **11** (8).
- Dragu, A., Taeger, C. D., Buchholz, R., Sommerfeld, B., Hubner, H., Birkholz, T., Kleinmann, J. A., Munch, F., Horch, R. E. and Prabst, K. (2012) Online oxygen measurements in ex vivo perfused muscle tissue in a porcine model using dynamic quenching methods. *Archives of Orthopaedic and Trauma Surgery* **132** (5): 655-661.
- Egorov, S., Kamalov, V. F., Koroteev, N. I., Krasnovsky Jr, A., Toleutaev, B. N. and Zinukov, S. V. (1989). *Rise and decay kinetics of photosensitized singlet oxygen luminescence in water. Measurements with nanosecond time-correlated single photon counting technique.*
- Eklund, S. E., Taylor, D., Kozlov, E., Prokop, A. and Cliffel, D. E. (2004) A microphysiometer for simultaneous measurement of changes in extracellular glucose, lactate, oxygen, and acidification rate. *Analytical Chemistry* **76** (3): 519-527.
- Erapaneedi, R., Belousov, V. V., Schafers, M. and Kiefer, F. (2016) A novel family of fluorescent hypoxia sensors reveal strong heterogeneity in tumor hypoxia at the cellular level. *Embo Journal* **35** (1): 102-113.
- Esipova, T. V., Karagodov, A., Miller, J., Wilson, D. F., Busch, T. M. and Vinogradov, S. A. (2011) Two New "Protected" Oxyphors for Biological Oximetry: Properties and Application in Tumor Imaging. *Analytical Chemistry* **83** (22): 8756-8765.
- Fang, H. M., Huang, S. J., Yang, C. L., Young, K. C. and Yu, C. K. (2013) Miniaturized Real-Time Oxygen Detection Systems Integrated with Optical Fiber by Doping Ru-Based Fluorescence Sensors. *Journal of Medical and Biological Engineering* **33** (1): 117-123.
- Feldenberg, L. R., Thevananther, S., Del Rio, M., De Leon, M. and Devarajan, P. (1999) Partial ATP depletion induces Fas- and caspase-mediated apoptosis in MDCK cells. *American Journal of Physiology-Renal Physiology* **276** (6): F837-F846.
- Feng, Y., Cheng, J., Zhou, L., Zhou, X. and Xiang, H. (2012) Ratiometric optical oxygen sensing: a review in respect of material design. *Analyst* **137** (21): 4885-4901.
- Ferdinand, P. and Roffe, C. (2016) Hypoxia after stroke: a review of experimental and clinical evidence. *Exp Transl Stroke Med* **8**: 9.
- Fischer, J. P. and Wenzhofer, F. (2010) A novel planar optode setup for concurrent oxygen and light field imaging: Application to a benthic phototrophic community. *Limnology and Oceanography- Methods* **8**: 254-268.

- Freyer, J. P. (1988) Role of necrosis in regulating the growth saturation of multicellular spheroids. *Cancer Research* **48** (9): 2432-2439.
- Giaever, I. and Keese, C. R. (1984) Monitoring fibroblast behavior in tissue culture with an applied electric field. *Proc Natl Acad Sci U S A* **81** (12): 3761-3764.
- Giang, A. H., Raymond, T., Brookes, P., de Mesy Bentley, K., Schwarz, E., O'Keefe, R. and Eliseev, R. (2013) Mitochondrial dysfunction and permeability transition in osteosarcoma cells showing the Warburg effect. *Journal of Biological Chemistry* **288** (46): 33303-33311.
- Goddette, D. W. and Frieden, C. (1986) Actin Polymerization - the Mechanism of Action of Cytochalasin-D. *Journal of Biological Chemistry* **261** (34): 5974-5980.
- Goense, J., Bohraus, Y. and Logothetis, N. K. (2016) fMRI at High Spatial Resolution: Implications for BOLD-Models. *Frontiers in Computational Neuroscience* **10**.
- Grimes, D. R., Kelly, C., Bloch, K. and Partridge, M. (2014) A method for estimating the oxygen consumption rate in multicellular tumour spheroids. *Journal of the Royal Society Interface* **11** (92).
- Grist, S. M., Chrostowski, L. and Cheung, K. C. (2010) Optical Oxygen Sensors for Applications in Microfluidic Cell Culture. *Sensors* **10** (10): 9286-9316.
- Groebe, K. and MuellerKlieser, W. (1996) On the relation between size of necrosis and diameter of tumor spheroids. *International Journal of Radiation Oncology Biology Physics* **34** (2): 395-401.
- Gross, M. W., Karbach, U., Groebe, K., Franko, A. J. and Muellerklieser, W. (1995) Calibration of Misonidazole Labeling by Simultaneous Measurement of Oxygen-Tension and Labeling Density in Multicellular Spheroids. *International Journal of Cancer* **61** (4): 567-573.
- Guarino, R. D., Dike, L. E., Haq, T. A., Rowley, J. A., Pitner, J. B. and Timmins, M. R. (2004) Method for determining oxygen consumption rates of static cultures from microplate measurements of pericellular dissolved oxygen concentration. *Biotechnology and Bioengineering* **86** (7): 775-787.
- Hajek, K., Schmittlein, C., Oberleitner, M., Shin, I.-S. and Wegener, J. (2016). Biosensors. *eLS*, John Wiley & Sons, Ltd.
- Hamblin, M. R. (2016) Antimicrobial photodynamic inactivation: a bright new technique to kill resistant microbes. *Current Opinion in Microbiology* **33**: 67-73.
- Hanahan, D. and Weinberg, R. A. (2011) Hallmarks of cancer: the next generation. *Cell* **144** (5): 646-674.

Herst, P. M. and Berridge, M. V. (2007) Cell surface oxygen consumption: a major contributor to cellular oxygen consumption in glycolytic cancer cell lines. *Biochimica Et Biophysica Acta* **1767** (2): 170-177.

Hirakawa, Y., Yoshihara, T., Kamiya, M., Mimura, I., Fujikura, D., Masuda, T., Kikuchi, R., Takahashi, I., Urano, Y., Tobita, S. and Nangaku, M. (2015) Quantitating intracellular oxygen tension in vivo by phosphorescence lifetime measurement. *Scientific Reports* **5**.

Hirschhaeuser, F., Menne, H., Dittfeld, C., West, J., Mueller-Klieser, W. and Kunz-Schughart, L. A. (2010) Multicellular tumor spheroids: An underestimated tool is catching up again. *Journal of Biotechnology* **148** (1): 3-15.

Hoeffner, E. G. (2005) Cerebral perfusion imaging. *Journal of Neuro-Ophthalmology* **25** (4): 313-320.

Hofmann, J., Meier, R. J., Mahnke, A., Schatz, V., Brackmann, F., Trollmann, R., Bogdan, C., Liebsch, G., Wang, X. D., Wolfbeis, O. S. and Jantsch, J. (2013) Ratiometric luminescence 2D in vivo imaging and monitoring of mouse skin oxygenation. *Methods and Applications in Fluorescence* **1** (4).

Holst, G., Kohls, O., Klimant, I., Konig, B., Kuhl, M. and Richter, T. (1998) A modular luminescence lifetime imaging system for mapping oxygen distribution in biological samples. *Sensors and Actuators B-Chemical* **51** (1-3): 163-170.

<http://www.unisense.com/O2/>

Hupf, C. (2016). Impedance-based analysis of 3D tissue models: A novel measurement setup for novel measurement modes. *Chemistry*, University of Regensburg.

Ippolito, J. E., Brandenburg, M. W., Ge, X., Crowley, J. R., Kirmess, K. M., Som, A., D'Avignon, D. A., Arbeit, J. M., Achilefu, S., Yarasheski, K. E. and Milbrandt, J. (2016) Extracellular pH Modulates Neuroendocrine Prostate Cancer Cell Metabolism and Susceptibility to the Mitochondrial Inhibitor Niclosamide. *Plos One* **11** (7): e0159675.

Itoh, T., Yaegashi, K., Kosaka, T., Kinoshita, T. and Morimoto, T. (1994) In-Vivo Visualization of Oxygen-Transport in Microvascular Network. *American Journal of Physiology-Heart and Circulatory Physiology* **267** (5): H2068-H2078.

Itoh, Y. and Nagase, H. (2002) Matrix metalloproteinases in cancer. *Proteases in Biology and Medicine* **38**: 21-36.

Jenkins, J., Dmitriev, R. I., Morten, K., McDermott, K. W. and Papkovsky, D. B. (2015) Oxygen-sensing scaffolds for 3-dimensional cell and tissue culture. *Acta Biomaterialia* **16**: 126-135.

- Jeong, E. K., Lee, S. Y., Jeon, H. M., Ju, M. K., Kim, C. H. and Kang, H. S. (2010) Role of extracellular signal-regulated kinase (ERK)1/2 in multicellular resistance to docetaxel in MCF-7 cells. *International Journal of Oncology* **37** (3): 655-661.
- Jez, M., Rozman, P., Ivanovic, Z. and Bas, T. (2015) Concise Review: The Role of Oxygen in Hematopoietic Stem Cell Physiology. *J Cell Physiol* **230** (9): 1999-2005.
- Jin, P. and Ringertz, N. R. (1990) Cadmium induces transcription of proto-oncogenes c-jun and c-myc in rat L6 myoblasts. *Journal of Biological Chemistry* **265** (24): 14061-14064.
- Jones, C. I., Han, Z. S., Presley, T., Varadharaj, S., Zweier, J. L., Ilangovan, G. and Alevriadou, B. R. (2008) Endothelial cell respiration is affected by the oxygen tension during shear exposure: role of mitochondrial peroxynitrite. *American Journal of Physiology-Cell Physiology* **295** (1): C180-C191.
- Jonkman, J. E. N., Cathcart, J. A., Xu, F., Bartolini, M. E., Amon, J. E., Stevens, K. M. and Colarusso, P. (2014) An introduction to the wound healing assay using live-cell microscopy. *Cell Adhesion & Migration* **8** (5): 440-451.
- Jorjani, P. and Ozturk, S. S. (1999) Effects of cell density and temperature on oxygen consumption rate for different mammalian cell lines. *Biotechnology and Bioengineering* **64** (3): 349-356.
- Kagawa, Y., Haraguchi, Y., Tsuneda, S. and Shimizu, T. (2016) Real-time quantitation of internal metabolic activity of three-dimensional engineered tissues using an oxygen microelectrode and optical coherence tomography. *J Biomed Mater Res B Appl Biomater*.
- Kaiser, S., Di Mascio, P., Murphy, M. E. and Sies, H. (1990) Physical and Chemical Scavenging of Singlet Molecular-Oxygen by Tocopherols. *Archives of Biochemistry and Biophysics* **277** (1): 101-108.
- Kajihara, N., Kukidome, D., Sada, K., Motoshima, H., Furukawa, N., Matsumura, T., Nishikawa, T. and Araki, E. (2017) Low glucose induces mitochondrial reactive oxygen species via fatty acid oxidation in bovine aortic endothelial cells. *J Diabetes Investig*.
- Kamal-Eldin, A. and Appelqvist, L. A. (1996) The chemistry and antioxidant properties of tocopherols and tocotrienols. *Lipids* **31** (7): 671-701.
- Kamalian, L., Chadwick, A. E., Bayliss, M., French, N. S., Monshouwer, M., Snoeys, J. and Park, B. K. (2015) The utility of HepG2 cells to identify direct mitochondrial dysfunction in the absence of cell death. *Toxicol In Vitro* **29** (4): 732-740.

- Kase, E. T., Nikolic, N., Bakke, S. S., Bogen, K. K., Aas, V., Thoresen, G. H. and Rustan, A. C. (2013) Remodeling of oxidative energy metabolism by galactose improves glucose handling and metabolic switching in human skeletal muscle cells. *Plos One* **8** (4): e59972.
- Kaufman, N., Bicher, H. I., Hetzel, F. W. and Brown, M. (1981) A System for Determining the Pharmacology of Indirect Radiation Sensitizer Drugs on Multicellular Spheroids. *Cancer Clinical Trials* **4** (2): 199-204.
- Kautsky, H. and Hirsch, A. (1935) Nachweis geringster Sauerstoffmengen durch Phosphoreszenztilgung. *Zeitschrift für anorganische und allgemeine Chemie* **222** (2): 126-134.
- Kawamata, H., Starkov, A. A., Manfredi, G. and Chinopoulos, C. (2010) A kinetic assay of mitochondrial ADP-ATP exchange rate in permeabilized cells. *Analytical Biochemistry* **407** (1): 52-57.
- Keese, C. R., Wegener, J., Walker, S. R. and Giaever, I. (2004) Electrical wound-healing assay for cells in vitro. *Proc Natl Acad Sci U S A* **101** (6): 1554-1559.
- Kellner, K., Liebsch, G., Klimant, I., Wolfbeis, O. S., Blunk, T., Schulz, M. B. and Gopferich, A. (2002) Determination of oxygen gradients in engineered tissue using a fluorescent sensor. *Biotechnology and Bioengineering* **80** (1): 73-83.
- Khaitan, D., Chandna, S., Arya, M. B. and Dwarakanath, B. S. (2006) Establishment and characterization of multicellular spheroids from a human glioma cell line; Implications for tumor therapy. *J Transl Med* **4**: 12.
- Khan, N., Hou, H. G., Eskey, C. J., Moodie, K., Gohain, S., Du, G. X., Hodge, S., Culp, W. C., Kuppusamy, P. and Swartz, H. M. (2015) Deep-Tissue Oxygen Monitoring in the Brain of Rabbits for Stroke Research. *Stroke* **46** (3): E62-E66.
- Kindig, C. A., Kelley, K. M., Howlett, R. A., Stary, C. M. and Hogan, M. C. (2003) Assessment of O₂ uptake dynamics in isolated single skeletal myocytes. *J Appl Physiol* **94** (1): 353-357.
- King, M. A. and Radicchi-Mastroianni, M. A. (2002) Antimycin A-induced apoptosis of HL-60 cells. *Cytometry* **49** (3): 106-112.
- Kinh, C. T., Suenaga, T., Hori, T., Riya, S., Hosomi, M., Smets, B. F. and Terada, A. (2017) Counter-diffusion biofilms have lower N₂O emissions than co-diffusion biofilms during simultaneous nitrification and denitrification: Insights from depth-profile analysis. *Water Research* **124**: 363-371.
- Klimant, I., Meyer, V. and Kuhl, M. (1995) Fiberoptic Oxygen Microsensors, a New Tool in Aquatic Biology. *Limnology and Oceanography* **40** (6): 1159-1165.

Klotz, L. O., Kroncke, K. D. and Sies, H. (2003) Singlet oxygen-induced signaling effects in mammalian cells. *Photochemical & Photobiological Sciences* **2** (2): 88-94.

Klutznny, S., Lesche, R., Keck, M., Kaulfuss, S., Schlicker, A., Christian, S., Sperl, C., Neuhaus, R., Mowat, J., Steckel, M., Riefke, B., Prechtel, S., Parczyk, K. and Steigemann, P. (2017) Functional inhibition of acid sphingomyelinase by Fluphenazine triggers hypoxia-specific tumor cell death. *Cell Death Dis* **8** (3): e2709.

Kondrashina, A. V., Dmitriev, R. I., Borisov, S. M., Klimant, I., O'Brien, I., Nolan, Y. M., Zhdanov, A. V. and Papkovsky, D. B. (2012) A Phosphorescent Nanoparticle-Based Probe for Sensing and Imaging of (Intra)Cellular Oxygen in Multiple Detection Modalities. *Advanced Functional Materials* **22** (23): 4931-4939.

Koo, Y. E., Cao, Y., Kopelman, R., Koo, S. M., Brasuel, M. and Philbert, M. A. (2004) Real-time measurements of dissolved oxygen inside live cells by organically modified silicate fluorescent nanosensors. *Analytical Chemistry* **76** (9): 2498-2505.

Koppenol, W. H., Bounds, P. L. and Dang, C. V. (2011) Otto Warburg's contributions to current concepts of cancer metabolism. *Nature Reviews Cancer* **11** (5): 325-337.

Koren, K., Dmitriev, R. I., Borisov, S. M., Papkovsky, D. B. and Klimant, I. (2012) Complexes of IrIII-Octaethylporphyrin with Peptides as Probes for Sensing Cellular O₂. *Chembiochem* **13** (8): 1184-1190.

Koren, K., Hutter, L., Enko, B., Pein, A., Borisov, S. M. and Klimant, I. (2013) Tuning the dynamic range and sensitivity of optical oxygen-sensors by employing differently substituted polystyrene-derivatives. *Sensors and Actuators B-Chemical* **176**: 344-350.

Korzeniowska, B., Raspe, M., Wencel, D., Woolley, R., Jalink, K. and McDonagh, C. (2015) Development of organically modified silica nanoparticles for monitoring the intracellular level of oxygen using a frequency-domain FLIM platform. *Rsc Advances* **5** (46): 36938-36947.

Krebs, H. A. (1951) The use of 'CO₂ buffers' in manometric measurements of cell metabolism. *Biochemical Journal* **48** (3): 349-359.

Kruse, C. R., Singh, M., Targosinski, S., Sinha, I., Sorensen, J. A., Eriksson, E. and Nuutila, K. (2017) The effect of pH on cell viability, cell migration, cell proliferation, wound closure, and wound reepithelialization: In vitro and in vivo study. *Wound Repair Regen* **25** (2): 260-269.

Kudomi, N., Hirano, Y., Koshino, K., Hayashi, T., Watabe, H., Fukushima, K., Moriwaki, H., Teramoto, N., Iihara, K. and Iida, H. (2013) Rapid quantitative CBF and CMRO₂ measurements from a single PET

scan with sequential administration of dual O-15-labeled tracers. *Journal of Cerebral Blood Flow and Metabolism* **33** (3): 440-448.

Kurner, J. M., Klimant, I., Krause, C., Preu, H., Kunz, W. and Wolfbeis, O. S. (2001) Inert phosphorescent nanospheres as markers for optical assays. *Bioconjugate Chemistry* **12** (6): 883-889.

Kurokawa, H., Ito, H., Inoue, M., Tabata, K., Sato, Y., Yamagata, K., Kizaka-Kondoh, S., Kadonosono, T., Yano, S., Inoue, M. and Kamachi, T. (2015) High resolution imaging of intracellular oxygen concentration by phosphorescence lifetime. *Scientific Reports* **5**.

L'Azou, B., Passagne, I., Mounicou, S., Treguer-Delapierre, M., Puljalte, I., Szpunar, J., Lobinski, R. and Ohayon-Courtes, C. (2014) Comparative cytotoxicity of cadmium forms (CdCl₂, CdO, CdS micro- and nanoparticles) in renal cells. *Toxicology Research* **3** (1): 32-41.

Lakowicz, J. R. (2006). *Principles of fluorescence spectroscopy*. New York, Springer.

Lambrechts, D., Roeffaers, M., Kerckhofs, G., Roberts, S. J., Hofkens, J., Van de Putte, T., Van Oostervyck, H. and Schrooten, J. (2013) Fluorescent oxygen sensitive microbead incorporation for measuring oxygen tension in cell aggregates. *Biomaterials* **34** (4): 922-929.

Lang, F. and Paulmichl, M. (1995) Properties and regulation of ion channels in MDCK cells. *Kidney International* **48** (4): 1200-1205.

Langan, L. M., Dodd, N. J. F., Owen, S. F., Purcell, W. M., Jackson, S. K. and Jha, A. N. (2016) Direct Measurements of Oxygen Gradients in Spheroid Culture System Using Electron Parametric Resonance Oximetry (vol 11, e0149492, 2016). *Plos One* **11** (8).

Lasia, A. (2014). *Electrochemical Impedance Spectroscopy and its Applications*, Springer-Verlag New York.

Laurent, J., Frongia, C., Cazales, M., Mondesert, O., Ducommun, B. and Lobjois, V. (2013) Multicellular tumor spheroid models to explore cell cycle checkpoints in 3D. *BMC Cancer* **13**.

Lebedev, A. Y., Cheprakov, A. V., Sakadzic, S., Boas, D. A., Wilson, D. F. and Vinogradov, S. A. (2009) Dendritic Phosphorescent Probes for Oxygen Imaging in Biological Systems. *Acs Applied Materials & Interfaces* **1** (6): 1292-1304.

Lee, Y. E. K., Smith, R. and Kopelman, R. (2009) Nanoparticle PEBBLE Sensors in Live Cells and In Vivo. *Annual Review of Analytical Chemistry* **2**: 57-76.

Lemberger, M. M. (2016). *Carbon Nanomaterials for Bioanalytical Sensing and Multicolor Cell Imaging*. Chemistry, University of Regensburg.

Li, C. L., Ou, C. M., Huang, C. C., Wu, W. C., Chen, Y. P., Lin, T. E., Ho, L. C., Wang, C. W., Shih, C. C., Zhou, H. C., Lee, Y. C., Tzeng, W. F., Chiou, T. J., Chu, S. T., Cang, J. and Chang, H. T. (2014) Carbon dots prepared from ginger exhibiting efficient inhibition of human hepatocellular carcinoma cells. *Journal of Materials Chemistry B* **2** (28): 4564-4571.

Liang, C. C., Park, A. Y. and Guan, J. L. (2007) In vitro scratch assay: a convenient and inexpensive method for analysis of cell migration in vitro. *Nat Protoc* **2** (2): 329-333.

Lopci, E., Grassi, I., Chiti, A., Nanni, C., Cicoria, G., Toschi, L., Fonti, C., Lodi, F., Mattioli, S. and Fanti, S. (2014) PET radiopharmaceuticals for imaging of tumor hypoxia: a review of the evidence. *Am J Nucl Med Mol Imaging* **4** (4): 365-384.

Lott, P. F. and Hurtubise, R. J. (1974) Topics in Chemical Instrumentation .77. Instrumentation for Fluorescence and Phosphorescence. *Journal of Chemical Education* **51** (6): A315-A320.

Lu, H. G., Jin, Y. G., Tian, Y. Q., Zhang, W. W., Holl, M. R. and Meldrum, D. R. (2011) New ratiometric optical oxygen and pH dual sensors with three emission colors for measuring photosynthetic activity in cyanobacteria. *Journal of Materials Chemistry* **21** (48): 19293-19301.

Lynch, R. M. and Balaban, R. S. (1987) Energy-Metabolism of Renal-Cell Lines, A6 and Mdck - Regulation by Na-K-ATPase. *American Journal of Physiology* **252** (2): C225-C231.

Madigan, M. T. (2015). *Brock biology of microorganisms*.

Maltepe, E. and Saugstad, O. D. (2009) Oxygen in Health and Disease: Regulation of Oxygen Homeostasis-Clinical Implications. *Pediatr Res* **65** (3): 261-268.

Mamchaoui, K. and Saumon, G. (2000) A method for measuring the oxygen consumption of intact cell monolayers. *Am J Physiol Lung Cell Mol Physiol* **278** (4): L858-863.

Mao, W. P., Ye, J. L., Guan, Z. B., Zhao, J. M., Zhang, C., Zhang, N. N., Jiang, P. and Tian, T. (2007) Cadmium induces apoptosis in human embryonic kidney (HEK) 293 cells by caspase-dependent and -independent pathways acting on mitochondria. *Toxicol In Vitro* **21** (3): 343-354.

Marine, A., Krager, K. J., Aykin-Burns, N. and MacMillan-Crow, L. A. (2014) Peroxynitrite induced mitochondrial biogenesis following MnSOD knockdown in normal rat kidney (NRK) cells. *Redox Biology* **2**: 348-357.

Marroquin, L. D., Hynes, J., Dykens, J. A., Jamieson, J. D. and Will, Y. (2007) Circumventing the crabtree effect: Replacing media glucose with galactose increases susceptibility of HepG2 cells to mitochondrial toxicants. *Toxicological Sciences* **97** (2): 539-547.

- Martinez-Zaguilan, R., Seftor, E. A., Seftor, R. E. B., Chu, Y. W., Gillies, R. J. and Hendrix, M. J. C. (1996) Acidic pH enhances the invasive behavior of human melanoma cells. *Clinical & Experimental Metastasis* **14** (2): 176-186.
- Masuzzo, P., Van Troys, M., Ampe, C. and Martens, L. (2016) Taking Aim at Moving Targets in Computational Cell Migration. *Trends in Cell Biology* **26** (2): 88-110.
- Mayow, J., Brown, A. C. and Dobbin, L. (1907). *Medico-physical works; being a translation of Tractatus quinque medico-physici*. Edinburgh,, The Alembic club.
- McConnell, H. M., Owicki, J. C., Parce, J. W., Miller, D. L., Baxter, G. T., Wada, H. G. and Pitchford, S. (1992) The cytosensor microphysiometer: biological applications of silicon technology. *Science* **257** (5078): 1906-1912.
- Mclaughlin, S. G. A. and Dilger, J. P. (1980) Transport of Protons across Membranes by Weak Acids. *Physiological Reviews* **60** (3): 825-863.
- Mehta, G., Hsiao, A. Y., Ingram, M., Luker, G. D. and Takayama, S. (2012) Opportunities and challenges for use of tumor spheroids as models to test drug delivery and efficacy. *Journal of Controlled Release* **164** (2): 192-204.
- Meier, J. K., Prantl, L., Muller, S., Moralis, A., Liebsch, G. and Gosau, M. (2012) Simple, fast and reliable perfusion monitoring of microvascular flaps. *Clinical Hemorheology and Microcirculation* **50** (1-2): 13-24.
- Michaelis, S., Robelek, R. and Wegener, J. (2012) Studying cell-surface interactions in vitro: a survey of experimental approaches and techniques. *Adv Biochem Eng Biotechnol* **126**: 33-66.
- Michaelis, S., Wegener, J. and Robelek, R. (2013) Label-free monitoring of cell-based assays: Combining impedance analysis with SPR for multiparametric cell profiling. *Biosensors & Bioelectronics* **49**: 63-70.
- Mik, E. G., Stap, J., Sinaasappel, M., Beek, J. F., Aten, J. A., van Leeuwen, T. G. and Ince, C. (2006) Mitochondrial PO₂ measured by delayed fluorescence of endogenous protoporphyrin IX. *Nature Methods* **3** (11): 939-945.
- Mikhail, A. S., Eetezadi, S. and Allen, C. (2013) Multicellular Tumor Spheroids for Evaluation of Cytotoxicity and Tumor Growth Inhibitory Effects of Nanomedicines In Vitro: A Comparison of Docetaxel-Loaded Block Copolymer Micelles and Taxotere (R). *Plos One* **8** (4).

Mills, A. (2005) Oxygen indicators and intelligent inks for packaging food. *Chemical Society Reviews* **34** (12): 1003-1011.

Minsky, M. (1988) Memoir on inventing the confocal scanning microscope. *Scanning* **10** (4): 128-138.

Misra, U. K., Gawdi, G. and Pizzo, S. V. (2003) Induction of mitogenic signalling in the 1LN prostate cell line on exposure to submicromolar concentrations of cadmium(+). *Cellular Signalling* **15** (11): 1059-1070.

Mitra, S. and Foster, T. H. (2000) Photochemical oxygen consumption sensitized by a porphyrin phosphorescent probe in two model systems. *Biophysical Journal* **78** (5): 2597-2605.

Motterlini, R., Kerger, H., Green, C. J., Winslow, R. M. and Intaglietta, M. (1998) Depression of endothelial and smooth muscle cell oxygen consumption by endotoxin. *Am J Physiol* **275** (3 Pt 2): H776-782.

Mueller-Klieser, W. (2000) Tumor biology and experimental therapeutics. *Critical Reviews in Oncology Hematology* **36** (2-3): 123-139.

Mueller-Klieser, W. F. and Sutherland, R. M. (1982) Influence of convection in the growth medium on oxygen tensions in multicellular tumor spheroids. *Cancer Research* **42** (1): 237-242.

Mueller-Klieser, W. F. and Sutherland, R. M. (1982) Oxygen-Tensions in Multicell Spheroids of 2 Cell-Lines. *Br J Cancer* **45** (2): 256-264.

Naciri, M., Kuystermans, D. and Al-Rubeai, M. (2008) Monitoring pH and dissolved oxygen in mammalian cell culture using optical sensors. *Cytotechnology* **57** (3): 245-250.

Nakayama, K., Okamoto, F. and Harada, Y. (1956) Antimycin A: isolation from a new *Streptomyces* and activity against rice plant blast fungi. *J Antibiot (Tokyo)* **9** (2): 63-66.

Nandi, S., Malishev, R., Kootery, K. P., Mirsky, Y., Kolusheva, S. and Jelinek, R. (2014) Membrane analysis with amphiphilic carbon dots. *Chemical Communications* **50** (71): 10299-10302.

Nangaku, M. and Eckardt, K. U. (2007) Hypoxia and the HIF system in kidney disease. *Journal of Molecular Medicine-Jmm* **85** (12): 1325-1330.

Neal, A., Rountree, A. M., Philips, C. W., Kavanagh, T. J., Williams, D. P., Newham, P., Khalil, G., Cook, D. L. and Sweet, I. R. (2015) Quantification of Low-Level Drug Effects Using Real-Time, in vitro Measurement of Oxygen Consumption Rate. *Toxicol Sci* **148** (2): 594-602.

Nelson, N. and Ben-Shem, A. (2004) The complex architecture of oxygenic photosynthesis. *Nature Reviews Molecular Cell Biology* **5** (12): 971-982.

Nichols, A. J., Roussakis, E., Klein, O. J. and Evans, C. L. (2014) Click-Assembled, Oxygen-Sensing Nanoconjugates for Depth-Resolved, Near-Infrared Imaging in a 3 D Cancer Model. *Angew Chem Int Ed Engl.*

Nock, V., Blaikie, R. J. and David, T. (2008) Patterning, integration and characterisation of polymer optical oxygen sensors for microfluidic devices. *Lab on a Chip* **8** (8): 1300-1307.

Noronha, C. M., de Carvalho, S. M., Lino, R. C. and Barreto, P. L. (2014) Characterization of antioxidant methylcellulose film incorporated with alpha-tocopherol nanocapsules. *Food Chem* **159**: 529-535.

O'Donovan, C., Hynes, J., Yashunski, D. and Papkovsky, D. B. (2005) Phosphorescent oxygen-sensitive materials for biological applications. *Journal of Materials Chemistry* **15** (27-28): 2946-2951.

Oh, C. J., Ha, C. M., Choi, Y. K., Park, S., Choe, M. S., Jeoung, N. H., Huh, Y. H., Kim, H. J., Kweon, H. S., Lee, J. M., Lee, S. J., Jeon, J. H., Harris, R. A., Park, K. G. and Lee, I. K. (2017) Pyruvate dehydrogenase kinase 4 deficiency attenuates cisplatin-induced acute kidney injury. *Kidney International* **91** (4): 880-895.

Orlando, G., Soker, S., Stratta, R. J. and Atala, A. (2013) Will Regenerative Medicine Replace Transplantation? *Cold Spring Harbor Perspectives in Medicine* **3** (8).

Ozturk, S. S. and Palsson, B. O. (1991) Growth, metabolic, and antibody production kinetics of hybridoma cell culture: 2. Effects of serum concentration, dissolved oxygen concentration, and medium pH in a batch reactor. *Biotechnol Prog* **7** (6): 481-494.

Paddock, S. W. (2000) Principles and practices of laser scanning confocal microscopy. *Mol Biotechnol* **16** (2): 127-149.

Pan, C., Bai, X. M., Fan, L. M., Ji, Y., Li, X. Y. and Chen, Q. (2005) Cytoprotection by glycine against ATP-depletion-induced injury is mediated by glycine receptor in renal cells. *Biochemical Journal* **390**: 447-453.

Papkovsky, D. B. and Dmitriev, R. I. (2013) Biological detection by optical oxygen sensing. *Chemical Society Reviews* **42** (22): 8700-8732.

- Pedersen, B. W., Sinks, L. E., Breitenbach, T., Schack, N. B., Vinogradov, S. A. and Ogilby, P. R. (2011) Single Cell Responses to Spatially Controlled Photosensitized Production of Extracellular Singlet Oxygen. *Photochemistry and Photobiology* **87** (5): 1077-1091.
- Pimenta, F. M., Jensen, R. L., Holmegaard, L., Esipova, T. V., Westberg, M., Breitenbach, T. and Ogilby, P. R. (2012) Singlet-Oxygen-Mediated Cell Death Using Spatially-Localized Two-Photon Excitation of an Extracellular Sensitizer. *Journal of Physical Chemistry B* **116** (34): 10234-10246.
- Ponten, J. and Macintyre, E. H. (1968) Long term culture of normal and neoplastic human glia. *Acta Pathol Microbiol Scand* **74** (4): 465-486.
- Poteet, E., Choudhury, G. R., Winters, A., Li, W. J., Ryou, M. G., Liu, R., Tang, L., Ghorpade, A., Wen, Y., Yuan, F., Keir, S. T., Yan, H., Bigner, D. D., Simpkins, J. W. and Yang, S. H. (2013) Reversing the Warburg Effect as a Treatment for Glioblastoma. *Journal of Biological Chemistry* **288** (13): 9153-9164.
- Pratt, B. M., Harris, A. S., Morrow, J. S. and Madri, J. A. (1984) Mechanisms of cytoskeletal regulation. Modulation of aortic endothelial cell spectrin by the extracellular matrix. *American Journal of Pathology* **117** (3): 349-354.
- Preedy, V. R. and Watson, R. R. (2007). *The encyclopedia of vitamin E*. Wallingford, Oxon, UK ; Cambridge, MA, CABI.
- Quaranta, M., Borisov, S. M. and Klimant, I. (2012) Indicators for optical oxygen sensors. *Bioanal Rev* **4** (2-4): 115-157.
- Raleigh, J. A., Franko, A. J., Koch, C. J. and Born, J. L. (1985) Binding of Misonidazole to Hypoxic Cells in Monolayer and Spheroid Culture - Evidence That a Side-Chain Label Is Bound as Efficiently as a Ring Label. *Br J Cancer* **51** (2): 229-235.
- Ramamoorthy, R., Dutta, P. K. and Akbar, S. A. (2003) Oxygen sensors: Materials, methods, designs and applications. *Journal of Materials Science* **38** (21): 4271-4282.
- Ray, A., Rajian, J. R., Lee, Y. E. K., Wang, X. D. and Kopelman, R. (2012) Lifetime-based photoacoustic oxygen sensing in vivo. *Journal of Biomedical Optics* **17** (5).
- Redmond, R. W. and Kochevar, I. E. (2006) Spatially resolved cellular responses to singlet oxygen. *Photochemistry and Photobiology* **82** (5): 1178-1186.
- Reinhart-King, C. A. (2008) Endothelial cell adhesion and migration. *Angiogenesis: In Vitro Systems* **443**: 45-+.

- Reitzer, L. J., Wice, B. M. and Kennell, D. (1979) Evidence That Glutamine, Not Sugar, Is the Major Energy-Source for Cultured Hela-Cells. *Journal of Biological Chemistry* **254** (8): 2669-2676.
- Renger, G. and Hanssum, B. (2009) Oxygen detection in biological systems. *Photosynthesis Research* **102** (2-3): 487-498.
- Riahi, R., Yang, Y., Zhang, D. D. and Wong, P. K. (2012) Advances in wound-healing assays for probing collective cell migration. *J Lab Autom* **17** (1): 59-65.
- Riahi, R., Yang, Y. L., Zhang, D. D. and Wong, P. K. (2012) Advances in Wound-Healing Assays for Probing Collective Cell Migration. *Jala* **17** (1): 59-65.
- Ricciarelli, R., Zingg, J. M. and Azzi, A. (2001) Vitamin E: protective role of a Janus molecule. *Faseb Journal* **15** (13): 2314-2325.
- Richardson, J. C. W., Scalera, V. and Simmons, N. L. (1981) Identification of 2 Strains of Mdck Cells Which Resemble Separate Nephron Tubule Segments. *Biochimica Et Biophysica Acta* **673** (1): 26-36.
- Rickelt, L. F., Askaer, L., Walpersdorf, E., Elberling, B., Glud, R. N. and Kuhi, M. (2013) An Optode Sensor Array for Long-Term In Situ Oxygen Measurements in Soil and Sediment. *J Environ Qual* **42** (4): 1267-1273.
- Rossignol, R., Gilkerson, R., Aggeler, R., Yamagata, K., Remington, S. J. and Capaldi, R. A. (2004) Energy substrate modulates mitochondrial structure and oxidative capacity in cancer cells. *Cancer Research* **64** (3): 985-993.
- Ruffieux, P. A., von Stockar, U. and Marison, I. W. (1998) Measurement of volumetric (OUR) and determination of specific (qO₂) oxygen uptake rates in animal cell cultures. *Journal of Biotechnology* **63** (2): 85-95.
- Ruggiero, C., Elks, C. M., Kruger, C., Cleland, E., Addison, K., Noland, R. C. and Stadler, K. (2014) Albumin-bound fatty acids but not albumin itself alter redox balance in tubular epithelial cells and induce a peroxide-mediated redox-sensitive apoptosis. *American Journal of Physiology - Renal Physiology* **306** (8): F896-F906.
- Sabhachandani, P., Motwani, V., Cohen, N., Sarkar, S., Torchilin, V. and Konry, T. (2016) Generation and functional assessment of 3D multicellular spheroids in droplet based microfluidics platform. *Lab on a Chip* **16** (3): 497-505.
- Sakadzic, S., Roussakis, E., Yaseen, M. A., Mandeville, E. T., Srinivasan, V. J., Arai, K., Ruvinskaya, S., Devor, A., Lo, E. H., Vinogradov, S. A. and Boas, D. A. (2010) Two-photon high-resolution

measurement of partial pressure of oxygen in cerebral vasculature and tissue. *Nature Methods* **7** (9): 755-U125.

Sauer, L. (2016). Nanopartikel-basierte Messung des intrazellulären pH-Wertes. *Chemistry*, University of Regensburg. **Master Thesis**.

Schlyer, D. J. (2004) PET tracers and radiochemistry. *Ann Acad Med Singapore* **33** (2): 146-154.

Schreml, S., Meier, R. J., Kirschbaum, M., Kong, S. C., Gehmert, S., Felthaus, O., Kuchler, S., Sharpe, J. R., Woltje, K., Weiss, K. T., Albert, M., Seidl, U., Schroder, J., Morsczech, C., Prantl, L., Duschl, C., Pedersen, S. F., Gosau, M., Berneburg, M., Wolfbeis, O. S., Landthaler, M. and Babilas, P. (2014) Luminescent Dual Sensors Reveal Extracellular pH-Gradients and Hypoxia on Chronic Wounds That Disrupt Epidermal Repair. *Theranostics* **4** (7): 721-735.

Seemann, A., Egelhaaf, H. J., Brabec, C. J. and Hauch, J. A. (2009) Influence of oxygen on semi-transparent organic solar cells with gas permeable electrodes. *Organic Electronics* **10** (8): 1424-1428.

Semenza, G. L. (2011) Mechanisms of Disease - Oxygen Sensing, Homeostasis, and Disease. *New England Journal of Medicine* **365** (6): 537-547.

Senkowski, W., Zhang, X. N., Olofsson, M. H., Isacson, R., Hoglund, U., Gustafsson, M., Nygren, P., Linder, S., Larsson, R. and Fryknas, M. (2015) Three-Dimensional Cell Culture-Based Screening Identifies the Anthelmintic Drug Nitazoxanide as a Candidate for Treatment of Colorectal Cancer. *Molecular Cancer Therapeutics* **14** (6): 1504-1516.

Severinghaus, J. W. (2002) Priestley, the furious free thinker of the enlightenment, and Scheele, the taciturn apothecary of Uppsala. *Acta Anaesthesiol Scand* **46** (1): 2-9.

Shinawi, T. F., Kimmel, D. W. and Cliffel, D. E. (2013) Multianalyte microphysiometry reveals changes in cellular bioenergetics upon exposure to fluorescent dyes. *Analytical Chemistry* **85** (24): 11677-11680.

Simon, M. C. and Keith, B. (2008) The role of oxygen availability in embryonic development and stem cell function. *Nat Rev Mol Cell Biol* **9** (4): 285-296.

Sirenko, O. (2016) High-Throughput Confocal Imaging of 3D Spheroids. *G.I.T. Imaging & Microscopy* **2**: 16 - 17.

Sottile, J., Shi, F., Rublyevska, I., Chiang, H. Y., Lust, J. and Chandler, J. (2007) Fibronectin-dependent collagen I deposition modulates the cell response to fibronectin. *American Journal of Physiology-Cell Physiology* **293** (6): C1934-C1946.

- Soule, H. D., Vazquez, J., Long, A., Albert, S. and Brennan, M. (1973) A human cell line from a pleural effusion derived from a breast carcinoma. *J Natl Cancer Inst* **51** (5): 1409-1416.
- Steinlechner-Maran, R., Eberl, T., Kunc, M., Margreiter, R. and Gnaiger, E. (1996) Oxygen dependence of respiration in coupled and uncoupled endothelial cells. *Am J Physiol* **271** (6 Pt 1): C2053-2061.
- Stephens, D. J. and Allan, V. J. (2003) Light microscopy techniques for live cell imaging. *Science* **300** (5616): 82-86.
- Stich, M. I., Fischer, L. H. and Wolfbeis, O. S. (2010) Multiple fluorescent chemical sensing and imaging. *Chemical Society Reviews* **39** (8): 3102-3114.
- Stock, C., Gassner, B., Hauck, C. R., Arnold, H., Mally, S., Eble, J. A., Dieterich, P. and Schwab, A. (2005) Migration of human melanoma cells depends on extracellular pH and Na⁺/H⁺ exchange. *J Physiol* **567** (Pt 1): 225-238.
- Stolwijk, J. A., Michaelis, S. and Wegener, J. (2012). Cell Growth and Cell Death Studied by Electric Cell-Substrate Impedance Sensing. *Electric Cell-Substrate Impedance Sensing and Cancer Metastasis*. W. G. Jiang. Dordrecht, Springer Netherlands: 85-117.
- Streeter, I. and Cheema, U. (2011) Oxygen consumption rate of cells in 3D culture: The use of experiment and simulation to measure kinetic parameters and optimise culture conditions. *Analyst* **136** (19): 4013-4019.
- Swartz, H. M., Williams, B. B., Zaki, B. I., Hartford, A. C., Jarvis, L. A., Chen, E. Y., Comi, R. J., Ernstoff, M. S., Hou, H. G., Khan, N., Swarts, S. G., Flood, A. B. and Kuppusamy, P. (2014) Clinical EPR: Unique Opportunities and Some Challenges. *Academic Radiology* **21** (2): 197-206.
- Tai, H., Yang, Y., Liu, S. and Li, D. (2012). A Review of Measurement Methods of Dissolved Oxygen in Water. *Computer and Computing Technologies in Agriculture V: 5th IFIP TC 5/SIG 5.1 Conference, CCTA 2011, Beijing, China, October 29-31, 2011, Proceedings, Part II*. D. Li and Chen, Y. Berlin, Heidelberg, Springer Berlin Heidelberg: 569-576.
- Takahashi, E., Takano, T., Numata, A., Hayashi, N., Okano, S., Nakajima, O., Nomura, Y. and Sato, M. (2005) Genetic oxygen sensor: GFP as an indicator of intracellular oxygenation. *Oxygen Transport to Tissue Xxvi* **566**: 39-44.
- Tan, B., Xiao, H., Li, F., Zeng, L. and Yin, Y. (2015) The profiles of mitochondrial respiration and glycolysis using extracellular flux analysis in porcine enterocyte IPEC-J2. *Animal Nutrition* **1** (3): 239-243.

- Temma, T., Koshino, K., Moriguchi, T., Enmi, J. and Iida, H. (2014) PET Quantification of Cerebral Oxygen Metabolism in Small Animals. *Scientific World Journal*.
- Terada, H. (1981) The Interaction of Highly-Active Uncouplers with Mitochondria. *Biochimica Et Biophysica Acta* **639** (3-4): 225-242.
- Thomas, P. C., Halter, M., Tona, A., Raghavan, S. R., Plant, A. L. and Forry, S. P. (2009) A noninvasive thin film sensor for monitoring oxygen tension during in vitro cell culture. *Analytical Chemistry* **81** (22): 9239-9246.
- Thorpe, W. P., Toner, M., Ezzell, R. M., Tompkins, R. G. and Yarmush, M. L. (1995) Dynamics of photoinduced cell plasma membrane injury. *Biophysical Journal* **68** (5): 2198-2206.
- Tokumoto, M., Fujiwara, Y., Shimada, A., Hasegawa, T., Seko, Y., Nagase, H. and Satoh, M. (2011) Cadmium toxicity is caused by accumulation of p53 through the down-regulation of Ube2d family genes in vitro and in vivo. *Journal of Toxicological Sciences* **36** (2): 191-200.
- Topman, G., Sharabani-Yosef, O. and Gefen, A. (2012) A standardized objective method for continuously measuring the kinematics of cultures covering a mechanically damaged site. *Med Eng Phys* **34** (2): 225-232.
- Trepat, X., Chen, Z. Z. and Jacobson, K. (2012) Cell Migration. *Comprehensive Physiology* **2** (4): 2369-2392.
- Tsytsarev, V., Akkentli, F., Pumbo, E., Tang, Q., Chen, Y., Erzurumlu, R. S. and Papkovsky, D. B. (2017) Planar implantable sensor for in vivo measurement of cellular oxygen metabolism in brain tissue. *J Neurosci Methods* **281**: 1-6.
- Tsytsarev, V., Hu, S., Yao, J. J., Maslov, K., Barbour, D. L. and Wang, L. V. (2011) Photoacoustic microscopy of microvascular responses to cortical electrical stimulation. *Journal of Biomedical Optics* **16** (7).
- Tumkur, S. M., Vu, A. T., Li, L. P., Pierchala, L. and Prasad, P. V. (2006) Evaluation of intra-renal oxygenation during water diuresis: a time-resolved study using BOLD MRI. *Kidney International* **70** (1): 139-143.
- Turrens, J. F. (1997) Superoxide production by the mitochondrial respiratory chain. *Bioscience Reports* **17** (1): 3-8.
- Ungerböck, B., Charwat, V., Ertl, P. and Mayr, T. (2013) Microfluidic oxygen imaging using integrated optical sensor layers and a color camera. *Lab on a Chip* **13** (8): 1593-1601.

Valk, P. E., Delbeke, D., Bailey, D. L., Townsend, D. W. and Maisey, M. N. (2006). *Positron Emission Tomography: Clinical Practice*, Springer London.

Varani, J., Orr, W. and Ward, P. A. (1978) A comparison of the migration patterns of normal and malignant cells in two assay systems. *American Journal of Pathology* **90** (1): 159-172.

Varia, M. A., Calkins-Adams, D. P., Rinker, L. H., Kennedy, A. S., Novotny, D. B., Fowler, W. C. and Raleigh, J. A. (1998) Pimonidazole: A novel hypoxia marker for complementary study of tumor hypoxia and cell proliferation in cervical carcinoma. *Gynecologic Oncology* **71** (2): 270-277.

Venkatasubramanian, R., Henson, M. A. and Forbes, N. S. (2006) Incorporating energy metabolism into a growth model of multicellular tumor spheroids. *Journal of Theoretical Biology* **242** (2): 440-453.

Vikram, D. S., Zweier, J. L. and Kuppusamy, P. (2007) Methods for noninvasive imaging of tissue hypoxia. *Antioxidants & Redox Signaling* **9** (10): 1745-1756.

von Heimbürg, D., Hemmrich, K., Zachariah, S., Staiger, H. and Pallua, N. (2005) Oxygen consumption in undifferentiated versus differentiated adipogenic mesenchymal precursor cells. *Respir Physiol Neurobiol* **146** (2-3): 107-116.

Vonzglinicki, T., Edwall, C., Ostlund, E., Lind, B., Nordberg, M., Ringertz, N. R. and Wroblewski, J. (1992) Very Low Cadmium Concentrations Stimulate DNA-Synthesis and Cell-Growth. *J Cell Sci* **103**: 1073-1081.

Waalkes, M. P. (2003) Cadmium carcinogenesis. *Mutation Research-Fundamental and Molecular Mechanisms of Mutagenesis* **533** (1-2): 107-120.

Wagner, A., Marc, A., Engasser, J. M. and Einsele, A. (1991) Growth and metabolism of human tumor kidney cells on galactose and glucose. *Cytotechnology* **7** (1): 7-13.

Wagner, B. A., Venkataraman, S. and Buettner, G. R. (2011) The rate of oxygen utilization by cells. *Free Radic Biol Med* **51** (3): 700-712.

Wallace, K. B. and Starkov, A. A. (2000) Mitochondrial targets of drug toxicity. *Annual Review of Pharmacology and Toxicology* **40**: 353-388.

Wang, X. D., Gorris, H. H., Stolwijk, J. A., Meier, R. J., Groegel, D. B. M., Wegener, J. and Wolfbeis, O. S. (2011) Self-referenced RGB colour imaging of intracellular oxygen. *Chemical Science* **2** (5): 901-906.

Wang, X. D., Meier, R. J., Link, M. and Wolfbeis, O. S. (2010) Photographing Oxygen Distribution. *Angewandte Chemie-International Edition* **49** (29): 4907-4909.

Wang, X. D. and Wolfbeis, O. S. (2014) Optical methods for sensing and imaging oxygen: materials, spectroscopies and applications. *Chemical Society Reviews* **43** (10): 3666-3761.

Wang, X. D. and Wolfbeis, O. S. (2014) Optical methods for sensing and imaging oxygen: materials, spectroscopies and applications. *Chemical Society Reviews* **43** (10): 3666-3761.

Wang, X. D., Zhou, T. Y., Song, X. H., Jiang, Y., Yang, C. J. and Chen, X. (2011) Chameleon clothes for quantitative oxygen imaging. *Journal of Materials Chemistry* **21** (44): 17651-17653.

Warburg, O. (1924) Über den Stoffwechsel der Carcinomzelle. *Naturwissenschaften* **12** (50): 1131-1137.

Webb, B. A., Chimenti, M., Jacobson, M. P. and Barber, D. L. (2011) Dysregulated pH: a perfect storm for cancer progression. *Nature Reviews Cancer* **11** (9): 671-677.

Wegener, J., Keese, C. R. and Giaever, I. (2000) Electric cell-substrate impedance sensing (ECIS) as a noninvasive means to monitor the kinetics of cell spreading to artificial surfaces. *Experimental Cell Research* **259** (1): 158-166.

Weiswald, L. B., Bellet, D. and Dangles-Marie, V. (2015) Spherical Cancer Models in Tumor Biology. *Neoplasia* **17** (1): 1-15.

Wenzel, C., Riefke, B., Grundemann, S., Krebs, A., Christian, S., Prinz, F., Osterland, M., Golfier, S., Rase, S., Ansari, N., Esner, M., Bickle, M., Pampaloni, F., Mattheyer, C., Stelzer, E. H., Parczyk, K., Pechtl, S. and Steigemann, P. (2014) 3D high-content screening for the identification of compounds that target cells in dormant tumor spheroid regions. *Experimental Cell Research* **323** (1): 131-143.

Westbrook, C., Roth, C. K. and Talbot, J. (2011). *MRI in Practice*, Wiley.

Westphal, I., Jedelhauser, C., Liebsch, G., Wilhelmi, A., Aszodi, A. and Schieker, M. (2017) Oxygen mapping: Probing a novel seeding strategy for bone tissue engineering. *Biotechnology and Bioengineering* **114** (4): 894-902.

Wiest, J., Brischwein, M., Ressler, J., Otto, A. M., Grothe, H. and Wolf, B. (2005) Cellular Assays with Multiparametric Bioelectronic Sensor Chips. *CHIMIA International Journal for Chemistry* **59** (5): 243-246.

Wilson, D. F. (2008) Quantifying the role of oxygen pressure in tissue function. *American Journal of Physiology-Heart and Circulatory Physiology* **294** (1): H11-H13.

Winkler, L. W. (1888) Die Bestimmung des im Wasser gelösten Sauerstoffes. *Berichte der deutschen chemischen Gesellschaft* **21** (2): 2843-2854.

Wodnicka, M., Guarino, R. D., Hemperly, J. J., Timmins, M. R., Stitt, D. and Pitner, J. B. (2000) Novel fluorescent technology platform for high throughput cytotoxicity and proliferation assays. *J Biomol Screen* **5** (3): 141-152.

Wolfbeis, O. S. (2008) Sensor Paints. *Advanced Materials* **20** (19): 3759-3763.

Wolfbeis, O. S. (2015) Luminescent sensing and imaging of oxygen: Fierce competition to the Clark electrode. *Bioessays* **37** (8): 921-928.

Wolfbeis, O. S. (2015) An overview of nanoparticles commonly used in fluorescent bioimaging. *Chemical Society Reviews* **44** (14): 4743-4768.

Wu, C. C., Luk, H. N., Lin, Y. T. T. and Yuan, C. Y. (2010) A Clark-type oxygen chip for in situ estimation of the respiratory activity of adhering cells. *Talanta* **81** (1-2): 228-234.

Wu, D. L. and Yotnda, P. (2011) Induction and Testing of Hypoxia in Cell Culture. *Jove-Journal of Visualized Experiments* (54).

www.leica-microsystems.com/science-lab/.

www.microscopyu.com.

Xia, J., Yao, J. J. and Wang, L. V. (2014) Photoacoustic Tomography: Principles and Advances. *Progress in Electromagnetics Research-Pier* **147**: 1-22.

Xu, H., Aylott, J. W., Kopelman, R., Miller, T. J. and Philbert, M. A. (2001) A real-time ratiometric method for the determination of molecular oxygen inside living cells using sol-gel-based spherical optical nanosensors with applications to rat C6 glioma. *Analytical Chemistry* **73** (17): 4124-4133.

Xu, L. J., Xu, J., Liu, S. C. and Yang, Z. (2014) Induction of apoptosis by antimycin A in differentiated PC12 cell line. *Journal of Applied Toxicology* **34** (6): 651-657.

Xu, X. Y., Ray, R., Gu, Y. L., Ploehn, H. J., Gearheart, L., Raker, K. and Scrivens, W. A. (2004) Electrophoretic analysis and purification of fluorescent single-walled carbon nanotube fragments. *Journal of the American Chemical Society* **126** (40): 12736-12737.

- Yahara, I., Harada, F., Sekita, S., Yoshihira, K. and Natori, S. (1982) Correlation between Effects of 24 Different Cytochalasins on Cellular Structures and Cellular Events and Those on Actin In vitro. *Journal of Cell Biology* **92** (1): 69-78.
- Yang, P. M., Chiu, S. J., Lin, K. A. and Lin, L. Y. (2004) Effect of cadmium on cell cycle progression in chinese hamster ovary cells. *Chemico-Biological Interactions* **149** (2-3): 125-136.
- Yazgan, G., Dmitriev, R. I., Tyagi, V., Jenkins, J., Rotaru, G. M., Rottmar, M., Rossi, R. M., Toncelli, C., Papkovsky, D. B., Maniura-Weber, K. and Fortunato, G. (2017) Steering surface topographies of electrospun fibers: understanding the mechanisms. *Scientific Reports* **7**.
- Yoshihara, T., Yamaguchi, Y., Hosaka, M., Takeuchi, T. and Tobita, S. (2012) Ratiometric Molecular Sensor for Monitoring Oxygen Levels in Living Cells. *Angewandte Chemie-International Edition* **51** (17): 4148-4151.
- Zernike, F. (1935) Das Phasenkontrastverfahren bei der mikroskopischen Beobachtung. *Z. technische Physik* **16**: 454-457.
- Zhang, G., Palmer, G. M., Dewhirst, M. W. and Fraser, C. L. (2009) A dual-emissive-materials design concept enables tumour hypoxia imaging. *Nature Materials* **8** (9): 747-751.
- Zhang, J., Nuebel, E., Wisidagama, D. R., Setoguchi, K., Hong, J. S., Van Horn, C. M., Imam, S. S., Vergnes, L., Malone, C. S., Koehler, C. M. and Teitell, M. A. (2012) Measuring energy metabolism in cultured cells, including human pluripotent stem cells and differentiated cells. *Nat Protoc* **7** (6): 1068-1085.
- Zhang, X. N., Fryknas, M., Hernlund, E., Fayad, W., De Milito, A., Olofsson, M. H., Gogvadze, V., Dang, L., Pahlman, S., Schughart, L. A. K., Rickardson, L., Darcy, P., Gullbo, J., Nygren, P., Larsson, R. and Linder, S. (2014) Induction of mitochondrial dysfunction as a strategy for targeting tumour cells in metabolically compromised microenvironments. *Nat Commun* **5**.
- Zhao, D., Jiang, L., Hahn, E. W. and Mason, R. P. (2009) Comparison of 1H blood oxygen level-dependent (BOLD) and 19F MRI to investigate tumor oxygenation. *Magn Reson Med* **62** (2): 357-364.
- Zhao, F. Q. and Keating, A. F. (2007) Functional properties and genomics of glucose transporters. *Curr Genomics* **8** (2): 113-128.
- Zhao, M., Song, B., Pu, J., Forrester, J. V. and McCaig, C. D. (2003) Direct visualization of a stratified epithelium reveals that wounds heal by unified sliding of cell sheets. *Faseb Journal* **17** (3): 397-406.

- Zhdanov, A. V., Ogurtsov, V. I., Taylor, C. T. and Papkovsky, D. B. (2010) Monitoring of cell oxygenation and responses to metabolic stimulation by intracellular oxygen sensing technique. *Integrative Biology* **2** (9): 443-451.
- Zhdanov, A. V., Waters, A. H. C., Golubeva, A. V., Dmitriev, R. I. and Papkovsky, D. B. (2014) Availability of the key metabolic substrates dictates the respiratory response of cancer cells to the mitochondrial uncoupling. *Biochimica Et Biophysica Acta-Bioenergetics* **1837** (1): 51-62.
- Zheng, X. C., Wang, X., Mao, H., Wu, W., Liu, B. R. and Jiang, X. Q. (2015) Hypoxia-specific ultrasensitive detection of tumours and cancer cells in vivo. *Nat Commun* **6**.
- Zholobak, N. M., Popov, A. L., Shcherbakov, A. B., Popova, N. R., Guzyk, M. M., Antonovich, V. P., Yegorova, A. V., Scrypynets, Y. V., Leonenko, I. I., Baranchikov, A. Y. and Ivanov, V. K. (2016) Facile fabrication of luminescent organic dots by thermolysis of citric acid in urea melt, and their use for cell staining and polyelectrolyte microcapsule labelling. *Beilstein Journal of Nanotechnology* **7**: 1905-1917.
- Zhu, F., Baker, D., Skommer, J., Sewell, M. and Wlodkowic, D. (2015) Real-Time 2D Visualization of Metabolic Activities in Zebrafish Embryos Using a Microfluidic Technology. *Cytometry Part A* **87A** (5): 446-450.
- Zink, S., Rosen, P., Sackmann, B. and Lemoine, H. (1993) Regulation of endothelial permeability by beta-adrenoceptor agonists: contribution of beta 1- and beta 2-adrenoceptors. *Biochimica Et Biophysica Acta* **1178** (3): 286-298.

11 APPENDIX

11.1 SUPPLEMENTARY INFORMATION

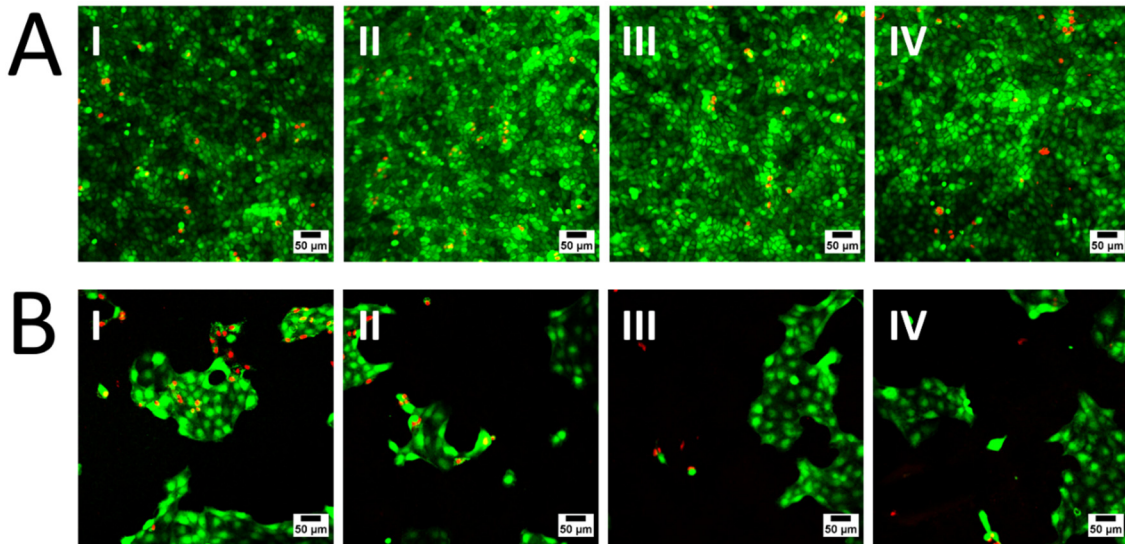


Fig. 11.1 Live-dead stained of confluent and subconfluent MDCK II cells on oxygen sensor foils pre-incubated with different adhesion promoting agents. Green cytoplasmic fluorescence of CaAM shows viable cells, while the nuclei of dead cells exhibit a bright red fluorescence of EthD-1. (A) MDCK II cells seeded in a density of 4.5×10^5 cells cm^{-2} on oxygen sensor foils pre-incubated with MDCK culture medium (I), FCS (II), 25 $\mu\text{g}/\text{ml}$ fibronectin (III) or 100 $\mu\text{g}/\text{ml}$ poly-L-lysine (IV). (B) MDCK II cells seeded subconfluently (5.0×10^4 cells cm^{-2}) on oxygen sensor foils pre-incubated with MDCK culture medium (I), FCS (II), 25 $\mu\text{g}/\text{ml}$ fibronectin (III) and 100 $\mu\text{g}/\text{ml}$ poly-L-lysine.

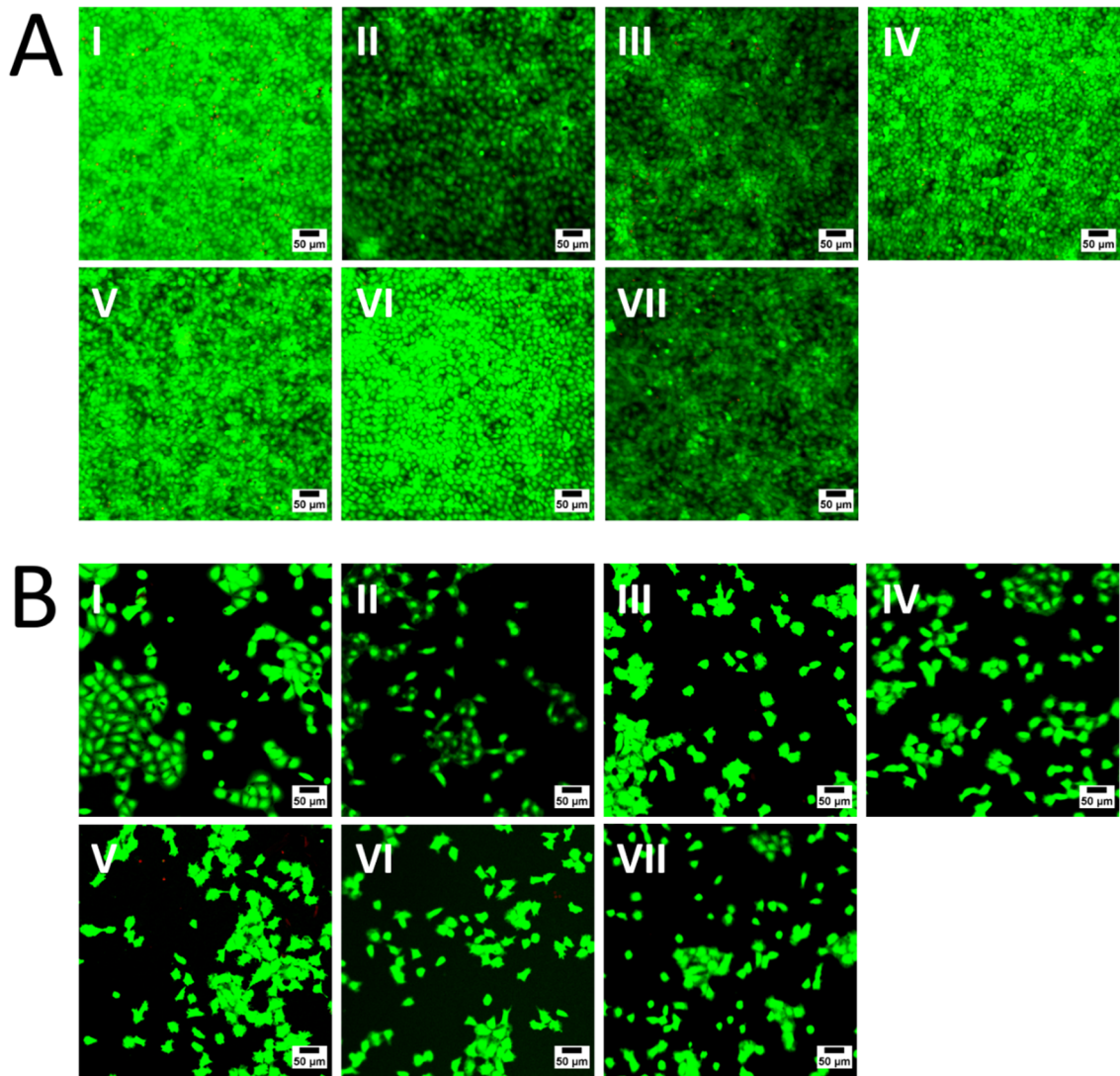


Fig. 11.2 Live-dead stained of confluent and subconfluent NRK cells on oxygen sensor foils pre-incubated with different adhesion promoting agents. Green cytoplasmic fluorescence of CaAM shows viable cells, while the nuclei of dead cells exhibit a bright red fluorescence of EthD-1. (A) NRK cells seeded confluent with a density of $4.5 \times 10^5 \text{ cells cm}^{-2}$ on standard cell culture petri dishes (I), uncoated oxygen sensor foil (II) or foil pre-incubated with NRK culture medium (III), FCS (IV), 25 $\mu\text{g/ml}$ fibronectin (V), 0.5 % (w/v) gelatin (VI) or 100 $\mu\text{g/ml}$ poly-L-lysine (VII). (B) NRK cells seeded subconfluent ($5.0 \times 10^4 \text{ cells cm}^{-2}$) on a control culture substrate (I), uncoated oxygen sensor foils (II) or oxygen sensor foils pre-incubated with NRK culture medium (III), FCS (IV), 25 $\mu\text{g/ml}$ fibronectin (V), 0.5 % (w/v) gelatin (VI) or 100 $\mu\text{g/ml}$ poly-L-lysine (VII).

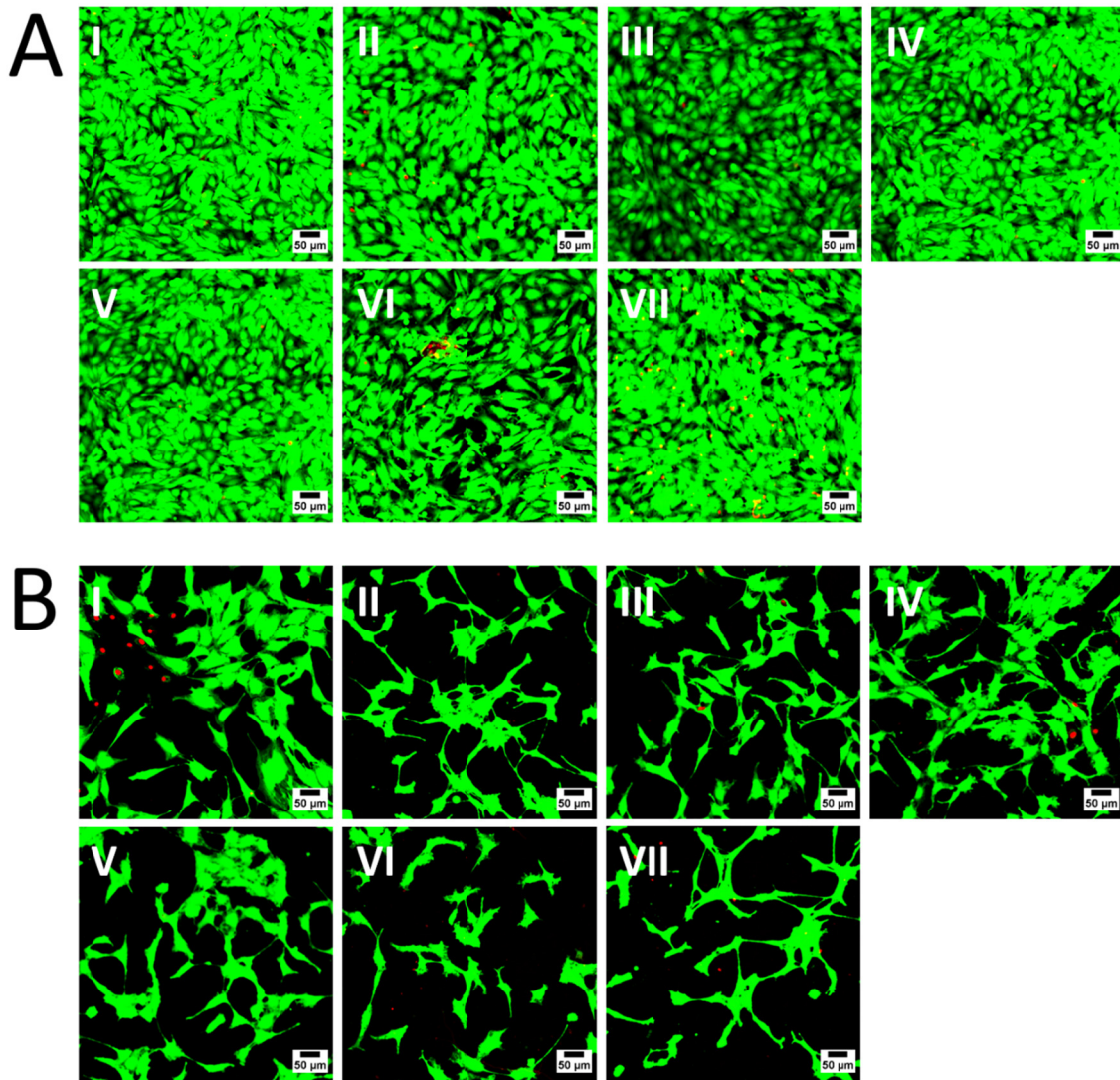


Fig. 11.3 Live-dead stained of confluent and subconfluent BAEC cells on oxygen sensor foils pre-incubated with different adhesion promoting agents. Green cytoplasmic fluorescence of CaAM shows viable cells, while the nuclei of dead cells exhibit a bright red fluorescence of EthD-1. (A) BAEC cells seeded confluent with a density of 1.5×10^5 cells cm^{-2} on a standard cell culture petri dish (I), uncoated oxygen sensor foil (II) or foil pre-incubated with BAEC culture medium (III), FCS (IV), 25 $\mu\text{g}/\text{ml}$ fibronectin (V), 0.5 % (w/v) gelatin (VI) or 100 $\mu\text{g}/\text{ml}$ poly-L-lysine (VII). (B) BAEC cells seeded subconfluent (2.0×10^4 cells cm^{-2}) on a control culture substrate (I), uncoated oxygen sensor foil (II) or an oxygen sensor foil pre-incubated with BAEC culture medium (III), FCS (IV), 25 $\mu\text{g}/\text{ml}$ fibronectin (V), 0.5 % (w/v) gelatin (VI) or 100 $\mu\text{g}/\text{ml}$ poly-L-lysine (VII).

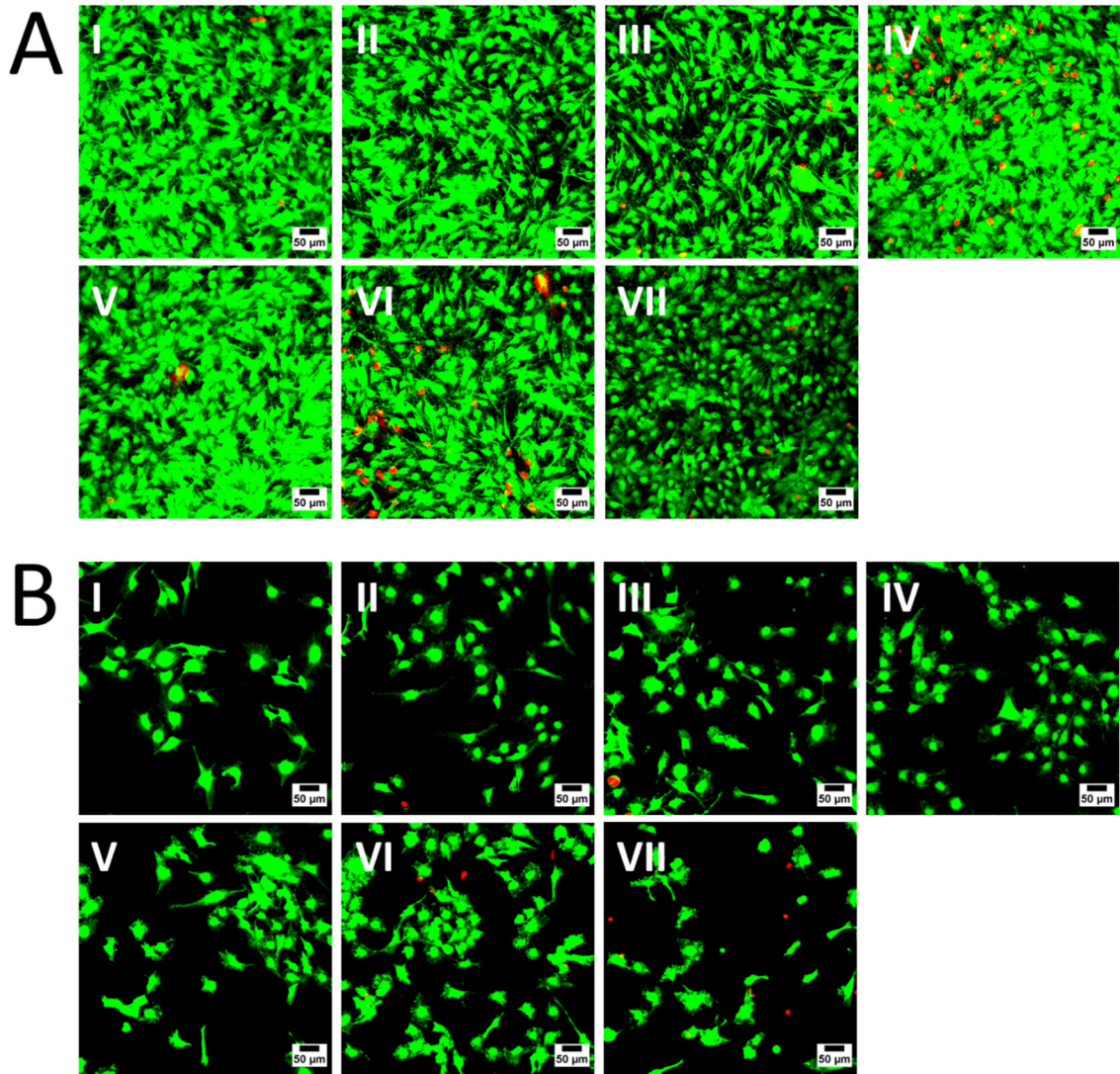


Fig. 11.4 Live-dead stained of confluent and subconfluent U-373 MG cells on oxygen sensor foils pre-incubated with different adhesion promoting agents. Green cytoplasmic fluorescence of CaAM shows viable cells, while the nuclei of dead cells exhibit a bright red fluorescence of EthD-1. (A) U-373 MG cells seeded confluent with a density of $1.5 \times 10^5 \text{ cells cm}^{-2}$ on standard cell culture petri dishes (I), uncoated oxygen sensor foil (II) or foil pre-incubated with U-373 MG culture medium (III), FCS (IV), 25 $\mu\text{g/ml}$ fibronectin (V), 0.5 % (w/v) gelatin (VI) or 100 $\mu\text{g/ml}$ poly-L-lysine (VII). (B) U-373 MG cells seeded subconfluent ($2.0 \times 10^4 \text{ cells cm}^{-2}$) on a control culture substrate (I), uncoated oxygen sensor foil (II) or oxygen sensor foils pre-incubated with U-373 culture medium (III), FCS (IV), 25 $\mu\text{g/ml}$ fibronectin (V), 0.5 % (w/v) gelatin (VI) or 100 $\mu\text{g/ml}$ poly-L-lysine (VII).

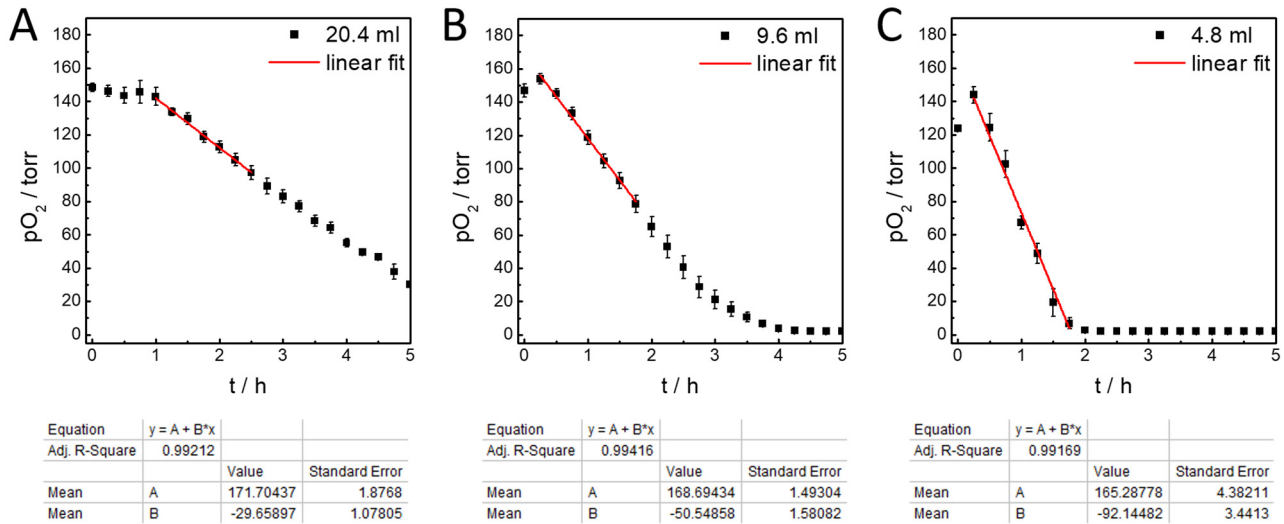


Fig. 11.5 Linear fits to determine the apparent oxygen consumption rates of confluent MDCK II cells cultivated in closed systems with different volumes of L-15 medium. Oxygen measurements were conducted 24 h after seeding in a cell density of 4.5×10^5 c cm⁻². (A) Linear fit for a closed system filled with 20.4 ml L-15 medium. (B) Linear fit for a closed system filled with 9.6 ml L-15 medium. (C) Linear fit for a closed system filled with 4.8 ml L-15 medium. Respective values of AOCR were determined from the negative slope of the fit (AOCR = -B). Parameter estimates as returned from the fitting procedure were not processed with respect to significant digits. Mean \pm SE, n \geq 3, T = 37 °C.

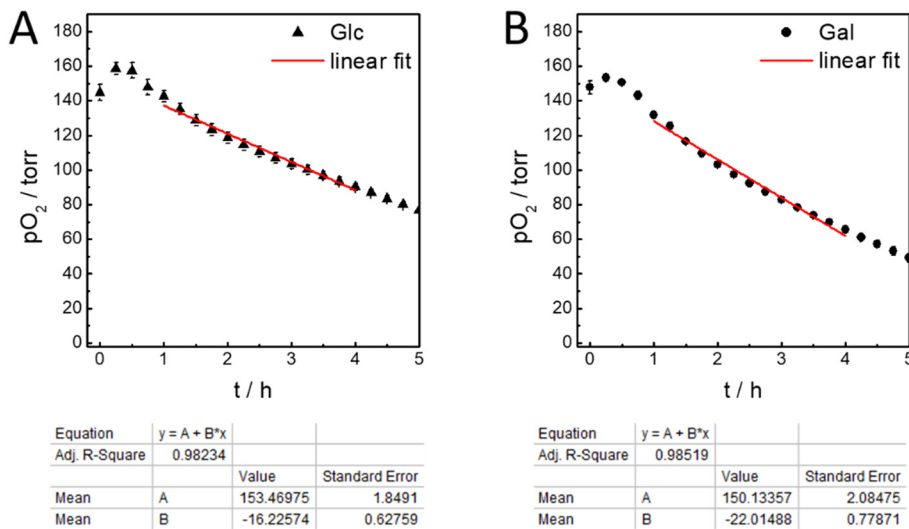


Fig. 11.6 Linear fits to determine the apparent oxygen consumption rates of confluent MDCK II cells cultivated in (A) PBS⁺⁺/Glc (1 g l⁻¹) or (B) PBS⁺⁺/Gal (1 g l⁻¹). Oxygen measurements were conducted 24 h after seeding in a cell density of 4.5×10^5 c cm⁻². Respective values of AOCR were determined from the negative slope of the fit (AOCR = -B). Parameter estimates as returned from the fitting procedure were not processed with respect to significant digits. Mean \pm SE, n = 3, T = 37 °C.

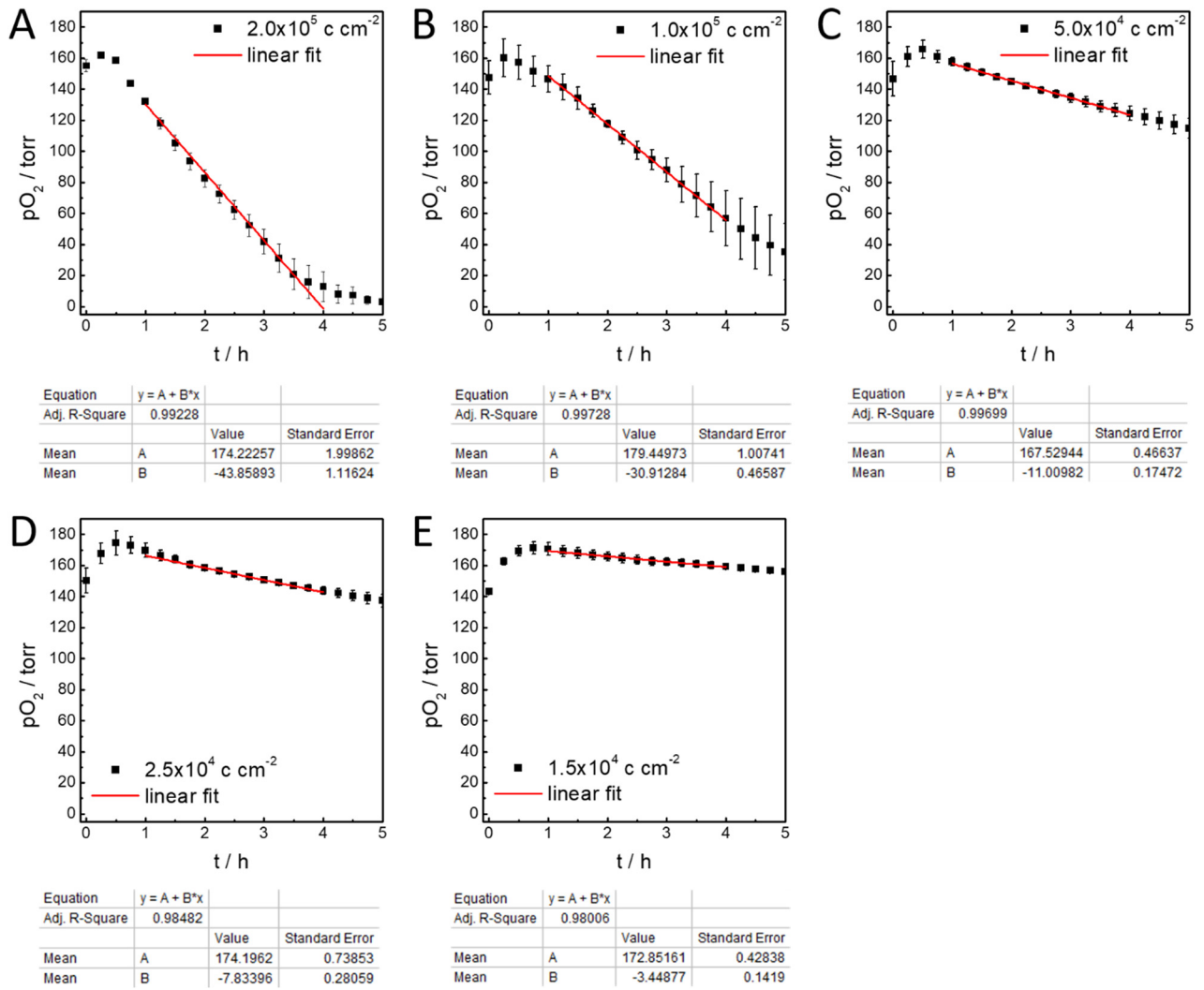


Fig. 11.7 Linear fits to determine the AOCRs of MDCK II cells seeded in different densities. MDCK II cells were seeded with initial densities of $2.0 \times 10^5 \text{ c cm}^{-2}$ (A), $1.0 \times 10^5 \text{ c cm}^{-2}$ (B), $5.0 \times 10^4 \text{ c cm}^{-2}$ (C), $2.5 \times 10^4 \text{ c cm}^{-2}$ (D) and $1.5 \times 10^4 \text{ c cm}^{-2}$ (E) 24 h before cellular oxygen consumption was analyzed in 9.6 ml L-15 medium. Respective values of AOCR were determined from the negative slope of the fit (AOCR = -B). Parameter estimates as returned from the fitting procedure were not processed with respect to significant digits. Mean \pm SE, $n = 3$, $T = 37 \text{ }^\circ\text{C}$.

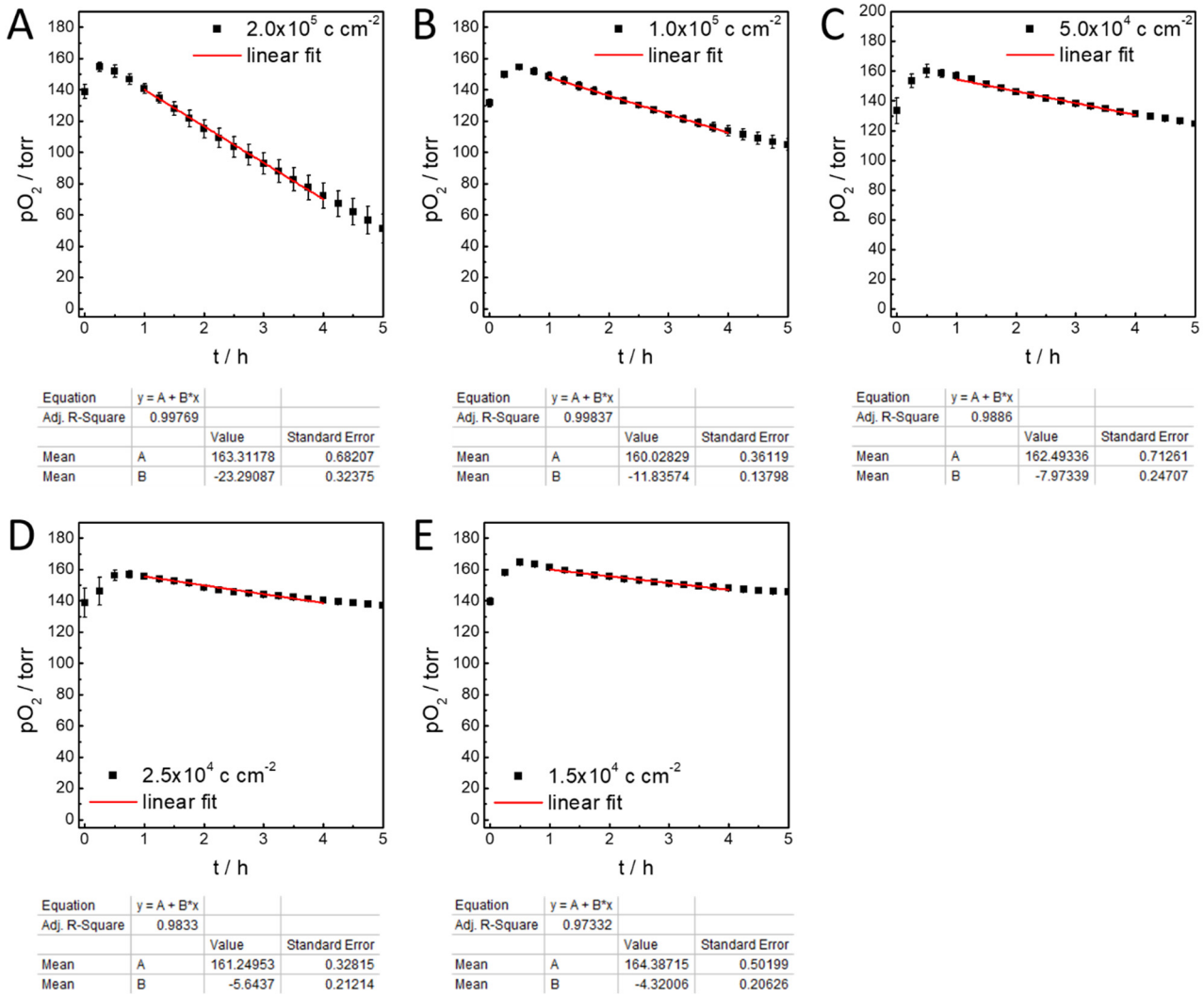


Fig. 11.8 Linear regression analysis to determine the AOCRs of NRK cells inoculated at different cell densities on oxygen sensor foils. Cells were seeded with initial densities of $2.0 \times 10^5 \text{ c cm}^{-2}$ (A), $1.0 \times 10^5 \text{ c cm}^{-2}$ (B), $5.0 \times 10^4 \text{ c cm}^{-2}$ (C), $2.5 \times 10^4 \text{ c cm}^{-2}$ (D) and $1.5 \times 10^4 \text{ c cm}^{-2}$ (E) 24 h before cellular oxygen consumption was analyzed in 9.6 ml L-15 medium. Respective values of AOCR were determined from the negative slope of the fit (AOCR = -B). Parameter estimates as returned from the fitting procedure were not processed with respect to significant digits. Mean \pm SE, $n = 3$, $T = 37^\circ \text{C}$.

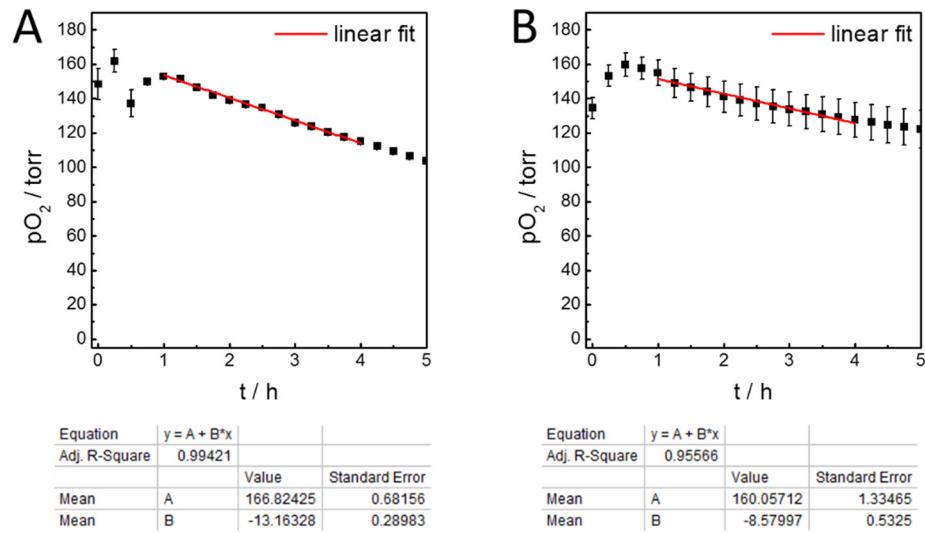


Fig. 11.9 Linear regression analysis to determine AOOCR of U-373 MG cells (A) and BAEC cells (B) inoculated with a density of 1.5×10^5 c cm^{-2} 24 h before oxygen imaging was conducted in L-15 medium. Respective values of AOOCR were determined from the negative slope of the fit (AOOCR = -B). Parameter estimates as returned from the fitting procedure were not processed with respect to significant digits. Mean \pm SE, n = 3, T = 37 °C.

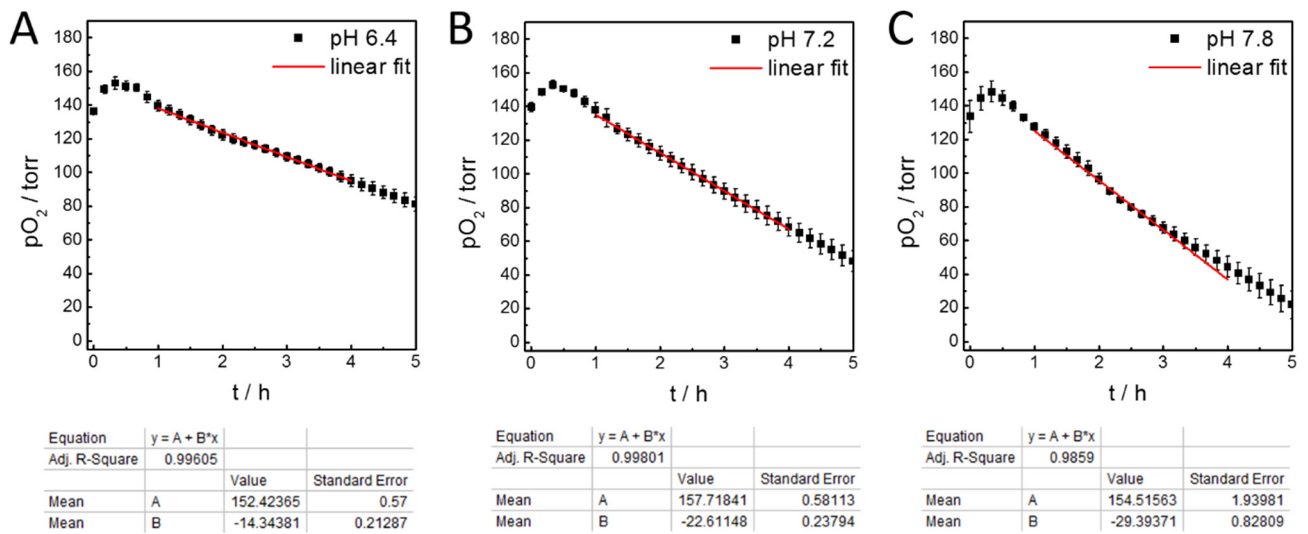


Fig. 11.10 Linear fits to determine the apparent oxygen consumption rates of NRK cells that were incubated with L-15 medium adjusted to different pH values. Cells were seeded in a density of 2.5×10^5 c cm^{-2} 24 h before oxygen consumption was monitored. Linear fits for an extracellular pH of 6.4 (A), 7.2 (B) and 7.8 (C). AOOCRs were determined from the negative slope of the fit (AOOCR = -B). Parameter estimates as returned from the fitting procedure were not processed with respect to significant digits. Mean \pm SE, n = 3, T = 37 °C.

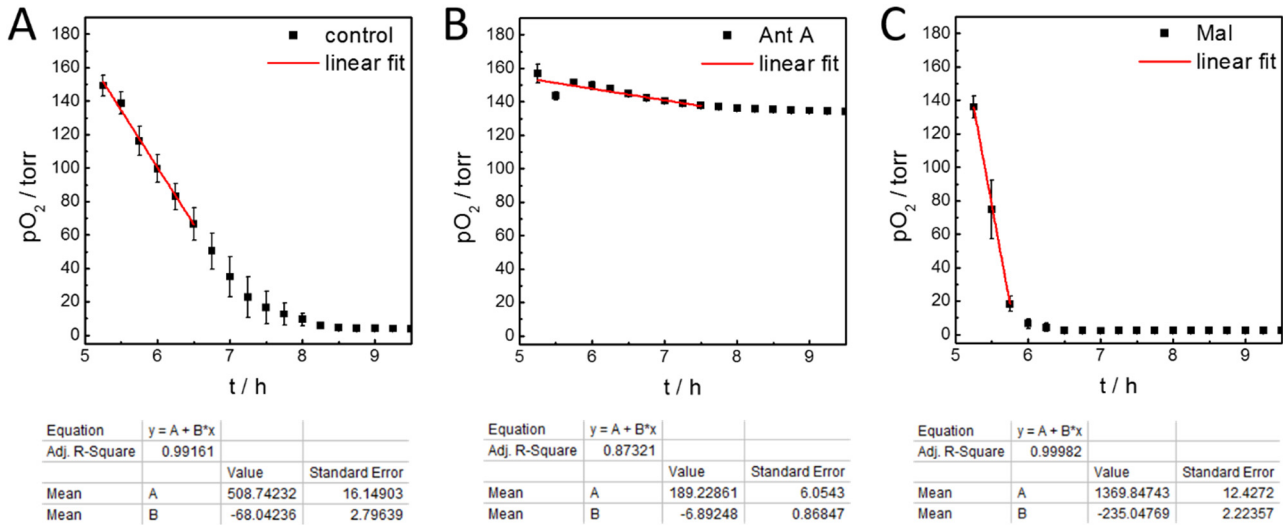


Fig. 11.11 Linear fits for the determination of the AOOCR of confluent MDCK II cells. Oxygen measurements were conducted 24 h after seeding in a cell density of $4.5 \times 10^5 \text{ c cm}^{-2}$. (A) Control samples treated with L-15 medium. (B) MDCK II cells treated with 2 μM Ant A in L-15 medium. (C) Cells treated with 100 nM Mal in L-15 medium. Respective values of AOOCR were determined from the negative slope of the fit (AOOCR = -B). Parameter estimates as returned from the fitting procedure were not processed with respect to significant digits. Mean \pm SE, $n \geq 3$, $T = 37^\circ\text{C}$.

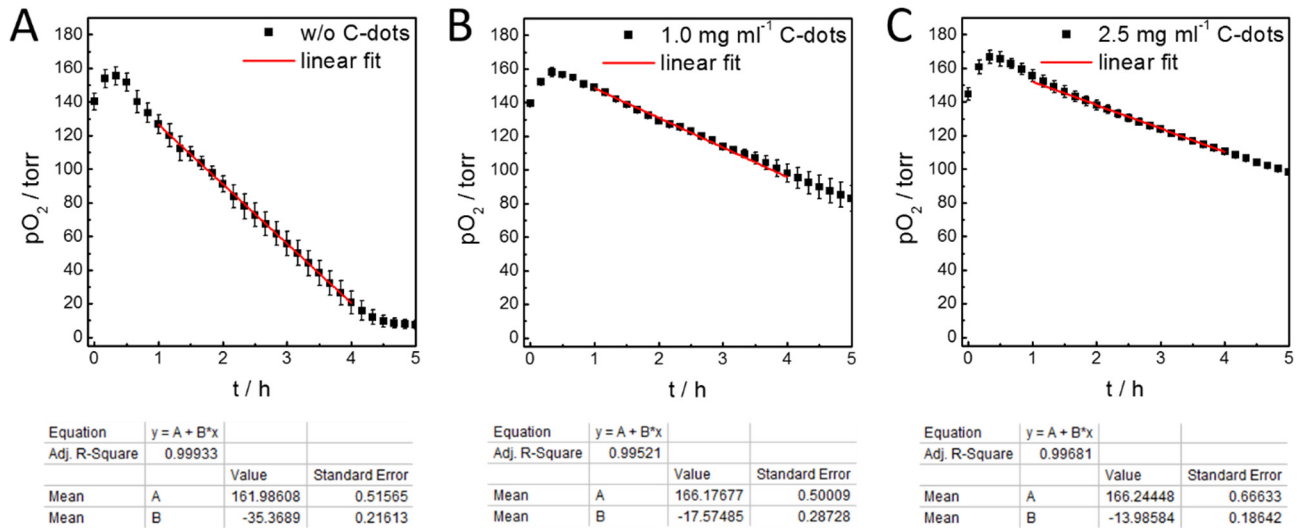


Fig. 11.12 Linear fits to determine the apparent oxygen consumption rates of NRK cells incubated with C-dots for 5 h. Cellular oxygen consumption was monitored 24 h after seeding NRK cells in a cell density of $2.5 \times 10^5 \text{ c cm}^{-2}$. (A) Medium control, (B) NRK cells treated with 1.0 mg ml^{-1} C-dots or (C) 2.5 mg ml^{-1} C-dots. Respective values of AOOCR were determined from the negative slope of the fit (AOOCR = -B). Parameter estimates as returned from the fitting procedure were not processed with respect to significant digits. Mean \pm SE, $n = 3$, $T = 37^\circ\text{C}$.

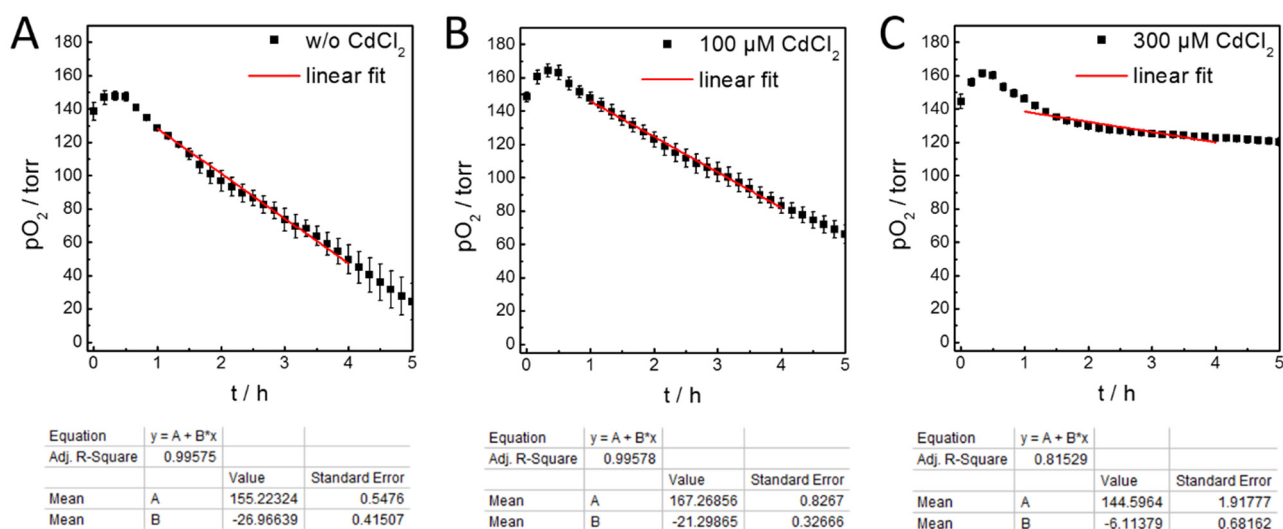


Fig. 11.13 Linear regression analysis to determine the apparent oxygen consumption rates of NRK cells seeded in a cell density of 2.5×10^5 c cm⁻² 24 h before oxygen consumption was monitored. Cells were incubated with CdCl₂ or NRK cell culture medium 2 h before oxygen content was measured. (A) Cell culture medium control, (B) cells treated with 100 μM CdCl₂ or (C) 300 μM CdCl₂. Respective values of AOCR were determined from the negative slope of the fit (AOCR = -B). Parameter estimates as returned from the fitting procedure were not processed with respect to significant digits. Mean ± SE, n = 3.

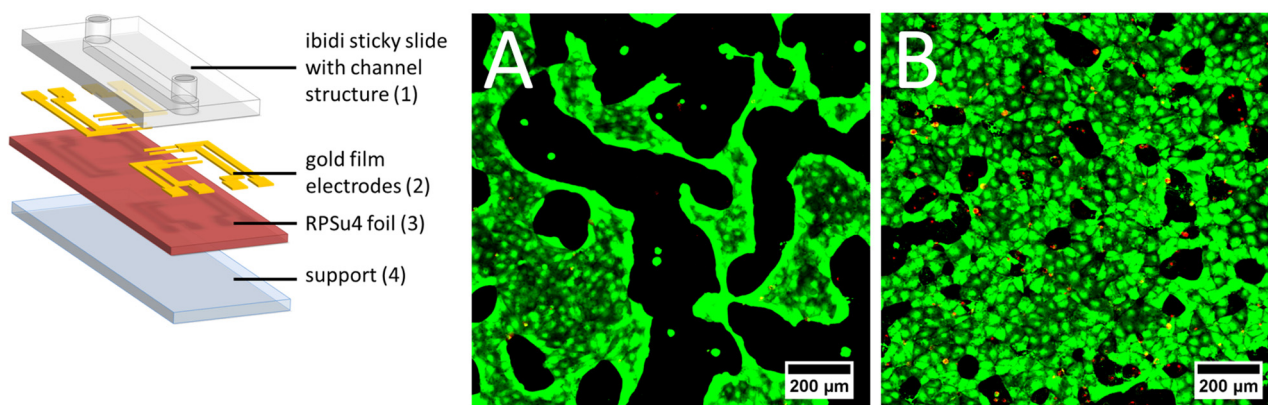


Fig. 11.14 CLSM image of MDCK II cells seeded in a density of (1.0×10^5) c cm⁻² into the ECIS-O₂ chip covered with an ibidi sticky-Slide I^{0.4}luer used as cultivation chamber. Schematic view illustrating the different components. The chip is composed of a self-adhesive microchannel ((1) ibidi sticky-Slide I 0.4luer), 100 nm thin Au film electrodes (2), a RPSu4 oxygen sensor foil (3) and a microscope slide as support (4). (A) CLSM micrograph of MDCK II cells 24 h after inoculation. (B) CLSM image of MDCK II cells 96 h after inoculation. Although cells were supplied with fresh culture medium every day, they do not grow to confluence. Cells were stained using 2 μM CaAM and 4 μM EthD-1 to mark live (green fluorescence) and dead cells (red fluorescence).

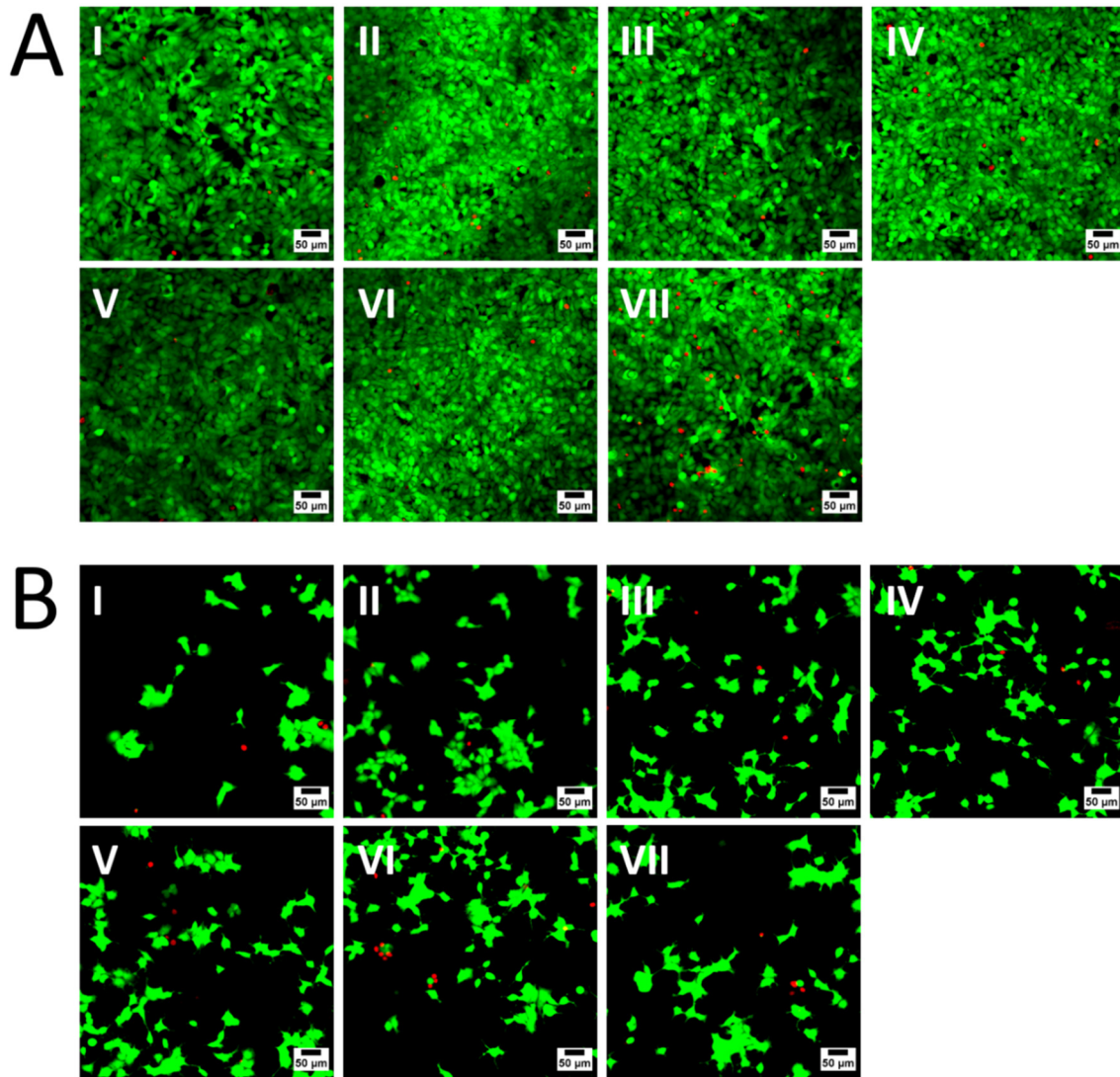


Fig. 11.15 Live-dead stained of confluent and subconfluent MCF-7 cells on oxygen sensor foils pre-incubated with different adhesion promoting agents. Green cytoplasmic fluorescence of CaAM shows viable cells, while the nuclei of dead cells exhibit a bright red fluorescence of EthD-1. (A) MCF-7 breast cancer cells seeded to confluence in a density of 4.5×10^5 cells cm^{-2} on standard cell culture petri dishes (I), uncoated oxygen sensor foil (II) or foil pre-incubated with MCF-7 culture medium (III), FCS (IV), 25 $\mu\text{g}/\text{ml}$ fibronectin (V), 0.5 % (w/v) gelatin (VI) or 100 $\mu\text{g}/\text{ml}$ poly-L-lysine (VII). (B) MCF-7 cells seeded subconfluent (5.0×10^4 cells cm^{-2}) on control culture substrate (I), uncoated oxygen sensor foil (II) or oxygen sensor foil pre-incubated with MCF-7 culture medium (III), FCS (IV), 25 $\mu\text{g}/\text{ml}$ fibronectin (V), 0.5 % (w/v) gelatin (VI) or 100 $\mu\text{g}/\text{ml}$ poly-L-lysine (VII).

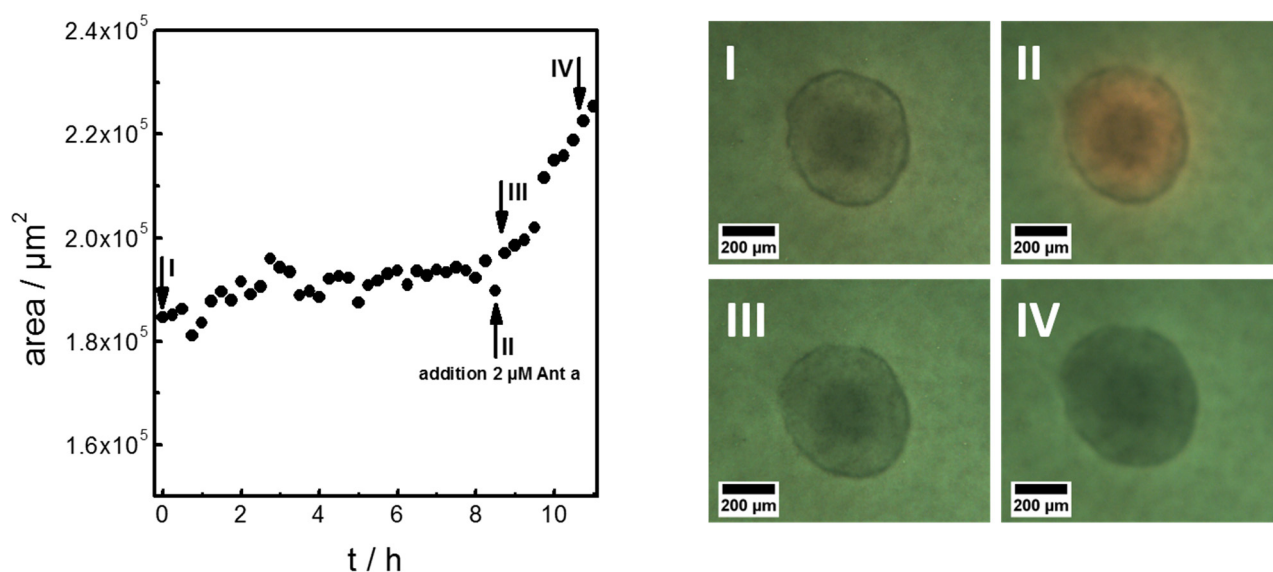


Fig. 11.16 Changes in MCF-7 cross section area as a function of time during exposure to 2 μM Antimycin A. Corresponding raw data images depicting spheroids were recorded at $t = 0$ h (I), $t = 8.5$ h (II), $t = 8.75$ h (III) and $t = 10.75$ h (IV). Cross sectional area of the 3D spherical part increases about 15 % from (II) to (IV). Raw data images were used to determine the area using the NIH ImageJ software. $T = 37$ °C.

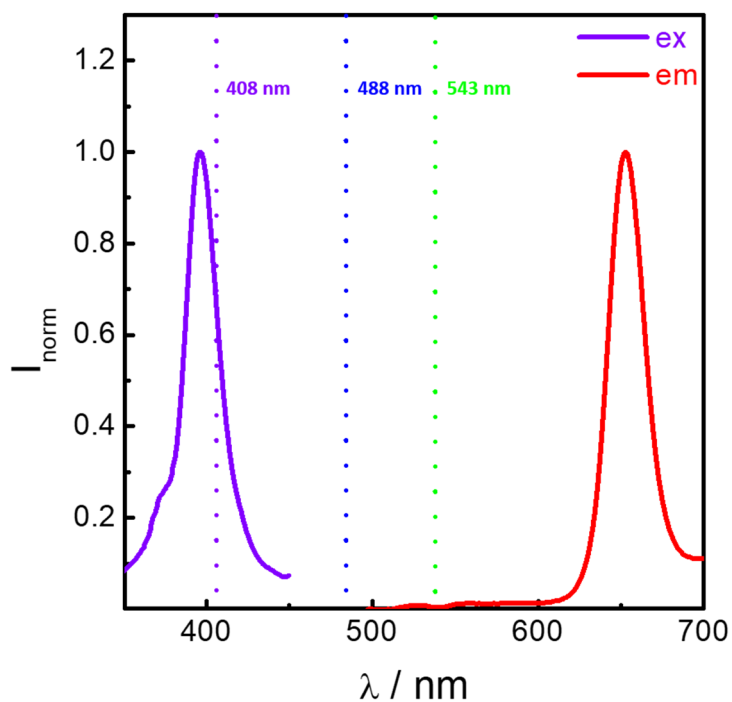


Fig. 11.17 Normalized excitation and emission spectra of PtTFPP in polystyrene with an excitation maximum at 396 nm and an emission maximum at 653 nm. Dotted lines indicate laser lines of three microscopy lasers at 408 nm, 488 nm and 543 nm. Note, that only the 408 nm laser is suitable to excite the sensor dye.

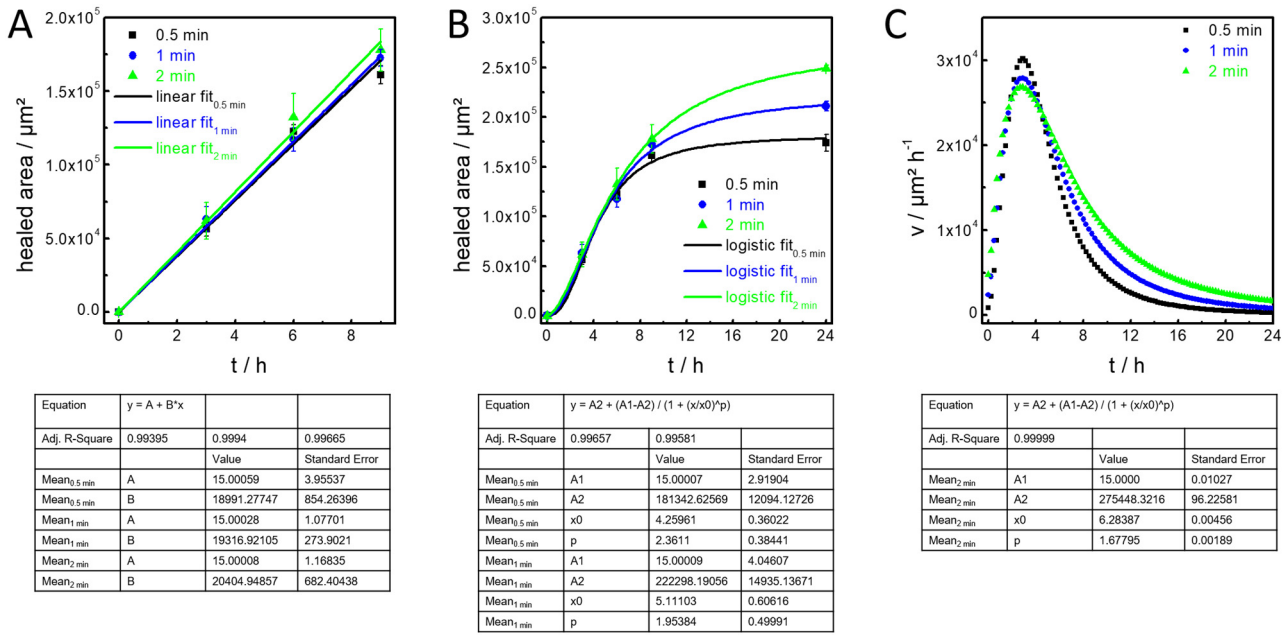


Fig. 11.18 (A) Linear fits to determine the wound healing rates for samples irradiated for 0.5 min (■), 1 min (●) and 2 min (▲) with 408 nm laser light together with the best fit parameter estimates. Data was fitted covering the linear range from 0 h to 9 h. Wound healing rate v was determined from the slope ($v / \mu\text{m}^2 \text{h}^{-1} = B$). Mean \pm SE; $n = 6$. (B) Logistic fit of the data presented in (A) from 0 h to 24 h to determine wound healing rates and corresponding fit parameters for samples irradiated for 0.5 min (■), 1 min (●) and 2 min (▲). Time of half closure of the wound is expressed as x_0 . (C) Wound healing rate was determined as a function of time by differentiation of the logistic fit curve confined to 100 points per experiment. Parameter estimates as returned from the fitting procedure were not processed with respect to significant digits. Mean \pm SE, $n = 6$, $T = 37^\circ\text{C}$.

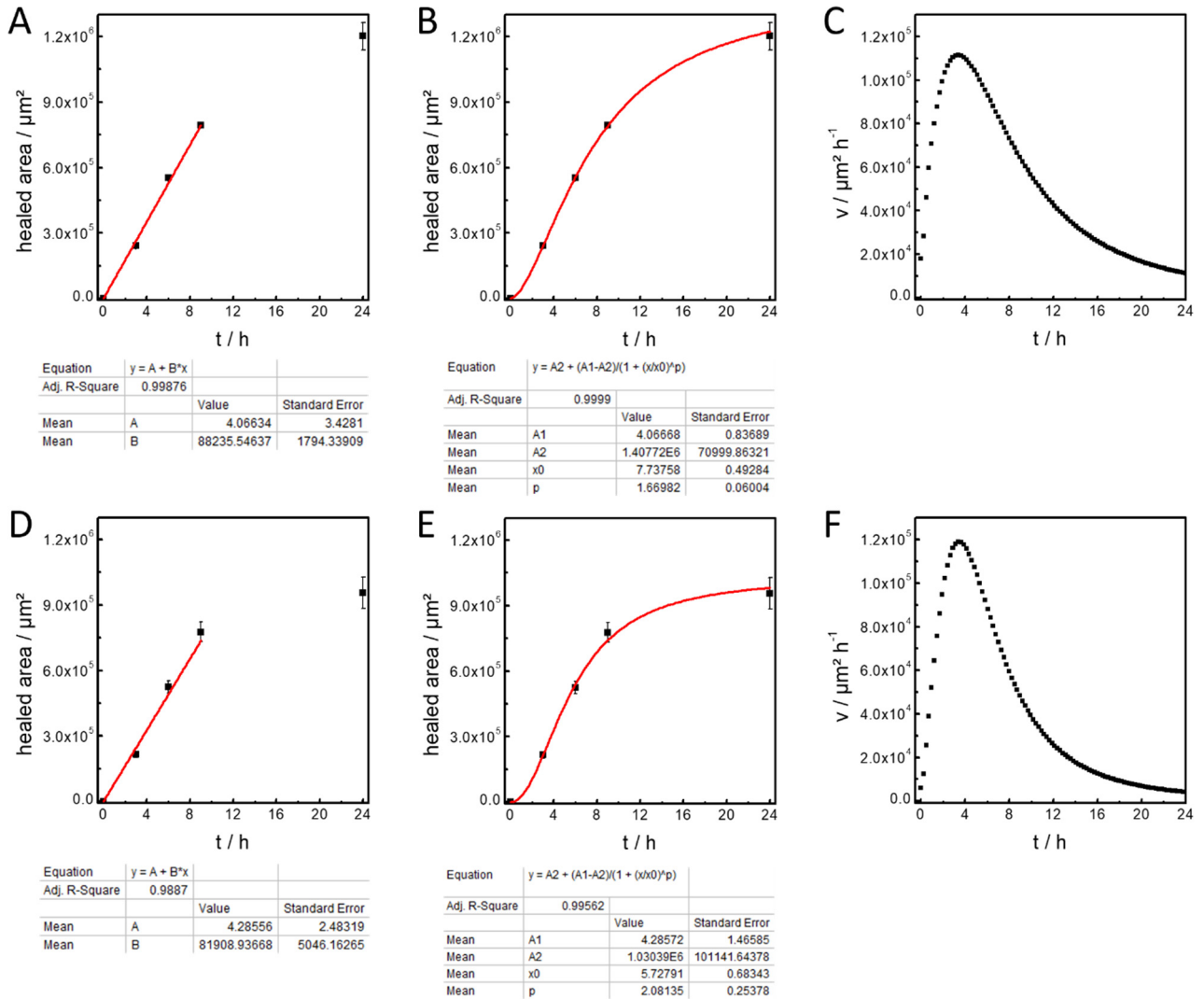


Fig. 11.19 Fit results for the scratch wound healing assay to determine wound healing rates. (A) Linear fit with corresponding fit parameters to determine the wound healing rate of NRK cells on standard cell culture petri dishes wounded by scratching. Wound healing rate v was determined from the slope ($v / \mu\text{m}^2 \text{h}^{-1} = B$). Mean \pm SE; $n = 15$. (B) Logistic fit to determine wound healing rate and additional fit parameters. Time of half closure of the wound was determined by x_0 . (C) Wound healing rate was determined by differentiation of the fit data. (D) Linear fit to determine wound healing rate of NRK cells on PS/PtTFPP substrates with corresponding fit parameters. Wound healing rate v was determined from the slope ($v / \mu\text{m}^2 \text{h}^{-1} = B$). Mean \pm SE; $n = 13$. (E) Logistic fit to determine wound healing rate and corresponding fit parameters. Time of half closure of the wound was determined by x_0 . (F) Wound healing rate was determined by differentiation of the logistic fit curve shown in (E) confined to 100 points per experiment. Parameter estimates as returned from the fitting procedure were not processed with respect to significant digits. $T = 37^\circ\text{C}$.

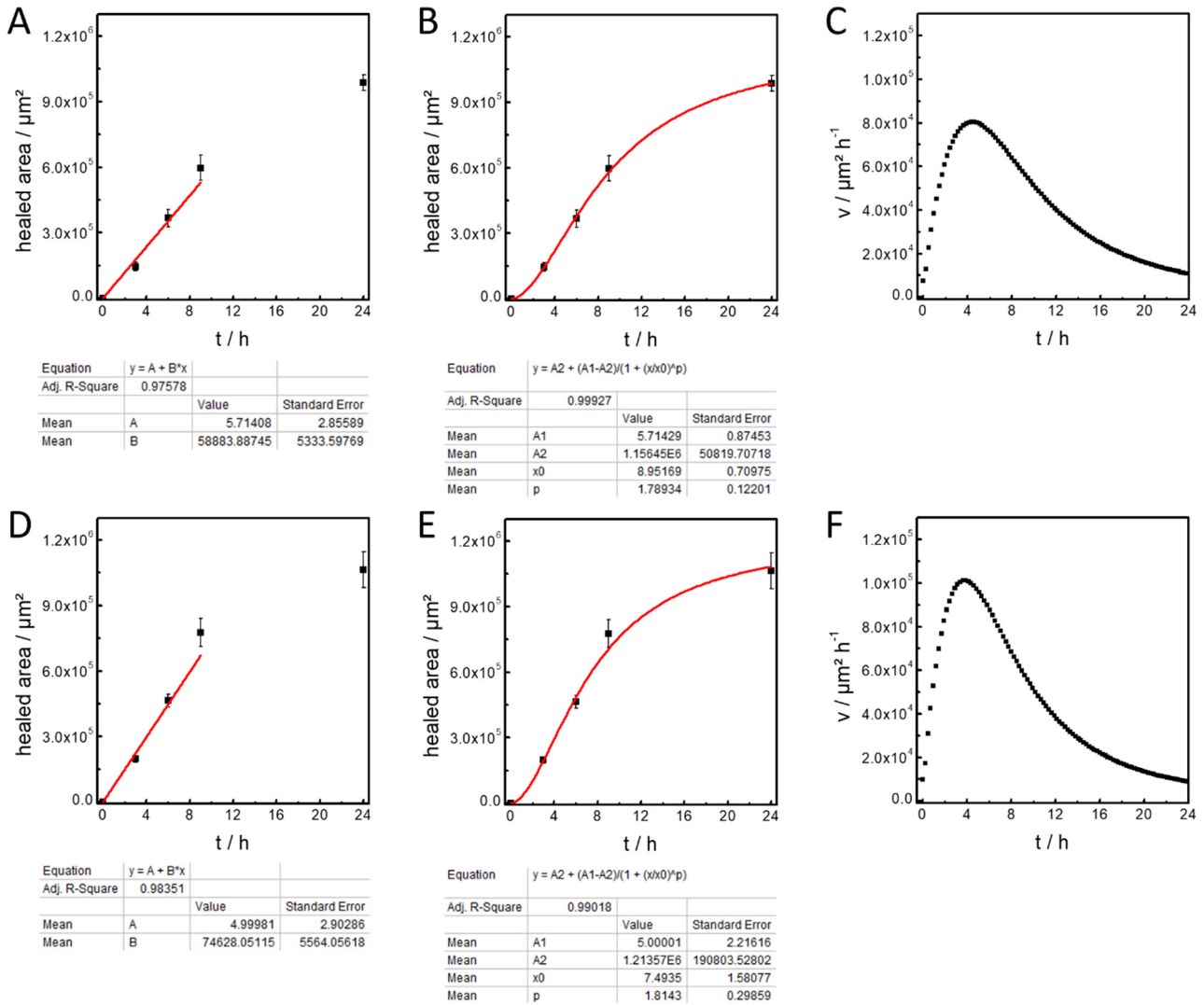


Fig. 11.20 Analysis of raw data as recorded for the barrier wound healing assay. (A) Linear fit to determine the wound healing rate of NRK cells on standard cell culture petri dishes with corresponding fit parameters. Wound healing rate v was determined from the slope ($v / \mu\text{m}^2 \text{h}^{-1} = B$). Mean \pm SE; $n = 7$, $T = 37^\circ\text{C}$. (B) Logistic fit to determine wound healing rate and additional fit parameter estimates. Time of half closure of the wound was determined by x_0 . (C) Wound healing rate was determined by differentiation of the logistic fit curve confined to 100 points per experiment. (D) Linear fit to determine wound healing rate of NRK cells on PS/PtTFPP substrates with corresponding fit parameters. Wound healing rate v was determined from the slope ($v / \mu\text{m}^2 \text{h}^{-1} = B$). Mean \pm SE; $n = 10$, $T = 37^\circ\text{C}$. (E) Logistic fit to determine wound healing rate and corresponding fit parameters. Time of half closure of the wound is expressed as x_0 . (F) Wound healing rate was determined by differentiation of the fitted data. Parameter estimates as returned from the fitting procedure were not processed with respect to significant digits.

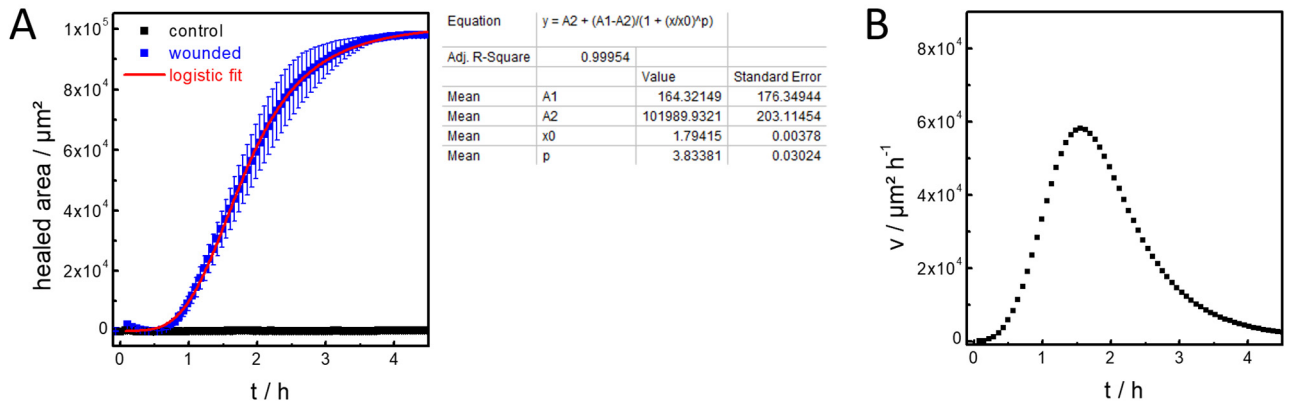


Fig. 11.21. (A) Logistic fit to determine the wound healing rate of NRK cells electrically wounded on ECIS® gold film electrodes and corresponding fit parameter estimates. Time of half closure of the wound is expressed as x_0 . (B) Wound healing rate was determined by differentiation of the logistic fit curve confined to 100 points per experiment. Mean \pm SE, $n \geq 2$, $T = 37^\circ\text{C}$.

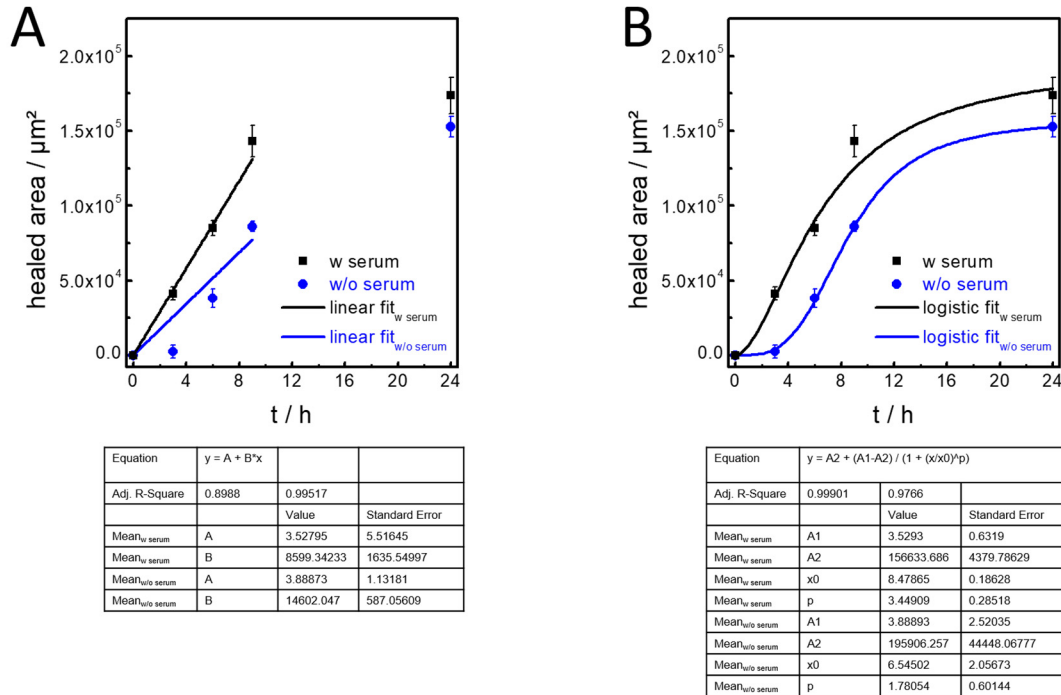


Fig. 11.22 Analysis of raw data as recorded for serum deprived NRK cells after optical wounding on PS/PtTFPP substrates. Confluent NRK monolayers were deprived of serum 24 h before wounding. (A) Linear fit to determine the wound healing rate of control (■) and serum deprived cells (●) with additional fit parameter estimates. Wound healing rate v was determined from the slope ($v / \mu\text{m}^2 \text{h}^{-1} = B$). (B) Logistic fit to determine wound healing rate and corresponding fit parameters of serum deprived cells (●) and control cells (■). Time of half closure of the wound is expressed as x_0 . Parameter estimates as returned from the fitting procedure were not processed with respect to significant digits. Mean \pm SE; $n = 17$, $T = 37^\circ\text{C}$.

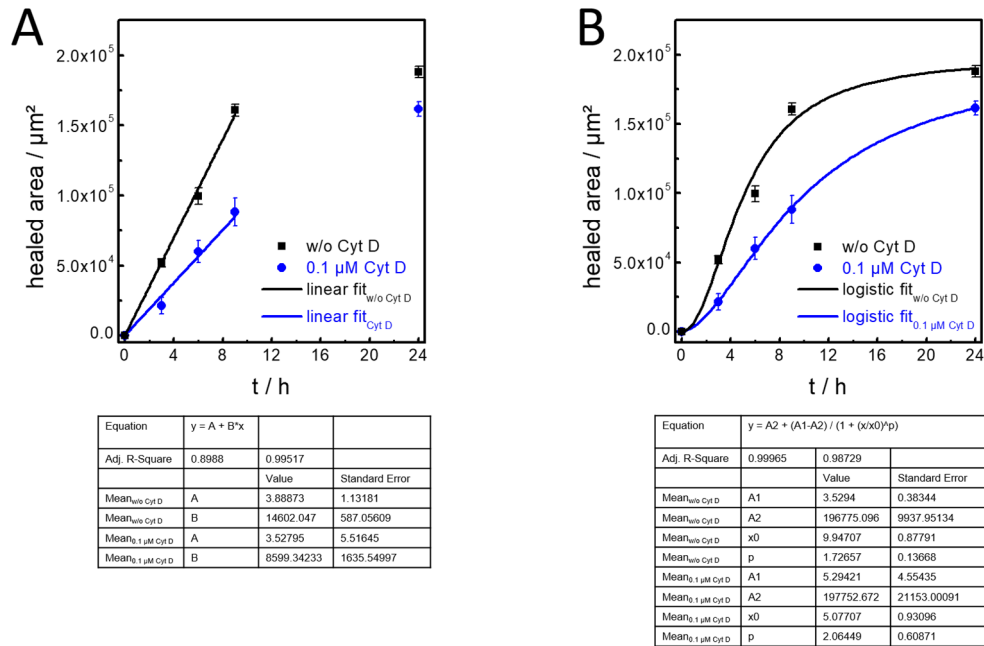


Fig. 11.23 Fitted data for NRK cells after optical wounding on PS/PtTFPP substrates. NRK cells were treated with 0.1 μM Cyt D after wounding to reduce cell motility. (A) Linear fit to determine the wound healing rate of control (■) and Cyt D treated cells (●) with corresponding fit parameters. Wound healing rate v was determined from the slope ($v / \mu\text{m}^2 \text{h}^{-1} = B$). (B) Logistic fit to determine wound healing rate and corresponding fit parameters of Cyt D treated cells (●) and control cells (■). Time of half closure of the wound is expressed as x_0 . Parameter estimates as returned from the fitting procedure were not processed with respect to significant digits. Mean \pm SE; $n = 17$, $T = 37$ °C.

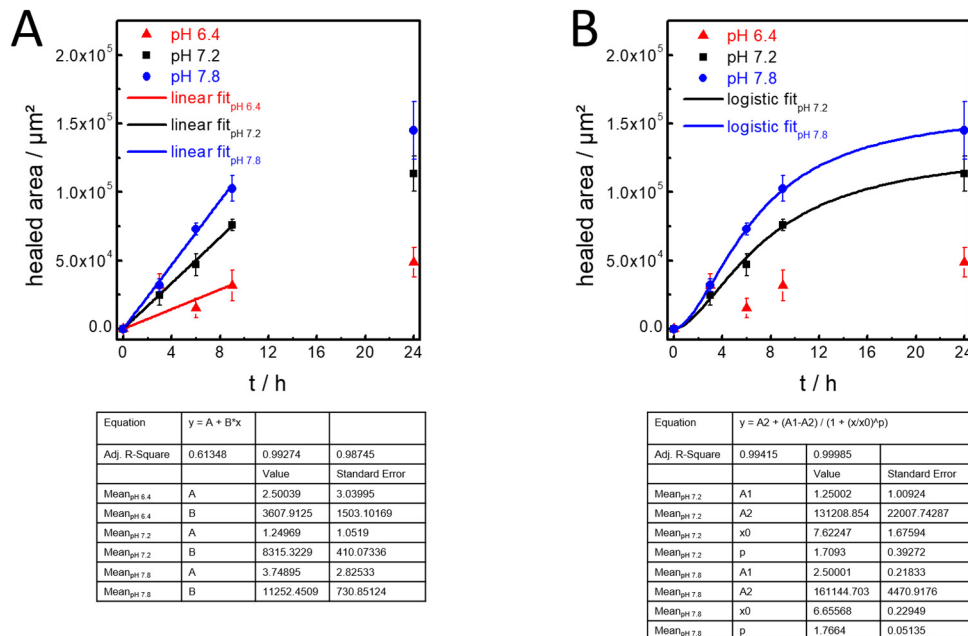
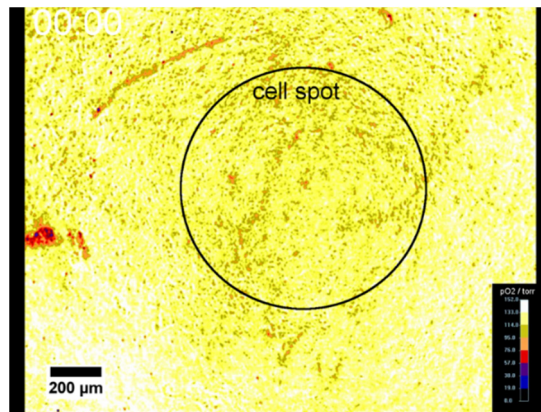
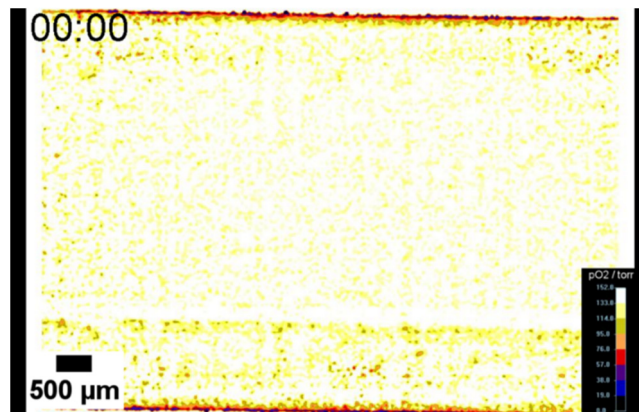


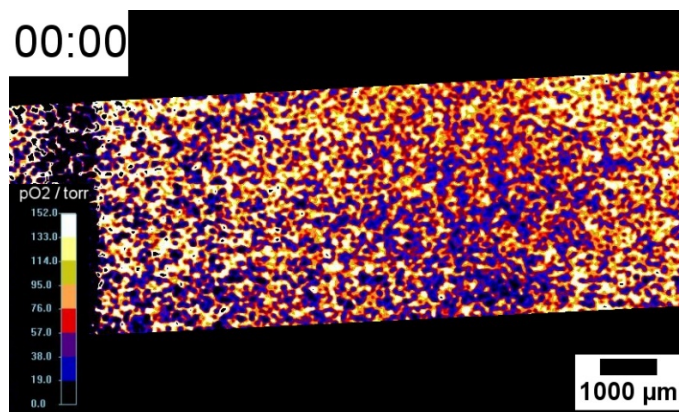
Fig. 11.24 Analysis of raw data as recorded for NRK cells after optical wounding on PS/PtTFPP substrates. Wound closure was monitored in L-15 medium adjusted to different pH values. (A) Linear fit to determine the wound healing rate of NRK cells incubated in L-15 medium with pH values adjusted to 6.4 (▲), 7.2 (■) and 7.8 (●). Wound healing rate v was determined from the slope ($v / \mu\text{m}^2 \text{h}^{-1} = B$). (B) Logistic fit to determine wound healing rates and corresponding fit parameters of NRK cells incubated with L-15 medium with pH values adjusted to 7.2 (■) and 7.8 (●). Time of half closure of the wound is expressed as x_0 . At pH 6.4 (▲), data could not be fitted successfully. Parameter estimates as returned from the fitting procedure were not processed with respect to significant digits. Mean \pm SE; $n = 17$, $T = 37$ °C.

Video Stills (videos on the enclosed DVD)

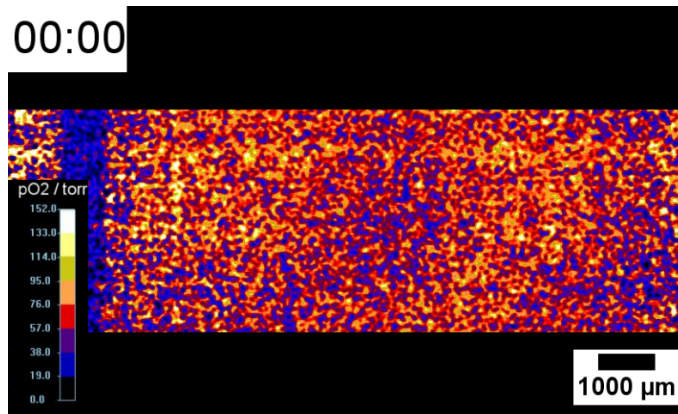
Video 11.1 Oxygen gradient formation by a respiring MDCK II cell patch monitored at $T = 37\text{ }^{\circ}\text{C}$. The video shows false color images of the spatial changes of $p\text{O}_2$ as a function of time over a period of 60 h. Time delay between each image is 15 min.



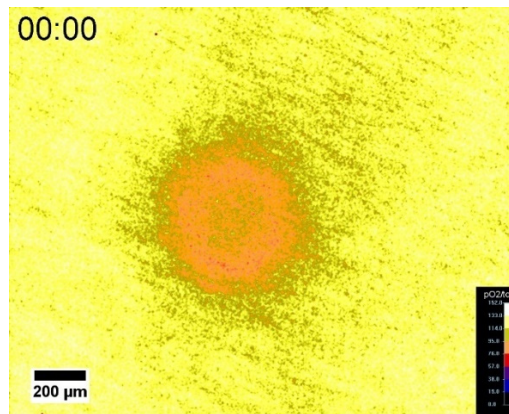
Video 11.2 Time lapse video of MDCK II cells cultivated in a microchannel (ibidi sticky-Slide I 0.4 luer) with a time delay of 5 min between each image. Cells were cultivated in L-15 medium. Fresh medium was added at $t = 0\text{ h}$, $t = 2.58\text{ h}$ and $t = 5.25\text{ h}$. Spatial distribution of $p\text{O}_2$ is displayed as false color oxygen images. $T = 37\text{ }^{\circ}\text{C}$.



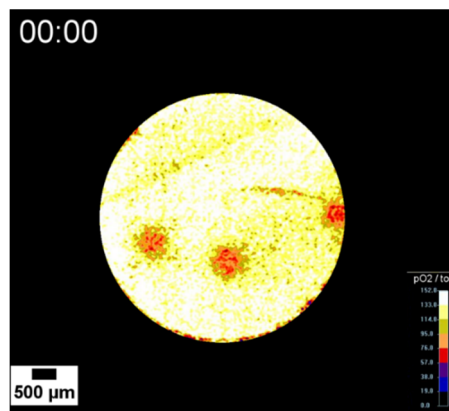
Video 11.3 Time lapse video of MDCK II cells cultivated in the ECIS- O_2 chip. Images were recorded every 15 min. Basal oxygen consumption was monitored for 5 h in L-15 medium before medium was exchanged to L-15 medium containing 100 nM of the uncoupling agent malonoben. After 10 h 45 min cells were permeabilized by addition of L-15 medium + 0.3 % saponin. Spatial distribution of $p\text{O}_2$ is displayed as false color oxygen images. For better visualization of the culture well, areas outside of the channel were outlined in black using the NIH ImageJ software. $T = 37\text{ }^{\circ}\text{C}$.



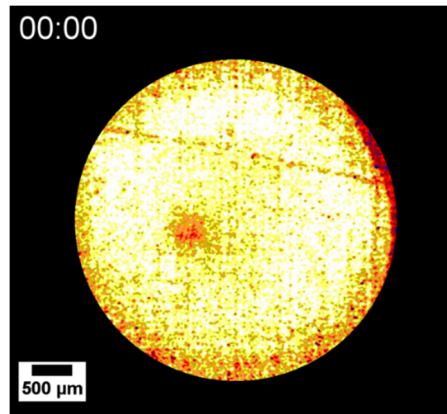
Video 11.4 Time lapse video of MDCK II cells cultivated in the ECIS-O₂ chip. Images were recorded every 15 min. Basal oxygen consumption was monitored for 5 h in L-15 medium before medium was exchanged to L-15 medium containing 2 μM of the blocking agent antimycin A. After 10 h 45 min cells were permeabilized by addition of L-15 medium + 0.3 % saponin. Spatial distribution of pO₂ is displayed as false color oxygen images. For better visualization of the culture well, areas outside of the channel were outlined in black using the NIH ImageJ software. T = 37 °C.



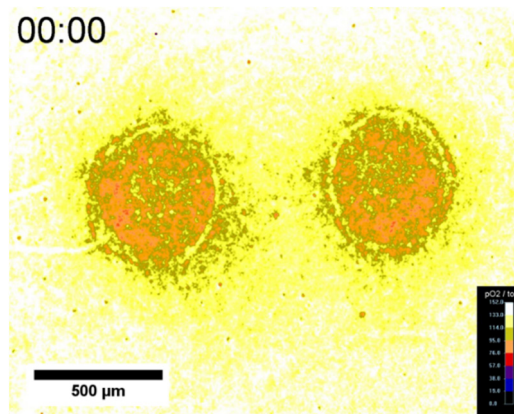
Video 11.5 Oxygen gradient formation of a MCF-7 spheroid adhered to the surface of the oxygen sensor foil. Oxygen recordings were made in L-15 medium at T = 37 °C. The video shows the spatial changes of pO₂ as a function of time over a period of 9.5 h depicted in false color images. The time delay between each image is 10 min.



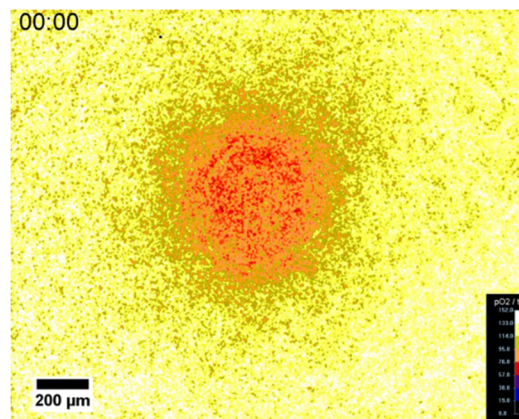
Video 11.6 Time lapse video of oxygen gradients caused by three actively respiring 9 d old MCF-7 spheroids grown on the RPsU4 oxygen sensor foil, monitored in L-15 medium. Oxygen levels are displayed in false color. Images were recorded every 15 min using the VisiSens A1 camera system with a suitable tube (tube 1) for a period of 24 h. T = 37 °C.



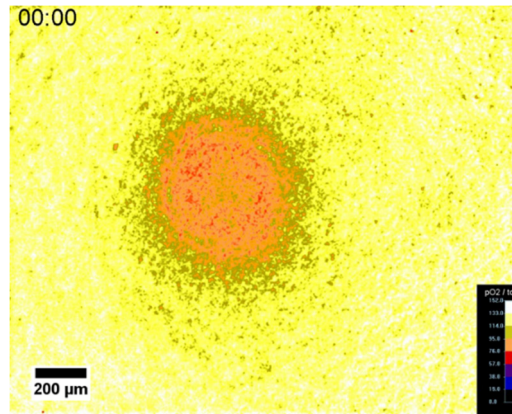
Video 11.7 Time lapse video of oxygen gradient formation by a respiring 9 d old MCF-7 spheroid grown on the RPsU4 oxygen sensor foil. Oxygen recordings of the spheroids were done in L-15 medium. Oxygen levels are displayed in false color. Images were recorded every 15 min using the VisiSens A1 camera system with a suitable tube (tube 2) for a period of 24 h. $T = 37\text{ }^{\circ}\text{C}$.



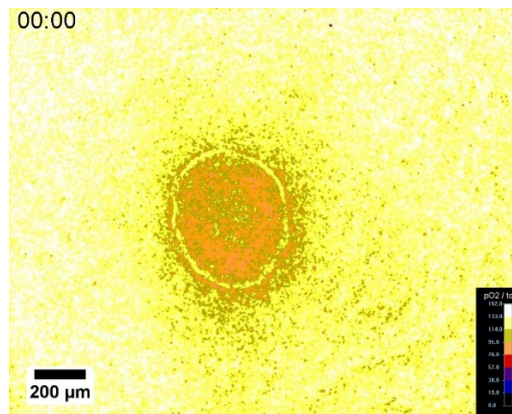
Video 11.8 Time lapse video of two respiring MCF-7 spheroids forming oxygen gradients. The spheroids were monitored in L-15 medium at $T = 37\text{ }^{\circ}\text{C}$. Oxygen levels are displayed in false color. Images were recorded every 10 min for 24 h using the novel VisiSens TD mic imaging system.



Video 11.9 Time lapse video of a respiring 9 d old MCF-7 spheroid grown on the surface of the oxygen sensor foil displaying 2D oxygen distribution in false color. Formation of the oxygen gradient was first monitored in L-15 medium. After 8 h fresh L-15 medium was added. Images were recorded every 15 min using the VisiSens TD mic system. $T = 37\text{ }^{\circ}\text{C}$.



Video 11.10 Time lapse video of a respiring 9 d old MCF-7 spheroid grown on the surface of the oxygen sensor foil, displaying 2D oxygen distribution in false color. Formation of the oxygen gradient was first monitored in L-15 medium at $T = 37\text{ }^{\circ}\text{C}$. After 8 h, fresh L-15 medium containing 50 nM of the uncoupling drug malonoben was added. Images were recorded every 15 min using the VisiSens TD mic imaging system.



Video 11.11 Time lapse video of a 9 d respiring MCF-7 spheroid grown on the surface of the oxygen sensor foil, displaying 2D oxygen distribution in false color. Formation of the oxygen gradient was first monitored in L-15 medium. After 8.5 h, fresh L-15 medium containing 2 μM of the blocking agent antimycin A was added. Images were recorded every 15 min using the VisiSens TD mic imaging system. $T = 37\text{ }^{\circ}\text{C}$.

11.2 LIST OF ABBREVIATIONS

A	
AC	Alternating current
Ant A	Antimycin A
Ar	Argon
ATP	Adenosine triphosphate
B	
β	Mass concentration
C	
C	Capacitance
c	Concentration
C-dot	Carbon (nano)dot
CaAM	Calcein acetoxymethylester
CCCP	Carbonyl cyanide 3-chlorophenylhydrazone
CCD	Charge coupled device
CLSM	Confocal laser scanning microscope
Cyt D	Cytochalasin D
D	
d	Diameter
DC	Direct current
DMEM	Dulbecco's modified eagle's medium
DMSO	Dimethyl sulfoxide
DNP	2,4-dinitrophenol
E	
ECIS	Electric cell-substrate impedance sensing
ECM	Extracellular matrix
EDTA	Ethylenediaminetetraacetic acid
EthD-1	Ethidium homodimer
F	
f	Frequency
FCCP	carbonyl cyanide p-trifluoromethoxyphenyl-hydrazone
FCS	Fetal calf serum
Fig.	Figure
G	
Gal	D-Galactose
Glc	D-Glucose
H	
h	Height
HEPES	4-(2-hydroxyethyl)-1-piperazineethane-sulfonic acid
L	
L-15	Leibovitz medium
LED	Light emitting diode
M	
Mal	Malonoben
MDCK II	Madin-Darby canine kidney strain II

MFT	Multi-frequency/time
MMP	Matrix metalloproteinase
M _w	Molecular weight
N	
ND	Neutral density
NRK	Normal rat kidney
O	
OCR	Oxygen consumption rate
P	
PBS ⁻	Phosphate buffered saline (without Ca ²⁺ and Mg ²⁺)
PBS ⁺	Phosphate buffered saline (with Ca ²⁺ and Mg ²⁺)
PDMS	Polydimethylsiloxane
PFA	Paraformaldehyde
PLIM	Phosphorescence lifetime imaging microscopy
pO ₂	Oxygen partial pressure
PS	Polystyrene
PtTFPP	5,10,15,20-Tetrakis(2,3,4,5,6-pentafluorophenyl)- porphyrin-platinum(II)
R	
R	Resistance
RLD	Rapid lifetime determination
ROI	Region of interest
RT	Room temperature
S	
Sap	Saponin
SFM	Serum free medium
SPR	Surface plasmon resonance
T	
t	Time
Tab.	Table
V	
Vit E	Vitamin E (D-α-tocopherol)
Z	
Z	Impedance
Other Abbreviations	
8W2LE	ECIS [®] array consisting of 8 wells with a single linear electrode in each well

11.3 MATERIALS AND INSTRUMENTATIONS

A

Agarose
 Alexa Fluor 488 phalloidin
 Antimycin A
 Argon Plasma Cleaner PDC 32G-2
 Artificial Air (20.9% O₂)
 Autoclave DX-45

Sigma-Aldrich, St. Louis, USA
 Invitrogen, Darmstadt, GER
 Sigma-Aldrich, St. Louis, USA
 Harrick Plasma, Ithaca, USA
 Linde, Pullach, GER
 Systec, Wetzlar, GER

B

Blu-Tack®
 Bunsen Burner for Cell Culture
 Bürker Hemocytometer

Bostik Ltd., Stafford, UK
 IBS Tecnomara GmbH, Fernwald, GER
 The Paul Marienfeld GmbH & Co. KG, Lauda-Königshofen, GER

C

Calcein AM
 Carbofuchsin
 Cell Culture Flasks (25 cm²)
 Cell Culture Incubator
 Cell Culture Medium (DMEM, MEM Eagle)
 Cell Culture Petridishes (d = 3.5 cm, d = 9 cm)
 Cell Culture Plate 96 Well
 Centrifuge Heraeus Multifuge 1 S-R for Cell

Invitrogen, Darmstadt, GER
 Sigma-Aldrich, St. Louis, USA
 Sarstedt, Nümbrecht, GER
 Thermo Fisher Scientific Inc., München, GER
 Sigma-Aldrich, St. Louis, USA
 Sarstedt, Nümbrecht, GER
 Sarstedt, Nümbrecht, GER
 Thermo Fisher Scientific Inc., München, GER

Centrifuge Tubes (15 ml, 50 ml)

Sarstedt, Nümbrecht, GER

Cryovial TPP®
 Culture insert® (2 chamber)
 Cytochalasin D

Sigma-Aldrich, St. Louis, USA
 ibidi GmbH, Martinsried, GER
 Sigma-Aldrich, St. Louis, USA

D

D- α -tocopherol
 DMSO

Caesar & Loretz, Hilden, GER
 Carl Roth GmbH, Karlsruhe, GER

E

ECIS® Impedance Analyzer
 EDTA
 Electrode Arrays (8W2LE)
 Elma Clean
 Eth-D1
 Ethanol

Applied BioPhysics Inc., Troy, USA
 Sigma-Aldrich, St. Louis, USA
 Applied BioPhysics Inc., Troy, USA
 Hans Schmidbauer GmbH & Co KG, Singen, GER
 Biotrend Chemikalien GmbH, Köln, GER
 Merck, Darmstadt, GER

F

FCS
 FCS (for spheroid cultivation)
 Fibronectin from human plasma

Sigma-Aldrich, St. Louis, USA
 Biochrom KG, Berlin, GER
 Sigma-Aldrich, St. Louis, USA

G

D-Galactose
 Gelatin
 D-Glucose
 L-Glutamine

Merck, Darmstadt, GER
 Sigma-Aldrich, St. Louis, USA
 Merck, Darmstadt, GER
 Biochrom KG, Berlin, GER

H

HEPES

Carl Roth GmbH, Karlsruhe, GER

I

Impedance Analyzer SI 1260

Solartron, Farnborough, UK

L

LabVIEW™ software

National Instruments, Austin, USA

Laminar Air Flow Work Bench HERAsafe®

Thermo Fisher Scientific Inc., München, GER

Latex Gloves

Carl Roth GmbH, Karlsruhe, GER

Leibovitz Medium

Sigma-Aldrich, St. Louis, USA

Liquid Nitrogen Tank GC-BR2150 M

German-Cryo GmbH, Jüchen, GER

M

Malonoben

Sigma-Aldrich, St. Louis, USA

Micro Centrifuge

Carl Roth GmbH, Karlsruhe, GER

Microscope Lens EC Epiplan-Neofluar 5x

Zeiss, Jena, GER

Microscope Nikon Diaphot & Nikon Eclipse 90i

Nikon Instruments Europe, Amstelveen, NLD

Microscope Nikon SMZ 1500 C-DSD230 CMO

Nikon Instruments Europe, Amstelveen, NLD

N

Nalgene® CryoBox™

Sigma-Aldrich, St. Louis, USA

O

Orbital Shaker KM-2 AKKU

Edmund Bühler GmbH, Hechingen, GER

Oxygen Imaging System VisiSens TD

PreSens GmbH, Regensburg, GER

Oxygen Imaging System VisiSens VA

PreSens GmbH, Regensburg, GER

Oxygen Sensor Foil SF-RPSu4

PreSens GmbH, Regensburg, GER

P

Parafilm®

Pechiney Plastic Packaging, Chicago, USA

Paraformaldehyde

Sigma-Aldrich, St. Louis, USA

PBS⁻/PBS⁺⁺

Sigma-Aldrich, St. Louis, USA

Penicillin/Streptomycin

Sigma-Aldrich, St. Louis, USA

Pipettes (10 µl, 200 µl, 100 µl)

Brand GmbH, Wertheim, GER

Pipette Tips (10 µl, 200 µl, 100 µl)

Sarstedt, Nümbrecht, GER

Poly-L-Lysine Hydrobromide

Sigma-Aldrich, St. Louis, USA

(M_w = 30000 – 70000 g/mol)

Polystyrene

Sigma-Aldrich, St. Louis, USA

(M_n = 140000 g/mol, M_w = 230000 g/mol)

Potassium phosphate

Sigma-Aldrich, St. Louis, USA

PtTFPP

Porphyrin Systems GbR, Appen, GER

R

Reaction Tubes 500 µl – 2 ml

Sarstedt, Nümbrecht, GER

S

Saponin

Sigma-Aldrich, St. Louis, USA

Silicon Glue Aquadicht PROBAU

Bauhaus, Regensburg, GER

Silicone Glue Type SG-1

PreSens GmbH, Regensburg, GER

Sodium dihydrogen phosphate

Sigma-Aldrich, St. Louis, USA

Sodium sulfite

Merck, Darmstadt, GER

Sputter Coater Bal-Tec SCD 050

Capovani Brothers Inc., Scotia, USA

Sterile filter (pore diameter 0.2 µm)

TPP, Trasachingen, CH

Sticky-Slide I^{0.4} Luer

ibidi GmbH, Martinsried, GER

Sylgard® 182 Silicone Elastomer Kit

Dow Corning, Midland, USA

T

TI Prime
Toluene
Triton-X-100
Trypsin 0.05% (w/v), 0.25% (w/v)
TV-Tube

Microchemicals, Ulm, GER
Merck, Darmstadt, GER
Sigma-Aldrich, St. Louis, USA
Sigma-Aldrich, St. Louis, USA
Opto, Gräfelfing, GER

U

Ultrasonic Bath Sonorex Digitech

Bandelin Electronics, Berlin, GER

V

Vitamin E
Vortex Mixer
VisiSens A1

Caesar & Loretz GmbH, Hilden, GER
Heidolph Elektro GmbH & Co. KG, Kelheim, GER
PreSens GmbH, Regensburg, GER

W

Waterbath TW12
Weighting Instrument

Julabo GmbH, Seelbach, GER
Mettler-Toledo, Columbus, USA

11.4 CURRICULUM VITAE



Personal Information

Name	Carina Schmittlein
Date of Birth	December 23 rd 1988
Place of Birth	Ingolstadt, Germany
Nationality	German

University Studies and School Education

09/2017 – now	Osram Opto Semiconductors GmbH, Regensburg Process Engineer Photolithography
06/2013 – 08/2017	University of Regensburg, Germany Doctoral Student for a PhD in science (Dr. rer. nat.) Working Group Bioanalytics and Biosensors, Prof. Dr. J. Wegener Institute of Analytical Chemistry, Chemo- and Biosensors
10/2008 – 04/2013	University of Regensburg, Germany Studies of Biology and Chemistry (State Examination) <u>Thesis:</u> Klonierung und Analyse von drei Überexpressionskonstrukten: dfuselBkC, dfuselBkC-GFP und dfuselBk-GFP in <i>Drosophila melanogaster</i> Department of Developmental Biology, Prof. Dr. S. Schneuwly Institute of Zoology
09/2002 – 06/2008	Gymnasium Beilngries, Germany Graduation: University-entrance Diploma (Abitur)
09/1999 – 07/2002	Ostendorfer Gymnasium, Neumarkt i.d. Opf., Germany

List of Publications

Wang X.-D., Meier R. J., Schmittlein C., Schreml S., Schäferling M., Wolfbeis O. S., (2015) ***A water-sprayable, thermogelating and biocompatible polymer host for use in fluorescent chemical sensing and imaging of oxygen, pH values and temperature***, Sensors and Actuators B: Chemical 221, 37-44

Hajek K.*, Schmittlein C.*, Oberleitner M., I.-S. Shin, Wegener J., (2016) ***Biosensors***, eLS. John Wiley & Sons Ltd, [doi: 10.1002/9780470015902.a0026401]

(* both authors contributed equally to the work)

Schmittlein C., Meier R. J., Hupf C., Wegener J., ***Visualizing Locally Resolved Hypoxia in MCF-7 Spheroids with High Spatial Resolution via a Luminescent Oxygen Imaging System*** (in preparation)

Poster Presentations

Measuring Oxygen Consumption of Adherent Cells and Oxygen Tissue Gradients, Schmittlein C., Hupf C., Oberleitner M., Wegener J., 9. Deutsches BioSensor Symposium, Munich, Germany, March 2015

Measuring Oxygen Consumption of Adherent Cells and Oxygen Tissue Gradients, Schmittlein C., Hupf C., Oberleitner M., Wegener J., 11th Workshop on Biosensors & Bioanalytical Microtechniques in Environmental, Food & Clinical Analysis, Regensburg, Germany, September 2015

An Optical Imaging System for Monitoring of Oxygen Gradients within Live Tumor Spheroids, Schmittlein C., Meier R. J., Hupf C., Wegener J., 3D Cell Culture, Freiburg, Germany, April 2016

An Optical Imaging System capable of Monitoring Oxygen Consumption and Oxygen Gradients in Monolayers of Adherent Mammalian Cells, Schmittlein C., Meier R. J., Hupf C., Wegener J., Biosensors, Gothenburg, Sweden, May 2016

Impedimetric/Luminescent Dual Mode Readout for Multiparametric Online Analysis of Adherent Cells, Schmittlein C., Meier R. J., Wegener J., 3rd Conference on Impedance-Based Cellular Assays, Regensburg, Germany, August 2016

An Optical Imaging System capable of Monitoring Oxygen Consumption and Gradients within Live Tumor Spheroids, Schmittlein C., Meier R. J., Hupf C., Wegener J., 1st European Biosensor Symposium, Potsdam, Germany, March 2017

11.5 DANKSAGUNG

Hiermit möchte ich mich ganz herzlich bei allen Menschen bedanken, die mich während meiner Doktorarbeit unterstützt haben und mir mit Rat und Tat zur Seite gestanden sind!

Mein größter Dank gilt Prof. Dr. Joachim Wegener, der es mir ermöglicht hat dieses Promotionsthema zu bearbeiten. Vielen Dank für deine fachliche Unterstützung, Betreuung und schöne Zeit in der Arbeitsgruppe!

Bei Prof. Dr. Jörg Heilmann möchte mich für die Übernahme des Zweitgutachtens bedanken. Mein Dank gilt auch PD Dr. Miriam Breunig für die Übernahme des Amtes als Drittprüferin, sowie Prof. Dr. Rainer Müller für den Prüfungsvorsitz. Vielen Dank, dass Sie sich Zeit für mich genommen haben.

Ganz herzlich möchte ich mich auch bei der Firma PreSens (Regensburg) für die gemeinsame Zusammenarbeit, die materielle, sowie finanzielle Unterstützung bedanken. Mein besonderer Dank gilt hierbei Dr. Robert Meier, der keine Zeit und Mühen gescheut hat mir bei Fragen und Problemen zu helfen.

Mein Dank gilt allen Mitgliedern und ehemaligen Mitstreitern des AK Wegener. Vielen Dank für die super Arbeitsatmosphäre, angeregte Diskussionen, Kaffee und „Kaltgetränke“, diverse Kanufahrten und alle lustigen Grillabende!

Ein besonderes Dankeschön möchte ich an Dr. Stefanie Michaelis aussprechen. Bei Fragen hattest du immer ein offenes Ohr für mich! Vielen Dank für deine Korrektur meiner Arbeit – deinen Augen entgeht nichts! – und unsere gemeinsamen Ausflüge ins Sportzentrum!

Vielen Dank an meine Laborkollegen Zlatko Paric und Maria Zinkl. Ich werde mich immer gern an unser „balkanesisches Sonnenscheinlabor“ erinnern!

Bedanken möchte ich mich außerdem bei Dr. Christina Hupf und Pierre Pütz für die Herstellung und das Bereitstellen der MCF-7 Sphäroide. Sowie bei Dr. Michael Lemberger und Pierre Pütz für das Bereitstellen der C-dots. Außerdem möchte ich mich bei Lisa Sauer und Michael Skiba bedanken, die mich im Rahmen ihrer Masterarbeit bzw. seiner Bachelorarbeit an einigen Studien beteiligt waren.

Abschließend möchte ich meiner und Johannes Familie danken, die mir immer den nötigen Rückhalt geboten hat, egal was auch passiert ist. Bei Johannes möchte ich mich bedanken, der immer für mich da war. Vielen Dank für eure Unterstützung in Form von offenen Ohren, Essensversorgung, Arbeitsbeschaffungsmaßnahmen und vieles mehr. Ohne euch wäre diese Arbeit nicht entstanden!

11.6 EIDESSTATTLICHE ERKLÄRUNG

Ich erkläre hiermit an Eides statt, dass ich die vorliegende Arbeit ohne unzulässige Hilfe Dritter und ohne Benutzung anderer als der angegebenen Hilfsmittel angefertigt habe; die aus anderen Quellen direkt oder indirekt übernommenen Daten und Konzepte sind unter Angabe des Literaturzitats gekennzeichnet.

Weitere Personen waren an der inhaltlich-materiellen Herstellung der vorliegenden Arbeit nicht beteiligt. Insbesondere habe ich hierfür nicht die entgeltliche Hilfe eines Promotionsberaters oder anderer Personen in Anspruch genommen. Niemand hat von mir weder unmittelbar noch mittelbar geldwerte Leistungen für Arbeiten erhalten, die im Zusammenhang mit dem Inhalt der vorgelegten Dissertation stehen.

Die Arbeit wurde bisher weder im In- noch im Ausland in gleicher oder ähnlicher Form einer anderen Prüfungsbehörde vorgelegt.

Ort, Datum

Unterschrift